

Teleoperation from Movable Bases: Modeling, Analysis, Design and Experiments with a Hydraulic Motion Platform

by

Mohammad Reza Sirouspour

B.Sc. (Electrical Engineering) Sharif University of Technology, Tehran/Iran, 1995

M.Sc. (Electrical Engineering) Sharif University of Technology, Tehran/Iran, 1997

A THESIS SUBMITTED IN PARTIAL FULFILLMENT OF
THE REQUIREMENTS FOR THE DEGREE OF
DOCTOR OF PHILOSOPHY

in

THE FACULTY OF GRADUATE STUDIES
(Department of Electrical and Computer Engineering)

We accept this thesis as conforming
to the required standard

THE UNIVERSITY OF BRITISH COLUMBIA

March 2003

© Mohammad Reza Sirouspour, 2003

In presenting this thesis in partial fulfilment of the requirements for an advanced degree at the University of British Columbia, I agree that the Library shall make it freely available for reference and study. I further agree that permission for extensive copying of this thesis for scholarly purposes may be granted by the head of my department or by his or her representatives. It is understood that copying or publication of this thesis for financial gain shall not be allowed without my written permission.

Department of Electrical & Computer Eng.

The University of British Columbia
Vancouver, Canada

Date April 02, 2003

Abstract

There are manual control and teleoperation systems in which the operator is subject to base motion. Examples are aircraft piloting and joystick control of heavy hydraulic machines such as excavators. This thesis presents a new framework for the modeling, analysis, design and evaluation of controllers for teleoperation/manual control from movable bases.

First, a general model for teleoperation/manual control from movable bases is presented. Second, models for the operator dynamics are introduced and identified experimentally. Third, a novel robust μ -synthesis based control system design approach is proposed that addresses robust stability and performance issues. The approach is illustrated by a prototype single-degree-of-freedom manual control task in which the operator positions his/her base, a hydraulic motion simulator, using a force-feedback joystick. The designed controllers are robustly stable with respect to parametric uncertainties in the arm/joystick as well as the feedthrough dynamics, and achieve a desired level of performance based on relevant measures. The proposed methods are compared with controllers that ignore the base motion through analysis and a set of experiments. The robust controllers suppress the operator-induced oscillations and produce well-damped responses, whereas the fixed base controllers become unstable.

Motivated by the need for high performance motion simulation in the evaluation of controllers for feedthrough cancellation, the position control of mechanical systems driven by hydraulic actuators is studied. This includes single-cylinder hydraulic servo-systems and multiple-degree-of-freedom hydraulic robots. Nonlinear dynamics of the actuators and nonlinear rigid body dynamics are considered in the model of hydraulic robots. For single-degree-of-freedom systems, valve dynamics are also included. Parametric uncertainties are allowed in these models.

Using the *backstepping* technique, novel nonlinear and adaptive/nonlinear control laws are proposed that incorporate the system dynamics into their design. It is proven via Lyapunov

analysis that the closed-loop systems are stable and that the tracking errors converge to zero under the proposed feedback laws. The effectiveness of these approaches is demonstrated through a series of simulations and experiments carried out with the UBC hydraulic motion simulator.

Finally, a numerical approach is developed to optimize the feedback gains for a simplified version of the proposed nonlinear controllers for hydraulic servo-systems.

Contents

Abstract	ii
Table of Contents	iv
List of Tables	viii
List of Figures	ix
Glossary	xiii
Acknowledgments	xviii
Dedication	xix
1 Introduction	1
1.1 Background	1
1.2 Prior Work	5
1.2.1 Modeling and Analysis of Manual Control/Teleoperation Systems	5
1.2.2 Effect of Base Motion	7
1.2.3 Control of Hydraulic Actuators	9
1.2.4 Control of Hydraulic Robots	11
1.3 Thesis Outline	13
2 Modeling of Teleoperation Systems with Movable Bases	17
2.1 Overview	17
2.2 A Bilateral Four-Channel Teleoperation Architecture	18

2.3	Models for Manual Control Systems	19
2.4	Teleoperation as Manual Control	22
2.5	Stability in Presence of Biodynamic Feedthrough	24
2.5.1	A two-channel position-position architecture	27
2.5.2	A four-channel architecture	29
2.6	Conclusions	30
3	Identification of Biodynamic Feedthrough and Arm/Joystick Dynamics	32
3.1	Overview	32
3.2	System Identification Using Stochastic Embedding	33
3.2.1	Estimating Measurement Noise and Undermodeling Parameters	38
3.3	Identification Experiments	40
3.4	Arm/Joystick and Acceleration Based Feedthrough Models	45
3.5	Comparison of the Feedthrough Models	49
3.6	Conclusions	49
4	Controller Design for Suppression of Biodynamic Feedthrough	52
4.1	Overview	52
4.2	Problem Statement	53
4.3	Robust Control Problem Formulation	58
4.4	Controller Design Assuming a Stationary Base	62
4.5	Robust Controller Design	64
4.5.1	Position-mode controller:	65
4.5.2	Feedthrough Cancellation Using Acceleration Compensation	69
4.5.3	Velocity mode controller:	70
4.6	Experimental Results	74
4.7	Conclusions	77
5	Adaptive Nonlinear Control of Hydraulic Servo-systems	78
5.1	Overview	78
5.2	System Dynamics	79
5.3	Controller Design	81

5.3.1	Non-adaptive Case	81
5.3.2	Adaptive Case	84
5.4	Simulation Results	86
5.4.1	Nonadaptive Controller	87
5.4.2	Adaptive Controller	88
5.5	Experimental Results	89
5.6	Conclusions	91
6	Numerical Optimization of a Single Cylinder Hydraulic Servo-system	93
6.1	Overview	93
6.2	System Dynamics	94
6.3	Control Law and Closed-loop Dynamics	95
6.4	Suboptimal Control Problem	100
6.5	Evaluation of the Performance Index and its Gradient	102
6.6	Optimization Results	103
6.6.1	Case 1	104
6.6.2	Case 2: Effect of initial position	106
6.6.3	Case 3: Effect of valve dynamics	107
6.6.4	Case 4: Effect of change in time horizon	109
6.6.5	Case 5: Effect of step length	110
6.7	Conclusions	110
7	Adaptive Nonlinear Control of Hydraulic Robots	112
7.1	Overview	112
7.2	Manipulator/Actuators Dynamics	113
7.3	Nonadaptive Controller	114
7.4	Adaptive Controllers	117
7.4.1	Adaptive Controller/ Adaptive Observer	118
7.4.2	Adaptive Controller/ Robust Observer	124
7.4.3	Effect of Friction	127
7.5	Simulation Results	128

7.6	Experimental Results	131
7.7	Conclusions	135
8	Conclusions	137
8.1	Thesis Contributions	137
8.2	Future Work	140
	Bibliography	142
	Appendices	152
A	Evaluation of the Objective Function and its Gradient	152
A.1	Objective Function	152
A.2	Gradient of Objective Function	154
B	Stewart Platform Kinematics and Dynamics	160
B.1	Platform Kinematics	160
B.1.1	Inverse Kinematics	160
B.1.2	Platform Jacobian	162
B.1.3	Forward Kinematics	164
B.2	UBC Motion Simulator Dynamics	165
B.2.1	Platform Rigid Body Dynamics	165
B.2.2	Actuator Dynamics	169
C	Joystick Kinematics and Control	171
C.1	Joystick Kinematics	171
C.2	Gravity Compensation	176
C.2.1	Identification of the Parameters	177

List of Tables

3.1	Identification results.	41
6.1	Performance of the optimization routines.	103
7.1	The parameters used in the simulations	128
B-1	Platform and base actuator endpoint angles.	163

List of Figures

1.1	A general manual control system.	2
1.2	The UBC motion simulator.	4
1.3	The twin-pantograph joystick.	4
2.1	A modified four-channel teleoperation configuration.	19
2.2	Crossover model of human-machine system.	20
2.3	Structural model of human-machine system.	21
2.4	A teleoperation system within the framework of manual control.	22
2.5	The teleoperation system without vision feedback.	26
2.6	Nyquist of a typical two-channel position-position architecture with biodynamic feedthrough.	28
2.7	Root locus of a typical two-channel position-position architecture with biodynamic feedthrough.	29
2.8	Nyquist of a typical four-channel teleoperation architecture with biodynamic feedthrough.	30
2.9	Root locus of a typical four-channel teleoperation architecture with biodynamic feedthrough.	30
3.1	The modified model structure.	34
3.2	The actual and predicted joystick displacements in one of the experiments.	42
3.3	Estimated biodynamic feedthrough response and its uncertainty ellipses.	43
3.4	Feedthrough model with uncertainty block.	44

3.5	Estimated magnitude of the biodynamic feedthrough response and its uncertainty bounds.	45
3.6	Simplified model of the arm/joystick and biodynamic feedthrough.	46
3.7	The arm/joystick model with uncertain parameters.	47
3.8	Arm/joystick identification results: (a) measured position. (b) computed velocity. (c) computed acceleration. (d) measured and estimated applied force.	48
3.9	The identified feedthrough responses.	50
3.10	The compensated identified feedthrough responses.	50
4.1	Schematic of the manual control task.	54
4.2	Experimental setup.	55
4.3	System block diagram.	59
4.4	(a) Controller in the μ -synthesis framework. (b) Robust performance problem.	60
4.5	Simplified block diagram of the system.	63
4.6	Frequency responses of the original, the reduced-order, and the fixed base controllers (position mode).	67
4.7	Robust (reduced-order) controller.	67
4.8	Frequency responses of the original, the reduced-order (with acceleration compensation).	70
4.9	Robust controller with acceleration compensation.	71
4.10	Frequency responses of the original, the reduced-order, and the fixed base controllers (velocity mode).	73
4.11	(a) Performance of the robust controller (velocity mode). (b) Upper bounds on $\mu_{\Delta_{pert}}$ (velocity mode).	73
4.12	Responses of the controllers with $c_k = -1.0$	74
4.13	(a) Response of the controllers with $c_k = -1.1$. (b) Response of the robust controller with acceleration compensation.	76
4.14	Response of controllers in the velocity mode.	76
4.15	The manual control tracking behavior.	77
5.1	A hydraulic servo-system with three-way valve configuration.	79

5.2	Block diagram of the hydraulic servo-system.	81
5.3	Position tracking with $f = 6\text{Hz}$ (simulation).	87
5.4	Actuator force tracking with $f = 6\text{Hz}$ (simulation).	87
5.5	The step response of the controllers (simulation).	88
5.6	Position tracking error for the adaptive controller (simulation).	88
5.7	The estimated parameters (simulation). Solid lines show the actual values.	89
5.8	The experimental setup.	90
5.9	The schematic of the controller.	91
5.10	The position tracking with $f = 2\text{Hz}$	92
5.11	Actuator force tracking with $f = 2\text{Hz}$	92
5.12	The position tracking with $f = 4\text{Hz}$	92
6.1	Single-rod hydraulic servo-system.	95
6.2	Profile of the performance index (SR1).	106
6.3	The trajectory of parameters (SR1).	106
6.4	Position of the actuator (case 1).	107
6.5	Velocity of the actuator (case 1).	107
6.6	Force tracking of the actuator (case 1).	107
6.7	Control command (case 1).	107
6.8	Position of the actuator (case 2).	108
6.9	Velocity of the actuator (case 2).	108
6.10	Force tracking of the actuator (case 2).	108
6.11	Control command (case 2).	108
6.12	Position of the actuator (case 3).	109
6.13	Control command (case 3).	109
6.14	Position of the actuator (case 4).	111
6.15	Velocity of the actuator (case 4).	111
6.16	Force tracking of the actuator (case 4).	111
6.17	Control command (case 4).	111
7.1	Position tracking errors for the controller with robust observer (simulation).	129

7.2	Parameter estimation errors for the controller with robust observer (simulation).	129
7.3	Position tracking errors for the controller with adaptive observer (simulation).	130
7.4	Parameter estimation errors for the controller with adaptive observer (simulation).	130
7.5	Controller with adaptive observer.	131
7.6	Controller with robust observer.	131
7.7	The experimental setup.	132
7.8	Position tracking (1Hz) along z coordinate (experiment).	133
7.9	Position tracking (2Hz) along z coordinate (experiment).	134
7.10	Position tracking (1Hz) along ψ coordinate (experiment).	134
7.11	Position tracking (1Hz) along θ coordinate (experiment).	135
7.12	Step response along z coordinate (experiment).	135
B.1	The schematic of the UBC Stewart platform.	162
B.2	A typical three-way valve configuration.	170
C.1	The schematic of the twin-pantograph force-feedback joystick.	173

Glossary

Z_h	The passive dynamics of the operator.
Z_{PF}	Models the operator's active position control of the joystick.
Z_F	Models the operator's active force control of the joystick.
Z_{BF}	Model of biodynamic feedthrough.
Z_e	The environment impedance.
Y_{NM}	The operator's neuromuscular dynamics.
Y_m	The master dynamics.
Y_s	The slave dynamics.
C_1	The position channel gain from master to slave.
C_2	The force channel gain from master to slave.
C_3	The force channel gain from slave to master.
C_4	The position channel gain from slave to master.
C_m	The joystick admittance shaping controller.
C_s	The slave local controller.
C_k	The desired kinematic correspondence between the joystick and the platform.
f_{bf}	Biodynamically induced force due to the base motion.
f_h	The hand force.
x_m	The master position.
x_s	The slave position.
m_{bf}	The actual biodynamic feedthrough mass.

m_f	The nominal (estimated) feedthrough mass.
G_T	The nominal transfer function of feedthrough dynamics.
G_Δ	The undermodeling in the feedthrough transfer function.
η	The vector of undermodeling parameters in the feedthrough model.
C_η	Covariance matrix of undermodeling parameters.
C_v	Covariance matrix of the noise vector in the feedthrough model.
σ_v^2	Variance of the noise in the feedthrough model.
σ_η^2	Variance of the undermodeling.
σ_{pe}^2	Variance of the prediction error.
z_p	Platform displacement.
z_j	Joystick displacement.
a_z	Platform acceleration.
P_θ	Covariance of the parameters vector θ in the feedthrough model.
$P_{\hat{g}}$	Covariance of the feedthrough estimation error.
m_m	The actual lumped mass of arm and joystick.
b_m	The actual lumped damping of arm and joystick.
k_m	The actual lumped stiffness of arm and joystick.
m	The estimated lumped mass of arm and joystick.
b	The estimated lumped damping of arm and joystick.
k	The estimated lumped stiffness of arm and joystick.
m_d	The desired lumped mass of arm and joystick.
b_d	The desired lumped damping of arm and joystick.
k_d	The desired lumped stiffness of arm and joystick.
δ_m	Uncertainty in the lumped arm and joystick mass.
δ_b	Uncertainty in the lumped arm and joystick damping.
δ_k	Uncertainty in the lumped arm and joystick stiffness.
δ_{mf}	Uncertainty in the feedthrough mass.

f_g	The gravitational force acting on arm and joystick.
τ_p	The time constant of the platform closed-loop dynamics.
W_{e1}	The frequency-dependent gain applied to the kinematic correspondence error.
W_{e2}	The frequency-dependent gain applied to the admittance shaping error.
W_{u_m}	The frequency-dependent gain applied to the joystick control force.
W_{u_s}	The frequency-dependent gain applied to the platform reference command.
W_f	The frequency-dependent gain applied to the hand force.
W_{nm}	The frequency-dependent gain applied to the joystick position measurement noise.
W_{ns}	The frequency-dependent gain applied to the platform position measurement noise.
W_{na}	The frequency-dependent gain applied to the platform acceleration measurement noise.
Y_D	The desired arm/joystick admittance.
u_m	The control force applied to the joystick.
\bar{u}_m	The normalized control force applied to the joystick.
u_s	The reference position command sent to the platform controller.
\bar{u}_s	The normalized reference position command sent to the platform controller.
τ_d	Time delay in data communication.
Δ_{pert}	Perturbation block.
Δ_{perf}	Virtual performance block.
G_{op}	Nominal open-loop transfer function.
\bar{x}_{ref}	Mean of the random target motion.
σ_{ref}^2	Variance of the random target motion.
\bar{x}_{err}	Mean of the tracking error.
σ_{err}^2	Variance of the tracking error.
f_{bw}	Bandwidth of the random target motion.
V_t	The volume of the trapped fluid in the control side.
L	The actuator stroke length.
q_l	The load flow.

β	The effective bulk modulus.
p_c	The pressure in the control side.
p_s	The pressure in the supply side.
x_v	The valve spool position.
c_l	The coefficient of the total leakage.
A	The piston area.
a	The annulus area.
c_d	The effective discharge coefficient.
w	The port width.
ρ	The density of the fluid.
d	The valve underlap length.
f_f	The friction force.
τ_e	The time constant of the valve dynamics.
g	The gravitational acceleration.
x_n	Position measurement noise.
v_n	Velocity measurement noise.
τ_n	Force (pressure) measurement noise.
n_x	The white noise that generates the position measurement noise.
n_v	The white noise that generates the velocity measurement noise.
n_τ	The white noise that generates the force (pressure) measurement noise.
τ_x	The time constant of the first-order filter for the position measurement noise.
τ_v	The time constant of the first-order filter for the velocity measurement noise.
τ_τ	The time constant of the first-order filter for the force (pressure) measurement noise.
J_x	Penalizes the state tracking error during the transition period.
J_{t_f}	Penalizes the state tracking error at the final time.
J_u	Penalizes excessive control action.
J_n	Penalizes noise amplification.

t_f	The control time horizon.
$D(q)$	The manipulator mass matrix.
$C(q, \dot{q})$	Matrix of Coriolis and centripetal terms.
$G(q)$	The gravitational effect.
γ_1	Vector of hydraulic parameters.
γ_2	Vector of hydraulic parameters.
θ	Vector of rigid body parameters.
$Y(q, \dot{q}, \ddot{q})$	The regressor matrix in the linear-in-parameter representation of the rigid body dynamics.
$\bar{\sigma}(\cdot)$	The maximum singular value.
$\underline{\sigma}(\cdot)$	The minimum singular value.
τ_{fm}	An upper bound for the Coulomb friction.
M_p	The platform mass.
I_x	The platform inertia along the x-axis.
I_y	The platform inertia along the y-axis.
I_z	The platform inertia along the z-axis.

Acknowledgments

I would like to express my foremost and deepest gratitude to my thesis supervisor, Professor Tim Salcudean for his invaluable guidance, excellent supervision and continuous support during the course of this research. I am very grateful to the members of the examination committee Dr. J. De Schutter, Dr. J. Jatskevich, Dr. P. Lawrence, Dr. P. Loewen, Dr. R. Ward and Dr. J. Yan for their fruitful comments on the content of thesis that have undoubtedly improved the quality of the work.

This work could not be accomplished without the help and support of the technical staff of the Robotics and Control Laboratory, in particular, Simon Bachmann, Ruediger Six, Henry Wong and Luca Filipozzi. I would like to thank all of them for their contribution. Many thanks go to my best friends in the RCL group, Purang Abolmaesumi, Daniela Constantinescu, Simon P. DiMaio and Parvaneh Saeedi for their help, encouragement, fruitful discussions, and the colorful memories that they have created for me during the past four and a half years.

I would like to express my utmost gratitude to my parents to whom I am heavily indebted, for their unconditional love and invaluable support from my childhood to this point.

Finally, the support of this research by IRIS project IS-4 and also the UBC Faculty of Graduate Studies is gratefully acknowledged.

*To my beloved parents and
my dearest Paria*

Chapter 1

Introduction

1.1 Background

Despite significant advances in automatic control systems during the last few decades, the human operator still has an important role to play in many control applications. The presence of the operator is necessary in these applications mostly due to unstructured nature of the tasks they involve. Even though many of the low-level control activities are performed automatically, the operator has to carry out the high-level control actions. Piloted vehicles are good examples of such systems. Most modern aircraft are still controlled by human pilots and automobiles are driven by human drivers. Human operators employ joysticks to operate heavy hydraulic machines used in the construction, mining and forest industries, such as excavators, bulldozers, log-loaders, and feller-bunchers.

The human operator is also an essential part of any telerobotic system. Applications include space exploration, underwater operations such as inspection and repair of deep water equipment, tele-surgery, operation in hazardous environments such as nuclear industry, mining and many others [82]. In conventional teleoperation systems, the operator utilizes an input device (master robot) to control the slave robot (usually located in a remote place) and to interact with the environment. Sensory information such as the operator's hand force, environment reaction forces, and master and slave positions are used to coordinate the master and slave operation.

The examples cited here are similar in the sense that in all of them the human operator uses the provided sensory information and an input device to control the system. These applications

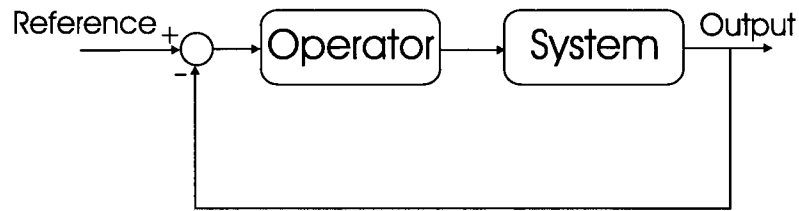


Figure 1.1: A general manual control system.

can be placed into the broad class of manual control systems. A simple block diagram of a typical human-machine control system is shown in Figure 1.1. Research in the area of classical manual control systems (e.g., aircraft piloting) has yielded models for the analysis of the closed-loop behavior of the human operator [45, 46, 59, 80, 81]. Teleoperation systems have also been the subject of research during the course of the last two decades. Several control architectures have been proposed for these systems. Stability and performance of these architectures have been extensively studied [4, 5, 22, 41, 43, 57, 62, 95, 98, 135].

In some teleoperation/manual control applications, the operator is exposed to base motion. For example, the operator of an excavator uses a joystick to control the bucket and to carry out an assigned task. As the bucket comes in contact with a hard environment, the excavator cab jolts back in response to the environment reaction forces. In an aircraft, the pilot is subject to base accelerations when he/she maneuvers the plane. Some other examples are operation of telescopic boom lifters, control of high speed vehicles over rough terrain or waves, control of fly-by-wire systems and operation of powered wheelchairs.

The base motion can affect the performance of a teleoperation/manual control system in several ways. The relative motion between the operator and the task can disrupt vision acuity and hence adversely affect the operation. It may also interfere with the neuromuscular process. Such interferences could reduce the signal-to-noise ratio between intentional, task related muscle activities and random activities (increased remnant noise) [69, 79]. The operator's body response to base accelerations can also generate unintentional forces at the hand/joystick interface and introduce involuntary commands in addition to the voluntary commands. This is referred to as *biodynamic feedthrough* in joystick-controlled systems [31, 51, 55, 124, 125].

Biodynamic interferences can be classified as either open-loop or closed-loop. In open-loop cases, the base acceleration is uncorrelated with the operator voluntary command and

is caused by external disturbances, e.g., in weapon aiming on-board moving platforms. In another category of teleoperation/manual control tasks, the base acceleration is a result of the operator command. Piloted aircraft and joystick-controlled hydraulic machines belong to this category. In these systems, the existence of a feedback path through the human body and the hand controller can not only degrade the performance but it may also cause instability. For example, biodynamic feedthrough has been known to contribute to the pilot-coupled oscillations (PCO) and roll-ratchet phenomena in aircraft [47, 51, 115], operator-induced oscillations in the operation of excavators [6], and the oscillatory fore and aft motion known as *bucking* in powered wheelchairs [8].

One of the objectives of this thesis is to study the effects of biodynamic feedthrough on teleoperation/manual control systems with movable bases. This includes development of new models that can be used in the analysis of such systems. The design of controllers that can achieve optimized performance and robust stability in the presence of base motion is also addressed by the thesis. The evaluation of the proposed control methods could be costly and time consuming if each application of interest were to be prototyped and tested. An alternative approach is to use high performance motion simulation to generate the base motion according to the dynamics of the teleoperation/manual control system of interest.

This thesis proposes and develops an experimental testbed composed of a high performance motion simulator [99] (Figure 1.2) and a force-reflecting joystick [104] (Figure 1.3) to be used in the evaluation of control algorithms for feedthrough cancelation. This significantly reduces the time and cost associated with biodynamic feedthrough related experiments at the present time and in future. The motion simulator is a six-degree-of-freedom hydraulic Stewart platform. The use of hydraulic actuators and the parallel structure of this manipulator make it suitable for applications that require large accelerations and large forces. Hydraulic actuators, robots and machinery are widely used in construction and mining industries, as well as in motion simulators. They have rapid responses and high power-to-weight ratios. Traditionally, hydraulic systems are controlled by linear controllers based on local linearization of their nonlinear dynamics. The performance achievable by these controllers is limited because of conservative loop gains that sacrifice the performance of the system in favor of its stability. The proposed motion simulation testbed could be used to simulate a wide range of systems with different motion

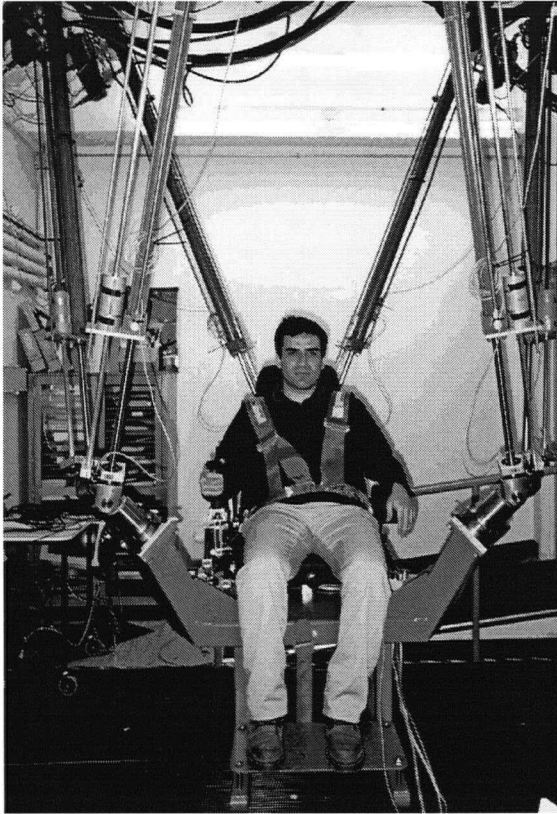


Figure 1.2: The UBC motion simulator.

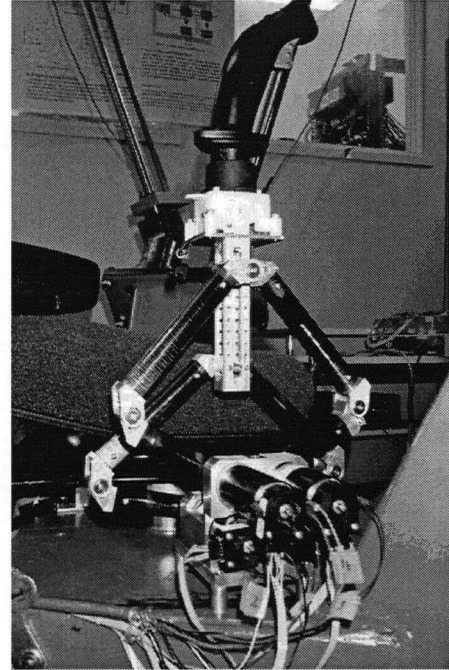


Figure 1.3: The twin-pantograph joystick.

dynamics. This motivates the development of high performance controllers that can faithfully reproduce the base motion in these applications. Therefore, the second part of this thesis is concerned with the position control of hydraulic actuators and robots.

It is well known that the hydraulic actuators have highly nonlinear dynamics [83]. The nonlinearities are due to nonlinear flow/pressure characteristics, variations in the trapped fluid volume because of piston motion, and fluid compressibility. Other factors such as transmission nonlinearities, flow forces and their effects on the spool position, and friction contribute to the nonlinear behavior. The nonlinear dynamics along with dynamic uncertainties such as time varying hydraulic parameters make the high performance control of these actuators challenging. The control of robot manipulators driven by hydraulic actuators is even more difficult. In addition to nonlinear actuator dynamics, their second-order rigid body dynamics are also nonlinear. The problem becomes extremely challenging if uncertainties in the rigid body dynamics and the hydraulic actuator dynamics are also taken into account. The uncertainties arise from

unknown and time varying hydraulic parameters, and also variable payload and unknown rigid body parameters. The high performance control of rigid link electrically driven (RLED) robots has been extensively addressed in the literature, e.g. see [11, 78, 90, 114, 117]. Nevertheless, these state of the art controllers are not applicable to hydraulically driven manipulators. These controllers mostly neglect the actuator dynamics and assume that ideal torque/force source actuators are available for the control. Although this is a reasonable assumption for electrical actuators, it is not valid for hydraulic actuators because they exhibit dominant nonlinear dynamics and resemble a velocity source rather than a torque/force source.

Remark: It should be mentioned that the proposed hydraulic controllers have not been used in the feedthrough cancellation experiments presented in this thesis. The current hardware used to control the UBC motion platform has limited computational power. We have been able to evaluate the new hydraulic controllers by developing a custom communication link between the present hardware and a Pentium PC which serves as the controller (see Chapter 7 for details). However, major modifications are required before the entire system including the platform and the joystick controllers can simultaneously run on a PC with safety features comparable to those of the current system in place. The amount of work turned out to be beyond the scope of this thesis and therefore, it was decided to use the existing hardware and proportional hydraulic controllers in the feedthrough related experiments. The new hydraulic controllers can be employed in future experiments after making the required changes. This will not affect the generality of the proposed framework by the thesis as outlined in Chapter 4.

1.2 Prior Work

1.2.1 Modeling and Analysis of Manual Control/Teleoperation Systems

Research in the area of human controlled machines has yielded several models for the human operator closed-loop behavior. McRuer et al. in [80, 81] give a survey of so called quasi-linear crossover models of the human operator in single-axis tracking tasks. These models are based on experimental evidences that revealed the operator-machine open-loop gain follows a slope of -20dB/dec around its crossover frequency. The structural model of the human operator in [44–48] is an extension of the basic crossover model. This model assumes that the primary

equalization capabilities of the human operator occur through operation on a proprioceptively sensed, as opposed to a visually sensed variable. It also embodies the use of motion cues in the manual control and the neuromuscular dynamics of the operator's arm. Models for the neuromuscular dynamics are proposed in the literature, e.g. in [91].

While the basic crossover and the structural models of the human operator are presented in the frequency domain, the model proposed by Kleinman et al. in [59] is based on optimal control and estimation theories. The underlying assumption in this approach is that the human operator adopts an optimal control strategy in manual pursuit tasks by trying to minimize some quadratic performance index. A Kalman filter is employed to estimate the system states to be used by the optimal control law. Greene in [36, 37] proposes a model for the human operator in tracking systems based on the so called sequential adaptive system theory. The reference input to be tracked is predicted linearly over discrete time intervals. An optimal second-order dynamics is obtained for the error between the predicted reference and the system output in each of the time intervals and used to predict the operator behavior.

Teleoperation systems can be viewed as non-conventional manual control systems. They have found vast application in areas such as space technology, underwater exploration, mining, health, nuclear and toxic material handling, and the entertainment industry [43, 82, 101]. Several control architectures have been proposed for teleoperation system design. Many of the proposed controllers use two communication channels between the master and the slave. In position-position approaches, the positions of the master and slave robots are used as reference commands for each other [95]. In the two-channel position-force approach, the master position is sent to the slave and the environment force is returned to the master [41, 65, 67, 118]. In the force-force architectures, the hand and environment forces are sent to the slave and master, respectively [57]. To eliminate the lack of coordination between the master and the slave, inherent in such an approach, a position-based coordinating force has been proposed by [100].

The most commonly used notion of performance in teleoperation systems is *transparency*. By definition, an ideal teleoperation system should create a human-machine interface of such high fidelity that the human operator feels that he is directly interacting with the remote environment and is performing the task. Perfect transparency is not achievable using two-channel teleoperation structures [41, 62]. All four channels of information, i.e., master and slave posi-

tions and hand and environment forces, must be communicated between the master and slave sides. This results in the four-channel bilateral teleoperation architecture [62, 135]. Achieving ideal transparency also requires acceleration measurement. Yokokhji et al. in [135] proposes a modified definition of transparency in which the operator interacts with the environment via a virtual tool. This eliminates the need for acceleration measurement.

The design of controllers for teleoperation systems is mainly a tradeoff between performance and stability [42, 62, 82, 98]. Time delays in communication channels, nonlinear and uncertain master and slave dynamics, unknown and usually time varying dynamics of the human operator and the environment are among the factors that limit the achievable level of transparency. Several control methods have been proposed in the literature to address the tradeoff between stability and transparency. These include passivity-based controllers [4, 5, 85, 86], designs based on H_∞ techniques and μ -synthesis loop shaping techniques [22, 50, 57, 67, 131], adaptive nonlinear controllers [140] and many others.

In teleoperation systems, the human operator uses kinesthetic and visual sensory information to generate his/her control commands. Most of the reported works in the literature concerning modeling, analysis and design of teleoperation systems employ passive mass-spring-damper models for the operator (e.g. see [41, 57, 62, 98]). Lee et al. in [64–66] use a more elaborate model of the operator in teleoperation. The model assumes that the operator intentional reaction to position and force tracking errors is produced by PD controllers acting on the corresponding errors followed by a delayed first-order dynamics representing the neuromuscular dynamics. A connection between the models for aircraft piloting and teleoperation systems is made in [94]. The authors employ the structural model [45] to model the operator behavior in a two-channel teleoperation system.

1.2.2 Effect of Base Motion

The motion of the operator's base can degrade the performance and stability of teleoperation or manual control systems. Lewis et al. [69] and McLeod et al. [79] survey the effects of whole-body vibration on continuous manual control performance. The reviews are comprehensive and address the effects of vibration variables (frequency, magnitude, axis etc.), control system variables (e.g., physical characteristic of the hand controller, its gain, system dynamics and

display variables), and vibration duration. The outcomes of these studies show that the base motion can degrade vision acuity and increase noise in muscle activities. The human body/arm response to base acceleration can also generate involuntary commands known as *biodynamic feedthrough* or *stick feedthrough* and interfere with the execution of the task [69, 79].

The biodynamic response of the operator is generally nonlinear and very complex to model. Jex et al. in [55] develop and validate a biomechanical model for an operator holding a passive joystick while subjected to base acceleration. They replace relevant body parts with their mechanical equivalents to derive a nonlinear model that can predict feedthrough transmission to the joystick and the operator's head. The complexity of this model and the difficulties associated with the identification of some of its parameters limit its application. Biodynamic interferences can be of open-loop or closed-loop nature [125]. Open-loop interferences occur in applications such as weapon aiming on-board moving platforms in which the base acceleration is uncorrelated with the operator's action. In [68], the author experimentally identifies the spectrum of feedthrough interferences and uses the results to predict the performance of the operator in an open-loop feedthrough manual tracking experiment. The author also claims that the feedthrough response exhibits approximately a linear behavior in the specific experiment conducted in this work. The open-loop and closed-loop feedthrough can be particularly troublesome if the system to be controlled has resonant modes within the frequency range that feedthrough content is significant [52].

In closed-loop biodynamic environments, such as in aircraft piloting or in joystick control of heavy hydraulic machines, the operator is exposed to base motions caused by his/her own action. Therefore, a feedback loop is established through the operator's body and arm, the hand controller and the dynamics of the controlled system. Serious stability issues may arise due to this loop. Feedthrough related oscillations have been reported in the operation of some aircraft [45, 115, 124, 125] and joystick controlled hydraulic machines [6, 31]. Arai et al. in [6] employ a feedthrough model similar to that introduced in [55] to numerically simulate the operation of an excavator and to show a potential oscillatory behavior due to biodynamic feedthrough. Idan et al. in [51] present a modified model of the human control behavior when subjected to closed-loop base accelerations using an ad hoc linear feedthrough model. By assuming that the crossover model is valid under the conditions of vehicle motion, the authors

show that instability can occur in aircraft piloting.

To the best of the author's knowledge, the work by Velger et al. in [125] is the first attempt at feedthrough compensation. The authors propose an adaptive filtering technique to suppress oscillations due to biodynamic feedthrough in applications with open-loop feedthrough interference. They claim their method also works for closed-loop feedthrough interferences provided that a spectral separation can be made between the system response to operator commands and biodynamic interference. However, they only report experimental results for an open-loop case in [124]. The idea of active feedthrough cancelation is first introduced in [31]. The authors use a force-feedback joystick to feed forward the base acceleration to the joystick based on an acceleration feedback model identified for feedthrough dynamics. Arai et al. in [6] propose to increase the damping of the joystick in order to suppress feedthrough induced oscillation in the operation of excavators. The prefiltering methods proposed in [52] and references therein attempt to avoid exciting the system resonant modes by filtering the joystick output signal. These methods do not address performance and robustness issues. They also treat the operator's command as an exogenous signal which is obviously not the case if closed-loop feedthrough is present.

1.2.3 Control of Hydraulic Actuators

The traditional and widely used approach to the control of electrohydraulic systems is based on local linearization of the nonlinear dynamics about a nominal operating point, e.g. see [83,102]. These controllers sacrifice the system performance to achieve stability in the presence of variations in the operating point and uncertainty in the dynamics [126].

Adaptive and robust controllers based on linearized models have been proposed to address performance and robustness issues. In [14], Bobrow et al. develop an adaptive controller that is locally stable and is able to cope with the changes in system parameters such as flow constants, fluid bulk modulus and variable loading. [137] addresses the velocity control problem of nonlinear hydraulic servosystems using an adaptive model following control scheme. The valve dynamics are ignored and no experimental data is reported. A drawback of the preceding methods is that they do not provide a global stability proof.

Lu et al. in [77] introduce a robust controller for hydraulic servosystems using a linearized

model of the system. The controller requires acceleration measurement. In [132], Yanada et al. also develop a robust controller for an electrohydraulic servo motor using a linearized model of the system and a sliding mode control law to deal with nonlinearities. The valve dynamics are ignored in the design and acceleration measurements are required for the implementation of the controller. In [138], an approach employing variable structure control with integral compensation is presented for an electrohydraulic position servo control system to achieve accurate servo tracking in the presence of load disturbances and plant parameter variation. Again, acceleration measurements are required for the controller implementation. Control action switching in variable structure control methods can also excite the system's unmodeled high-order dynamics and lead to instability which is another drawback of the proposed method.

The use of H_∞ control is proposed in [61] to robustly control the force exerted by a hydraulic servo-actuator on its environment. A linear model of the system is first obtained to relate the control command to the actuator output force. A robust controller is then designed to achieve force control and robust stability with respect to uncertainties in the actuator and environment dynamics. In [87], a class of linear models are obtained to represent the nonlinear hydraulic dynamics over the desired range of operation using the *Golubev* method [34]. A robust low-order controller is designed to achieve force tracking.

Dynamic feedback linearization has also been used for the control of hydraulic actuators. Vossoughi et al. in [126] propose a control law for a single-degree-of-freedom rotational joint driven by a linear actuator based on this idea. The authors conclude that for low inertia and high bandwidth systems, the valve dynamics play an important role in the overall system performance and may not be ignored. The load acceleration and derivative of actuator pressures are required in the implementation of the controller if the valve dynamics are considered. To incorporate the effects of parametric uncertainties on the feedback linearization, the authors also develop a state space linear fractional representation of the linearized system. [21] adopts feedback linearization to control a load sensing hydraulic servo system. The output of interest is the angular velocity. Although good performance has been claimed for the proposed controller based on simulation results, the control law includes the acceleration and jerk feedback which are not easily accessible. [40] and [13] also employ the idea of feedback linearization with acceleration feedback. Uncertainties in the dynamics are neglected and no experimental results are presented

in these reports.

Lyapunov-based methods have been proposed for force control of hydraulic actuators. In [3], a nonlinear sliding mode controller is developed for an active electro-hydraulic suspension system. In [2] and [75], nonlinear force controllers are proposed for electrohydraulic actuators. Adaptation laws are also introduced to accommodate uncertainties in the hydraulic parameters. However, the stability proof presented in these papers is incorrect since the unknown hydraulic parameters appear in some of the derivatives used in the proposed control laws. In [116], Sohl et al. present a force-based position control strategy for hydraulic actuators. The authors assume that electro-hydraulic valve dynamics in their experimental setup are fast enough to be ignored. Dynamic uncertainties are also neglected.

Lyapunov-based controllers can guarantee the stability of tracking errors in nonlinear control systems. However, they offer very little insight into the performance and the transient behavior of the system. The optimal control of linear systems has been widely studied and is standard today [15, 70]. The necessary and sufficient conditions under which a closed-loop nonlinear system becomes optimum have already been derived [70]. Nevertheless, synthesizing an optimal control law that satisfies these conditions is not easy and not always feasible [56]. Numerical methods can be used as an alternative approach to tackle this problem. There have been a few reports on the application of numerical routines to the optimization of nonlinear controllers, e.g. see [9, 32].

1.2.4 Control of Hydraulic Robots

Hydraulic robots present a highly challenging design task to a control engineer. They exhibit significantly nonlinear dynamics. In these manipulators, nonlinear actuators are used to drive the nonlinear rigid body dynamics. Uncertainties in the hydraulic and rigid body dynamics add to the complexity of the problem.

The high performance control of rigid link electrically driven (RLED) robots has been the subject of wide research. These efforts have produced several solutions for the problem. Among them are the computed torque [78] and passivity-based controllers [11, 90, 92, 121]. Control laws have been proposed that avoid velocity measurement with the aid of nonlinear observers [11, 23, 84]. There have been three underlying philosophies to deal with parametric and non-parametric

uncertainties in robot dynamics, namely adaptive control, robust control and robust/adaptive control schemes. Examples of adaptive control methods for RLED robots are given in [63, 90, 96, 97, 113, 114, 121, 130]. Robust controllers for RLED robots may be found in [1, 54, 117, 119]. Robust/adaptive control laws for RLED robots are introduced in [12, 18] and other references.

Efforts have been made to incorporate the electrical actuator dynamics into the design of high performance position tracking controllers for RLED robots. For example, Tarn et al. in [122], adopt feedback linearization to dynamically linearize the third-order nonlinear dynamics of an RLED robot. The drawback of this approach is the requirement for acceleration measurements. [33] presents a nonlinear adaptive controller for RLED robot manipulators that incorporates the linear actuator dynamics. This controller also requires acceleration feedback. [39] proposes a cascade control strategy combining an adaptive scheme for rigid-link robot control with a variable-structure control law for actuator control. Lim et al. in [74] introduce an output feedback controller for RLED robots augmented with a velocity observer and an electrical current observer using an integrator backstepping procedure. [136] synthesizes an adaptive controller which is able to cope with uncertainties in the robot and motor dynamics. An adaptive nonlinear observer is designed to avoid acceleration measurement. In [133] a hybrid adaptive/robust control scheme is proposed for RLED robot manipulators in the presence of arbitrary uncertain inertia parameters of the manipulator and electrical parameters of the actuators. The controller needs the measurement of motor armature current. The authors modify their control in [134] such that the need for velocity measurement and boundedness of estimated inertia parameters is eliminated. An adaptive partial state-feedback controller utilizing a filter to generate link velocity tracking error information is proposed in [17].

While the dynamics of electric actuators are linear and usually fast enough to be ignored in the design of controllers for RLED robots, the actuator dynamics are highly nonlinear and dominant in hydraulic robots. This prevents the application of the state of art controllers designed for RLED robots to hydraulic manipulators. There are few reports in the literature that address the control of hydraulic robots. In [120], Tafazoli et al. propose an observer-based friction compensating controller for a hydraulic manipulator. Li et al. in [72] suggest the use of pressure feedback to improve performance and stability in the control of the University of British Columbia hydraulic platform. In [89], the authors establish a simplified model in standard

form suitable for the application of singular perturbation methods [58] but no experimental or simulation results are provided. A decentralized adaptive controller is proposed for hydraulic robots by Edge et al. in [28, 29]. None of these approaches provides a proof of global stability, which is important from both a theoretical and a practical point of view. Only recently [16] proposed a controller for hydraulic robots that is provably stable in the Lyapunov sense. This work was performed at the same time as the work presented in this thesis. The result of our research was received by the *IEEE Transactions on Robotics and Automation* in April 3, 2000 [109]. Bu et al. [16] presented their work in the *IEEE International Conference on Robotics and Automation* held on April 24-27, 2000. The differences between our approach and their controller will be outlined in Chapter 7.

1.3 Thesis Outline

This thesis is concerned with the modeling, analysis, design, and evaluation of teleoperation/manual control systems with movable bases. A framework is proposed for the analysis of teleoperation/manual control systems in which the operator is subject to base motion. It is shown that the presence of closed-loop biodynamic feedthrough may cause instability in such systems. A μ -synthesis based control design approach is presented to achieve robust stability and optimized performance in teleoperation/manual control systems with movable bases. The methodology is illustrated by a design example. A model for feedthrough dynamics along with its uncertainty bounds are also obtained using the stochastic embedding approach. Motivated by a need for high performance motion simulation for feedthrough suppression experiments, the control of hydraulic systems is also addressed. A new nonlinear adaptive position controller for hydraulic servo-systems is proposed and evaluated experimentally. Numerical optimization of the controller for a simplified case is also studied. Finally, for the first time, provably stable adaptive/nonlinear controllers/observers for hydraulic robots are proposed and evaluated experimentally. This thesis is organized as follows:

Chapter 2: Modeling of Teleoperation Systems with Movable Bases. This chapter introduces the concept of teleoperation/manual control from movable bases. It begins with a brief introduction to conventional teleoperation controller architectures. The general four-channel teleoperation framework is then modified to include the effect of base motion. Results

from manual control theory are used to propose a new model that incorporates the human operator dynamics into the control loop. Relevant performance measures for the system are discussed. It is shown via analysis that the presence of closed-loop biodynamic feedthrough interferences may lead to instability in teleoperation/manual control systems with movable bases.

Chapter 3: Identification of Biodynamic Feedthrough and Arm/Joystick Dynamics. This chapter is concerned with the modeling and identification of feedthrough dynamics. First, it presents a system identification approach to feedthrough modeling. A model within the framework of the stochastic embedding approach is considered for the feedthrough dynamics. This approach allows for two sources of uncertainty, measurement noise and stochastic unmodeled dynamics. Quantitative properties of prior assumptions on the noise and the under-modeling can be estimated from the data. Identification experiments are carried out to identify a nominal feedthrough response. The method also generates appropriate confidence regions for the estimated response. The resultant model can be used in the robust control design for feedthrough cancellation. The identified response is compared with that of a simple acceleration based model and conclusions are drawn. A model for arm/joystick dynamics is presented and identified.

Chapter 4: Controller Design for Suppression of Biodynamic Feedthrough. This chapter proposes a novel approach for the design of active controllers that robustly cancel the effect of closed-loop biodynamic feedthrough interferences. The methodology is illustrated via an example. A single-degree-of-freedom manual control task is considered in which the operator uses a force-feedback joystick to position his/her base. The acceleration feedback based model is used for biodynamic feedthrough. It is shown analytically that a control approach that neglects the base motion can cause instability. μ -synthesis-based controllers are developed that robustly stabilize the system with respect to uncertainties in the arm/joystick and biodynamic feedthrough dynamics. The controllers also optimize performance measures defined to shape the admittance of the joystick and to ensure motion tracking between the joystick and the base. Experimental results are presented to show the effectiveness of the proposed control approaches.

Chapter 5: Adaptive Nonlinear Control of Hydraulic Servo-systems. In this chapter, the backstepping approach [60] is employed to develop a new Lyapunov-based position tracking

controller for hydraulic servo-systems. The first-order electro-hydraulic valve dynamics, nonlinear hydraulic pressure dynamics and load dynamics are incorporated in the design of controller. The tracking errors are shown to converge to zero using Lyapunov analysis. An adaptive version of the controller is also proposed to cope with parametric uncertainties in the hydraulic dynamics. The effectiveness of the proposed controllers is demonstrated via numerical simulations and experimental studies.

Chapter 6: Numerical Optimization of a Single Cylinder Hydraulic Servo-system.

This chapter presents a numerical approach to the optimization of the proposed nonlinear position tracking controller for hydraulic actuators. A simplified model of the system that ignores the parametric uncertainties and the valve dynamics is used for this purpose. This produces a feedback linearizing controller parameterized by the feedback gains, and guarantees the convergence of the tracking errors to zero. A performance index that captures some features of the transient response of the system and also penalizes measurement noise amplification in the controlled variables is defined. Various optimization techniques are used to optimize the performance index over the set of allowable controller gains. The results of numerical simulations with the optimized controller are given at the end of the chapter.

Chapter 7: Adaptive Nonlinear Control of Hydraulic Robots. This chapter addresses high performance position tracking control of hydraulic robots. The *backstepping* design methodology is adopted to develop a novel nonlinear controller for hydraulic manipulators that incorporates both rigid body and actuator dynamics. The controller is also extended to compensate for parametric uncertainties in the system dynamics, including hydraulic and rigid body dynamics. Nonlinear observers are proposed to avoid acceleration measurements. The controller-observer closed-loop dynamics are proven to be stable in the Lyapunov sense and consequently the tracking errors converge to zero. It is also shown that the tracking errors remain bounded in the presence of Coulomb friction in the actuators. Simulation and experimental results obtained from the application of the proposed controllers to the UBC hydraulic Stewart platform are presented to show the effectiveness of the approach.

Chapter 8: Conclusions. This chapter concludes the thesis by summarizing its results and contributions. Some recommendations for continuation of the work in future are also made.

Parts of this work have been published in the *IEEE Transactions on Control Systems Tech-*

nology [105], the *IEEE Transactions on Robotics and Automation* [109], *Springer Experimental Robotics VII* [107], *Springer Experimental Robotics VIII* [111], and have been presented in *IEEE International Conference on Robotics and Automation* [104, 106, 108, 110].

Chapter 2

Modeling of Teleoperation Systems with Movable Bases

2.1 Overview

In conventional teleoperation systems, the operator uses a fixed-base hand controller, the master arm, to remotely control the slave robot and complete the assigned task. Visual, kinesthetic and sometimes auditory feedback are provided to the human operator in order to assist him/her in performing the task. This chapter introduces the concept of teleoperation/manual control from movable bases. In some applications such as joystick control of heavy hydraulic machines or aircraft piloting, the operator is subject to base motion. This motion can degrade the performance of the system by interfering with the operator's action, a phenomenon referred to as biodynamic feedthrough. Feedthrough interference can cause instability if the base motion is due to the operator's command [6, 115, 125]. The chapter begins with a brief introduction to a conventional teleoperation controller architecture. The architecture is modified to include the effect of base motion. A new model is proposed that incorporates models for the operator control behavior from the manual control literature into the conventional four-channel teleoperation framework. Relevant performance measures for the system are discussed. It will be shown analytically that the presence of a feedback loop through the operator's body may lead to instability in teleoperation/manual control systems with movable bases.

2.2 A Bilateral Four-Channel Teleoperation Architecture

Any teleoperation system involves some basic elements; a master manipulator (usually a hand controller) a slave robot, communication channels, and controllers. The operator uses the master device to operate the slave manipulator and to interact with the environment. The position and force information are usually communicated between the master and slave to coordinate their operation. Several control architectures have been developed for teleoperation systems. Among them, two channel approaches, i.e., position-position [95], position-force [41] and force-force [57] methods. Figure 2.1 shows a general teleoperation system which is referred to as a four-channel control architecture [62]. In this approach, the master position and the applied force by the operator are transmitted to the slave side through controllers C_1 and C_2 . The slave position and environment force are sent back to the master side via controllers C_4 , C_3 , respectively. Z_m and Z_s are the impedances of the master and slave manipulators and Z_e represents the environment dynamics.

In some applications, the ideal teleoperation system should create a man-machine interface of such high fidelity that the human operator cannot detect that he/she is remote from the task. This is denoted as perfect transparency [62]. The level of transparency achievable by a teleoperation system depends largely upon the performance of the master, the slave and the controllers. Ideally, the master should be able to simulate any environment encountered by the slave, from free-space to infinitely stiff obstacles, i.e.

$$x_s = x_m \quad (\text{position tracking}) \quad (2.1)$$

$$f_h = -f_e \quad (\text{force tracking}) \quad (2.2)$$

In some systems it might be desirable to perform force and motion scaling between the master and slave manipulators [131]. The above definition can be easily modified for this purpose. It should be pointed out that this notion of transparency is not applicable to applications such as aircraft piloting. There is no environment force in such manual control systems.

The modeling, analysis and design of fixed-base teleoperation systems have extensively been addressed in the literature [4, 5, 22, 41, 43, 57, 62, 95, 98, 135]. In order to investigate the effect of the master's base motion on a teleoperation system, Z_{BF} in Figure 2.1 has been added to

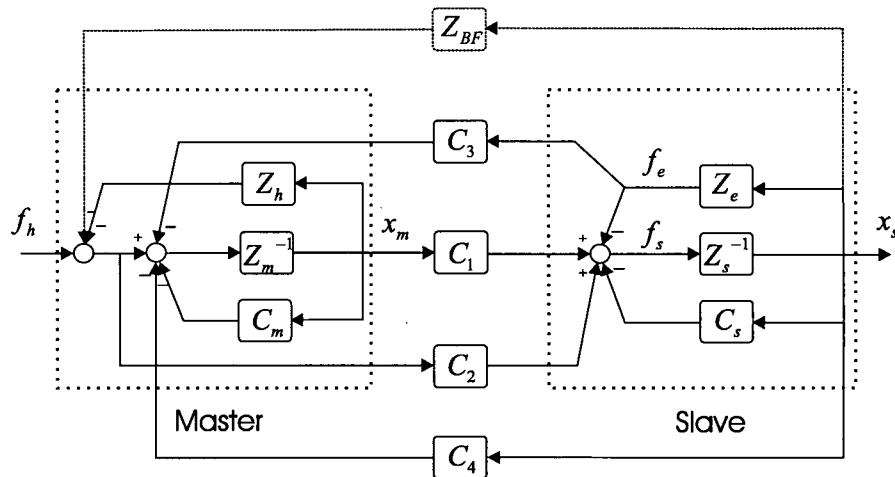


Figure 2.1: A modified four-channel teleoperation configuration.

the standard four-channel model in this thesis. The base motion excites the operator's body dynamics and induces a force at the hand/joystick interface. This is the rationale for including the impedance term Z_{BF} in the model. The underlying assumption here is that the base motion is due to the slave motion. This is the case in joystick-piloting of aircrafts where the operator uses a joystick (master) to maneuver the plane (slave). In the case of joystick control of excavators, the base (cab) motion is generated in response to both slave (bucket) motion and environment force (exerted on the bucket by the ground). The model in Figure 2.1 can be modified to accommodate this by adding another block that generates a reaction force in response to f_e . If f_e is a function of x_s , the block can be assimilated by Z_{BF} . The modeling of feedthrough dynamics, Z_{BF} , and its identification will be discussed in Chapter 3 of this thesis.

2.3 Models for Manual Control Systems

Research in the area of manually controlled vehicles has yielded several models for the behavior of the human operator in closed-loop systems. A human operator model based on classical control theory [51] is shown in Figure 2.2. In this figure, the operator is modeled by the linear describing function Y_p and additive remnant noise n . The plant to be controlled is Y_c and the tracking error is displayed to the operator. Several experimental studies [51, 80, 81] have

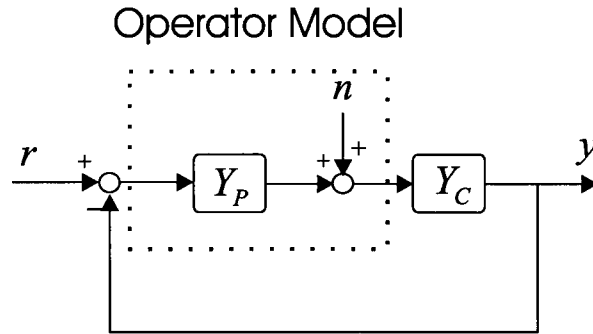


Figure 2.2: Crossover model of human-machine system.

revealed that a suitable operator model is given by,

$$Y_p(j\omega) = K_p \frac{e^{-j\omega\tau_d}}{j\omega T_N + 1} \frac{j\omega T_L + 1}{j\omega T_I + 1} \quad (2.3)$$

where $e^{-j\omega\tau_d}$ is the effective time delay of the human operator, $1/(j\omega T_N + 1)$ models the neuromuscular lag, and $G(j\omega) = (j\omega T_L + 1)/(j\omega T_I + 1)$ is an equalization term that enables the adjustment of the model to a wide variety of plant dynamics $Y_c(j\omega)$. It has been experimentally established that the operator adapts himself in accordance with the crossover model, which states that the overall transmission $Y_p Y_c$ maintains a slope of -20 dB/dec in the region of crossover [51, 80, 81].

$$Y_p Y_c(j\omega) \approx \frac{\omega_c}{j\omega} e^{-j\omega\tau_d} \quad (2.4)$$

The crossover frequency ω_c , along with phase margin and input bandwidth, are important parameters in determining man-machine system performance. The remnant noise $n(t)$ is defined as the portion of human operator control signal which is uncorrelated with the reference $r(t)$. Based on the crossover model, one may conclude the plant dynamics which have an effective integral form around the crossover frequency are easier to control since they require less adaptation by the operator. This provides an interesting guideline for the teleoperation controller design as will be pointed out later in this chapter.

The structural model presents a more elaborate description of the operator behavior in manual control systems. This model was originally developed to describe the pilot behavior in aircraft control [45, 46]. A slightly modified block diagram of the structural model of the human-

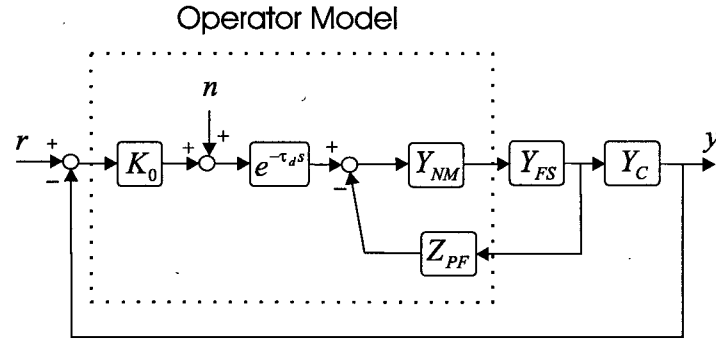


Figure 2.3: Structural model of human-machine system.

machine system is given in Figure 2.3. This is an extension to the basic quasi-linear crossover model. The key feature of this model is the inner proprioceptive feedback loop through Z_{PF} . In the forward path of this model, elements Y_{NM} and Y_{FS} are intended to represent the open-loop dynamics of the neuromuscular system driving the joystick and the dynamics of the joystick, respectively. The feedback part of the model includes Z_{PF} , whose input is the proprioceptively sensed joystick output. Z_{PF} and its location in the model are central to the philosophy of the structural model, i.e., that the primary equalization capabilities of the human pilot occur through operation upon a proprioceptively sensed, as opposed to visually sensed, variable. Y_{NM} is assumed to have the following form [45, 46]:

$$Y_{NM} = \frac{\omega_{NM}^2}{s^2 + 2\zeta\omega_{NM}s + \omega_{NM}^2} \quad (2.5)$$

A number of parameters are assumed to be constant between different tasks and operators. Typical values for these parameters are $\tau_d = 0.2s$, $\omega_{NM} = 10$ rad/sec, and $\zeta_{NM} = 0.7$ [46]. The proprioceptive feedback transfer function, Z_{PF} , is chosen according to the crossover model which requires

$$Y_p Y_c(j\omega) \approx \frac{\omega_c}{j\omega} e^{-\tau_d s} \quad \text{for } \omega \approx \omega_c \quad (2.6)$$

where

$$Y_p = K_0 e^{-\tau_d s} \frac{Y_{NM} Y_{FS}}{1 + Y_{NM} Y_{FS} Z_{PF}} \quad (2.7)$$

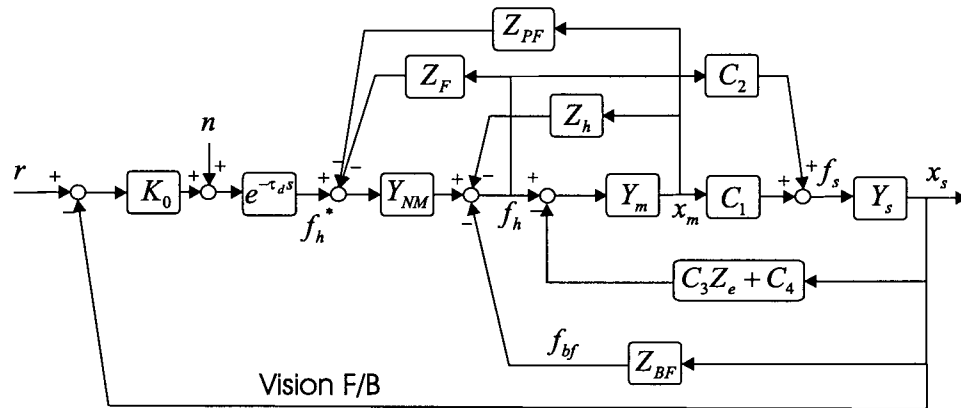


Figure 2.4: A teleoperation system within the framework of manual control.

The human operator bandwidth, ω_c , is believed to be somewhere around 2.0 rad/sec but this could be altered by the operator in a limited way [46]. It is also common to select Z_{PF} in the form of $K(s+a)$, K , or $K/(s+a)$ depending on the form of the vehicle dynamics [45, 46].

A limitation of the human operator models discussed here is that they are only valid under steady state conditions of operation and after allowing the operator enough time for learning and experiencing the process under control. During transient periods in performing the tasks, none of these models is valid. The models also need to be tuned for different operators even when they are performing the same task under the same conditions.

2.4 Teleoperation as Manual Control

The four-channel teleoperation architecture and the structural model of the human operator in manual control systems were introduced earlier in this chapter. A new model for teleoperation systems is proposed here by combining these models as shown in Figure 2.4. In this figure:

Z_h : represents the passive biomechanical dynamics of the human operator's arm. Second-order mass-spring-damper models have been used in the literature for these dynamics [19, 26, 57, 65]. This will be discussed in detail in Chapter 3.

Z_{PF} : is a term that models the operator active control of the joystick based on the sensed joystick position. It is assumed that the operator generates a force to correct a deviation in the joystick position from a desired position. Note that the operator may actively change the mass, spring and damping of his/her arm [19, 49] which can be modeled by Z_{PF} . Other forms for

Z_{PF} have been proposed in [45, 46] within the context of the structural model (i.e., $K(s + a)$, K , or $K/(s + a)$).

Z_F : models the operator reaction to the sensed force at the hand/joystick interface. A control action in the form of force is produced to compensate for the difference between the desired and the actual force. Lee et al. in [65] proposed a PD-type controller for this purpose although other types of controllers may also be used.

Z_{BF} : is included in the model to represent the effect of base motion in the form of biodynamic feedthrough.

Z_e : models the dynamics of the environment that the slave is in contact with.

Y_{NM} : is the operator's neuromuscular dynamics.

$K_0 e^{-\tau_d s}$: models the operator response to the visual tracking error between the actual and the desired position of the slave, assuming the operator is provided with visual information about the task. This is chosen according to [45, 46]. K_0 may be replaced by a PD controller as in [65].

Y_m and Y_s : are the dynamics of the master and slave, respectively. It should be pointed out that local controllers C_m and C_s in Figure 2.1 have been embedded in Y_m and Y_s .

C_1 , C_2 , C_3 , and C_4 : are the teleoperation controllers to be chosen by the control designer.

r : is the desired slave position.

n : is an additive remnant noise.

f_h^* : is the operator's control signal to compensate for the visual tracking error.

f_{bf} : is the biodynamically induced force due to the base motion.

f_h : is the total hand force applied to the joystick.

x_m : is the master (joystick) position.

x_s : is the slave (base) position.

Remark: Note that the relative importance of Z_{PF} and Z_F depends on the type of the hand controller used and also the mode of operation. For example, in force-sensing joysticks, the master motion range is usually small and the operator controls the interaction force. If a joystick with a relatively large workspace is used for teleoperation in free motion, Z_{PF} becomes dominant. However, if the slave is in contact with a rigid environment, the operator controls the force through Z_F . In other modes of operation, a combination of both may be employed.

In Figure 2.4, the effective controlled element Y_C is a combination of the master, the slave

and the teleoperation controllers. The proposed model allows for the use of results from manual control theory in the analysis and design of teleoperation systems. For example, as stated earlier, it has been found that the human operator follows a control strategy dictated by the crossover model. This can be used to design the teleoperation controllers such that the crossover behavior is achieved with minimal control effort by the operator (i.e., $Z_{PF} \approx 0$, and $Z_F \approx 0$). This can be obtained if

$$Y_p Y_c = K_0 e^{-j\omega\tau_d} \frac{X_s}{F_h^*} \approx \frac{\omega_c}{j\omega} e^{-j\omega\tau_d} \quad \omega \approx \omega_c \quad (2.8)$$

The above design objective, if achieved, would improve the *handling quality* as defined in [46]. It is assumed that the values of τ_d and ω_c are constant. Note that the operator visual feedback gain, K_0 , required to achieve the crossover model, is dictated by the dynamics of the master and slave and also the teleoperation controllers. The tradeoff is between a large control effort by the operator for large values of K_0 and increased sensitivity and noise to signal ratio for small values of K_0 . Obviously, other performance measures such as position and force tracking between the master and slave (transparency) are still applicable within this framework. An effective way of improving the performance in teleoperation and manual control systems is to shape the impedance of the master device. This leads to the definition of another performance measure based on the error between the desired and actual impedances of the master which will be used later in Chapter 4.

2.5 Stability in Presence of Biodynamic Feedthrough

The presence of biodynamic feedthrough can cause instability in a teleoperation/manual control system that is stable in the absence of feedthrough dynamics. In order to show the potential instability due to biodynamic feedthrough, the model in Figure 2.4 is reconfigured as in Figure 2.5. It should be mentioned that some of the blocks in this figure have no physical meaning and they have been combined to simplify the analysis. Note that the outer vision-based feedback loop has been removed in this figure. This loop that includes the operator as visual controller has a low 0dB crossover frequency such that it does not affect the stability of the overall system unless there is a significant delay in the loop. As can be seen in Figure 2.5, biodynamic feedthrough

appears as an additional feedback loop in the system. It is not difficult to show that:

$$G_{eq} = \frac{P_1 + P_2}{1 - (L_1 + L_2 + L_3 + L_4) + L_2L_4} \quad (2.9)$$

where

$$L_1 = -Y_m (Z_h + Z_{PF}Y_{NM}) \quad (2.10)$$

$$L_2 = -C_1Y_mY_s (C_3Z_e + C_4) \quad (2.11)$$

$$L_3 = C_2Y_mY_s (C_3Z_e + C_4) (Z_h + Z_{PF}Y_{NM}) \quad (2.12)$$

$$L_4 = -Z_FY_{NM} \quad (2.13)$$

$$P_1 = C_1Y_mY_s \quad (2.14)$$

$$P_2 = C_2Y_s \quad (2.15)$$

The closed-loop characteristic equation is given by

$$1 + Z_{BF}G_{eq} = 0 \quad (2.16)$$

The position tracking between the master and slave is not affected by biodynamic feedthrough.

$$\frac{X_s(s)}{X_m(s)} = \frac{Y_s [C_1Y_m + C_2]}{Y_m [1 - C_2Y_s (C_3Z_e + C_4)]} \quad (2.17)$$

It can also be shown that:

$$\frac{X_s}{F_h^*} = \frac{Y_{NM}G_{eq}}{1 + G_{eq}Y_{BF}} = \frac{Y_{NM}Y_s (C_1Y_m + C_2)}{1 - (L_1 + L_2 + L_3 + L_4 + L_5 + L_6) + L_2L_4} \quad (2.18)$$

$$\frac{X_m}{F_h^*} = \frac{Y_{NM}Y_m [1 - C_2Y_s (C_3Z_e + C_4)]}{1 - (L_1 + L_2 + L_3 + L_4 + L_5 + L_6) + L_2L_4} \quad (2.19)$$

with

$$L_5 = -C_1Y_sY_mZ_{BF} \quad (2.20)$$

$$L_6 = -C_2Y_sZ_{BF} \quad (2.21)$$

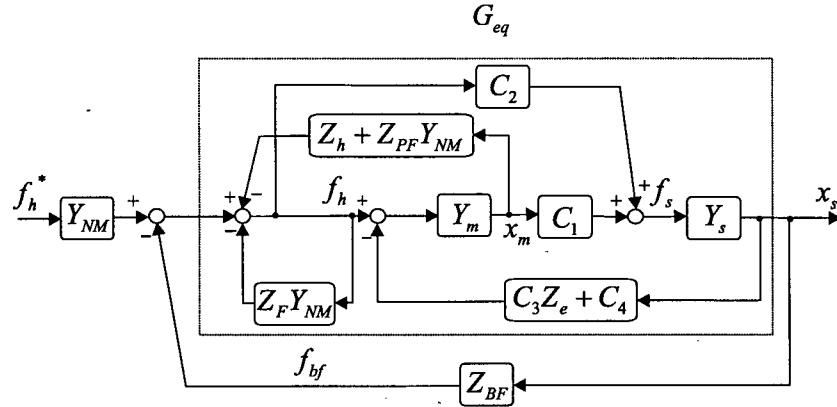


Figure 2.5: The teleoperation system without vision feedback.

Note that (2.18) and (2.19) are affected by the base motion.

A simple acceleration based model is employed for biodynamic feedthrough [31,45,115] for the purpose of analysis here. In this approach, the effect of base acceleration on the master motion with respect to the base is modeled as an inertial force acting on the master (joystick).

$$Z_{BF}(s) = \frac{\omega_{bf}^2 m_{bf} s^2}{s^2 + 2\zeta_{bf} \omega_{bf} s + \omega_{bf}^2} \quad (2.22)$$

where m_{bf} is the biodynamic feedback mass that can be equal to the total mass of the arm and master device. Inclusion of a second-order low-pass filter in the model reflects the fact that the compliance of the arm-master interface prevents high frequency feedthrough forces from being conveyed to the joystick. The identification of this model is discussed in Chapter 3. Note that the model neglects the effect of body and shoulder motion on the arm and master. In Chapter 3, a system identification approach to the modeling of feedthrough dynamics will be proposed that considers this. In the analysis presented here, the values of ω_{bf} and ζ_{bf} are assumed to be known and the stability of system is investigated as m_{bf} varies. It is also assumed that:

$Z_{PF} = 0$, $Z_F = 0$: As stated earlier, these gains model the operator's active control behavior. They vary from one operator to another and they may not even be constant for a single operator under different circumstances. For the purpose of stability analysis, one can assume that the operator does not intentionally destabilize the system. It is plausible to presume that the operator would stop controlling the joystick if his/her actions generate instability. While it is

always possible that the operator improves the stability through active control, assuming no active control leads to a worst case analysis.

$\mathbf{Z}_h = \mathbf{0}$: There is no loss of generality due to this assumption since Z_h may always be included in Y_m .

$\mathbf{Z}_e = \mathbf{0}$: The slave is assumed to be in free motion.

2.5.1 A two-channel position-position architecture

The first case studied here is a typical two-channel position-position teleoperation architecture.

The above assumptions simplify the characteristic equation in (2.16) to the following:

$$1 + Z_{BF} \frac{C_1 Y_m Y_s}{1 + C_1 C_4 Y_m Y_s} = 0 \quad (2.23)$$

It is further assumed that

$$Y_m = \frac{1}{m_m s^2 + b_m s + k_m} \quad (2.24)$$

$$Y_s = \frac{1}{m_s s^2 + b_s s + k_s} \quad (2.25)$$

$$C_1 = k_s \quad C_4 = -k_m \quad C_2 = 0 \quad (2.26)$$

Using (2.22)-(2.26) the characteristic equation (2.23) can be written as:

$$1 + \frac{m_{bf}}{m_m m_s} \frac{\omega_{bf}^2 s}{\left(s^2 + 2\zeta_{bf} \omega_{bf} s + \omega_{bf}^2\right)} \frac{k_s}{s^3 + \left(\frac{b_m}{m_m} + \frac{b_s}{m_s}\right) s^2 + \left(\frac{k_m}{m_m} + \frac{k_s}{m_s} + \frac{b_m b_s}{m_m m_s}\right) s + \frac{k_m b_s}{m_m m_s} + \frac{k_s b_m}{m_s m_m}} = 0 \quad (2.27)$$

Although it is possible to derive an exact range of m_{bf} for which the system remains stable (e.g., by applying the Routh stability test), this will not be done here because of its limited application. To show the possibility of instability, the following numerical values are used for

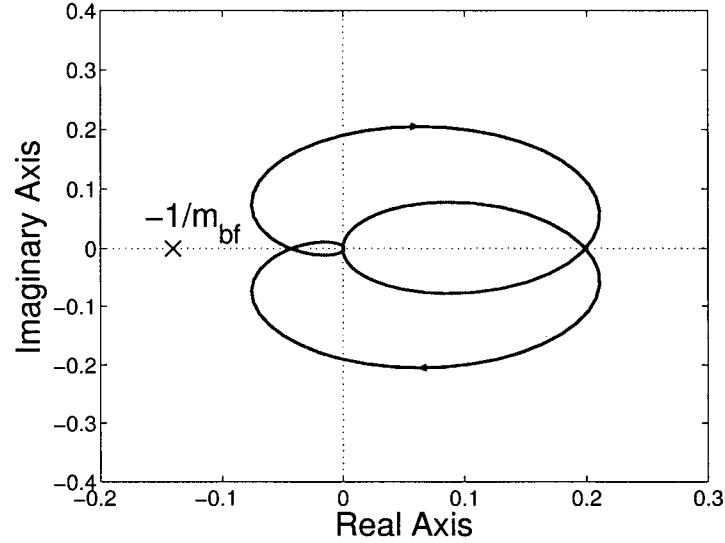


Figure 2.6: Nyquist of a typical two-channel position-position architecture with biodynamic feedthrough.

the system parameters:

$$\begin{aligned}
 m_m &= 1\text{kg} & b_m &= 2 \times 0.7 \times 30\text{N.s/m} & k_m &= 30^2\text{N/m} \\
 m_s &= 10\text{kg} & b_s &= 10 \times 2 \times 0.7 \times 20\text{N.s/m} & k_s &= 10 \times 20^2\text{N/m} \\
 \omega_{bf} &= 2\pi \times 30\text{rad/sec} & \zeta_{bf} &= 0.7 & &
 \end{aligned} \tag{2.28}$$

The Nyquist diagram of the system with these values is plotted in Figure 2.6. According to this diagram, the system is stable for $-5.01 < m_{bf} < 23.1$. A negative value of m_{bf} can be interpreted as negative correspondence between the positions of the master and slave. It is worth noting that the system is more prone to instability for negative values of m_{bf} . The Nyquist diagram also shows that the presence of a time delay in the loop would produce instability for smaller values of positive m_{bf} . The root loci of the system for positive and negative m_{bf} 's are given in Figures 2.7(a) and 2.7(b), respectively. Note how two of the closed-loop poles move toward the unstable region as $|m_{bf}|$ increases.

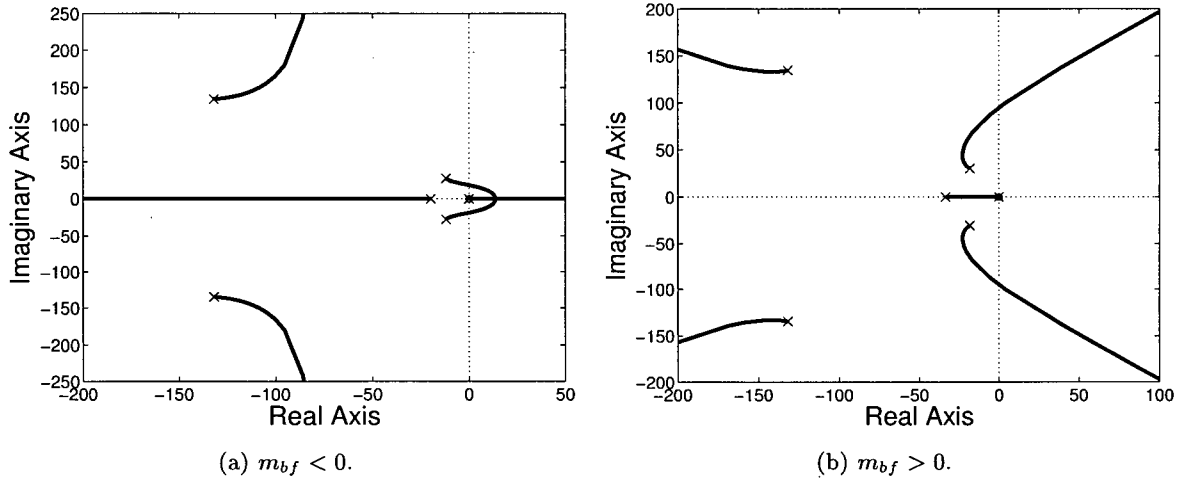


Figure 2.7: Root locus of a typical two-channel position-position architecture with biodynamic feedthrough.

2.5.2 A four-channel architecture

A typical four-channel teleoperation system is considered now. Again, the slave is assumed to be in free motion. Obviously, C_3 is irrelevant in this case since there is no environment force (i.e., $Z_e = 0$). For this case, the characteristic equation is given by:

$$1 + \frac{m_{bf}}{m_m m_s} \frac{\omega_{bf}^2 s}{s^2 + 2\zeta_{bf} \omega_{bf} s + \omega_{bf}^2} \frac{k_s + C_2 (m_m s^2 + b_m s + k_m)}{s^3 + \left(\frac{b_m}{m_m} + \frac{b_s}{m_s}\right) s^2 + \left(\frac{k_m}{m_m} + \frac{k_s}{m_s} + \frac{b_m b_s}{m_m m_s}\right) s + \frac{k_m b_s}{m_m m_s} + \frac{k_s b_m}{m_s m_m}} = 0 \quad (2.29)$$

All parameters are chosen to be the same as those in the previous example in (2.28). The feedforward force gain from the master to the slave is selected $C_2 = 5$. The force is scaled up by a factor of five to compensate for the difference between the master and slave masses. The Nyquist diagram of the system in this case is presented in Figure 2.8. In this case, the system becomes unstable for $m_{bf} < -2.37$. The system remains stable for all positive values of m_{bf} . This would change if there was time delay in the loop. It is also worth noting that the value of $|m_{bf}|$ for which instability occurs is less than that of the previous case. Similar conclusions can be deduced from the root locus plots in Figures 2.9(a) and 2.9(b)

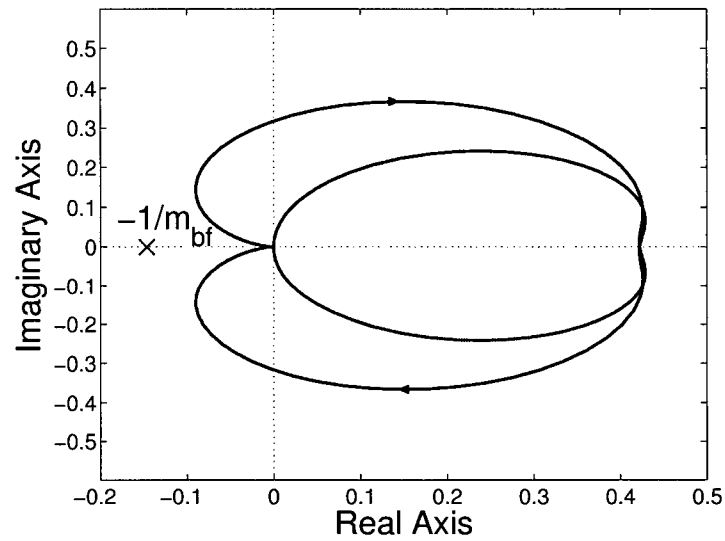


Figure 2.8: Nyquist of a typical four-channel teleoperation architecture with biodynamic feedthrough.

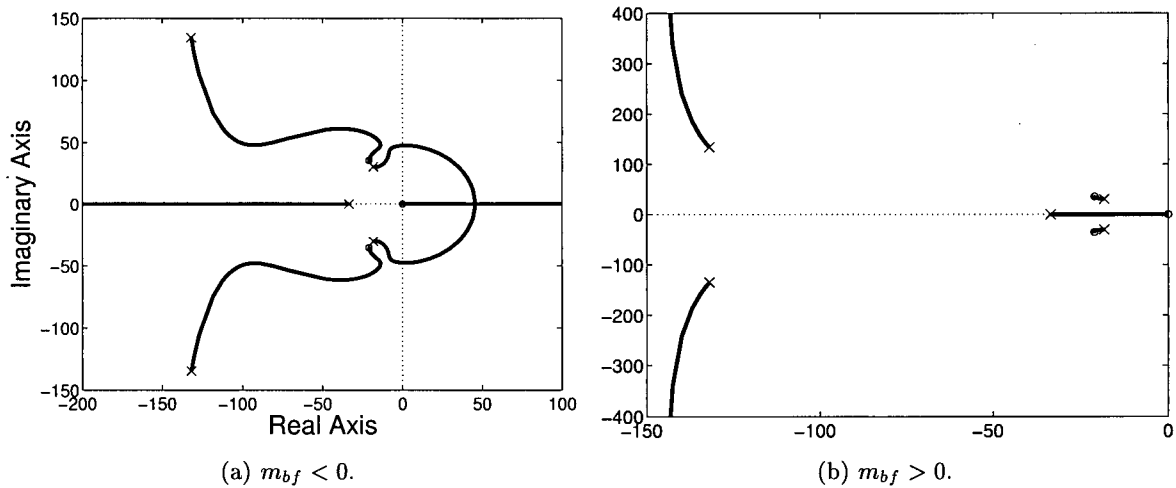


Figure 2.9: Root locus of a typical four-channel teleoperation architecture with biodynamic feedthrough.

2.6 Conclusions

This chapter proposed a framework for modeling and analysis of teleoperation/manual control systems with movable bases. First a modified four-channel teleoperation architecture was introduced. The effect of base motion was modeled by applying an inertial force to the master device in response to slave (base) motion. The model was further refined by using results

from manual control theory. The proposed model links the analysis and design of teleoperation systems to that of manual control systems. The chapter concluded with the analysis of the stability of typical two-channel and four-channel teleoperation architectures in the presence of biodynamic feedthrough. The Nyquist and root locus methods were employed to demonstrate potential instability due to feedthrough interferences. Although the position tracking between the master and the slave is not affected by base motion, the feedthrough dynamics can change the perceived dynamics of the controlled system and therefore affect the task completion.

Chapter 3

Identification of Biodynamic Feedthrough and Arm/Joystick Dynamics

3.1 Overview

In Chapter 2, a general model for teleoperation/manual control from movable bases was presented. The biodynamic feedthrough was represented by the impedance Z_{BF} that converts the base position to an unintentional force acting on the joystick. This chapter is concerned with developing models for biodynamic feedthrough. The problem has been considered by other researchers before. The most comprehensive model has been proposed by Jex et al. in [55]. Although the model can be useful for simulation, it can be hardly used in analysis and design because of its nonlinearity, complexity and the difficulties with its identification. Feedthrough models based on the *bobweight* effect have been presented in a few reports, e.g. in [31,45,46,115]. Similar linear models have been proposed and employed by [51] and the references therein.

A popular approach to modeling is system identification based on the input-output data [76]. Identification for robust control has been a subject of research. The goal is to obtain an estimate of the system transfer function using a finite set of noisy measurements. The error bounds on the estimated transfer function must also be calculated. Classical methods [76,123] assume that the structure of the system model is known by the identification process and the uncertainty only

arises from measurement noise. However, this is not always true as in the case of biodynamic feedthrough, the actual form of the model is unknown. The estimation in such cases may be biased because of the unmodeled dynamics. Therefore, another source of uncertainty can be a mismatch between the actual model of the system and the model used in the identification (undermodeling) [123]. There have been two classes of identification methods for robust control that address this problem. In the so called *hard bound* methods, the undermodeling is assumed to be deterministic and using some prior knowledge about noise and the unmodeled dynamics, hard bounds are obtained for the estimation errors [38,123,129]. These approaches usually yield conservative error bounds [35]. The second group of techniques, *soft bound* methods, assume that the undermodeling has some a priori known stochastic structure parameterized by some parameters [35,123]. The noise and undermodeling parameters can be identified using the data set in the *stochastic embedding* approach proposed by Goodwin et al. in [35]. The parameter values are used to estimate the error bounds on the estimated nominal transfer function.

In this chapter, first, a system identification-based approach to feedthrough modeling is proposed. To begin with, a slightly revised version of the system configuration in Figure 2.4 is presented. A model within the framework of *stochastic embedding* is developed for biodynamic stick feedthrough. The results of the identification experiments using this model are presented.

The modeling and identification of feedthrough dynamics based on the *bobweight* effect and using the least squares estimation is also addressed in this chapter. The resulting model is simpler and produces responses comparable to those of the stochastic embedding approach. A mass-spring-damper type model is used and identified for the lumped arm/joystick dynamics. The experimental setup is composed of the UBC motion simulator (Figure 1.2) and the twin-pantograph joystick (Figure 1.3). The experiments are performed along the z -axis (vertical axis). A schematic of the system is given in Figure 4.1. More details about the setup and its components will be presented in Chapter 4.

3.2 System Identification Using Stochastic Embedding

This section explains the identification of feedthrough dynamics within the framework of stochastic embedding. The input and the output of the feedthrough model are specified. The prior assumptions on measurement noise and the stochastic structure of unmodeled dynamics are

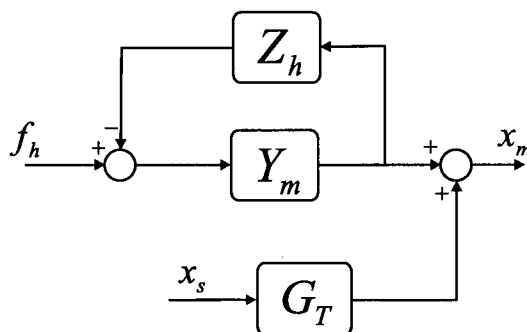


Figure 3.1: The modified model structure.

stated. The estimation of the nominal feedthrough response, the noise and undermodeling parameters, and the uncertainty affiliated with the identified response are discussed.

The system configuration presented in Figure 2.4 of Chapter 2 incorporates the effect of feedthrough as a force acting on the joystick. In practice, this model cannot be identified because its output is not measurable (i.e., there is no force sensor attached to the joystick used in this research). Figure 3.1 introduces a solution that eliminates this problem. In this configuration, the output of the biodynamic feedthrough block is the feedthrough-induced joystick displacement, which can be measured. It is worth noticing that this model decouples changes in the feedthrough dynamics from those in the lumped arm/joystick dynamics. The problem is treated in the discrete time domain here. The final results can be transformed to the continuous time domain for use in the μ -synthesis design.

During the identification experiments, the operator does not exert any intentional force on the joystick (i.e., $f_h = 0$ in Figure 3.1). By adopting the stochastic embedding approach, it is assumed that the input-output relationship is governed by the following difference equation:

$$y(k) = G_T(z^{-1})u(k) + v(k) \quad (3.1)$$

where $G_T(z^{-1})$ is a rational transfer function, $y(k)$ and $u(k)$ are the output and input (i.e., joystick displacement x_m and the platform displacement x_s in Figure 3.1) at the k 'th sample time and $v(k)$ is measurement noise. The sequence $v(k)$ is a zero mean i.i.d (independent identically distributed) random process. $u(k)$ is a quasi-stationary sequence [76] and is assumed to be independent from $v(k)$. It is further assumed that the transfer function $G_T(z^{-1})$, or

equivalently $G_T(e^{-j\omega})$, can be written in the following form:

$$G_T(e^{-j\omega}) = G(e^{-j\omega}, \theta) + G_\Delta(e^{-j\omega}) \quad (3.2)$$

where the first term is the nominal transfer function and the second term, usually referred to as undermodeling, is a realization of a zero mean random process, i.e.,

$$E\{G_\Delta(e^{-j\omega})\} = 0 \quad (3.3)$$

$$E\{G_T(e^{-j\omega})\} = G(e^{-j\omega}, \theta) \quad (3.4)$$

Note that the nominal part, $G(e^{-j\omega}, \theta)$, is parameterized in terms of some unknown parameter vector θ to be estimated. Assuming a general fixed denominator model for this term,

$$G(e^{-j\omega}, \theta) = \left[\lambda_1(e^{-j\omega}) \quad \lambda_2(e^{-j\omega}) \quad \dots \quad \lambda_p(e^{-j\omega}) \right] \theta \triangleq \Lambda(e^{-j\omega}) \theta \quad (3.5)$$

with $\theta = \left[\theta_1 \quad \theta_2 \quad \dots \quad \theta_p \right]^T$. Several fixed denominator models have been proposed in the literature including FIR, *Laguerre* and *Kautz* models [123,127–129]. FIR models are the simplest among these and their parameters are the impulse response samples. The problem with FIR models is that if the system has poles close to the unit circle, the number of parameters to be used becomes unacceptably large. This is normally the case if the sampling frequency is high compared to the system modes. Kautz models are particularly suited for the systems that have highly resonant modes [127–129]. Experimental data revealed that Laguerre models are suitable for the modeling of biodynamic feedthrough for the problem subject of this research. The discrete Laguerre model set is given by

$$\lambda_k(z^{-1}) = \frac{\sqrt{1-a^2}z^{-1}}{1-az^{-1}} \left(\frac{z^{-1}-a}{1-az^{-1}} \right)^{k-1}, \quad -1 < a < 1. \quad (3.6)$$

The Laguerre parameter, a , should be chosen close to the dominant pole of the system to be

identified. The nonparametric part of the transfer function $G_{\Delta}(z^{-1})$ can be modeled by

$$G_{\Delta}(z^{-1}) = D(z^{-1})\Delta(z^{-1}) \quad (3.7)$$

where

$$\Delta(z^{-1}) = \sum_{k=1}^m \eta_k z^{-k} \quad (3.8)$$

$$D(z^{-1}) = \left(\frac{z^{-1}-a}{1-az^{-1}} \right)^p \quad (3.9)$$

It can be shown that $G_{\Delta}(z^{-1})$ as defined above spans the orthogonal complement of $G(z^{-1}, \theta)$ [129]. Now, the model of system in (3.1) can be rewritten in the following form:

$$y(k) = \phi^T(k)\theta + \zeta^T(k)\eta + v(k) \quad (3.10)$$

where

$$\eta^T = \begin{bmatrix} \eta_1 & \eta_2 & \cdots & \eta_m \end{bmatrix} \quad (3.11)$$

$$\phi^T(k) = \begin{bmatrix} \lambda_1(z^{-1})u(k) & \lambda_2(z^{-1})u(k) & \cdots & \lambda_p(z^{-1})u(k) \end{bmatrix} \quad (3.12)$$

$$\zeta^T(k) = \begin{bmatrix} D(z^{-1})u(k-1) & D(z^{-1})u(k-2) & \cdots & D(z^{-1})u(k-m) \end{bmatrix} \quad (3.13)$$

The input-output relationship given in (3.10) can be converted into a stacked matrix format.

$$Y = \Phi\theta + \Psi\eta + V \quad (3.14)$$

with

$$Y = \begin{bmatrix} y(1) & y(2) & \cdots & y(N) \end{bmatrix}^T \quad (3.15)$$

$$\Phi = \begin{bmatrix} \phi(1) & \phi(2) & \cdots & \phi(N) \end{bmatrix}^T \quad (3.16)$$

$$\Psi = \begin{bmatrix} \zeta(1) & \zeta(2) & \cdots & \zeta(N) \end{bmatrix}^T \quad (3.17)$$

$$V = \begin{bmatrix} v(1) & v(2) & \cdots & v(N) \end{bmatrix}^T \quad (3.18)$$

The Least Squares criterion may be used to estimate the unknown parameters vector θ .

$$\hat{\theta}_N = \arg \min_{\theta} \left(Y - \hat{Y}(\theta) \right)^T \left(Y - \hat{Y}(\theta) \right) = (\Phi^T \Phi)^{-1} \Phi^T Y \quad (3.19)$$

It is not difficult to show that the covariance of the estimation error is given by [35]

$$P_{\theta} = E\{(\hat{\theta}_N - \theta)(\hat{\theta}_N - \theta)^T\} = (\Phi \Phi^T)^{-1} \Phi^T (\Psi C_{\eta} \Psi^T + C_v) \Phi (\Phi^T \Phi)^{-1} \quad (3.20)$$

where

$$C_{\eta} \triangleq E\{\eta \eta^T\} \quad C_v \triangleq E\{V V^T\} \quad (3.21)$$

It can also be shown that the modeling error in the frequency domain is given by [35]

$$G_T(e^{-j\omega}) - G(e^{-j\omega}, \hat{\theta}_N) = (\Pi - \Lambda \Omega \Psi) \eta - \Lambda \Omega V \quad (3.22)$$

where $\Omega = (\Phi^T \Phi)^{-1} \Phi^T$ and $\Pi = D(e^{-j\omega}) \begin{bmatrix} e^{-j\omega} & e^{-j2\omega} & \cdots & e^{-jm\omega} \end{bmatrix}$. To obtain the error bounds in the frequency domain the following must be defined

$$\tilde{g}(e^{-j\omega}) = \begin{bmatrix} \text{Re}\{G_T(e^{-j\omega}) - G(e^{-j\omega}, \hat{\theta}_N)\} \\ \text{Im}\{G_T(e^{-j\omega}) - G(e^{-j\omega}, \hat{\theta}_N)\} \end{bmatrix} \quad (3.23)$$

Then,

$$P_{\tilde{g}}(\omega) = E\{\tilde{g}(e^{-j\omega})\tilde{g}(e^{-j\omega})^T\} = \Gamma(e^{-j\omega})\Upsilon\Gamma^T(e^{-j\omega}) \quad (3.24)$$

where

$$\Upsilon = \begin{bmatrix} \Omega(\Psi C_\eta \Psi^T + C_v)\Omega^T & -\Omega\Psi C_\eta \\ -C_\eta\Psi^T\Omega^T & C_\eta \end{bmatrix} \quad (3.25)$$

and

$$\Gamma(e^{-j\omega}) = \begin{bmatrix} \text{Re}\{\Lambda(e^{-j\omega}), \Pi(e^{-j\omega})\} \\ \text{Im}\{\Lambda(e^{-j\omega}), \Pi(e^{-j\omega})\} \end{bmatrix} \quad (3.26)$$

Using (3.24) and assuming a Gaussian distribution for $\tilde{g}(e^{-j\omega})$ one can construct confidence ellipses in the complex plane at each frequency around the estimated nominal frequency response, i.e.

$$\tilde{g}(e^{-j\omega})^T P_{\tilde{g}}^{-1} \tilde{g}(e^{-j\omega}) \sim \chi_{(2)}^2 \quad (3.27)$$

and χ^2 is a Chi-square distribution.

3.2.1 Estimating Measurement Noise and Undermodeling Parameters

The undermodeling and measurement noise covariances are used in the covariance of the parameter estimates in (3.20) and also in the covariance of the frequency domain errors (3.24). In practice, these quantities are unknown and must be identified based on available data. To this end, the following assumptions are made:

$$C_\eta = E\{\eta\eta^T\} = \sigma_\eta^2 I_{m \times m} \quad C_v = E\{VV^T\} = \sigma_v^2 I_{N \times N} \quad (3.28)$$

A modified version of the estimation method proposed in [35] and [123] is presented here. This approach is applicable to large data sets whereas the method proposed in these references

is restricted to small size data sets [123]. By applying QR factorization to Φ , (3.14) may be written as

$$Y = \begin{bmatrix} R_{1N \times p} & R_{2N \times N-p} \end{bmatrix} \begin{bmatrix} Q \\ 0 \end{bmatrix} \theta + \Psi\eta + V \quad (3.29)$$

and therefore,

$$R_2^T Y = R_2^T \Psi \eta + R_2^T V \quad (3.30)$$

Note that (3.30) is of dimension $N - p$ and if used in a maximum likelihood identification, it would lead to matrix inversion of order of $N - p$ at each optimization step. This could be computationally expensive [123]. To avoid this problem, we propose another QR factorization to be performed on $R_2^T \Psi$, i.e.

$$R_2^T \Psi = \begin{bmatrix} X_{1N-p \times m} & X_{2N-p \times N-p-m} \end{bmatrix} \begin{bmatrix} P_{m \times m} \\ 0 \end{bmatrix} \eta \quad (3.31)$$

Using (3.30) and (3.31),

$$W_1 \text{ (} m \times 1 \text{)} \triangleq X_1^T R_2^T Y = P\eta + X_1^T R_2^T V \quad (3.32)$$

$$W_2 \text{ (} N-p-m \times 1 \text{)} \triangleq X_2^T R_2^T Y = X_2^T R_2^T V \quad (3.33)$$

Note that

$$P_{W_1} \triangleq E \{W_1 W_1^T\} = \sigma_\eta^2 P P^T + \sigma_v^2 X_1^T R_2^T R_2 X_1 \quad (3.34)$$

$$P_{W_2} \triangleq E \{W_2 W_2^T\} = \sigma_v^2 X_2^T R_2^T R_2 X_2 = \sigma_v^2 M \quad (3.35)$$

with $M = X_2^T R_2^T R_2 X_2$. The log-likelihood of vectors W_1 and W_2 are given by (assuming Gaussian distribution)

$$l(W_1 | \sigma_v^2, \sigma_\eta^2) = -\frac{m}{2} \ln(2\pi) - \frac{1}{2} \ln(\det(P_{W_1})) - \frac{1}{2} W_1^T P_{W_1}^{-1} W_1 \quad (3.36)$$

$$l(W_2|\sigma_v^2) = -\frac{N-p-m}{2} \ln(2\pi) - \frac{1}{2} [(N-p-m) \ln(\sigma_v^2) + \ln(\det(M))] - \frac{1}{2} (\sigma_v^2)^{-1} W_2^T M^{-1} W_2 \quad (3.37)$$

(3.36), (3.37) can be used to find the maximum likelihood estimation of unknown parameters σ_v^2 and σ_η^2 . An initial estimate of σ_v^2 is found from (3.37),

$$\sigma_v^2 = \frac{1}{N-p-m} W_2^T M^{-1} W_2 \quad (3.38)$$

One may either accept this as the estimate of σ_v^2 and maximize (3.36) with respect to σ_η^2 or use this as an initial estimate and maximize (3.36) with respect to σ_v^2 and σ_η^2 . This problem is not necessarily convex. The optimization routine should be repeated with a few initial estimates to increase the chance of reaching a global maximum point.

3.3 Identification Experiments

The experimental setup used in the feedthrough identification experiments is the same as the one that will be used in the feedthrough cancellation experiments (see Figures 4.1 and 4.2). A single subject was used in the identification experiments throughout the rest of this chapter. The operator (the author) was seated on the UBC motion simulator while holding the gravity compensated joystick. He was instructed to relax his arm and not to try to control the joystick but to keep his grasp on the joystick handle while the platform was moving. Therefore, one may assume that $f_h = 0$ in Figure 3.1. The platform was excited with a reference position command obtained by applying a fifth-order Butterworth filter with bandwidth of $f_{bw} = 5Hz$ to a white noise. Several runs of experiment were carried out each of which lasted for 100s. The platform position and acceleration and also the joystick position were measured using the installed sensors. The sampling rate was chosen to be $f_s = 42.67Hz$. The following parameters were used in the identification

$$a = 0.9 \quad p = 18 \quad m = 50 \quad N = 2136$$

Table 3.1: Identification results.

	experiment 1	experiment 2	experiment 3	experiment 4
$z_p(rms)$ m	0.011	0.011	0.011	0.011
$z_j(rms)$ m	0.016	0.017	0.015	0.016
$a_z(rms)$ m/s ²	3.97	4.01	4.05	4.09
σ_v	0.0141	0.0167	0.0149	0.0124
σ_η	0.0224	0.0350	0.0173	0.0233
σ_{pe}	0.0084	0.0095	0.0072	0.0074

The value of a in the Laguerre models should be chosen such that it is close to a dominant pole of the system to be identified [127]. However, since the actual dynamics are unknown, a reasonable guess was made for this dominant pole and a was selected accordingly. p , the number of Laguerre bases was selected such that the resultant prediction time domain error is minimized. This was done by trial and error where p was increased until there was no significant improvement in the model prediction error. A 50s window of the data was selected from each set of data to carry out the identification. Note that the low frequency content of the feedthrough response is not reliable due to the drift in the joystick position. The high frequency content of the measurements is also noisy. Therefore, the measurement data were pre-filtered with a band-pass filter with low and high frequencies of $f_l = 0.6\text{Hz}$ and $f_h = 10\text{Hz}$, respectively. Function *fmincon* from the *Matlab Optimization Toolbox*® was employed to find the maximum likelihood estimates. The routine converged fast in all cases (less than 15 steps) and the same results were obtained from different initial points. The estimation results from four separate experiments are summarized in Table 3.1. In this table, σ_v and σ_η have been introduced in (3.28) and σ_{pe} is the root mean square prediction error. $z_p(rms)$ and $a_z(rms)$ are the RMS values of the platform displacement and platform acceleration, respectively. $z_j(rms)$ is the RMS joystick displacement measured during the experiments. The estimation results are consistent among these four experiments. The predicted output (joystick displacement) and the actual output profiles from one of the experiments are shown in Figure 3.2.

The estimated Laguerre, noise and undermodeling parameters were used to estimate the nominal feedthrough response, $G(e^{-j\omega}, \theta_N)$ and the confidence ellipses in the complex plane.

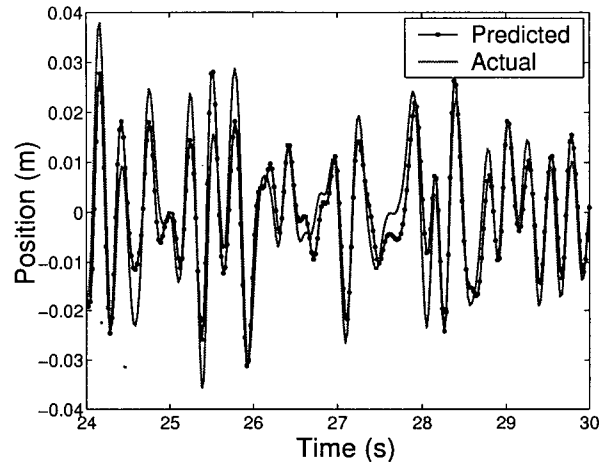


Figure 3.2: The actual and predicted joystick displacements in one of the experiments.

The estimation results from the experiments were combined together using [76],

$$\theta_N = P_\theta \sum_{i=1}^4 P_{\theta_i}^{-1} \theta_N^i \quad (3.39)$$

where

$$P_\theta = \left(\sum_{i=1}^4 P_{\theta_i}^{-1} \right)^{-1} \quad (3.40)$$

Similarly, for the covariance of the frequency domain errors,

$$P_{\hat{g}}(\omega) = \left(\sum_{i=1}^4 P_{\hat{g}_i}^{-1} \right)^{-1} \quad (3.41)$$

Figures 3.3(a)-3.3(d) show the $G(e^{-j\omega}, \theta_N)$, $G(e^{-j\omega}, \theta_N^i)$ and also the 99% confidence ellipses for four different experiments. Based on these results, the confidence ellipses describe the uncertainties in the biodynamic feedthrough response very well with the exception of experiment 2 at low frequencies.

The uncertainty ellipses cannot be directly incorporated into the μ -synthesis design framework. One way to tackle this problem is first to circumscribe these ellipses with circles defined

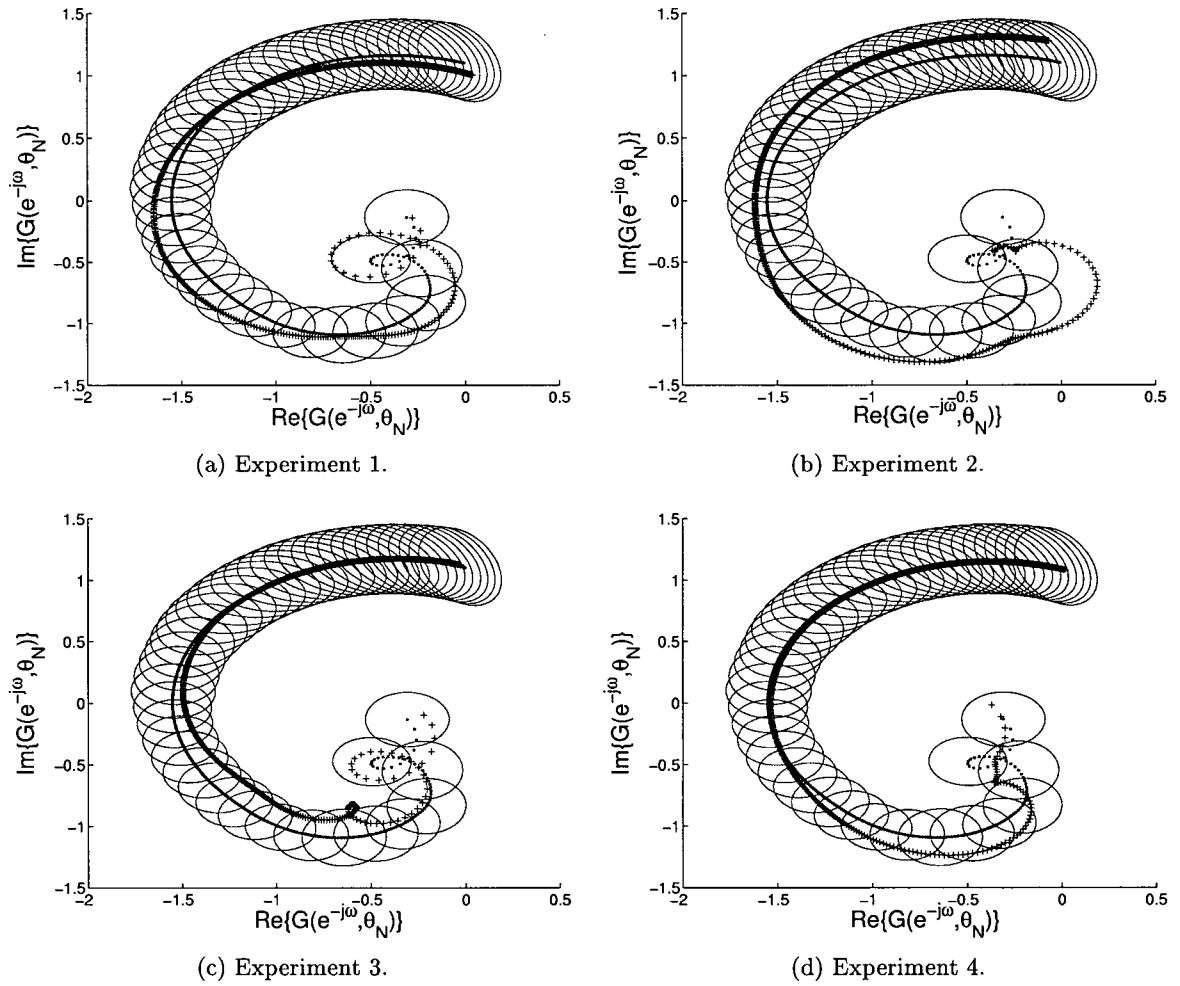


Figure 3.3: Estimated biodynamic feedthrough response and its uncertainty ellipses.

by $R(\omega)$. Then, a stable continuous transfer function, $W_u(\omega)$, can be fitted to $R(\omega)$ such that

$$|W_u(\omega)| \approx R(\omega) \quad (3.42)$$

This approach leads to the feedthrough model shown in Figure 3.4 which can be used in the μ -synthesis design framework. Obviously, there is some conservatism in this approach because of the loss of phase information in the error bounds. A stable transfer function can also be fitted to $G(e^{-j\omega}, \theta_N)$. *Matlab* provides functions for the frequency domain fitting. Following the above approach, 12'th order stable transfer functions were fitted to the estimated biodynamic response and error bounds on its magnitude, respectively. The results are presented in Figures 3.5(a)-

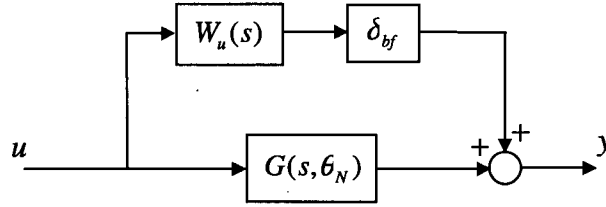


Figure 3.4: Feedthrough model with uncertainty block.

3.5(d). As it can be seen, all four estimated biodynamic feedthrough responses are within the uncertainty bounds. The numerator and denominator of the estimated feedthrough response, $G(s, \theta_N)$ in descending powers of s are as follows:

$$\begin{aligned} \text{num}(1-6) &= \begin{bmatrix} 4.81e-9 & -1.35e-7 & -2.88e-5 & -2.49e-5 & 2.0e-3 & 1.140e-2 \end{bmatrix} \\ \text{num}(7-13) &= \begin{bmatrix} 0.3882 & 0.5446 & 14.78 & 6.77 & 214.83 & 19.94 & 1084.2 \end{bmatrix} \\ \text{den}(1-6) &= \begin{bmatrix} 1.0e-8 & 8.81e-7 & 3.55e-5 & 6.02e-4 & 4.9e-3 & 3.25e-2 \end{bmatrix} \\ \text{den}(7-13) &= \begin{bmatrix} 0.1388 & 0.4926 & 1.184 & 2.277 & 2.744 & 2.360 & 0.7153 \end{bmatrix} \end{aligned}$$

Remark: As stated earlier, one subject has been used in the above experiments and therefore, the resultant uncertainties only account for the changes in that specific operator dynamics. An alternative approach would be to carry out experiments with different subjects and fuse the resultant models and error bounds. This has not been done in this research partly because of concerns about potential undesirable effects of the high base accelerations in the experiments on human subjects. Nevertheless, it should be stressed that the design approach presented in the next chapter of this thesis is robust with respect to uncertainties in the operator related dynamics. Moreover, models obtained through identification experiments with several subjects can be easily incorporated in the control synthesis framework proposed by this thesis in future.

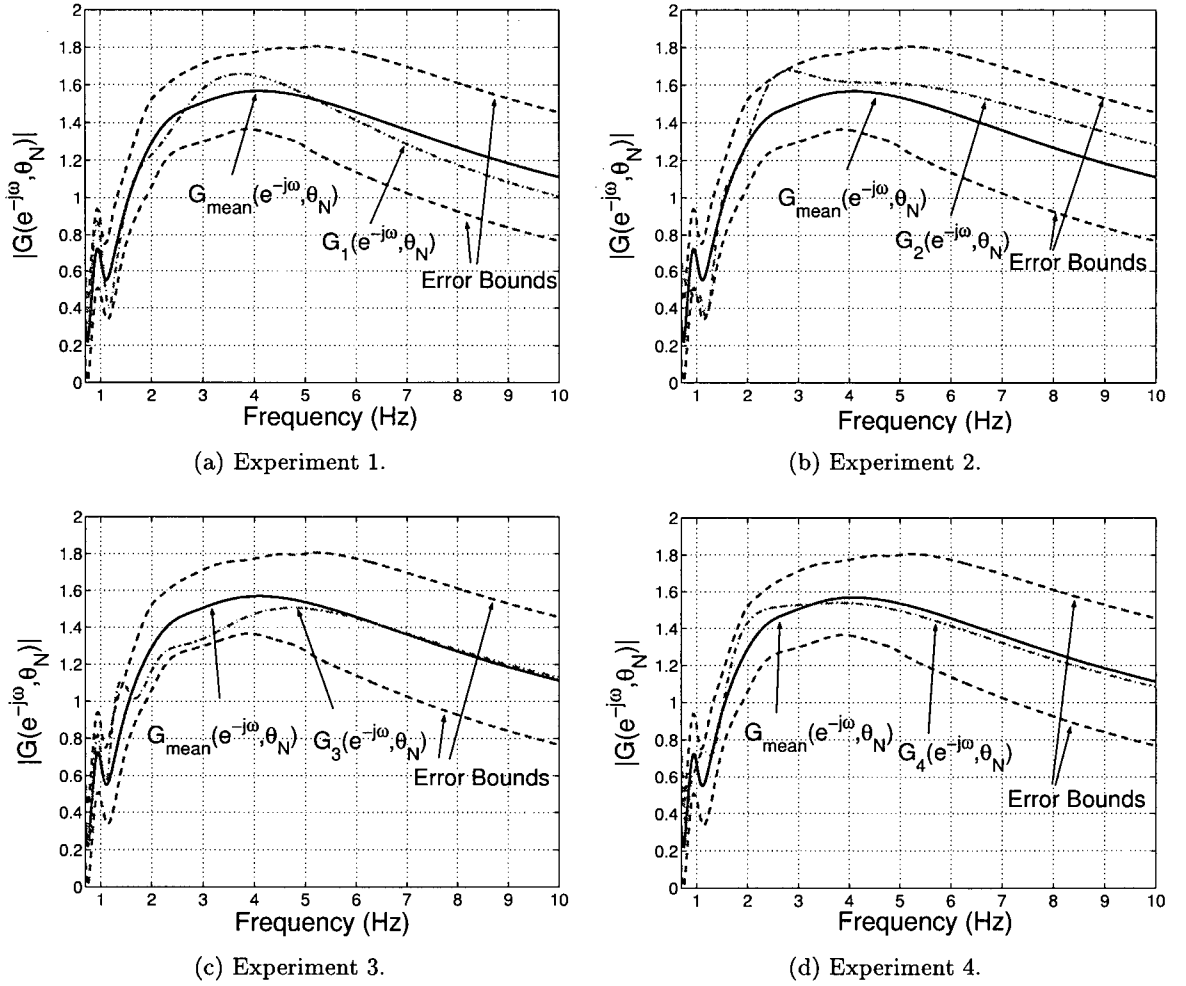


Figure 3.5: Estimated magnitude of the biodynamic feedthrough response and its uncertainty bounds.

3.4 Arm/Joystick and Acceleration Based Feedthrough Models

In this part of the thesis the modeling and identification of the arm/joystick dynamics is addressed. Also, a simpler model is proposed for biodynamic feedthrough that only considers the *bobweight* effect of the joystick and arm.

The arm/joystick subsystem is modeled as a mass-spring-damper system with uncertain parameters m_m , b_m and k_m (see Figure 3.6).

$$x_m(s) = \frac{f_h - u_m - f_{bf}}{m_m s^2 + b_m s + k_m} \quad (3.43)$$

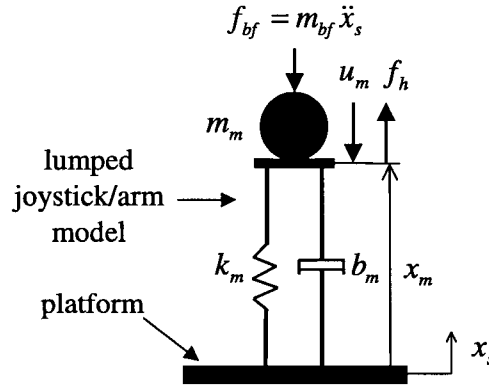


Figure 3.6: Simplified model of the arm/joystick and biodynamic feedthrough.

where f_h is the exogenous hand force and u_m is the applied force by the motors and f_{bf} , to be introduced in (3.45) below. $m_m = m + \delta_m$, $b_m = b + \delta_b$ and $k_m = k + \delta_k$ are the effective mass, damping and stiffness of the arm/joystick subsystem, respectively. m , b and k are their nominal (estimated) values and δ values represent uncertainty. One may write

$$\begin{aligned} \frac{1}{m_m s^2 + b_m s + k_m} &= \frac{1}{m s^2 + b s + k} \times \frac{m s^2 + b s + k}{m_m s^2 + b_m s + k_m} \\ &= \frac{1}{m s^2 + b s + k} \times \frac{1}{1 + \frac{\delta_m s^2 + \delta_b s + \delta_k}{m s^2 + b s + k}} \end{aligned} \quad (3.44)$$

which leads to the block digram representation of the arm/joystick given in Figure 3.7.

Mass-spring-damper models have been used by other researchers to represent an operator's arm passive dynamics, e.g., in [26, 57, 65]. The arm parameters are posture dependent and vary from one operator to another. This has been modeled by the parametric uncertainty in (3.43) and (3.44).

As an alternative to the stochastic embedding approach to the feedthrough modeling, a simple acceleration based model is presented here. Similar models have been used by other researchers [31, 45, 51, 115]. The model was introduced in Chapter 2 and is given here again.

$$f_{bf} = \frac{\omega_{bf}^2 m_{bf} s^2}{s^2 + 2\zeta_{bf} \omega_{bf} s + \omega_{bf}^2} x_s = G_a(s) m_{bf} x_s \quad (3.45)$$

where $m_{bf} = m_f + \delta_{m_f}$ is the biodynamic feedback mass that is usually equal to the total mass of the arm and joystick ($m_{bf} = m_m$). δ_{m_f} represents the uncertainty associated with the

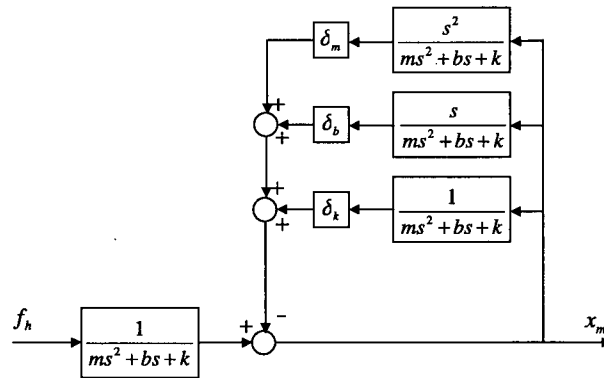


Figure 3.7: The arm/joystick model with uncertain parameters.

feedthrough mass. In other words, the base acceleration has an equivalent effect of an inertial force acting on the joystick. This force is proportional to the total mass of arm and joystick. The second-order lowpass filter in (3.45) makes the design problem that will be defined in Chapter 4 well-posed.

Remark: The above model neglects the transmission of motion to joystick through the chain formed by operator's body, shoulder, arm, and joystick. Therefore, its accuracy may degrade in the presence of a large base acceleration. Also, only parametric uncertainties are allowed here, whereas the stochastic embedding approach generates unstructured uncertainty bounds.

The nominal values of the arm/joystick parameters can be estimated through identification experiments along the z -axis of the joystick (see Figure 4.1). One can write

$$m_m \ddot{z} + b_m \dot{z} + k_m z + f_g = f_z \quad (3.46)$$

where m_m , b_m , and k_m are the lumped mass, damping and stiffness of the arm/joystick defined in (3.43). f_g is the gravitational force and f_z is the applied force along the z direction.

A work-space PD position controller augmented with a gravity compensation term was implemented to control the joystick (see Appendix C). The x and θ motions were locked by the controller. A band-limited noise (bandwidth=4.6Hz) was applied to the controller as the position command while the operator was holding the handle. The operator was instructed to relax his arm during the experiments each of which lasted 80 seconds. The applied motor torques (i.e. motor currents), and angular position of the motor shafts were measured. These measurements were used to compute the arm/joystick position and the applied work-space force

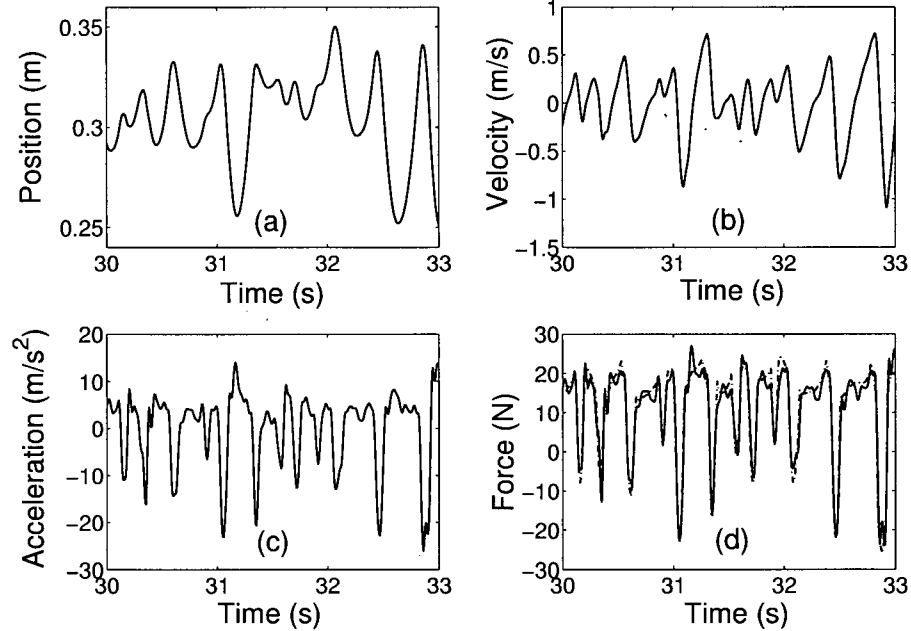


Figure 3.8: Arm/joystick identification results: (a) measured position. (b) computed velocity. (c) computed acceleration. (d) measured and estimated applied force.

using the device kinematics (Figures 3.8.a, 3.8.d).

The velocity and acceleration were computed by transforming the position signal to the frequency domain, applying $j\omega$ and $(j\omega)^2$ and converting them back to the time domain. A lowpass filter was used in the frequency domain to reduce the effect of noise (see Figures 3.8.b, 3.8.c). Finally, the Least Squares technique was employed to estimate the unknown parameters m_m , b_m , k_m , and f_g . Several runs of experiments were carried out and the estimated parameters were consistent across the runs. The estimated parameters are as follows:

$$m = 1.45\text{kg} \quad b = 10.0\text{N}\cdot\text{s}/\text{m} \quad k = 72.0\text{N}/\text{m} \quad f_g = 11.0\text{N} \quad (3.47)$$

Remark: The nominal feedthrough mass m_f is assumed to be the same as m which is the total mass of the arm and joystick.

It is also worth noting that the dynamic mass m is slightly larger than the static mass f_g/g . This might be due to the fact that the operator tends to hold the joystick against gravity. The measured and estimated work-space forces in one of the experiments are compared in Figure 3.8.d.

Remark: The uncertainties in the mass, spring and damping parameters can be determined based on engineering judgment. These parameters are generally posture dependent and they also vary among the different operators.

3.5 Comparison of the Feedthrough Models

The frequency responses of the two identified feedthrough models have been compared in Figure 3.9. In the acceleration-based model (3.45), $\omega_{bf} = 2\pi \times 12\text{rad/sec}$ and $\zeta_{bf} = 0.7$ were chosen. For this model, the following has been plotted in order to compare the two responses.

$$\frac{X_m(s)}{X_s(s)} = \frac{\omega_{bf}^2 m_f s^2}{(ms^2 + bs + k) (s^2 + 2\zeta_{bf}\omega_{bf}s + \omega_{bf}^2)} \quad (3.48)$$

Despite some differences, it is interesting to observe that the identified feedthrough responses demonstrate a similar trend, i.e. the magnitudes of the frequency responses increase at low frequency and then they flatten and start to decrease at high frequency. It should be pointed out that the level of base acceleration excitation in the stochastic embedding approach experiments was sufficiently high that it generated a significant body excitation and hence motion feedthrough via the shoulder and arm. This can explain the differences between the responses. Figure 3.10 compares the responses when the acceleration-based model is adjusted by a 50% increase in the estimated feedthrough mass m_f and the damping b . These responses reveal much more similarity in this case. The increase in effective feedthrough mass and damping is explainable by the excitation of a larger part of the operator's body in the stochastic embedding experiments. However, as will be seen in Chapter 4, the level of platform acceleration due to feedthrough-induced oscillations in our experiments is such that the simple acceleration-based model sufficiently describes the phenomenon for feedthrough cancellation.

3.6 Conclusions

This chapter addressed the modeling and identification of feedthrough and arm/joystick dynamics. The existing biomechanical models for feedthrough dynamics are nonlinear, complex and

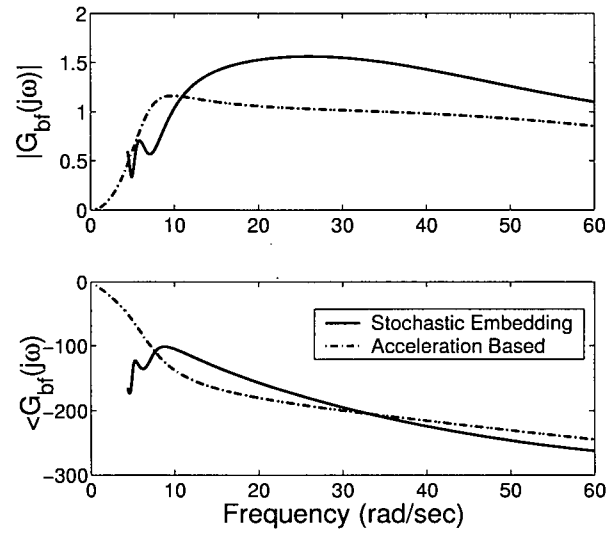


Figure 3.9: The identified feedthrough responses.

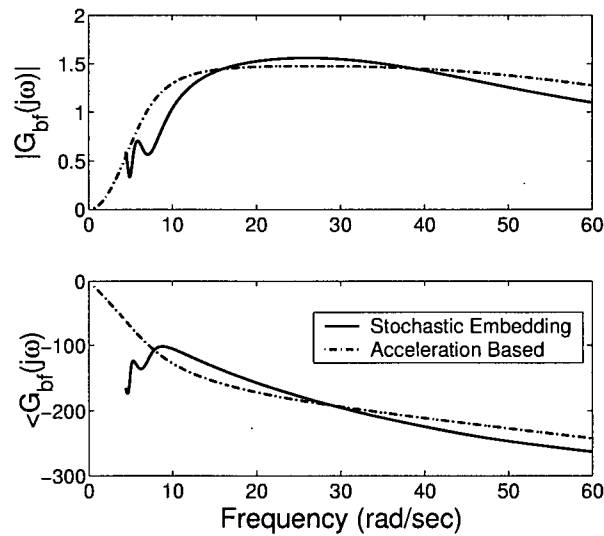


Figure 3.10: The compensated identified feedthrough responses.

do not consider uncertainties associated with human dynamics. This limits their application to the control synthesis. Two models were introduced for biodynamic feedthrough. First, the stochastic embedding methodology was adopted to estimate a nominal feedthrough response using experimental data. A feature of this approach is that it also provides an estimation of the errors associated with the identified transfer function. It should be noted that implicit assumption is that the nonlinearities and uncertainties in the feedthrough dynamics can be

accounted for by the stochastic embedding framework. Second, an acceleration-based model was introduced that considers the *bobweight* effect of the arm/joystick in response to the base acceleration.

A linear mass-spring-damper model with uncertain parameters was employed for the lump arm/joystick dynamics. The parameters were identified experimentally using the Least Squares technique. The identified lump arm/joystick mass was also used as the effective feedthrough mass in the second feedthrough model.

It was found out that the stochastic embedding based approach and the acceleration based feedthrough model produce comparable responses. While the former is more accurate in presence of large base accelerations, the latter is simpler and will result in lower order controllers if used in the design.

Chapter 4

Controller Design for Suppression of Biodynamic Feedthrough

4.1 Overview

In Chapter 2 of this thesis, it was shown that the performance and the stability of teleoperation/manual control systems with movable bases can be degraded by biodynamic interference. This chapter is concerned with the design of controllers for such systems. A novel approach is proposed for the design of controllers that robustly suppress feedthrough induced oscillations. The methodology is illustrated via an example. A single-degree-of-freedom manual control task is considered in which the operator uses a force-feedback joystick to position his/her base. It is shown analytically that a control approach that ignores the base motion can result in instability. Then, μ -synthesis-based controllers are proposed that robustly stabilize the system with respect to uncertainties in the arm/joystick and biodynamic feedthrough dynamics. The controllers also achieve a high level of performance based on the admittance shaping of the joystick and the motion tracking between the joystick and the base. Experimental studies demonstrate excellent responses of the system under the designed controllers. H_∞ and μ -synthesis based approaches have been used by other researches for the design of controllers in conventional fixed base teleoperation systems. For example, Kazerooni et al. in [57] proposed a two-channel force-force teleoperation controller using H_∞ design. Leung et al. in [67] employed μ -synthesis to develop a teleoperation system that is robust with respect to variations in time delay in

the communication while optimizing performance specifications. An application of H_∞ optimization to motion scaling in teleoperation is also given in [131]. However, the novelty of the present work lies in addressing the instability and reduced performance caused by closed-loop biodynamic feedthrough interference in manual control and teleoperation systems with movable bases. Uncertainties associated with the operator dynamics are also dealt with by the proposed framework.

This chapter is organized as follows. First, the prototype manual control task that is the subject of this research and the experimental setup are introduced. Next, the problem is formulated as a μ -synthesis robust performance design problem. The stability of the system under a fixed base PD-type controller that neglects the base motion is analyzed. Then, the identified arm/joystick and feedthrough dynamics from Chapter 3 are used in the design of the μ -synthesis based controllers. These controllers are successfully implemented on the experimental setup and the results are given. The chapter concludes with some remarks on the effectiveness of the proposed approaches.

4.2 Problem Statement

Closed-loop biodynamic interference occurs in situations in which operators are subjected to accelerations due to their action. For example, when a pilot uses a joystick to maneuver the aircraft the resultant aircraft acceleration can interfere with the voluntary control command through the pilot's arm dynamics. Similarly, the operator of an excavator employs a joystick to manipulate the environment and the environment forces induce cab accelerations that affect the operator's action. Details of these interactions differ from case to case, however, there are principal similarities between all cases. In this chapter, a single-degree-of-freedom manual control task is considered (see Figure 4.1). The operator uses a force-feedback joystick to position his/her base along the vertical axis. This relatively simple task highlights the problems associated with biodynamic feedthrough and is used to illustrate the proposed method for feedthrough cancelation.

The experimental setup is shown in Figure 4.2. The components of this system are as follows.

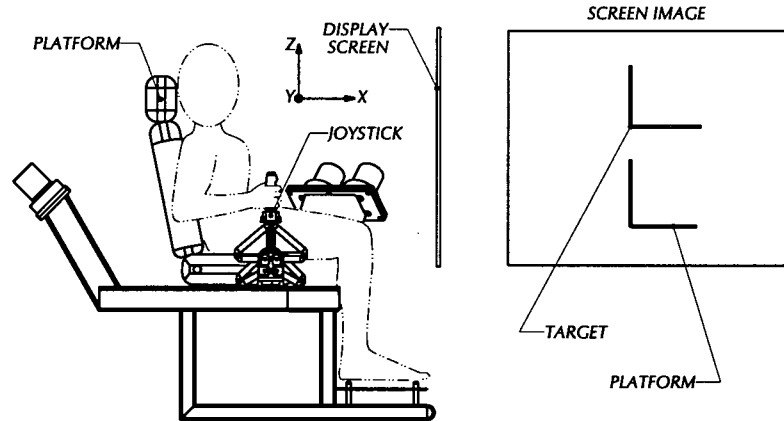


Figure 4.1: Schematic of the manual control task.

Motion Platform:

The UBC motion simulator [99] is used to simulate the base motion. This simulator is driven by six hydraulic cylinders. Each cylinder is capable of exerting forces in excess of 4000 N at 1 m/s, and over 8000 N at zero rod speed. This enables the platform to generate accelerations higher than 1g. The hydraulic actuation system is equipped with *Rexroth 4WRDE* three-stage proportional valves connected in a three-way configuration. Low friction Teflon seals are used in the hydraulic cylinders. The platform motion is controlled by link-space P controllers that use the link length measurements. The workspace position command is translated to a link-space command using the platform inverse kinematics (see Appendix B). A single-axis accelerometer is used to measure the platform acceleration along the z -axis. The output of the sensor is passed through a low-pass filter with bandwidth of 20Hz to remove noise and high frequency components of the acceleration due to vibration. For safety reasons and also to avoid singularities, the platform motion range is restricted to ± 20 cm, in x , y , z , and $\pm 20^\circ$ in roll, pitch and yaw coordinates, respectively. This has been done by imposing limits on the allowable reference position commands in the realtime control code. The platform controller runs on a *Themis Sparc 5*[®] board under *VxWorks*[®] operating system with a sampling rate of 256Hz. The code accepts position commands in work-space coordinates and returns the measured link lengths. The actual position of the platform in workspace coordinates is calculated by employing the forward kinematics which use the measured link lengths (see Appendix B).

Remark: In this particular example, a simple P controller suffices for the control of the platform.

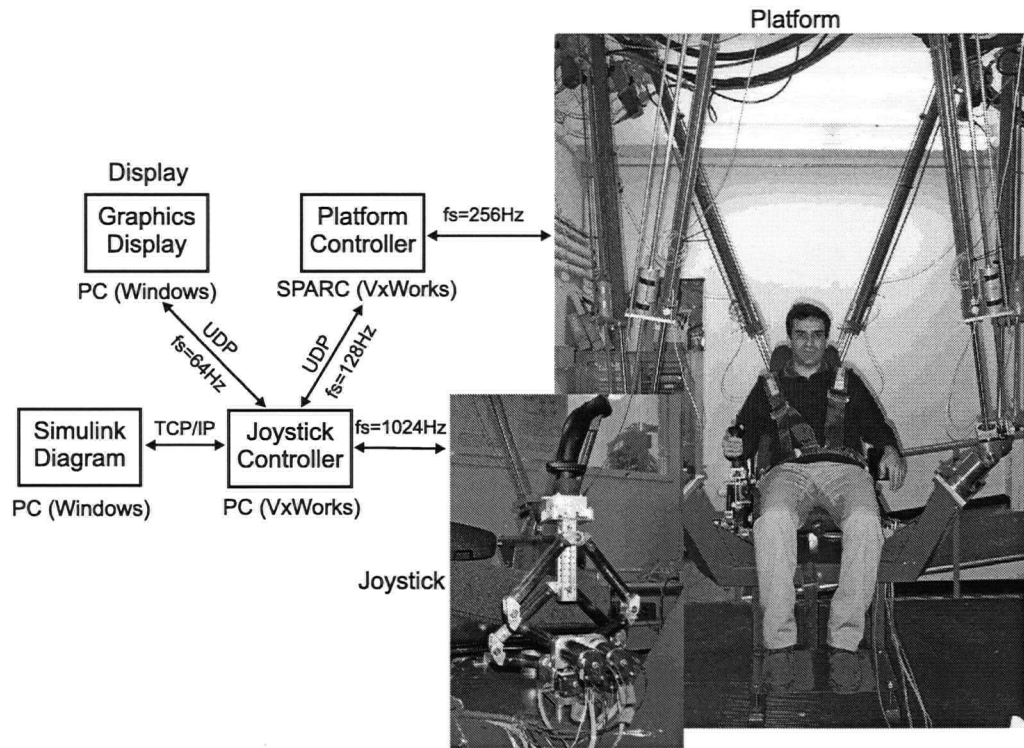


Figure 4.2: Experimental setup.

In fact, the resultant closed-loop dynamics are treated as the dynamics of the system to be controlled. Obviously, if the application of interest has base motion with frequency content beyond the bandwidth of the P controller, higher performance position controllers must be employed to simulate this motion. This will be addressed later in the thesis.

Joystick:

The joystick used in our experimental setup is a slightly modified version of the one in [104]. It has three degrees of freedom allowing for planar translation and rotation. The endpoints of two pantographs that move in different parallel planes are coupled by means of a linkage connected to the interface handle. The device is powered by four 90W Maxon RE35 DC motors. Maxon GP 32A planetary gearheads with 1-4.8 ratio are employed to increase the force/torque capability of the device. Each of the four joint angles is measured by a digital optical encoder with a resolution of 0.09 degrees. The encoders are placed on the motor side of the shafts to improve the measurement resolution. Identification experiments were performed to estimate the joystick inertial parameters. The parameters are used to compensate for gravity

(see Appendix C).

The joystick is controlled in work-space coordinates. The redundancy in actuation is exploited to minimize the norm of the motor torques vector (motor currents). For the purpose of the experiments, the x and θ coordinates are locked using PD controllers. The joystick controller is implemented using the *Matlab Real-time Workshop*[®] toolbox and *Tornado*[®] 2.0 development environment. The realtime code runs on a PC under the *VxWorks*[®] 5.4 operating system with a sampling frequency of 1024 Hz.

The joystick controller communicates with the platform controller and a graphical display via the UDP socket protocol. The UDP protocol has been chosen as opposed to TCP/IP because it has less overhead and allows for higher communication rates. The drawback is that some packets may be lost during the data exchange. A local dedicated switch has been used in the experimental setup so the traffic and data loss are minimal and more or less constant communication frequencies are achievable. The data exchange is monitored by the software such that if the number of subsequent missed packets exceeds a predefined value the system shuts down gracefully. This never occurred during the experiments. The data exchange rates between the joystick and the platform and the joystick and the display are 128 Hz and 64 Hz, respectively. The joystick controller also communicates with its *Simulink*[®] block diagram which runs on a host PC under *Windows NT*[®]. This allows for data logging and change of parameters during the experiments.

Graphical Display:

A graphical display was developed in order to assist the operator in performing the tracking task (see Figure 4.1). Two frames, one representing a random target, the other showing the position of the platform, were displayed. The operator was asked to move the platform using the joystick such that it tracked the target frame. The graphical display ran on a PC under *Windows 2000*[®] that projected the display image on a rear projection screen in front of the operator.

A general model for the analysis of teleoperation/manual control systems with movable bases was proposed in Chapter 2. To simplify the design problem, the operator-related active feedback gains, i.e. Z_{PF} and Z_F in Figure 2.4, are assumed to be zero. The passive impedance of the operator's arm is considered in the design. The assumption here is that the operator

does not try to destabilize the system. Instability due to the outer vision-based feedback loop is unlikely in this case because of the small time delay and relatively low crossover frequency of this loop.

A schematic of the manual control system is given in Figure 4.1. The following assumptions are made and will be used throughout this chapter:

A1. The arm/joystick subsystem is modeled as a mass-spring-damper system with uncertain parameters m_m , b_m and k_m are in (3.43) and (3.44) (see Figure 3.6). The nominal values of the parameters were identified in Chapter 3.

A2. Two models for biodynamic feedthrough were developed in Chapter 3. The acceleration based feedthrough model is used for control synthesis here. In fact, it turned out that the level of body excitation due to feedthrough-induced oscillations is within the range that this simple model can sufficiently describe the effect of feedthrough. This assumption has been validated by the success of the designed controllers in the suppression of the oscillations as will be seen later. Nevertheless, this can be specific to the prototype design problem studied in this chapter. The model based on the stochastic embedding could be employed as an alternative in applications with larger base excitation.

A3. The hydraulic actuators are modeled as velocity sources by ignoring the hydraulic resonances and the valve dynamics [83]. Therefore, the closed-loop behavior of the platform controller may be approximated by first-order linear dynamics if a proportional controller is used.

$$x_s = \frac{1}{\tau_p s + 1} x_{s_{ref}} \quad (4.1)$$

where τ_p , the closed-loop time constant, is known and $x_{s_{ref}}$ is the position reference command to the platform controller. A typical step response of the UBC motion simulator under such controller is given in Figure 7.12 of Chapter 7 which validates the above assumption.

Remark: A good estimate of the closed-loop dynamics of the controlled element (the hydraulic platform) is available here. In general, these dynamics could be subject to parametric and non-parametric uncertainties. The relevant uncertainties can be easily incorporated into the proposed control synthesis framework.

4.3 Robust Control Problem Formulation

In order to assist the operator in accomplishing the task, controllers must be designed to coordinate the motion of the joystick with that of the platform. The two main objectives for the design are:

1. To establish kinematic correspondence between the motion of the joystick and that of the platform. This is enforced by making the following error small:

$$e_1 = W_{e_1} [x_s - c_k(s)x_m] \quad (4.2)$$

where the tracking error is weighted by the frequency dependent gain W_{e_1} . In general, $c_k(s)$ can be any stable rational transfer function. For example, a constant $c_k(s)$ corresponds to position mode control strategy and a velocity mode controller is obtained by choosing $c_k(s) = c_k/s$. The gain W_{e_1} is a stable rational transfer function that can be chosen to emphasize a frequency range in which a small tracking error is desired (i.e., by increasing the gain over that frequency range).

2. To facilitate manual control through the shaping of the perceived admittance of the arm/joystick. This is achieved by making the following error small:

$$e_2 = W_{e_2} (Y_D f_h - x_m) \quad (4.3)$$

where x_m is the joystick position, f_h is the hand force, W_{e_2} is a stable rational transfer function, and Y_D is a desired admittance that may be found through human factors studies. Similarly, W_{e_2} can be designed such that it enforces the admittance shaping over a certain range of frequency.

Figure 4.3 shows a block diagram of the proposed control system. The controller to be designed is displayed by block $K(s)$ in this figure. This system can be viewed as a two-channel bilateral teleoperation system with a movable base. It is assumed that the master (joystick) and slave (base) positions and also the base acceleration are measured. The master-side control action, u_m , is the applied force/torque to the joystick by the motors. The slave-side control action, u_s , is the position command to the base controller.

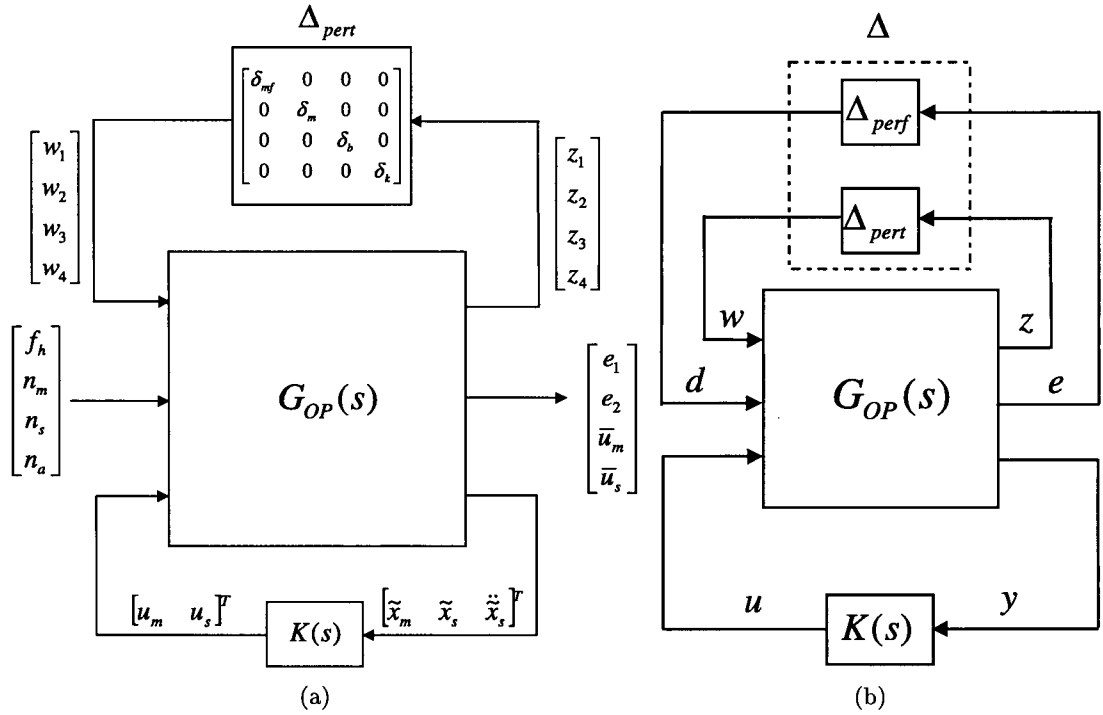


Figure 4.4: (a) Controller in the μ -synthesis framework. (b) Robust performance problem.

a major issue here. In applications with large and varying time delay, a similar approach to that presented in [67] can be adopted. The system model in Figure 4.3 can be easily modified to include an unstructured uncertainty block associated with the communication delay. This will not be done in this thesis because it could lead to a more conservative design.

The system shown in Figure 4.3 is redrawn in a standard μ -synthesis configuration in Figure 4.4(a). This diagram contains the exogenous input vector d , the output vector e , the control input vector u , the measurement vector y , the open-loop transfer function $G_{op}(s)$, the perturbation block Δ_{pert} , and the controller block $K(s)$, where the following have been defined:

$$\begin{aligned}
 d &= \begin{bmatrix} f_h & n_m & n_s & n_a \end{bmatrix}^T & e &= \begin{bmatrix} e_1 & e_2 & \bar{u}_m & \bar{u}_s \end{bmatrix}^T \\
 w &= \begin{bmatrix} w_1 & w_2 & w_3 & w_4 \end{bmatrix}^T & z &= \begin{bmatrix} z_1 & z_2 & z_3 & z_4 \end{bmatrix}^T \\
 u &= \begin{bmatrix} u_m & u_s \end{bmatrix}^T & y &= \begin{bmatrix} \tilde{x}_m & \tilde{x}_s & \ddot{x}_s \end{bmatrix}^T
 \end{aligned}$$

The open-loop plant, $G_{op}(s)$, has 10 inputs and 11 outputs. The exact form of G_{op} can be derived from Figure 4.3 and will not be presented here. Function *sysic* from the μ -*Analysis and Synthesis Toolbox*® has been used to find a state-space realization of the plant dynamics G_{op} for the controller synthesis. The order of the plant dynamics will depend on the frequency weights used and will be given for each design case later in this chapter.

The set of systems to be controlled is described by the following linear fractional transformation (LFT)

$$\left\{ F_U(G_{op}, \Delta_{pert}) : \max_{\omega} \bar{\sigma}(\Delta_{pert}(j\omega)) \leq 1 \right\} \quad (4.5)$$

where $F_U(G_{op}, \Delta_{pert})$ denotes the transfer function from the exogenous input d , to the output e when the upper block of G_{op} is closed with the perturbation block Δ_{pert} . The design objective is to find a stabilizing controller K , such that for all such perturbations Δ_{pert} , the closed-loop system is stable and satisfies

$$\|F_L(F_U(G_{op}, \Delta_{pert}), K)\|_{\infty} \leq 1 \quad (4.6)$$

Where $F_L(\cdot, K)$ is the transfer function from d to e when the loop is closed with the controller $K(s)$. Also, $\|\cdot\|_{\infty}$ denotes the H_{∞} norm, i.e.,

$$\|G(s)\|_{\infty} = \sup_{\omega} \bar{\sigma}(G(j\omega)) \quad (4.7)$$

$G(s)$ is assumed to be stable and $\bar{\sigma}(\cdot)$ is the maximum singular value. Clearly,

$$F_L(F_U(G_{op}, \Delta_{pert}), K) = F_U(F_L(G_{op}, K), \Delta_{pert}) \quad (4.8)$$

Therefore, the design objective can be equivalently stated as to find a nominally stabilizing controller K , such that for all Δ_{pert} , $\max_{\omega} \bar{\sigma}(\Delta_{pert}(j\omega)) \leq 1$, the closed-loop system is stable and satisfies

$$\|F_U(F_L(G_{op}, K), \Delta_{pert})\|_{\infty} \leq 1 \quad (4.9)$$

This problem can be posed as a robust stability problem. By introducing the virtual perturbation block Δ_{perf} , an augmented uncertainty structure can be formed (see Figure 4.4(b)),

$$\Delta := \left\{ \begin{bmatrix} \Delta_{pert} & 0 \\ 0 & \Delta_{perf} \end{bmatrix} : \Delta_{pert} \in \Delta_{\text{pert}}, \Delta_{perf} \in \mathbf{C}^{n_d \times n_e} \right\} \quad (4.10)$$

Then the controller K achieves robust performance if and only if

$$\max_{\omega} \mu_{\Delta}(F_L(G_{op}, K)(j\omega)) < 1 \quad (4.11)$$

where the structured singular value μ_{Δ} is defined as follows

$$\mu_{\Delta}(M) := \frac{1}{\max \{ \bar{\sigma}(\Delta) : \Delta \in \Delta, \det(I - M\Delta) = 0 \}} \quad (4.12)$$

unless $I - M\Delta$ is nonsingular for all Δ , in which case $\mu_{\Delta}(M) := 0$.

The controller K is the solution to the following μ -synthesis optimization problem [139]

$$\min_{\substack{K \\ \text{stabilizing}}} \max_{\omega} \mu_{\Delta}(F_L(G_{op}, K)(j\omega)) \quad (4.13)$$

4.4 Controller Design Assuming a Stationary Base

In this section, it will be shown that a design that achieves the control objectives while ignoring the base motion could potentially lead to instability if the base does move. The desired joystick admittance is assumed to be

$$Y_D = \frac{1}{m_d s^2 + b_d s + k_d} \quad (4.14)$$

and the desired kinematic correspondence is a position scaling by c_k . For simplicity, it is assumed that $m_d = m$ so no acceleration measurements of the joystick would be required. The following control laws can achieve the control objectives for a frequency range below the platform controller bandwidth, when no perturbations are present and the base does not move (see

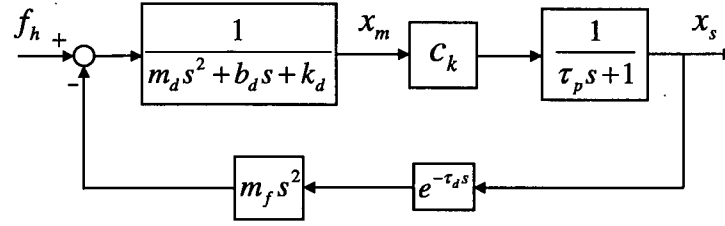


Figure 4.5: Simplified block diagram of the system.

Figure 4.3).

$$U_m(s) = C_m(s)\tilde{X}_m(s) = [(b_d - b)s + k_d - k]\tilde{X}_m(s) \quad (4.15)$$

$$U_s(s) = C_1(s)\tilde{X}_m(s) = c_k\tilde{X}_m(s) \quad (4.16)$$

We will refer to this controller as the *fixed base* controller throughout the rest of this chapter. Note that this controller is a special form of the more general control block $K(s)$ in Figure 4.3. The control gain $C_m(s)$ in (4.15) changes the admittance of the joystick to Y_D . The position of the joystick, scaled by c_k , is sent to the platform as a reference command. It should be pointed out that the effective admittance of the joystick would be different from Y_D because of the presence of biodynamic feedthrough.

Figure 4.5 shows a simplified block diagram of the system using the controller given in (4.15) and (4.16). According to this figure, the closed-loop characteristic equation can be written as

$$1 + LG = 1 + \frac{c_k m_f s^2}{(\tau_p s + 1)(m_d s^2 + b_d s + k_d)} e^{-\tau_d s} = 0 \quad (4.17)$$

where LG is the loop gain. To further simplify the analysis, let $\tau_d = 0$. Using the Nyquist criterion, it can be shown that the closed-loop system remains stable as long as

$$c_k m_f > -b_d \left(\frac{m_d}{b_d + k_d \tau_p} + \tau_p \right) \quad (4.18)$$

and the frequency of oscillations when the poles are on the $j\omega$ -axis is $\omega_0 = \sqrt{\frac{b_d + k_d \tau_p}{m_d \tau_p}}$.

Similarly, if a position-velocity kinematic correspondence is desired, c_k is replaced with $\frac{c_k}{s}$.

In this case, the characteristic equation is given by

$$1 + LG = 1 + \frac{c_k m_f s}{(\tau_p s + 1)(m_d s^2 + b_d s + k_d)} e^{-\tau_d s} = 0 \quad (4.19)$$

For stability (assuming no time delay)

$$c_k m_f > -b_d \left(1 + \frac{k_d \tau_p^2}{m_d + b_d \tau_p} \right) \quad (4.20)$$

with undamped oscillation frequency $\omega_0 = \sqrt{\frac{k_d}{m_d + b_d \tau_p}}$

Therefore, in the absence of time delay, the system remains stable for all positive $c_k m_f$, whether position or rate control is used. In practice, there is always some delay in the loop. It is not difficult to show that the system can become unstable for both positive and negative $c_k m_f$ in this case. Note how increasing the damping of the joystick (with respect to the base) improves the stability in both cases.

4.5 Robust Controller Design

The *Matlab μ -Analysis and Synthesis Toolbox*[®] [30] was used to solve the robust control problem defined earlier (4.13). The toolbox implements the $D - K$ iteration technique [139]. This technique does not provide an exact solution to (4.13). Instead, it uses a two-step iterative procedure to minimize an upper bound on μ_Δ over a set of discrete frequencies. Therefore, the resulting controller is not necessarily optimal in the sense of (4.13). Both position-mode and velocity-mode controllers have been developed. The identified arm/joystick and feedthrough parameters from Chapter 3 are used in the following design problems.

4.5.1 Position-mode controller:

The following parameters were used in this case:

$$\begin{aligned}
 m_d &= 1.45\text{kg} & b_d &= 15\text{N.s/m} \\
 k_d &= 88\text{N/m} & m_f &= 1.45\text{kg} \\
 \delta_{m_f} &= \delta_m, \|\delta_m\| \leq 0.5 \times 1.45\text{kg} & c_k &= -1.0 \\
 \|\delta_b\| &\leq 0.4 \times 10.0\text{N.s/m} & \|\delta_k\| &\leq 0.2 \times 72\text{N/m} \\
 \tau_p &= 0.04\text{s} & \tau_d &= 0.08\text{s} \\
 \omega_{bf} &= 2\pi \times 12\text{rad/sec} & \zeta_{bf} &= 0.7
 \end{aligned} \tag{4.21}$$

Note that $c_k = -1.0$ which means that when the joystick is pulled up the platform moves down and vice-versa. The platform time constant has been chosen based on the specification of the platform position controller. The value of time delay is based upon the estimated network communication delay between the joystick and the platform.

The weights used in the μ - *synthesis* design are as follows:

$$\begin{aligned}
 W_{e_1} &= 500 & W_{e_2} &= 2000 \\
 W_{um} &= \frac{5.3 \times 10^{-3}s}{5.3 \times 10^{-3}s + 1} & W_{us} &= \frac{5.3 \times 10^{-4}s}{5.3 \times 10^{-3}s + 1} \\
 W_{nm} &= \frac{3.5 \times 10^{-4}(s + 0.1)}{3.5 \times 10^{-3}s + 1} & W_{ns} &= W_{na} = W_{nm} \\
 W_f &= \frac{5}{(0.02s + 1)^2}
 \end{aligned} \tag{4.22}$$

Note that W_{e_1} and W_{e_2} have been chosen constant. Considering the lowpass behavior of the desired admittance and the platform dynamics, more emphasis is placed on the admittance shaping and the position tracking at low frequency. The control signal weights W_{um} and W_{us} have highpass forms. This penalizes high frequency control actions which are not desirable. Measurement noise is usually concentrated at high frequency and therefore, the noise weights W_{nm} , W_{ns} and W_{na} have been selected to be larger in high frequency. Finally, the operator intentional force command is a low frequency signal which explains the lowpass form of W_f in (4.22). The breakpoint frequencies and the gains in the above filters have been chosen based on

rough specifications of the sensors used in the experimental setup, allowable range for the control signals, and the expected bandwidth of the operator's force input. They have been further tuned through trial and error to achieve a satisfactory design. The above gains produce an open-loop plant, $G_{op}(s)$, with 23 states. The resulting problem, defined in (4.10) and (4.13), is a mixed- μ synthesis problem since both real (the actual uncertainties) and complex (performance block) perturbation blocks exist in the model. A controller with 61 states was obtained after five $D-K$ iterations using function *dkit* from the μ -synthesis toolbox. Interestingly, the controller $K(s)$ turned to have a special structure. The resulting controller can be decoupled into two control gains $C_m(s) = \frac{U_m(s)}{\tilde{X}_m(s)}$ and $C_1(s) = \frac{U_s(s)}{\tilde{X}_m(s)}$. All the other gains between the measured signals \tilde{x}_m , \tilde{x}_s , $\ddot{\tilde{x}}_s$ and the control signals u_m and u_s were effectively zero. The fact that the robust controller does not use platform position measurements is due to the absence of any uncertainties in the platform model and the use of a local platform controller. Introduction of a disturbance signal at the input or output of the platform model would change this. However, this is not a concern in the design problem presented in this chapter. One may also expect that the controller would use the acceleration measurement to partially cancel biodynamic feedthrough. This turned out not to be the case here for the reason explained below.

Model order reduction:

In order to be able to implement the controllers, their orders must be reduced. First, state-space balanced realizations were obtained for the controllers using function *sysbal* from the *Control Toolbox*[®]. Then, function *hankmr* was applied to the balanced models to reduce the orders based on the *Hankel* norm. This removed the uncontrollable and unobservable modes without altering the input-output relationships. The orders of the reduced controllers were chosen by comparing the original and reduced-order frequency responses. It was noticed the reduced-order controllers have a few very high frequency modes that are far beyond the frequency range of interest. This could complicate their implementation because of the limited sampling rate. Therefore, the reduced-order controllers were transformed to their modal canonical forms using *canon* from the *Control Toolbox*[®]. Then, function *modred* was employed to remove these modes without affecting the dc gains. The resulting C_m and C_1 are of order eight and six, respectively. The poles and zeros of the reduced order C_m are as follows:

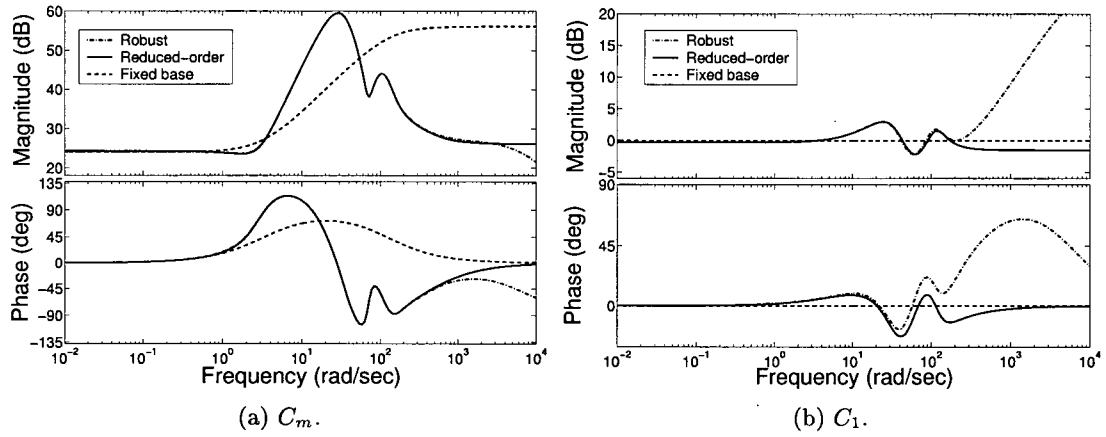


Figure 4.6: Frequency responses of the original, the reduced-order, and the fixed base controllers (position mode).

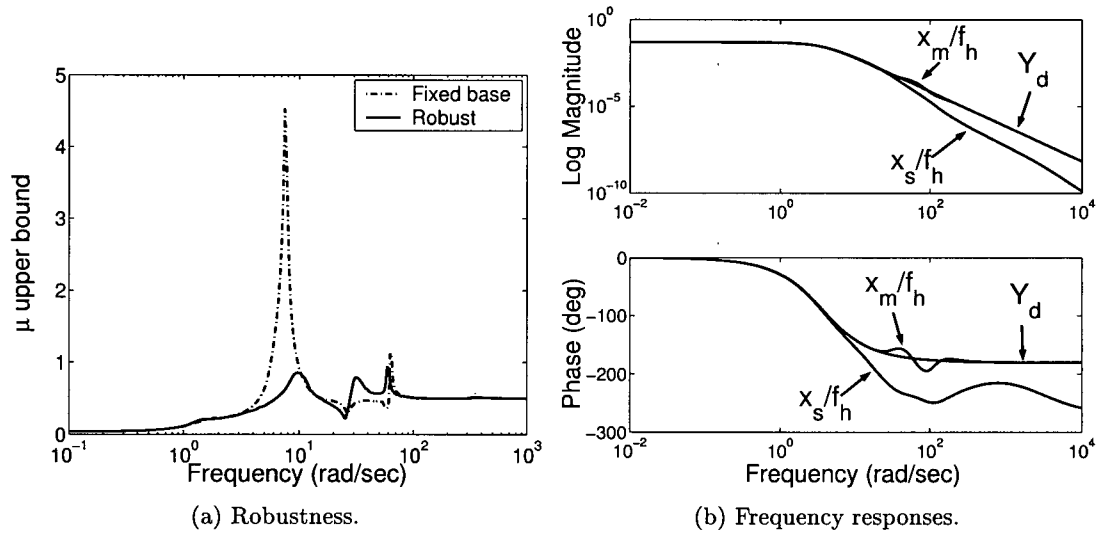


Figure 4.7: Robust (reduced-order) controller.

Poles:

$p_{1,2} = -16.49 \pm j16.28$	$\zeta = 0.71$	$\omega_n = 23.17\text{rad/sec}$
$p_{3,4} = -15.38 \pm j31.10$	$\zeta = 0.44$	$\omega_n = 34.69\text{rad/sec}$
$p_{5,6} = -36.47 \pm j104.66$	$\zeta = 0.33$	$\omega_n = 110.83\text{rad/sec}$
$p_{7,8} = -103.12 \pm j62.31$	$\zeta = 0.86$	$\omega_n = 120.48\text{rad/sec}$

Zeros:

$$z_1 = -414.67$$

$$z_2 = -200.24$$

$$z_{3,4} = -74.66 \pm j147.37$$

$$z_{5,6} = -8.65 \pm j69.84$$

$$z_{7,8} = -1.59 \pm j2.39$$

Similarly, for controller C_1 ,

Poles:

$$p_1 = -9.7$$

$$p_{2,3} = -18.89 \pm j26.06 \quad \zeta = 0.59 \quad \omega_n = 32.19\text{rad/sec}$$

$$p_4 = -61.20$$

$$p_{5,6} = -39.15 \pm j105.98 \quad \zeta = 0.35 \quad \omega_n = 112.98\text{rad/sec}$$

Zeros:

$$z_1 = -8.32$$

$$z_2 = -23.72$$

$$z_{3,4} = -28.00 \pm j51.51$$

$$z_{5,6} = -67.84 \pm j92.48$$

The continuous controllers were discretized using the bilinear transformation and a sampling rate of $f_s = 1024\text{Hz}$ for the implementation. The frequency response of the controllers are given in Figures 4.6(a) and 4.6(b) where the reduced-order controllers match very well with the original ones up to frequencies around 30Hz. It is noticeable from Figure 4.6(a) that the robust controller C_m has a slope close to 40dB/dec within the frequency range 3 – 30rad/sec. Considering the bandwidth of the platform closed-loop dynamics ($\approx 25\text{rad/sec}$), C_m behaves as acceleration feedback and compensates for the biodynamic feedthrough in this range. This can

explain why the controller is not using the platform acceleration measurement. These figures also contain the frequency response of the fixed base controller used for comparison. This controller was chosen according to Section 4.4:

$$C_m(s) = \frac{5s + 16}{0.0078s + 1} \quad C_1(s) = c_k = -1$$

Note that a first-order lowpass filter has been added to the PD-type controller C_m to reduce noise in the control action. The robustness of the designed controller is compared with that of the fixed base controller in Figure 4.7(a) which shows the upper bounds on $\mu_{\Delta_{pert}}$ for the two controllers. According to this figure, the fixed base controller is not robust with respect to uncertainties and can become unstable (i.e., $\mu_{\Delta_{pert}} > 1$). In fact, for $c_k = -1$ the nominal system under the fixed base controller is very close to instability. If larger c_k (in magnitude sense) had been used (e.g., $c_k = -2$), even the nominal system would be unstable. The use of $c_k = -1$ enables us to compare the time domain responses of the controllers.

The performance of the robust controller is presented in Figure 4.7(b) where Y_d , x_m/f_h , and x_s/f_h are compared. From these figures it is clear that both of the performance objectives, i.e. the admittance shaping of the joystick and the position tracking between the joystick and the platform are met over a reasonable range of frequency.

4.5.2 Feedthrough Cancellation Using Acceleration Compensation

Considering the simple biodynamic feedthrough model used in this chapter, it might seem reasonable to cancel the feedthrough by adding an inertial term $\hat{m}_{bf}\ddot{x}_s$ to the master control command. Then, a robust control law can be designed for the system with acceleration feedforward to account for uncertainties. The design parameters are all the same as those given in (4.21) and (4.22) except the uncertainty in the feedthrough mass which has been increased to

$$\|\delta_{m_f}\| \leq 0.8 \times 1.45\text{kg}$$

A controller with 57 states was obtained in this case. The orders for C_m and C_1 were reduced to six and five, respectively. The frequency responses are shown in Figures 4.8(a) and 4.8(b). The upper bound on the $\mu_{\Delta_{pert}}$ for such controller is plotted in Figure 4.9(a) ($c_k = -1$). The

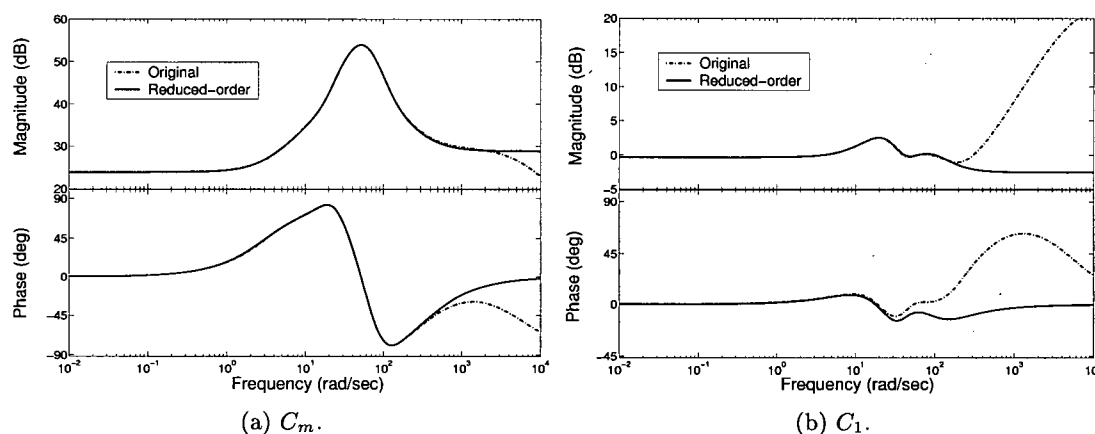


Figure 4.8: Frequency responses of the original, the reduced-order (with acceleration compensation).

nominal performance of this controller is shown in Figure 4.9(b). For the design example of this paper, a fixed base PD type controller with acceleration compensation can generate more or less the same result as the robust controller with acceleration compensation. Nevertheless, numerical experiments revealed that the fixed base controller is not robust with respect to variations in the feedthrough and the arm/joystick dynamics. The stability margins of the fixed based controller reduce as the desired position correspondence gain, c_k , is increased. The robust controller designed earlier has the advantage of not using acceleration measurement over the robust controller with acceleration compensation. Nevertheless, the latter controller can provide better performance and larger stability margins for higher values of c_k . The presence of uncertainty and disturbances in the controlled element (base) dynamics will force the controller to use the base acceleration measurement.

4.5.3 Velocity mode controller:

A robust controller was designed to achieve a position-velocity correspondence between the joystick and the platform. This type of control strategy is employed in applications where a joystick with limited motion range controls a slave with a large workspace such as in excavators. The following parameter values were used in the design

$$\begin{aligned}
 m_d &= 1.45\text{kg} & b_d &= 20\text{N}\cdot\text{s}/\text{m} \\
 k_d &= 170\text{ N}/\text{m} & c_k &= \frac{-10}{s+0.01}
 \end{aligned}$$

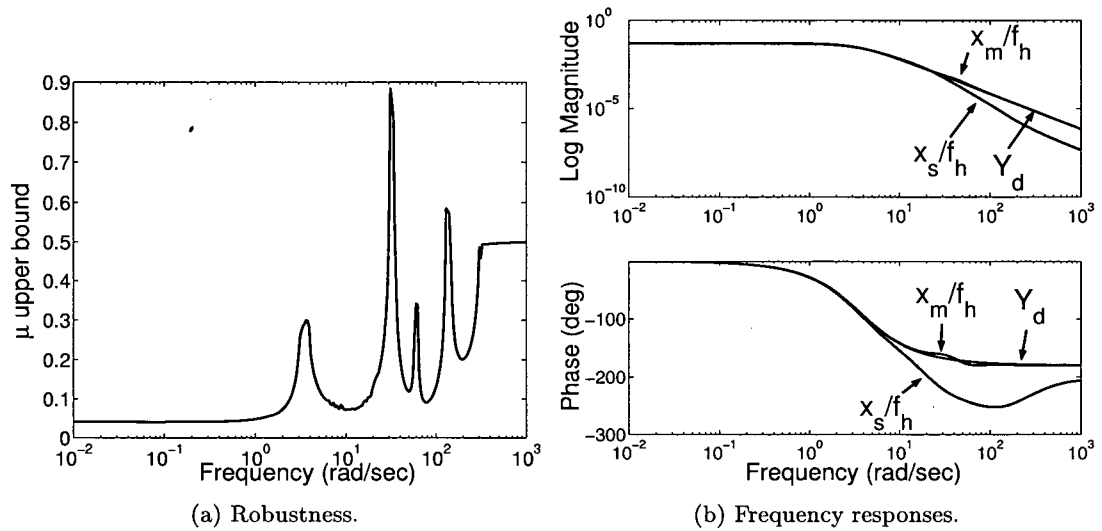


Figure 4.9: Robust controller with acceleration compensation.

The design weights W_{e_1} and W_{e_2} are

$$W_{e_1} = \frac{2500(s + 0.01)}{(s + 25)} \quad W_{e_2} = 500$$

while the rest of the parameters were chosen as in (4.21) and (4.22). Note a highpass W_{e_1} has been selected in this case. This is because c_k is very large at low frequency (and therefore the error) and a highpass W_{e_1} enforces the desired kinematic correspondence over the frequency more evenly. The open-loop plant has 25 states in this case. The application of D - K iterations produced a controller of order 67. As in the case of the position-mode control, all channels except C_m and C_1 turned out to be practically zero. Model order reduction techniques generated controllers of order five and four for C_m and C_1 , respectively. Their frequency responses are shown in Figures 4.10(a) and 4.10(b). The poles and zeros of C_m are as follows:

Poles:

$$p_1 = -26.26$$

$$p_{2,3} = -23.96 \pm j33.36 \quad \zeta = 0.58 \quad \omega_n = 41.08\text{rad/sec}$$

$$p_{4,5} = -30.32 \pm j57.74 \quad \zeta = 0.46 \quad \omega_n = 65.22\text{rad/sec}$$

Zeros:

$$z_1 = -301.12$$

$$z_2 = -195.14$$

$$z_3 = -3.38$$

$$z_{4,5} = -19.62 \pm j51.60$$

Similarly, for controller C_1 ,

Poles:

$$p_1 = -0.01$$

$$p_2 = -8.71$$

$$p_{3,4} = -14.59 \pm j35.42 \quad \zeta = 0.38 \quad \omega_n = 38.31\text{rad/sec}$$

Zeros:

$$z_1 = -44.19$$

$$z_2 = -7.54$$

$$z_{3,4} = -14.59 \pm j34.42$$

The fixed base controller, whose frequency responses are also given in Figures 4.10(a) and 4.10(b), is chosen as follows

$$C_m(s) = \frac{10s + 98}{0.0022s + 1} \quad C_1(s) = -\frac{10}{s} \quad (4.23)$$

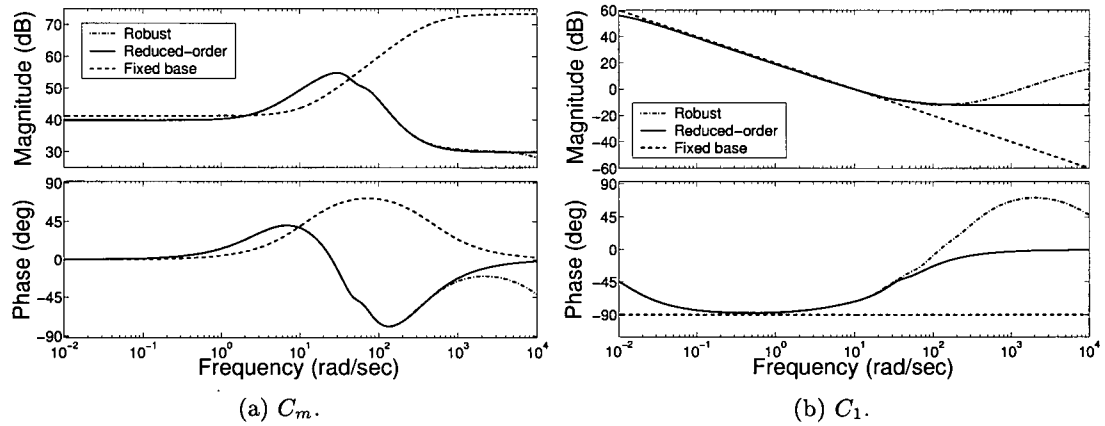


Figure 4.10: Frequency responses of the original, the reduced-order, and the fixed base controllers (velocity mode).

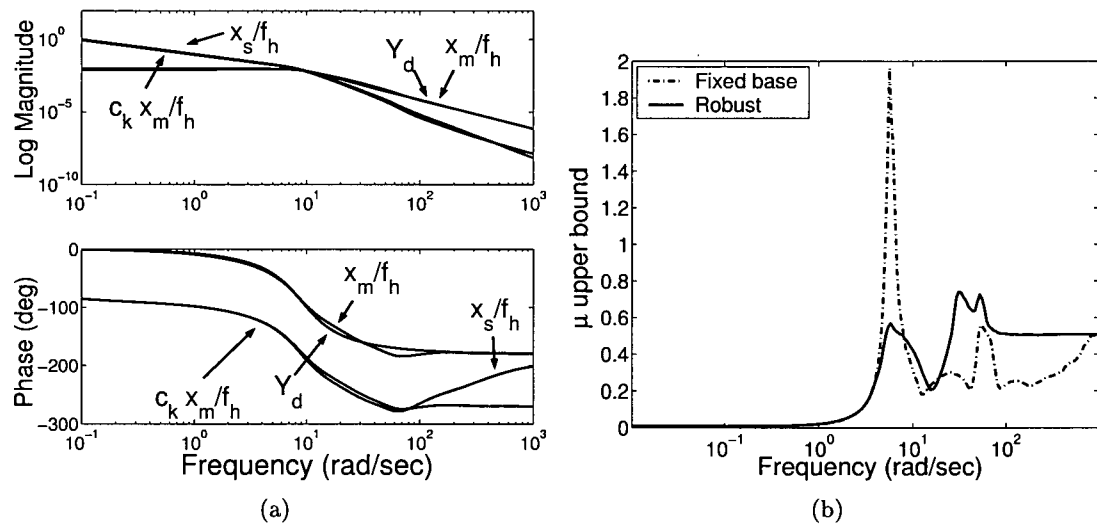


Figure 4.11: (a) Performance of the robust controller (velocity mode). (b) Upper bounds on $\mu_{\Delta_{pert}}$ (velocity mode).

The frequency response of the controller is shown in Figure 4.11(a). It clearly displays a good performance as both objectives, i.e., the admittance shaping and the kinematic correspondence, have been achieved.

The robustness of the controller is compared with that of the fixed base controller in Figure 4.11(b). The proposed controller remains stable in the presence of bounded uncertainties defined earlier whereas the fixed base controller can become unstable.

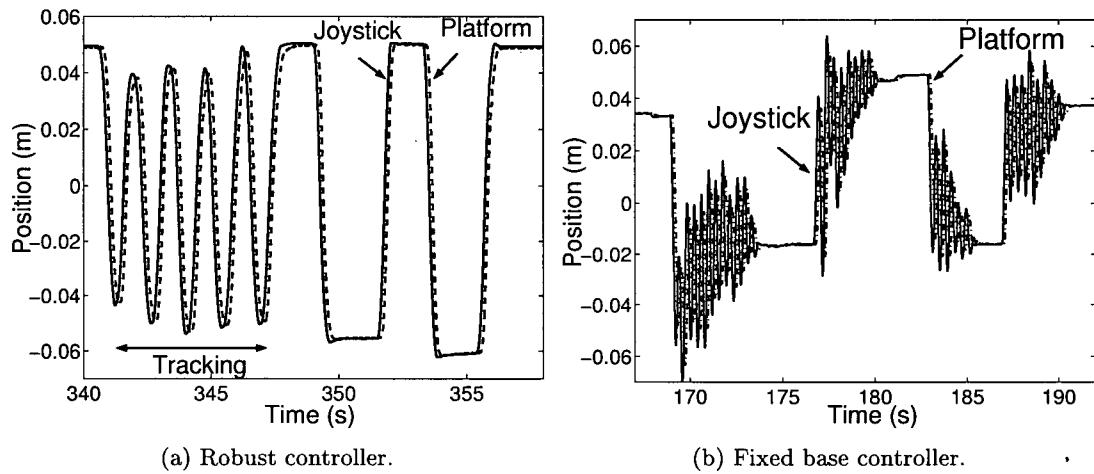


Figure 4.12: Responses of the controllers with $c_k = -1.0$.

4.6 Experimental Results

Experimental studies were carried out to evaluate the effectiveness of the proposed controllers. The author of this thesis was the subject of the experiments presented here. Similar experiments were conducted using another test subject as will be explained later in this section.

In the first set of the experiments, the operator was instructed to move the platform in step-wise and sinusoidal motions. The graphical display was not used in these experiments. Both the position-mode and velocity-mode controllers were examined.

Position mode controller:

The robust controller demonstrated an excellent response as can be seen in Figure 4.12(a). Note that the sinusoidal motion in part of this experiment is intentional and is performed to show the tracking behavior of the system. The fixed base controller performed poorly and exhibited a nearly unstable response as shown in Figure 4.12(b). The operator had to loosen the grasp on the joystick in order to stop the oscillations. Figure 4.13(a) shows the robustness of the proposed controller to changes in c_k where the position command to the platform were multiplied by 1.1. Note how this has worsened the response of the PD controller. The response of the robust controller with acceleration compensation was also examined. According to Figure 4.13(b) this controller also performs well and suppresses the biodynamic interferences.

Velocity-mode experiments:

The velocity mode controllers were also evaluated experimentally. It can be observed from

Figure 4.14(a) that the fixed base controller demonstrates a highly undamped oscillatory response and, in fact, it can easily be destabilized by a small change in the system parameters. The proposed robust rate-mode controller performed very well and exhibited a highly robust behavior in the experiments. Figure 4.14(b) shows a typical response of this controller. It should be noted the motion seen in this plot is executed voluntarily by the operator.

The nominal arm/joystick and feedthrough parameters were obtained using identification experiments performed on the author. The operator dynamics are used in the design of the controllers. However, these parameters may vary from one operator to another. To investigate the robustness of the system with respect to the variations in the operator dynamics, similar experiments were performed with another graduate student in our lab and without changing the controller. Similar behavior to that presented here was observed. Dynamic variations may even occur for a single operator. To study the robustness with respect to such changes, the operator was instructed to loosen and to firm his grasp on the joystick during some parts of the experiments. This can alter the effective mass, damping and stiffness of the operator. The robust controller consistently produced well-damped responses in all cases.

The operator performance in manual tracking under the proposed position-mode robust controllers was also investigated. It should be stressed that there is no intention to draw any general conclusions here since the system has not been tuned to improve the manual tracking performance. Moreover, any study in this regard must involve different subjects with enough training time allowed. Each experiment lasted four minutes during which the operator was asked to track a random target on the graphical display. The random target motion was generated by low-pass filtering of a white noise. The following results were obtained for two different variances of the random target motion:

$$\begin{array}{lll}
 (i) & \sigma_{ref} = 0.0204\text{m} & \bar{x}_{ref} = 0\text{m} & f_{bw} = 0.75\text{Hz} \\
 & \sigma_{err} = 0.009\text{m} & \bar{x}_{err} \approx 0.0\text{m} & t_d = 0.437\text{sec} \\
 (ii) & \sigma_{ref} = 0.0150\text{m} & \bar{x}_{ref} = 0\text{m} & f_{bw} = 0.75\text{Hz} \\
 & \sigma_{err} = 0.0062\text{m} & \bar{x}_{err} \approx 0.0\text{m} & t_d = 0.453\text{sec}
 \end{array}$$

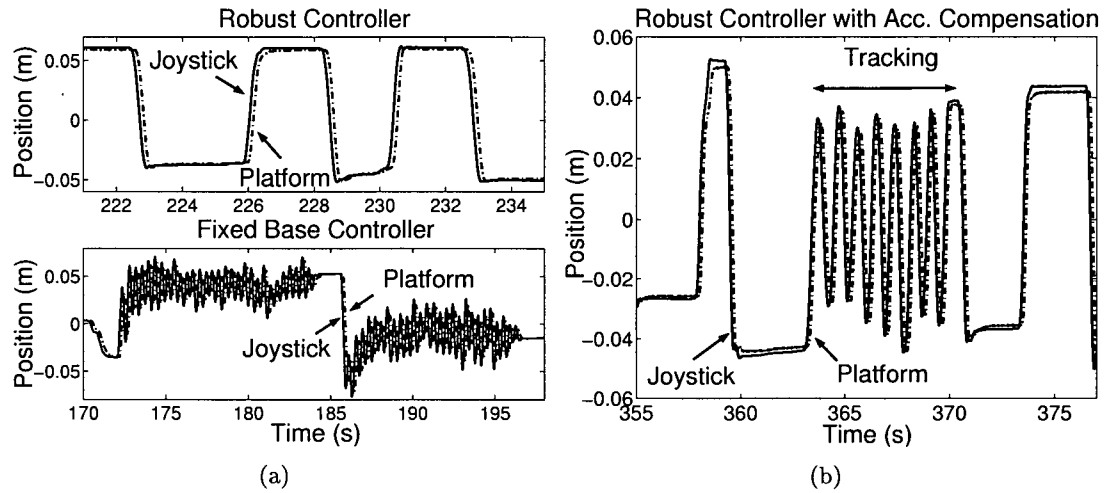


Figure 4.13: (a) Response of the controllers with $c_k = -1.1$. (b) Response of the robust controller with acceleration compensation.

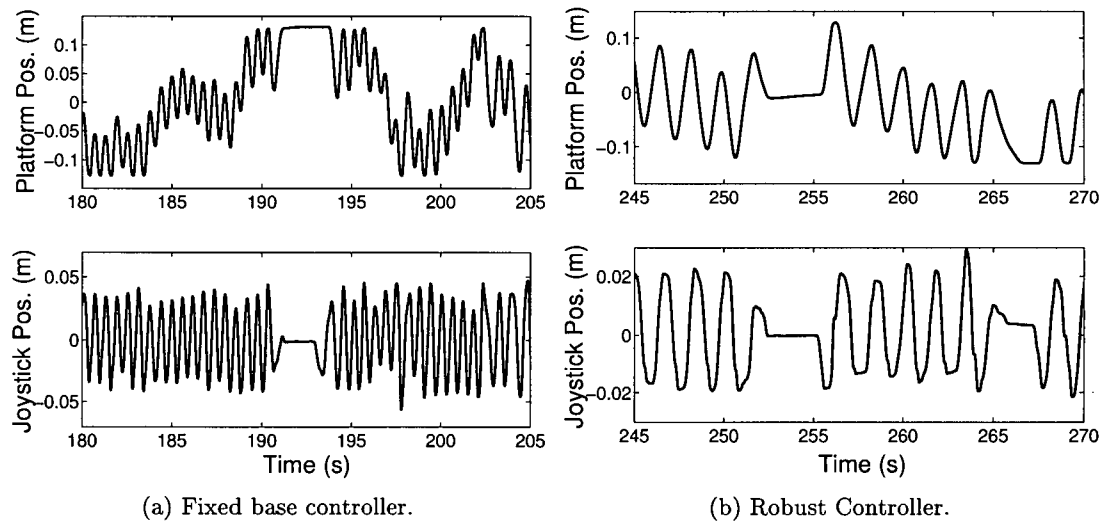


Figure 4.14: Response of controllers in the velocity mode.

where σ_{ref} , σ_{err} , \bar{x}_{ref} , and \bar{x}_{err} are the standard deviation and means of the target motion and the tracking error, respectively. f_{bw} is the bandwidth of the low-pass filter. t_d is the tracking time delay that is mostly due to the operator's delay in tracking the target. This was computed by correlating the platform motion with that of the random target. The time delay was compensated in the calculation of the tracking errors. Figure 4.15 shows a small portion of the tracking behavior in Case (i) (time delay has been removed).

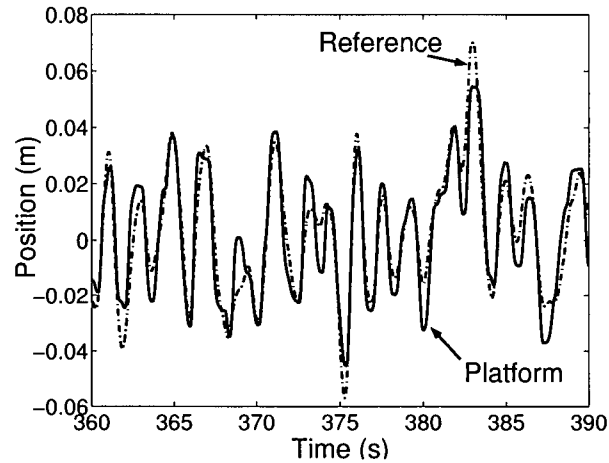


Figure 4.15: The manual control tracking behavior.

4.7 Conclusions

This chapter addressed the problem of closed-loop biodynamic feedthrough in joystick-controlled systems. A prototype single-degree-of-freedom manual control task was selected for this purpose. The simple acceleration based feedthrough model from Chapter 3 was found to be sufficient for the level of base excitation due to feedthrough-induced oscillations in the design example. It was shown via analysis that the feedback loop established through the feedthrough dynamics can cause instability if a controller is designed by ignoring the base motion. The μ -synthesis based controllers proposed in this chapter suppress biodynamic feedthrough, are robust with respect to variations in the system parameters, and at the same time perform well, although perhaps not optimally. The controllers were implemented and evaluated experimentally. The results demonstrated the effectiveness of the proposed approach. Robust controllers can be designed using the other feedthrough model developed in Chapter 3 and the design framework presented here for applications with larger base acceleration.

Chapter 5

Adaptive Nonlinear Control of Hydraulic Servo-systems

5.1 Overview

Electrohydraulic actuators are widely used in industrial applications. They can generate very high forces, exhibit rapid responses and have a high power-to-weight ratio compared with their electrical counterparts. However, it is well-known that they exhibit significant nonlinear behavior which makes controller design a challenging task. In this chapter, the backstepping approach [60] is employed to develop a new Lyapunov-based position tracking controller for hydraulic servo-systems. Load, hydraulic and first-order valve dynamics are incorporated in the design of the controller. An adaptive version of the controller is also presented to adapt for uncertainties in the hydraulic parameters. Stability of the proposed control laws is proven via Lyapunov analysis. The chapter is organized as follows. First, the dynamic equations of an electrohydraulic servo-system driving a mass load are presented. The nonadaptive and adaptive control laws are proposed next. Before the actual implementation of the controllers, their performance is investigated in simulation. Finally, the experimental results are presented and conclusions are drawn about the performance of the proposed controllers.

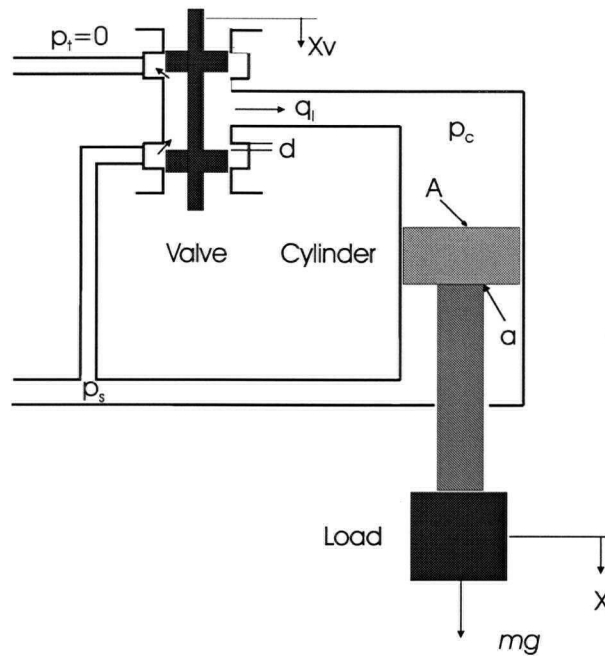


Figure 5.1: A hydraulic servo-system with three-way valve configuration.

5.2 System Dynamics

The differential equations governing the dynamics of a hydraulic actuator are given in [83]. The experimental hydraulic setup used in this research is connected in a three-way valve configuration as shown in Figure 5.1. For such a system, the control pressure dynamics are given by

$$\frac{V_t}{\beta} \dot{p}_c = q_l + c_l(p_s - p_c) - \dot{V}_t \quad (5.1)$$

where V_t is the trapped fluid volume in the control side, β is the effective bulk modulus, p_c is the control pressure acting on the control side, p_s is the supply pressure acting on the rod side, q_l is the load flow, and c_l is the coefficient of total leakage. V_t can be approximated by

$$V_t \approx A(x - L) \quad (5.2)$$

where A is the piston area, x is the actuator length and L is the actuator stroke length. The load flow, q_l , is a nonlinear function of control pressure and valve spool position and is given by

$$q_l = \begin{cases} c(x_v - d)\sqrt{p_c} & x_v < -d \\ c(x_v + d)\sqrt{p_s - p_c} + c(x_v - d)\sqrt{p_c} & -d \leq x_v \leq d \\ c(x_v + d)\sqrt{p_s - p_c} & x_v > d \end{cases} \quad (5.3)$$

and

$$c = c_d w \sqrt{\frac{2}{\rho}} \quad (5.4)$$

where c_d is the effective discharge coefficient, w is the port width of the valve, ρ is the density of the fluid, d is the valve underlap length and x_v is the valve spool position. In the ideal case in which the valve dynamics can be neglected, x_v is the control command. However, in practice, x_v is the response of the valve to a command signal. In particular, in the system that we have experimented with, the valve dynamics can be approximated by a first-order system:

$$\dot{x}_v = -\frac{1}{\tau_e} x_v + \frac{1}{\tau_e} u \quad (5.5)$$

In our experimental setup, described later in this chapter, a single hydraulic actuator drives a mass connected to its rod end in the vertical direction. Thus, the load dynamics are

$$p_c A - p_s a = m\ddot{x} + f_f(\dot{x}) - mg \quad (5.6)$$

where m is the total mass of the actuator and the load, $f_f(\dot{x})$ is the friction force (a nonlinear function of the actuator velocity) and g is the gravitational acceleration. A is the area of the piston and a is the annulus area. Equations (5.1), (5.5), (5.6) completely describe the fourth-order nonlinear dynamics of the system under study. The corresponding state space representation of these dynamics follows. By defining

$$X = \begin{bmatrix} x_1 & x_2 & x_3 & x_4 \end{bmatrix}^T = \begin{bmatrix} x & \dot{x} & p_c & x_v \end{bmatrix}^T \quad (5.7)$$

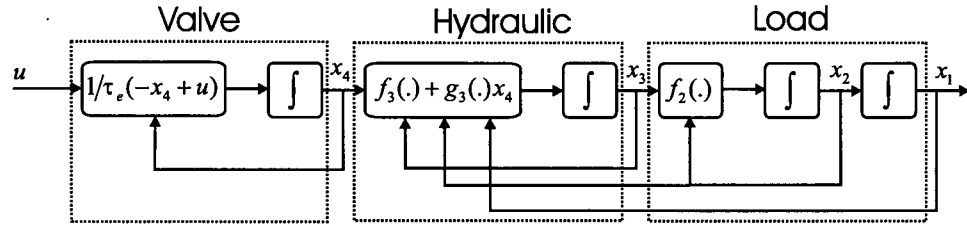


Figure 5.2: Block diagram of the hydraulic servo-system.

one can write (assuming $c_l = 0$)

$$\begin{aligned}
 \dot{x}_1 &= x_2 \\
 \dot{x}_2 &= \frac{A}{m}x_3 - \frac{1}{m}f_f(x_2) + g - \frac{a}{m}p_s \\
 \dot{x}_3 &= -\frac{\beta x_2}{x_1 - L} + \frac{\beta}{A(x_1 - L)}q_l(x_3, x_4) = f_3(x_1, x_2) + g_3(x_1, x_3, x_4) \\
 \dot{x}_4 &= -\frac{1}{\tau_e}x_4 + \frac{1}{\tau_e}u
 \end{aligned} \tag{5.8}$$

5.3 Controller Design

The nonlinear system described by (5.8) is in so called pure feedback form (see Figure 5.2). This special form allows the use of the recursive backstepping procedure for the controller design [60]. The method basically provides a recursive framework to construct a Lyapunov function and corresponding control action for system stabilization. In the rest of this chapter, this idea is adopted to design a nonlinear controller for position tracking in single cylinder hydraulic servo-systems.

5.3.1 Non-adaptive Case

First, the system parameters are assumed to be known. Let $e_i = x_i - x_i^d$, $i = 1, \dots, 4$ and $e = x - x^d$. The design procedure is started by defining the following Lyapunov-like function

$$V_1 = \frac{1}{2}m(x_2 - x_2^d)^2 + \frac{1}{2}k_1(x_1 - x_1^d)^2 \tag{5.9}$$

where $x_1^d = x_{1d}$ and $\dot{x}_2^d = \dot{x}_{1d}$ are the desired actuator position and velocity, respectively. The derivative of (5.9) is given by

$$\dot{V}_1 = \left(-f_f + Ax_3 + mg - ap_s - m\ddot{x}_1^d\right) \left(x_2 - x_2^d\right) + k_1 \left(\dot{x}_1 - \dot{x}_1^d\right) \left(x_1 - x_1^d\right) \quad (5.10)$$

With $x_3 = x_3^d + e_3$, and the following choice of x_3^d :

$$x_3^d = \frac{1}{A} \left[ap_s - mg + f_f + k_1 \left(x_1^d - x_1\right) + k_2 \left(x_2^d - x_2\right) + m\ddot{x}_1^d \right] \quad (5.11)$$

\dot{V}_1 becomes

$$\dot{V}_1 = -k_2 e_2^2 + Ae_2 e_3 \quad (5.12)$$

Now, in order to go one step ahead, V_2 is defined as

$$V_2 = V_1 + \frac{\gamma_3}{2} \left(x_3 - x_3^d\right)^2 \quad (5.13)$$

By taking the derivative of (5.13) and using (5.12)

$$\begin{aligned} \dot{V}_2 &= \dot{V}_1 + \gamma_3 \left(x_3 - x_3^d\right) \left(\dot{x}_3 - \dot{x}_3^d\right) = \dot{V}_1 + \gamma_3 e_3 \left(f_3 + g_3 - \dot{x}_3^d\right) \\ &= -k_2 e_2^2 + \gamma_3 e_3 \left(\frac{Ae_2}{\gamma_3} + f_3 + g_3(x_4^d) + g_3(x_4) - g_3(x_4^d) - \dot{x}_3^d\right) \end{aligned} \quad (5.14)$$

If x_4^d is chosen as the solution of the following algebraic equation

$$g_3(x_1, x_3, x_4^d) = -f_3 + \dot{x}_3^d - \frac{Ae_2}{\gamma_3} - k_3 e_3 \quad (5.15)$$

then (5.14) is simplified to

$$\dot{V}_2 = -k_2 e_2^2 - \gamma_3 k_3 e_3^2 + \gamma_3 \tilde{g}_3 e_3 \quad (5.16)$$

with $\tilde{g}_3 = g_3(x_1, x_3, x_4) - g_3(x_1, x_3, x_4^d)$. Let V_3 be defined as follows

$$V_3 = V_2 + \frac{1}{2}\gamma_4 (x_4 - x_4^d)^2 = \frac{1}{2} (k_1 e_1^2 + m e_2^2 + \gamma_3 e_3^2 + \gamma_4 e_4^2) \quad (5.17)$$

By taking the derivative of V_3 , one may write

$$\dot{V}_3 = \dot{V}_2 + \gamma_4 e_4 \left(-\frac{1}{\tau_e} x_4 + \frac{1}{\tau_e} u - \dot{x}_4^d \right) = -k_2 e_2^2 - \gamma_3 k_3 e_3^2 + \gamma_4 e_4 \left(-\frac{1}{\tau_e} x_4 + \frac{1}{\tau_e} u - \dot{x}_4^d + \frac{\gamma_3 \tilde{g}_3}{\gamma_4 e_4} e_3 \right) \quad (5.18)$$

To make \dot{V}_3 negative, (5.18) suggests the following choice for the control law u

$$u = \tau_e \left[\dot{x}_4^d - \frac{\gamma_3 \tilde{g}_3}{\gamma_4 e_4} e_3 - k_4 e_4 + \frac{1}{\tau_e} x_4 \right] \quad (5.19)$$

which renders \dot{V}_3 into

$$\dot{V}_3 = -k_2 e_2^2 - \gamma_3 k_3 e_3^2 - \gamma_4 k_4 e_4^2 \quad (5.20)$$

with $k_1, k_2, k_3, k_4, \gamma_3, \gamma_4 > 0$. In the control law given above,

$$\lim_{e_4 \rightarrow 0} \frac{\tilde{g}_3}{e_4} = \lim_{e_4 \rightarrow 0} \frac{g_3(x_1, x_3, x_4) - g_3(x_1, x_3, x_4 - e_4)}{e_4} = \left. \frac{\partial g_3}{\partial x_4} \right|_{x_4} \quad (5.21)$$

Note that (5.17) is a Lyapunov function for the system defined by (5.8), and the control law given by (5.11),(5.15),(5.19) renders its derivative negative semidefinite. It can be shown that $e = 0$ is the largest invariant set in $E = \{e \in \Omega | \dot{V}_3(e) = 0\}$. So, using LaSalle's principle [112], the tracking errors, which include position and velocity tracking errors, converge to zero asymptotically. The proposed control law requires measurements of the actuator position and velocity, control pressure, and the valve spool position. The derivative terms in the control law (i.e. \dot{x}_3^d, \dot{x}_4^d) can be obtained in terms of the system states. Nevertheless, the expressions are long and complex and may not be suitable for real-time implementation. Numerical differentiation was found to be adequate for this purpose.

5.3.2 Adaptive Case

In the controller development in the previous section, it was assumed that all of the system parameters are known. However, this assumption is not always valid. Sometimes, it may be necessary to identify some of these parameters off-line or estimate them using on-line adaptive schemes. The proposed controller was found to be more sensitive to changes in the hydraulic parameters than those in the load parameters. Therefore, these parameters might be estimated on-line. To develop an adaptive version of the controller, equations (5.1)-(5.3) are rewritten in the following form:

$$\dot{x}_3 = \theta_1 f'_3 + \theta_2 g'_3 \quad (5.22)$$

where $\theta = \begin{bmatrix} \beta & \beta c \end{bmatrix}^T$ is the actual parameter vector, and

$$f'_3 = -\frac{x_2}{x_1 - L} \quad (5.23)$$

$$g'_3 = \begin{cases} \frac{(x_4 - d)\sqrt{x_3}}{A(x_1 - L)} & x_4 < -d \\ \frac{(x_4 - d)\sqrt{x_3} + (x_4 + d)\sqrt{p_s - x_3}}{A(x_1 - L)} & -d \leq x_4 \leq d \\ \frac{(x_4 + d)\sqrt{p_s - x_3}}{A(x_1 - L)} & x_4 > d \end{cases} \quad (5.24)$$

Now, V_2 in (5.13) is redefined as

$$V'_2 = V_1 + \frac{\gamma_3}{2} (x_3 - x_3^d)^2 + \frac{1}{2}\gamma_{\theta_1}\tilde{\theta}_1^2 + \frac{1}{2}\gamma_{\theta_2}\tilde{\theta}_2^2 \quad (5.25)$$

where $\tilde{\theta} = \theta - \hat{\theta}$ and $\hat{\theta}$ is the estimate of θ . The derivative of (5.25) is given by

$$\dot{V}'_2 = \dot{V}_1 + \gamma_3 e_3 \left(\theta_1 f'_3 + \theta_2 g'_3 + \theta_2 \tilde{g}'_3 - \dot{x}_3^d \right) - \gamma_{\theta_1} \dot{\tilde{\theta}}_1 - \gamma_{\theta_2} \dot{\tilde{\theta}}_2 \quad (5.26)$$

\dot{x}_3^d can be calculated using (assuming $\frac{d}{dt} \left(\frac{\partial f_f}{\partial x_2} \right) = 0$)

$$\dot{x}_3^d = -\frac{k_1}{A}x_2 + \frac{1}{A} \left(\frac{\partial f_f}{\partial x_2} - k_2 \right) \left(\frac{A}{m}x_3 - \frac{1}{m}f_f(x_2) + g - \frac{a}{m}p_s \right) + \frac{m}{A}\ddot{x}_{1d} \quad (5.27)$$

and

$$\ddot{x}_3^d = -\frac{k_1}{A}\dot{x}_2 + \frac{1}{A}\left(\frac{\partial f_f}{\partial x_2} - k_2\right)\left[\frac{A}{m}\left(\theta_1 f'_3 + \theta_2 g'_3\right) - \frac{1}{m}\frac{\partial f_f}{\partial x_2}\dot{x}_2\right] + \frac{m}{A}x_{1d}^{(4)} \quad (5.28)$$

or, equivalently

$$\ddot{x}_3^d = \rho(X) + \frac{1}{m}\left(\frac{\partial f_f}{\partial x_2} - k_2\right)f'_3\theta_1 + \frac{1}{m}\left(\frac{\partial f_f}{\partial x_2} - k_2\right)g'_3\theta_2 \quad (5.29)$$

Let x_4^d be certainty equivalent to (5.15), i.e.

$$g_3^{d'} = g'_3(x_1, x_3, x_4^d) = \frac{1}{\hat{\theta}_2}\left[-\hat{\theta}_1 f'_3 + \dot{x}_3^d - \frac{A}{\gamma_3}e_2 - k_3 e_3\right] \quad (5.30)$$

is used as if the parameter estimate errors were all zero. This choice of x_4^d renders \dot{V}'_2 to

$$\dot{V}'_2 = -k_2 e_2^2 - k_3 \gamma_3 e_3^2 + \gamma_3 e_3 \left[\tilde{\theta}_1 f'_3 + \tilde{\theta}_2 g'_3 + \hat{\theta}_2 \tilde{g}'_3\right] - \gamma_{\theta_1} \dot{\hat{\theta}}_1 \tilde{\theta}_1 - \gamma_{\theta_2} \dot{\hat{\theta}}_2 \tilde{\theta}_2 \quad (5.31)$$

The derivative of x_4^d can be computed as follows

$$\begin{aligned} \dot{x}_4^d &= \frac{1}{\hat{\theta}_2 \partial g_3^{d'} / \partial x_4^d} \left[-\dot{\hat{\theta}}_1 f'_3 - \dot{\hat{\theta}}_2 g'_3 - \left(\dot{f}'_3 + \left(\frac{k_2}{m} - \frac{1}{m} \frac{\partial f_f}{\partial x_2} k_3 \right) f'_3 \right) \hat{\theta}_1 \right. \\ &\quad - \left(\frac{\partial g_3^{d'}}{\partial x_1} x_2 + \frac{k_2}{m} g'_3 - \frac{1}{m} \frac{\partial f_f}{\partial x_2} g'_3 + k_3 g'_3 \right) \hat{\theta}_2 - g'_3 \frac{\partial g_3^{d'}}{\partial x_3} \hat{\theta}_2^2 - f'_3 \frac{\partial g_3^{d'}}{\partial x_3} \hat{\theta}_1 \hat{\theta}_2 \\ &\quad - \left[\hat{\theta}_2 \frac{\partial g_3^{d'}}{\partial x_3} f'_3 + \left(\frac{k_2}{m} - \frac{1}{m} \frac{\partial f_f}{\partial x_2} + k_3 \right) f'_3 \right] \tilde{\theta}_1 \\ &\quad - \left(\hat{\theta}_2 \frac{\partial g_3^{d'}}{\partial x_3} + \frac{k_2}{m} - \frac{1}{m} \frac{\partial f_f}{\partial x_2} + k_3 \right) g'_3 \tilde{\theta}_2 + \rho(X) - \frac{A}{\gamma_3} (x_2 - x_{2d}) \\ &= \alpha \left(\hat{\theta}_1, \hat{\theta}_2, \dot{\hat{\theta}}_1, \dot{\hat{\theta}}_2, X \right) - \beta_1 \left(\hat{\theta}_1, \hat{\theta}_2, X \right) \tilde{\theta}_1 - \beta_2 \left(\hat{\theta}_1, \hat{\theta}_2, X \right) \tilde{\theta}_2 \end{aligned} \quad (5.32)$$

The system state equations in (5.8) and (5.29) have been used in the derivation of (5.32).

Similarly, V_3 is redefined as

$$V'_3 = V'_2 + \frac{1}{2} \gamma_4 e_4^2 \quad (5.33)$$

By taking the derivative of V_3' , one may write

$$\dot{V}_3' = \dot{V}_2' + \gamma_4 e_4 \left[-\frac{1}{\tau_e} x_4 + \frac{1}{\tau_e} u - \alpha + \tilde{\theta}_1 \beta_1 + \tilde{\theta}_2 \beta_2 \right] \quad (5.34)$$

Using the parameter adaptation laws given by

$$\dot{\hat{\theta}}_1 = \frac{1}{\gamma_{\theta_1}} \left[\gamma_3 f_3' e_3 + \gamma_4 \beta_1 \left(\hat{\theta}_1, \hat{\theta}_2, X \right) e_4 \right] \quad (5.35)$$

$$\dot{\hat{\theta}}_2 = \frac{1}{\gamma_{\theta_2}} \left[\gamma_3 g_3' e_3 + \gamma_4 \beta_2 \left(\hat{\theta}_1, \hat{\theta}_2, X \right) e_4 \right] \quad (5.36)$$

and the control law

$$u = \tau_e \left[\alpha + \frac{1}{\tau_e} x_4 - \frac{\gamma_3 \tilde{g}_3'}{\gamma_4 e_4} \hat{\theta}_2 e_3 - k_4 e_4 \right] \quad (5.37)$$

The derivative of V_3' becomes

$$\dot{V}_3' = -k_2 e_2^2 - \gamma_3 k_3 e_3^2 - \gamma_4 k_4 e_4^2 \quad (5.38)$$

Note that V_3' is a Lyapunov function for the closed-loop system. Therefore, the tracking errors converge to zero. However, the control and adaptation laws given here do not guarantee that the parameters converge to their actual values. For parameter convergence, the conditions of persistent excitation must be met [112].

5.4 Simulation Results

Simulations have been performed to investigate the performance of the proposed nonlinear controllers. The simulation results have also been used to tune the controller for the experimental studies discussed in the next section. The results obtained from simulation are presented in this section. The following values have been used for the system parameters.

$$\begin{aligned} A &= 1.14 \times 10^{-3} \text{m}^2 & a &= 6.33 \times 10^{-4} \text{m}^2 & L &= 1.37 \text{m} & p_s &= 1500 \text{psi} & d &= 55.4 \times 10^{-6} \text{m} \\ c &= 1.15 \times 10^{-4} & \beta &= 700 \text{Mpa} & m &= 30 \text{kg} & \tau_e &= 0.0035 \text{sec} \end{aligned}$$

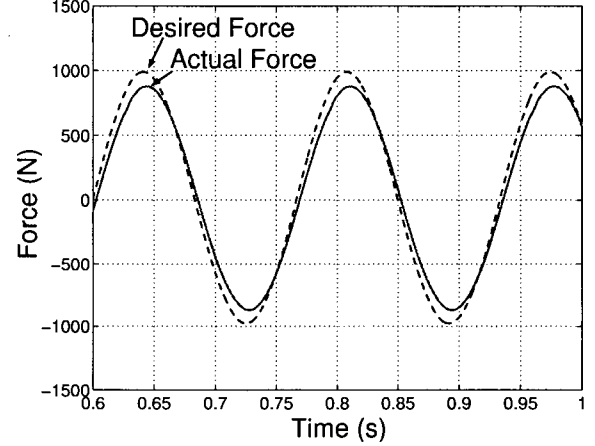
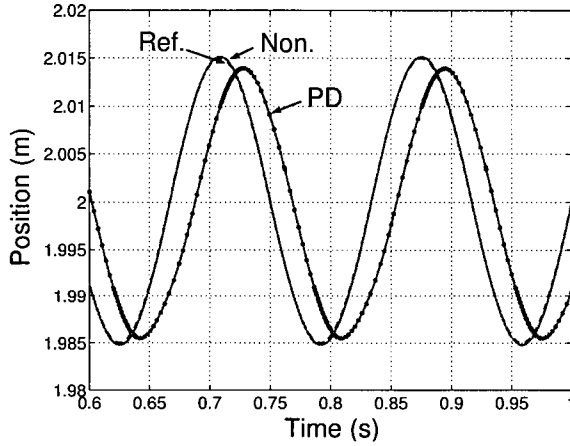


Figure 5.3: Position tracking with $f = 6\text{Hz}$ (simulation).

Figure 5.4: Actuator force tracking with $f = 6\text{Hz}$ (simulation).

The friction was modeled as viscous damping with $b = 1000 \text{ N}\cdot\text{s}/\text{m}$ ($f_f = bx_2$). The controller gains were chosen as

$$\begin{aligned} k_1 &= 400 \times 10^3 \text{ N}/\text{m} & k_2 &= 4000 \text{ N}\cdot\text{s}/\text{m} & k_3 &= 400 \text{ s}^{-1} & k_4 &= 800 \text{ s}^{-1} \\ \gamma_3 &= 10^{-10} & \gamma_4 &= 15 \times 10^7 \end{aligned}$$

5.4.1 Nonadaptive Controller

The position tracking performance of the proposed controller (nonadaptive) is compared with that of a standard PD controller for a sinusoidal reference trajectory with $f = 6 \text{ Hz}$ in Figure 5.3. The PD controller has been optimized to reduce the position tracking error. The nonlinear controller clearly outperforms the linear one. It tracks the reference trajectory almost perfectly whereas the linear controller exhibits a large tracking error. In the controller design, the control pressure (or, equivalently, the actuator output force) was an intermediate virtual control command. Figure 5.4 presents the force tracking behavior of the actuator. The force tracking error, seen in this figure, is due to the velocity estimation error. Actually, the effect of piston motion in (5.1) is canceled by (5.15) and because of the low compressibility of the fluid (huge β), the performance of force tracking is sensitive to this nonlinearity cancelation. To improve the performance, one should increase the pressure feedback gain k_3 . However, noise in the pressure loop can excite the high frequency modes and lead to system instability if a

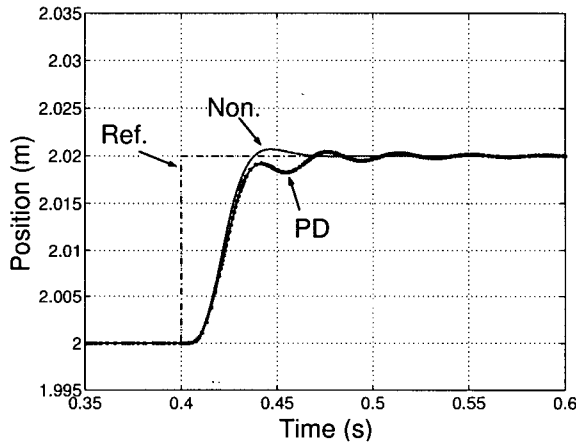


Figure 5.5: The step response of the con-

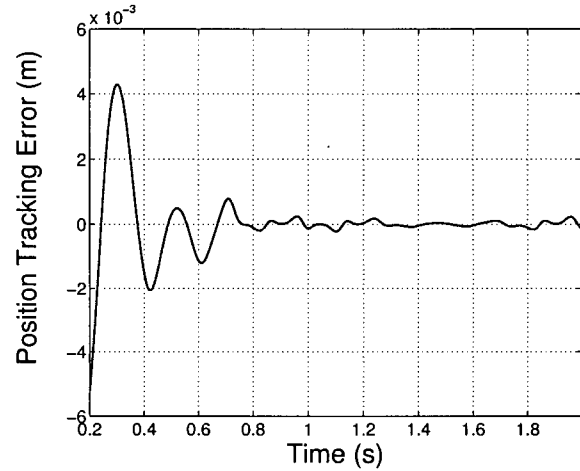


Figure 5.6: Position tracking error for the adaptive controller (simulation).

high pressure feedback gain is used. The step responses of the nonlinear and linear controllers are compared in Figure 5.5. Again, the proposed controller has better performance, especially a much smaller settling time compared with the PD controller. It should be pointed out that during the first rise phase both controllers saturate and therefore they behave almost identically.

5.4.2 Adaptive Controller

To investigate the effectiveness of the adaptive controller, another set of simulations were performed. The following adaptation gains were used to implement (5.35) and (5.36):

$$\gamma_{\theta_1} = 0.25 \times 10^{-14} \quad \gamma_{\theta_2} = 0.25 \times 10^{-6}$$

A multiple frequency reference trajectory was employed to excite the system. It was found that the controller is only sensitive to the ratio $c = \theta_2/\theta_1$, not the parameters themselves. In fact, the parameter estimations converge to values with the same ratio as the ratio of actual parameters, depending on their initial values. In the first simulation case, the initial estimates of the parameters were chosen to be 50% and 100% off from their actual values, respectively. The results are shown in Figure 5.7 (a, b). Solid lines represent the actual values of the parameters. In the second case, only one parameter was mismatched, and its adaptation law was active exclusively in each time. As a result the parameters converged to their actual values. The

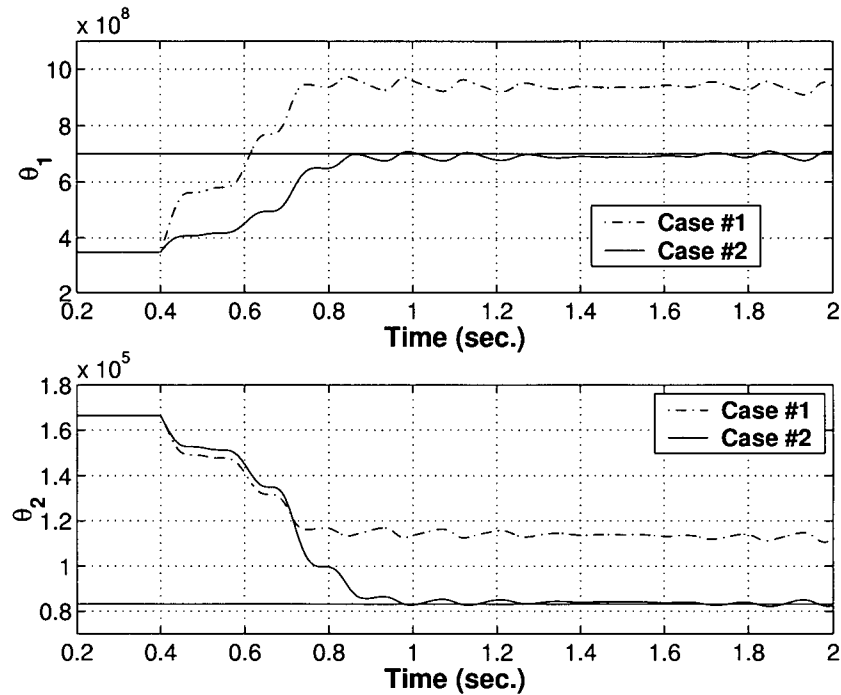


Figure 5.7: The estimated parameters (simulation). Solid lines show the actual values.

results are specified as Case 2 in Figure 5.7 (a, b). The tracking errors converge to zero in both cases. Figure 5.6 shows the position tracking error in the first case.

5.5 Experimental Results

The proposed controller was also implemented on one of the hydraulic actuators used in the UBC hydraulic motion simulator [99]. Necessary modifications were made in order to perform single cylinder experiments, as seen in Figure 5.8. The hydraulic actuation system is equipped with a Rexroth 4WRDE three-stage proportional valve connected in a three-way configuration. Low friction Teflon seals are used in the hydraulic cylinders. The computing setup consists of a VME-based real-time system running VxWorks on a Themis Sparc 5 board. Actuator length, valve spool position and supply and control pressures are measured through installed sensors. The schematic diagram of the controller is shown in Figure 5.9. In this figure, $N_1(\cdot)$, $N_2(\cdot)$ and $N_3(\cdot)$ have been defined in (5.11), (5.15) and (5.19), respectively. All derivatives required in the control law were implemented by $\alpha - \beta$ filters [10]. The control update frequency was $f = 1$ kHz. The actual system parameters are all the same as those given in the simulation

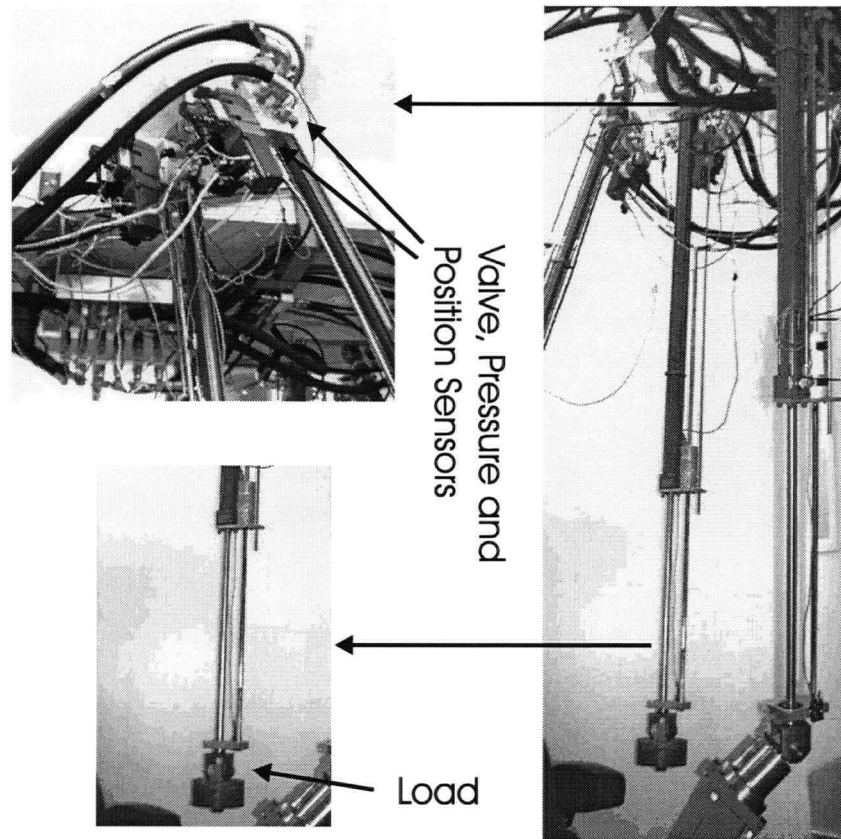


Figure 5.8: The experimental setup.

section. The controller gains were selected as:

$$k_1 = 400 \times 10^3 \text{N/m} \quad k_2 = 10 \times 10^3 \text{N.s/m} \quad k_3 = 100 \text{s}^{-1} \quad k_4 = 300 \text{s}^{-1}$$

During the experiments, it was found that it is difficult to increase the pressure feedback gain k_3 . Increasing this gain allows the noise to excite the high frequency modes of the system and can lead to instability. Both adaptive and fixed-parameter controllers were implemented. Adaptive controllers slightly improved the tracking performance but the parameters did not converge to constant values. Bounds on parameter estimations were used to avoid instability due to parameter drift. The very stiff pressure dynamics make the pressure control loop sensitive to measurement noise and prevent parameter convergence. It should be pointed out that the parameter convergence is not guaranteed by the proposed controller. The hydraulic parameters used in the nonadaptive controller were identified by an off-line least-squares estimation

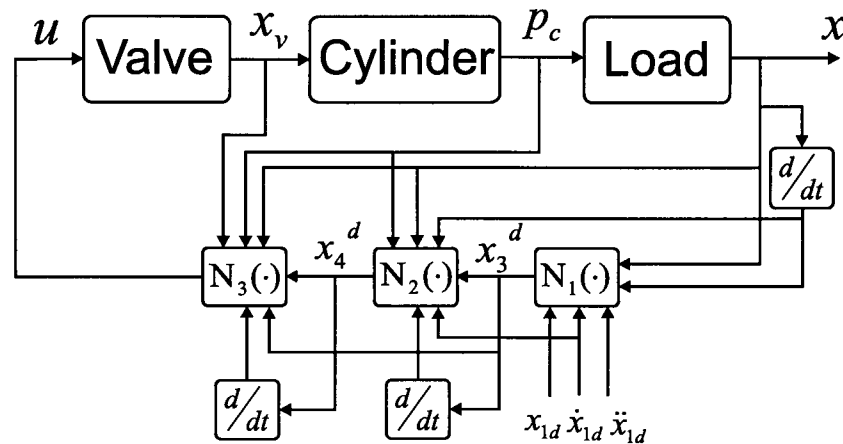


Figure 5.9: The schematic of the controller.

technique. The nonlinear controller performance is compared with a standard PD controller in Figures 5.10-5.12. The PD controller was tuned to obtain a good tracking performance while keeping the system stable. Figure 5.10 displays the position tracking for a reference trajectory with $f = 2\text{Hz}$. The nominal position of the load is at $l = 2.35\text{m}$ which is not shown in this figure. The nonlinear controller clearly outperforms the PD controller despite its poor force tracking as shown in Figure 5.11 (the maximum tracking errors are 5% and 28% for the controllers, respectively). In Figure 5.12 the controllers are compared in tracking a $f = 4\text{ Hz}$ reference position trajectory. Again, the superiority of the nonlinear controller is clearly observed where the peak tracking errors are 17% and 55% for the two controllers.

5.6 Conclusions

In this chapter, the position control problem of a hydraulic actuator was addressed. The highly nonlinear behavior of the system limits the performance of classical linear controllers used for this purpose. The backstepping design strategy was adopted to develop a nonlinear controller that considers the valve dynamics. An adaptation algorithm was also proposed for on-line identification of hydraulic parameters. The control laws proposed in this chapter require measurements of the actuator position and velocity, control pressure, and the valve spool position. It was found that the proposed controller outperforms a tuned PD controller both in simulation and experiments. Despite the fact that the stiff pressure dynamics makes the inner pressure

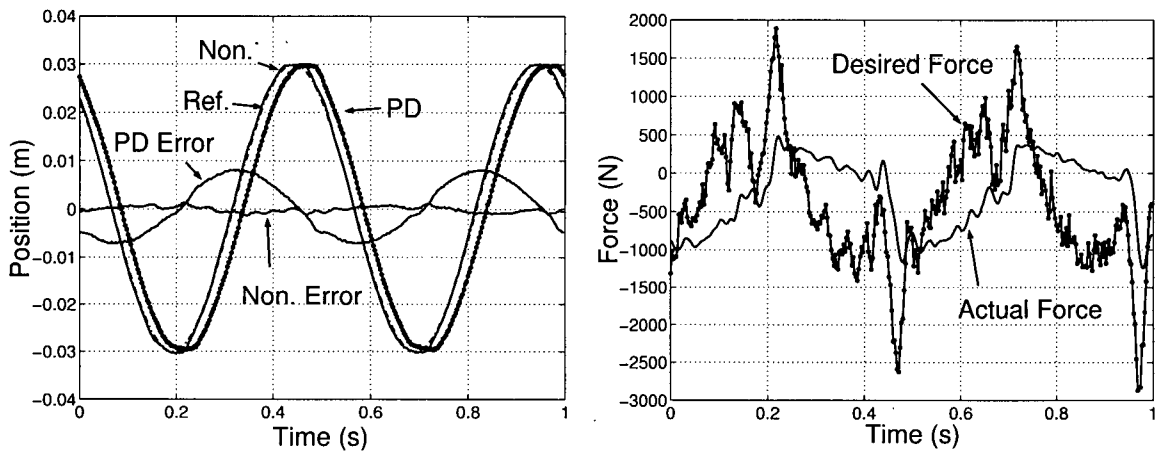


Figure 5.10: The position tracking with $f = 2\text{Hz}$. Figure 5.11: Actuator force tracking with $f = 2\text{Hz}$.

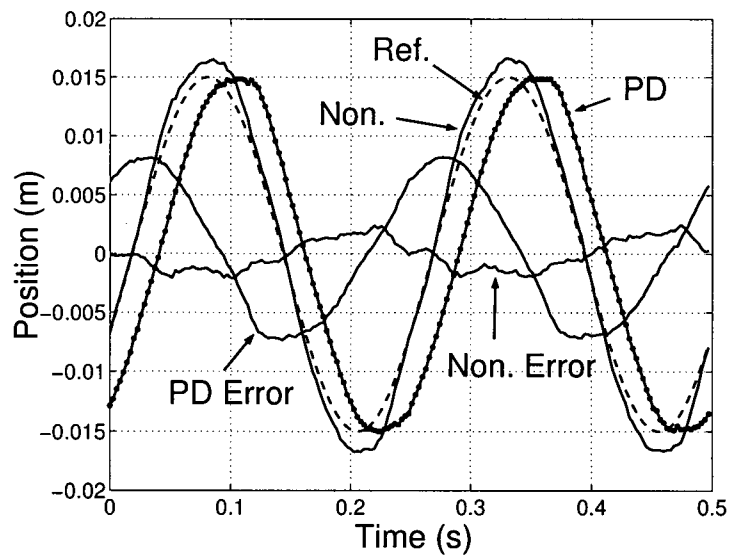


Figure 5.12: The position tracking with $f = 4\text{Hz}$.

control loop sensitive to system uncertainties, excellent position tracking performance is obtained. The method has the potential to be extended to the control of hydraulic manipulators incorporating the actuator dynamics. This will be demonstrated later in the thesis.

Chapter 6

Numerical Optimization of a Single Cylinder Hydraulic Servo-system

6.1 Overview

In Chapter 5 of the thesis a nonlinear position tracking controller was proposed for single cylinder hydraulic systems. The proposed controller guarantees the convergence of the tracking errors to zero if proper gains are used. However, it does not provide any information on the transient response of the system and the selection of the feedback gains for the improvement of this response. The gain tuning is usually performed by trial and error. This chapter proposes a numerical approach to the optimization of the nonlinear controller. Numerical methods for solving optimal control problems have been reported in the literature, e.g. see [9] and [32]. However, this work differs from them in the way it formulates the suboptimal control problem and finds its solution. A simplified version of the position tracking controller presented in Chapter 5 is used here. The valve dynamics and the hydraulic parametric uncertainty are ignored in the model. These assumptions lead to a feedback linearization based control law parameterized by the feedback gains. A performance index that captures some features of the transient response of the system is defined. This index also includes a term that penalizes measurement noise amplification in the controlled variables. Various optimization techniques are utilized to optimize the performance index over the set of controller gains that stabilize the system. The response of the system under the suboptimal nonlinear controller is simulated and

the results are presented. Note that the above assumptions have been made to simplify the problem and demonstrate the solution. The approach can be extended to the optimization of the original nonlinear controller laws.

The chapter is organized as follows. First, the simplified dynamics, the control law, and the subsequent closed-loop dynamics are presented. Then, the formulation of the suboptimal control problem is discussed. The evaluation of the performance index and its gradient are briefly explained next. The optimization routines used in this thesis and the results of their application to the problem under study are also presented. Conclusions about the approach are drawn at the end.

6.2 System Dynamics

The schematic of the system under study is shown in Figure 6.1. This is similar to the model discussed in Chapter 5 with some minor modifications. Gravity is not considered and the load is taken to be a mass-spring-damper system. The mass-spring-damper dynamics are governed by

$$m\ddot{x} + b\dot{x} + kx = \tau \quad (6.1)$$

where τ is the force exerted by the actuator, m is the mass, b is the damping and k is the stiffness of the load and x , \dot{x} and \ddot{x} are the position, velocity and acceleration of the actuator, respectively. The hydraulic dynamics are also simplified by ignoring the valve underlap and the electrohydraulic servo-valve dynamics. The effect of valve dynamics on the system response will be investigated later in the simulation studies. Valve saturation is also neglected in the design. The load flow is given by:

$$q_l = \begin{cases} cu\sqrt{p_c} & u \leq 0 \\ cu\sqrt{p_s - p_c} & u > 0 \end{cases} \quad (6.2)$$

Here, u is the control command (valve spool position). The rest has been defined in Chapter 5

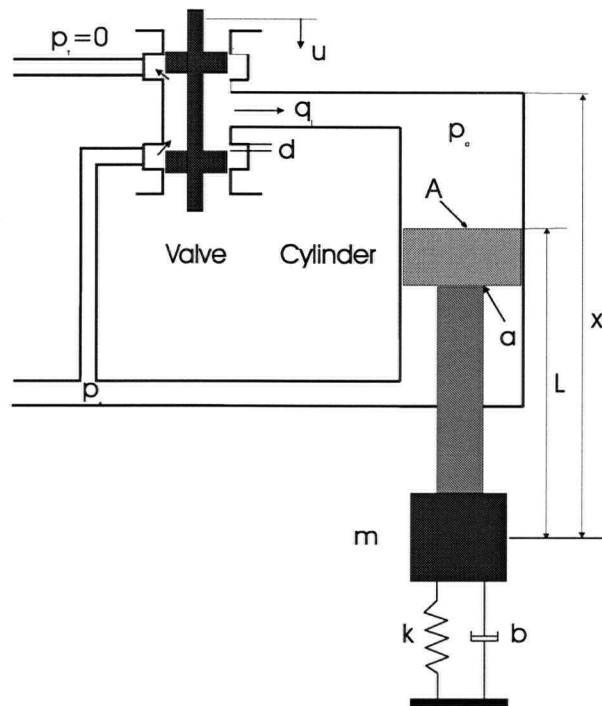


Figure 6.1: Single-rod hydraulic servo-system.

in (5.1) and (5.3). Note that force dynamics can be written as:

$$\dot{\tau} = -\frac{A\beta\dot{x}}{x-L} + \frac{\beta}{x-L}q_l(\tau, u) = f(x, \dot{x}) + g(x, \tau, u) \quad (6.3)$$

(6.1) and (6.3) describe a third-order nonlinear dynamic system.

6.3 Control Law and Closed-loop Dynamics

To derive the control law, the desired actuator force is chosen as

$$\tau_d = m\ddot{x}_d + b\dot{x}_d + kx_d - k_p e - k_d \dot{e} \quad (6.4)$$

where \ddot{x}_d , \dot{x}_d and x_d are the desired acceleration, velocity and position trajectories, respectively. $e = x - x_d$ and $\dot{e} = \dot{x} - \dot{x}_d$ are the position and velocity tracking errors. The constant coefficients

k_p and k_d are design parameters. By substituting (6.4) in (6.1),

$$m\ddot{e} + (b + k_d)\dot{e} + (k + k_p)e = \tilde{\tau} \quad (6.5)$$

where $\tilde{\tau} = \tau - \tau_d$ is the force tracking error due to the presence of the actuator dynamics. Consider the following nonlinear feedback law

$$u = \frac{1}{\bar{g}} (-f(x, \dot{x}) + \dot{\tau}_d - k_\tau \tilde{\tau}) \quad (6.6)$$

and

$$\bar{g} = \begin{cases} \frac{\beta c}{x-L} \sqrt{\frac{\tau + p_s a}{A}} & \text{if } u_d \leq 0 \\ \frac{\beta c}{x-L} \sqrt{p_s - \frac{\tau + p_s a}{A}} & \text{if } u_d > 0 \end{cases} \quad (6.7)$$

with

$$u_d = -f(x, \dot{x}) + \dot{\tau}_d - k_\tau \tilde{\tau} \quad (6.8)$$

and

$$\dot{\tau}_d = m\ddot{x}_d + b\dot{x}_d + kx_d + \frac{k_d(k + k_p)}{m}e + \left(\frac{k_d(b + k_d)}{m} - k_p \right) \dot{e} - \frac{k_d}{m} \tilde{\tau} \quad (6.9)$$

Equations (6.4) and (6.5) have been used in the derivation of (6.9).

Upon defining $X = [x_1, x_2, x_3]^T = [e, \dot{e}, \tilde{\tau}]^T$, it is not difficult to show that the error dynamics under the proposed control law have the following forms

$$\begin{aligned} \dot{x}_1 &= x_2 \\ \dot{x}_2 &= -p_1 x_1 - p_2 x_2 + \frac{1}{m} x_3 \\ \dot{x}_3 &= -p_3 x_3 \end{aligned} \quad (6.10)$$

or equivalently,

$$\dot{X}(t) = A_0(p)X(t) \quad (6.11)$$

Parameters p_1 , p_2 and p_3 are defined as

$$p_1 = \frac{k + k_p}{m} \quad p_2 = \frac{b + k_d}{m} \quad p_3 = k_\tau \quad (6.12)$$

and

$$A_0(p) = \begin{bmatrix} 0 & 1 & 0 \\ -p_1 & -p_2 & \frac{1}{m} \\ 0 & 0 & -p_3 \end{bmatrix} \quad (6.13)$$

The poles of the closed-loop system are the solutions of the following equation:

$$\det(sI - A_0) = (s + p_3)(s^2 + p_2s + p_1) = 0 \quad (6.14)$$

Clearly, the tracking errors are stable and converge to zero if all three parameters are fixed and positive. It should be pointed out that the special form of the dynamics has allowed the use of a feedback linearizing controller and has simplified the problem.

The proposed control law requires the measurement of the actuator position, velocity and output force (obtained from the supply and control pressure measurements). In the above formulation, measurement noise has not been considered. In practice, feedback signals are contaminated with some level of noise. The state equations are now modified to consider the noise, assumed to be zero-mean colored Gaussian, as follows.

$$x_m = x + x_n \quad (6.15)$$

$$\dot{x}_m = \dot{x} + v_n \quad (6.16)$$

$$\tau_m = \tau + \tau_n \quad (6.17)$$

$$E\{x_n^2\} = \sigma_{x_n}^2 \quad E\{v_n^2\} = \sigma_{v_n}^2 \quad E\{\tau_n^2\} = \sigma_{\tau_n}^2 \quad (6.18)$$

and

$$\dot{x}_n = -\frac{1}{\tau_x}x_n + \frac{1}{\tau_x}n_x \quad (6.19)$$

$$\dot{v}_n = -\frac{1}{\tau_v}v_n + \frac{1}{\tau_v}n_v$$

$$\dot{\tau}_n = -\frac{1}{\tau_\tau}\tau_n + \frac{1}{\tau_\tau}n_\tau \quad (6.20)$$

where n_x , n_v and n_τ denote zero-mean white Gaussian noise. This will affect τ_d in (6.4) as follows:

$$\begin{aligned} \tau_d^n &= m\ddot{x}_d + b\dot{x}_d + kx_d - k_p(e + x_n) - k_d(\dot{e} + v_n) \\ &= \tau_d - k_px_n - k_dv_n \end{aligned} \quad (6.21)$$

Corresponding changes in (6.9) produce

$$\dot{\tau}_d^n = \dot{\tau}_d + \frac{k_d k}{m}x_n + \left(\frac{k_d b}{m} - k_p\right)v_n - \frac{k_d}{m}n_\tau \quad (6.22)$$

Since f and \bar{g} in (6.6) are nonlinear functions of the states, nonlinear noise terms appear in these quantities and make the analysis complicated. To tackle this problem, the following linear approximations are made

$$f^n = -\frac{A\beta(\dot{x} + v_n)}{x - L + x_n} \approx -\frac{A\beta\dot{x}}{x - L} - \frac{A\beta}{x_d - L}v_n \quad (6.23)$$

$$\bar{g}^n \approx \bar{g} \quad (6.24)$$

Using (6.20)-(6.24) in the feedback law (6.6) and after performing some manipulations, we

obtain the error dynamics

$$\begin{aligned}
 \dot{x}_1 &= x_2 \\
 \dot{x}_2 &= -\frac{k+k_p}{m}x_1 - \frac{b+k_d}{m}x_2 + \frac{1}{m}x_3 \\
 \dot{x}_3 &= -k_\tau x_3 + \left(\frac{kk_d}{m} - k_\tau k_p\right)x_4 \\
 &\quad + \left(\frac{A\beta}{x_d-L} + \frac{k_d b}{m} - k_\tau k_d - k_p\right)x_5 - \left(\frac{k_d}{m} + k_\tau\right)x_6 \\
 \dot{x}_4 &= -\frac{1}{\tau_x}x_4 + \frac{1}{\tau_x}n_x \\
 \dot{x}_5 &= -\frac{1}{\tau_v}x_5 + \frac{1}{\tau_v}n_v \\
 \dot{x}_6 &= -\frac{1}{\tau_\tau}x_6 + \frac{1}{\tau_\tau}n_\tau
 \end{aligned} \tag{6.25}$$

with $[x_1, x_2, x_3, x_4, x_5, x_6]^T = [e, \dot{e}, \tilde{\tau}, x_n, v_n, \tau_n]^T$. The state equations can also be written in matrix form

$$\dot{X}(t) = \bar{A}(p)X(t) + BN \quad \bar{A} = \begin{bmatrix} A_0(p) & \bar{A}_{12}(p) \\ 0 & \bar{A}_{22} \end{bmatrix} \tag{6.26}$$

with

$$\bar{A}_{12}(p) = \begin{bmatrix} 0 & 0 & 0 \\ 0 & 0 & 0 \\ \frac{kk_d}{m} - k_\tau k_p & \frac{A\beta}{x_d-L} + \frac{k_d b}{m} - k_\tau k_d - k_p & -\frac{k_d}{m} - k_\tau \end{bmatrix} \tag{6.27}$$

$$\bar{A}_{22} = \begin{bmatrix} -\frac{1}{\tau_m} & 0 & 0 \\ 0 & -\frac{1}{\tau_v} & 0 \\ 0 & 0 & -\frac{1}{\tau_\tau} \end{bmatrix} \tag{6.28}$$

$$B = \begin{bmatrix} \frac{1}{\tau_x} & \frac{1}{\tau_v} & \frac{1}{\tau_\tau} \end{bmatrix}^T \tag{6.29}$$

6.4 Suboptimal Control Problem

Under the proposed control law, the tracking errors are stable and converge to zero whenever the parameters p_1 , p_2 and p_3 are positive. Nevertheless, the transient response of the closed-loop system is determined by these parameters and they should not be chosen arbitrarily. Moreover, the presence of measurement noise prevents the application of very large feedback gains. Also, in practice, the valve opening would saturate if very large inputs are commanded. To define a performance measure that quantifies the transient behavior of the closed-loop system and the above limitations, the response of the system to a position step input is considered. The goal is to move the actuator from rest at some known initial position to rest at some other known position within time t_f while minimizing a performance index that will be defined shortly. This problem can be stated as

$$\begin{aligned} \min_{p_i, s > 0} \quad & J(p) \quad \text{s.t.} \\ \dot{X}(t) = & A_0(p)X(t) \\ X_0 = & \begin{bmatrix} x_0 - x_d & 0 & -kx_d + k_p(x_0 - x_d) \end{bmatrix}^T \\ X(t_f) = & [0, 0, 0]^T \quad (\text{desired final state}) \end{aligned} \quad (6.30)$$

Despite the presence of noise, the problem is first treated as a deterministic optimization problem with the performance index

$$J(p) = J_x(p) + J_u(p) + J_{t_f}(p) \quad (6.31)$$

where

$$J_x(p) = \int_0^{t_f} X(t)^T Q X(t) dt \quad (6.32)$$

$$J_u(p) = \int_0^{t_f} r u^2(t) dt \quad (6.33)$$

$$J_{t_f}(p) = X(t_f)^T H X(t_f) \quad (6.34)$$

and Q , H and r are all positive. This formulation of the performance index has been widely used

in the optimal control literature [15,70]. J_x penalizes the tracking errors during the transition period and J_{t_f} does the same thing for the final state. The introduction of J_u penalizes excessive control commands and therefore discourages valve saturation. It is possible to introduce the effect of noise into the performance index without recourse to stochastic optimization. To this end, the steady state response of the closed-loop system under noise excitations is considered. That is the response of the dynamical system described by (6.26) when time approaches infinity. It can be shown that the state vector becomes a stationary random process with zero mean and covariance matrix P given by the solution of the Lyapunov equation [7]

$$\bar{A}P + P\bar{A}^T + BB^T = 0 \quad (6.35)$$

$$P = E\{XX^T\} = \int_0^\infty e^{\bar{A}t}BB^Te^{\bar{A}^Tt}dt \quad (6.36)$$

A new term is added to the performance index that penalizes for the first three diagonal elements of this matrix (the covariances of e , \dot{e} and $\tilde{\tau}$, respectively). Therefore, the overall performance measure is modified as

$$J(p) = J_x + J_u + J_{t_f} + J_n \quad (6.37)$$

with J_n defined as

$$J_n = r_x P(1,1) + r_v P(2,2) + r_\tau P(3,3) \quad (6.38)$$

and r_x , r_v and r_τ are all positive.

Remark: The magnitude of the step input is assumed to be fixed and the initial velocity and the output force of the actuator are assumed to be zero.

6.5 Evaluation of the Performance Index and its Gradient

Three terms in the performance index, namely, J_x , J_{t_f} and J_n , are computed analytically. It can be shown that (see Appendix A)

$$J_x = X_0^T U_t^* (V^* Q V) \cdot \left[\frac{1}{\lambda_i^* + \lambda_j} \left(e^{(\lambda_i^* + \lambda_j) t_f} - 1 \right) \right] U_t X_0 \quad (6.39)$$

$$J_{t_f} = X_0^T U_t^* e^{\Lambda^* t_f} V^* H V e^{\Lambda t_f} U_t X_0 \quad (6.40)$$

and

$$J_n = r_x P(1, 1) + r_v P(2, 2) + r_\tau P(3, 3) \quad (6.41)$$

where

$$P = \bar{V} (\bar{U}_t B B^T \bar{U}_t^*) \cdot \left[-\frac{1}{\bar{\lambda}_i + \bar{\lambda}_j^*} \right] \bar{V}^* \quad (6.42)$$

and “ $(\cdot)[\cdot]$ ” denotes component-wise product of two matrices. In (6.39), (6.40) and (6.42) U_t , V , \bar{U}_t and \bar{V} , are matrices of the left and right eigenvectors of A_0 and \bar{A} , respectively. Also, λ_i and $\bar{\lambda}_i$ are the eigenvalues of A_0 and \bar{A} .

Remark: Once \bar{U}_t , \bar{V} are computed, the upper (3×3) blocks of these matrices represent U_t and V . It is assumed that \bar{A} does not have any degenerate eigenvalues.

The term corresponding to the control effort in the performance index, J_u , has to be computed numerically. Once $X(t)$ is calculated, $u(t)$ can be derived from (6.6) and then used in an integration routine to compute J_u . In this work, function “quad” from *Matlab* was employed for this purpose.

The optimization algorithms used in this thesis also require the gradient of the performance index with respect to the parameters at each point. The expressions for the gradient have been derived in Appendix A. It should be mentioned that the computation of the gradient involves taking the partial derivatives of eigenvalues and eigenvectors with respect to parameters, i.e., $\frac{\partial U_t}{\partial p_m}$, $\frac{\partial V}{\partial p_m}$ and $\frac{\partial \lambda_i}{\partial p_m}$. This is addressed in [73] and [53].

Table 6.1: Performance of the optimization routines.

	SR1	BFGS	DFP	Conj. Grad.
Steps	32	30	13	21
Time (s)	21.2	27.3	61.2	108.4

6.6 Optimization Results

The optimization problem defined by (6.30) is a constrained optimization problem in principle. Nevertheless, the solution is always located in the stable region. This is because of the fact that any unstable pole can generate large tracking errors that would never converge to zero and hence would significantly increase the performance index. Therefore, unconstrained optimization routines were implemented to solve the problem. Special care was taken to prevent the algorithms from leaving the stable region in the intermediate steps. This is important since J_n is not defined in the presence of any unstable modes. The algorithms used in this thesis are SR1/Trust Region, BFGS, DFP and Conjugate Gradients [88].

The performance index defined in (6.37) has some parameters to be specified (see (6.32)-(6.34) and (6.38)). For simplicity, the matrices Q and H are chosen to be diagonal. In matrix Q a small weight is given to velocity tracking errors so the system can have a fast response. The other two terms are selected in such way that they roughly normalize their corresponding tracking errors. In matrix H all tracking errors have been treated in the same way. The velocity coefficient is not small here since a zero velocity is desired at the final time t_f . Furthermore, r_x, r_v are selected in accordance to measurement noise covariances to scale them to the same order. Noise in the force tracking error is not important so a small weight is given to it.

In order to properly weight J_x, J_{t_f}, J_u and J_n in the performance index, an iterative scheme is employed. At the minimum point \hat{p} one may write

$$\frac{\partial J}{\partial p} \delta p = \left(\frac{\partial J_x}{\partial p} + \frac{\partial J_{t_f}}{\partial p} + \frac{\partial J_u}{\partial p} + \frac{\partial J_n}{\partial p} \right) \delta p = 0 \quad (6.43)$$

It is reasonable to scale each component of the gradient at this point in such way that they roughly contribute the same amount to the change in the performance. Therefore, once a solution is found each term is scaled based on the norm of its gradients and the problem is

solved again using the new values. This process continues until the norms of the final gradients are within the same order of magnitude. Several cases of simulations have been carried out. The results follow.

6.6.1 Case 1

The initial and final positions of the piston, x_0 and x_d and also the control time horizon, t_f , are selected based on the author's experience. The covariance and bandwidth of the measurement noises are chosen based on the specifications of hydraulic experimental setup used in Chapter 5. The numerical values used in this case are as follows:

$$\begin{array}{cccc}
 x_0 = 1.9\text{m} & x_d = 1.93\text{m} & \dot{x}_d = 0 & \ddot{x}_d = 0 \\
 \ddot{x}_d = 0 & t_f = 0.1\text{s} & r = 4 \times 10^7 \text{m}^{-2}/\text{s} & \sigma_{x_n}^2 = 4 \times 10^{-8} \text{m}^2 \\
 \sigma_{v_n}^2 = 10^{-2} \text{m}^2/\text{s}^2 & \sigma_{\tau_n}^2 = 1600 \text{N}^2 & \tau_x = 1/170\text{s} & \tau_v = 1/180\text{s} \\
 \tau_r = 1/600\text{s} & r_x = 5 \times 10^8 \text{m}^{-2} & r_v = 2 \times 10^3 \text{s}^2/\text{m}^2 & r_\tau = 0.0125 \text{N}^{-2}
 \end{array}$$

$$Q = 5 \begin{bmatrix} 10^5 \text{m}^{-2} \text{s}^{-1} & 0 & 0 \\ 0 & 10^{-4} \text{m}^{-2} \text{s} & 0 \\ 0 & 0 & 1 \text{N}^{-2} \text{s} \end{bmatrix} \quad H = \begin{bmatrix} 25 \times 10^8 \text{m}^{-2} & 0 & 0 \\ 0 & 10^6 \text{m}^{-2} \text{s}^2 & 0 \\ 0 & 0 & 25 \times 10^3 \text{N}^{-2} \end{bmatrix}$$

The parameters of the hydraulic servo-system represent those of the experimental setup. These parameters have been defined earlier in this chapter.

$$\begin{aligned}
 A &= 1.14 \times 10^{-3} \text{m}^2 & a &= 6.33 \times 10^{-4} \text{m}^2 \\
 c_d &= 0.432 & w &= 5.7 \times 10^{-3} \text{m} \\
 \rho &= 858.2 \text{kg/m}^3 & L &= 1.37 \text{m} \\
 b &= 0 \text{N s/m} & k &= 0 \text{N/m} \\
 p_s &= 1200 \times 6894.757 \text{Pa} & \beta &= 700 \times 10^6 \text{Pa} \\
 m &= 40 \text{kg} & &
 \end{aligned}$$

All of the optimization algorithms started at the following initial point

$$p_0 = \begin{bmatrix} 3000 & 250 & 400 \end{bmatrix}^T \quad J_0 = 228334$$

and they all converged to following solution point.

$$\hat{p} = \begin{bmatrix} 4678.43 & 121.93 & 278.33 \end{bmatrix}^T \quad \hat{J} = 73.937$$

The results are compared in Table 6.1 in terms of their execution time and the number of the steps before convergence. To investigate whether the solution is a local minimum or not, the optimization routines were run from a number of other starting points and they all converged to the same minimum point even though the rates of convergence were different. The profiles of the performance index and its components obtained from running SR1/Trust Region optimization method are shown in Figure 6.2. The trajectory of the parameters in the parameter space from the initial point to the final point is drawn in Figure 6.3.

The responses of the system with the optimized gains are presented in Figures 6.4-6.7. Clearly, the system exhibits a very fast response with no overshoot and reasonable noise in the controlled variables and the goals of the optimization are all achieved.

Remark: In Figures 6.3-6.13 the step input is commanded at time $t_0 = 0.1$ sec so the actual final time is $t_f = t_0 + 0.1 = 0.2$ sec.

The predicted measurement noise covariances obtained from the solution of the Lyapunov

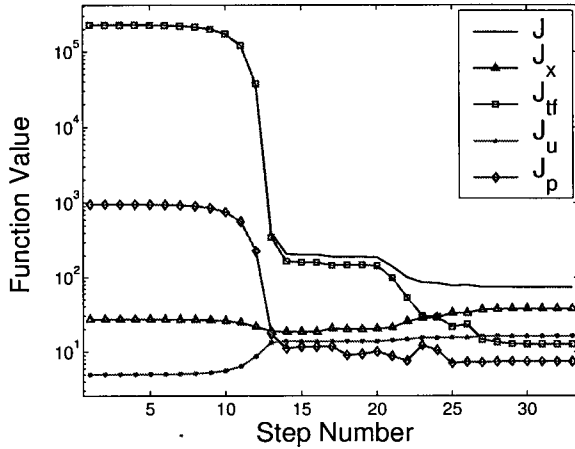


Figure 6.2: Profile of the performance index (SR1).

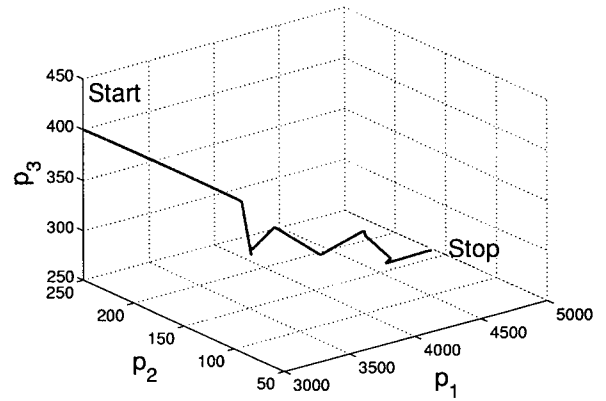


Figure 6.3: The trajectory of parameters (SR1).

equation match their numerical estimates obtained from simulation very well. Note that small discrepancies are due to the approximation of nonlinear noise effects in the analytical model and also numerical approximation errors.

$$\begin{array}{ll}
 \sigma_x^2 = 1.4818 \times 10^{-8} (\text{simulation}) & \sigma_x^2 = 1.2108 \times 10^{-8} (\text{predicted}) \\
 \sigma_v^2 = 3.933 \times 10^{-5} (\text{simulation}) & \sigma_v^2 = 4.0489 \times 10^{-5} (\text{predicted}) \\
 \sigma_\tau^2 = 2.0371 \times 10^3 (\text{simulation}) & \sigma_\tau^2 = 2.318 \times 10^3 (\text{predicted})
 \end{array}$$

6.6.2 Case 2: Effect of initial position

The nonlinear control law proposed here linearizes the dynamics and the closed-loop behavior of the system under this feedback law should not depend on the operating point of the system. To show this, the initial and the desired final position of the actuator are chosen to be different from those of the previous case.

$$x_0 = 1.6\text{m} \qquad x_d = 1.63\text{m}$$

The system responses in this case are shown in Figures 6.8-6.11. The only noticeable difference is an increase in the amount of noise specially in the force signal. This is can be explained

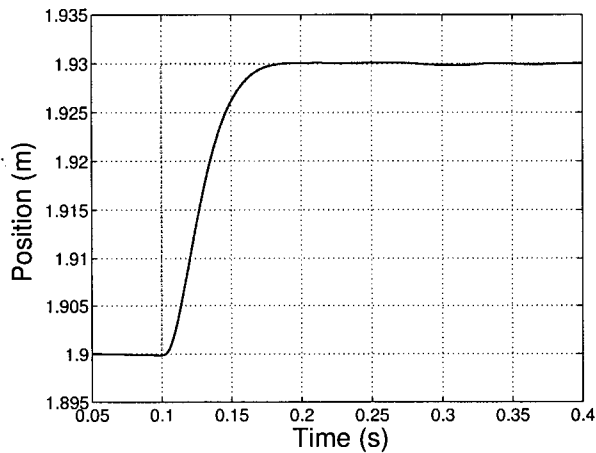


Figure 6.4: Position of the actuator (case 1).

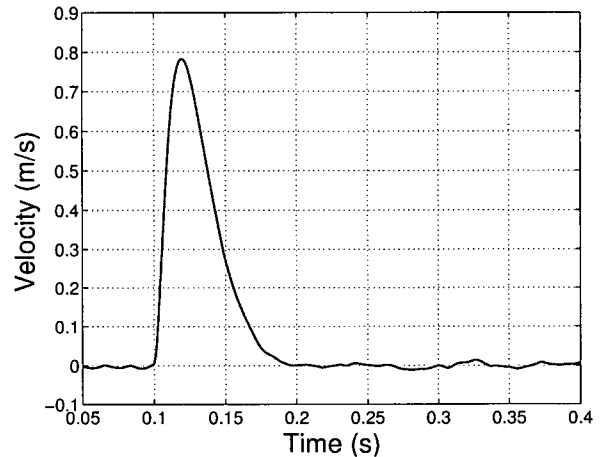


Figure 6.5: Velocity of the actuator (case 1).

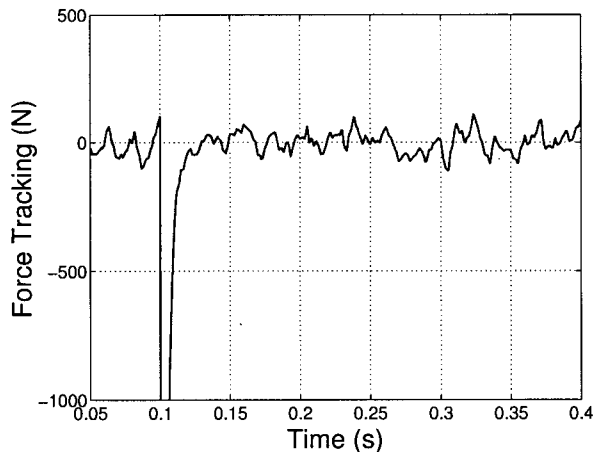


Figure 6.6: Force tracking of the actuator (case 1).

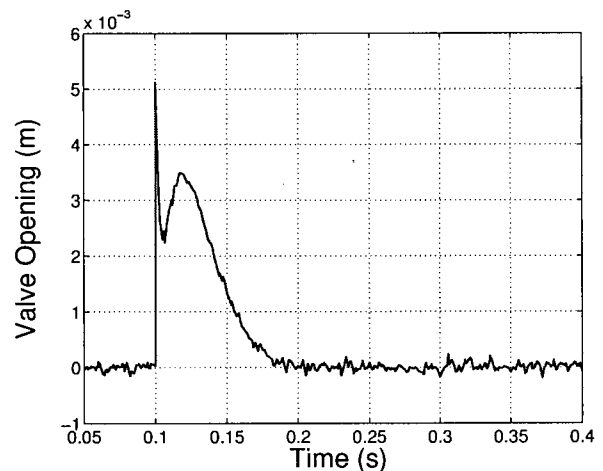


Figure 6.7: Control command (case 1).

by the decrease in the trapped oil volume in the control side of cylinder ($V_t = A(x - L)$) that increases sensitivity to velocity measurement noise (see \dot{x}_3 in (6.25)). It is worth noticing that part of the induced noise is independent of the feedback gains. Therefore, if the controller is to be used with small rod strokes, the velocity measurement (estimation) noise must be small.

6.6.3 Case 3: Effect of valve dynamics

In the modeling of the hydraulic servo-system earlier in this chapter, the electro-hydraulic valve dynamics were ignored. The effect of a second-order linear valve dynamics with $\omega_e = 400\text{rad/sec}$

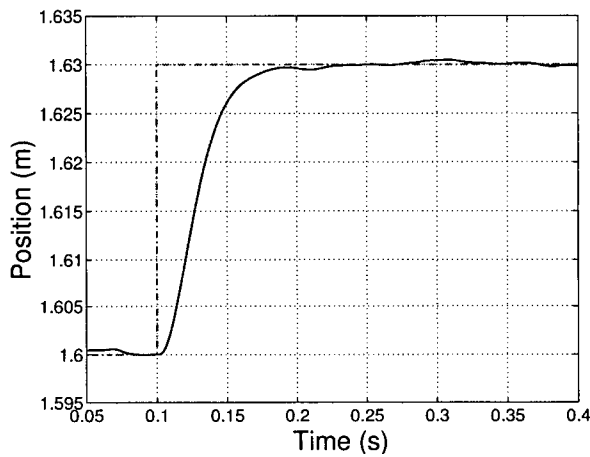


Figure 6.8: Position of the actuator (case 2).

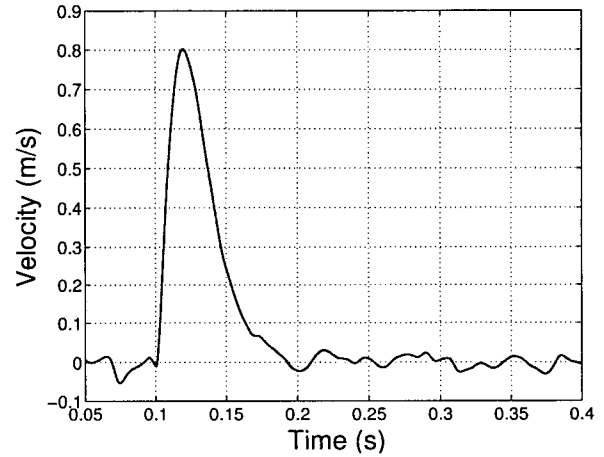


Figure 6.9: Velocity of the actuator (case 2).

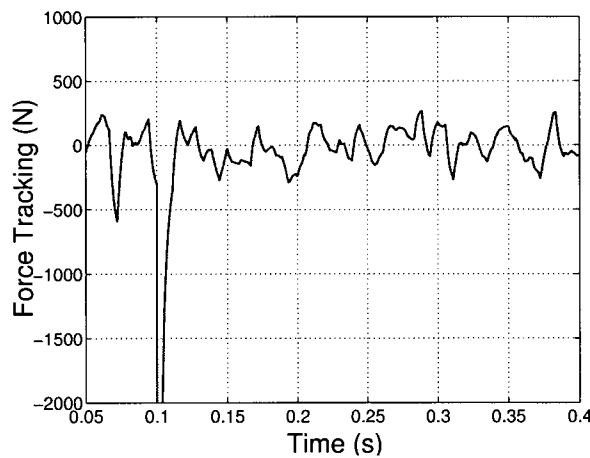


Figure 6.10: Force tracking of the actuator (case 2).

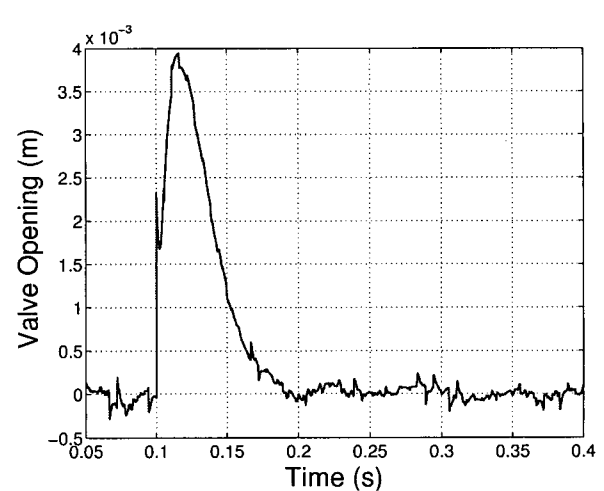


Figure 6.11: Control command (case 2).

and $\zeta_e = 0.7$ on the performance of the controller designed above can be seen in Figures 6.12-6.13. There is a small overshoot in the position response and the settling time is longer, but the system behavior is still satisfactory. Obviously, the valve dynamics may not be ignored if slow servo-valves are used. The presence of these dynamics can even lead to instability if they are neglected in the design.

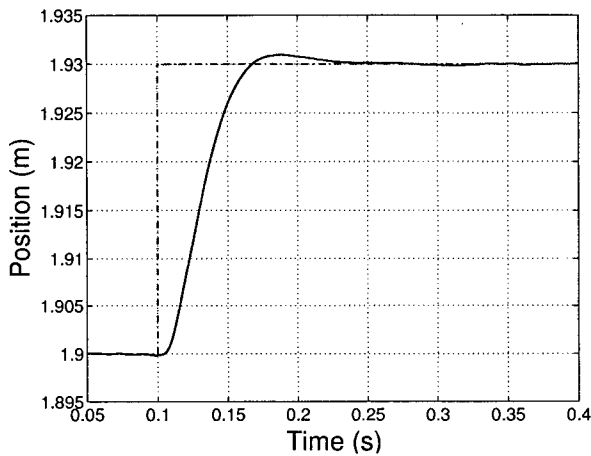


Figure 6.12: Position of the actuator (case 3).

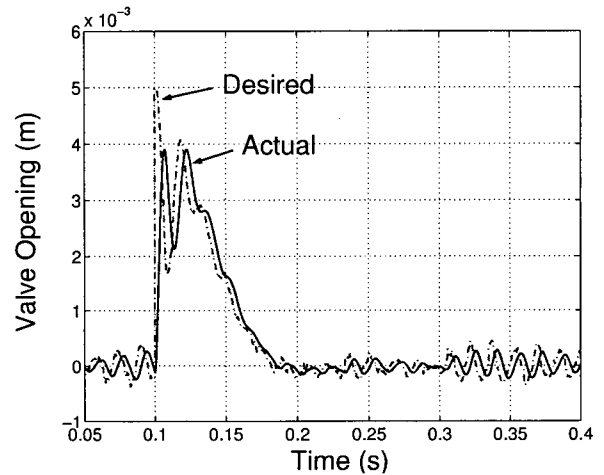


Figure 6.13: Control command (case 3).

6.6.4 Case 4: Effect of change in time horizon

Optimization was performed with the same parameters as in Cases 1&2 except that $t_f = 0.15$ sec in this case. Only SR1 was used to solve the problem and the outcomes follow

$$\begin{aligned}
 p_0 &= \begin{bmatrix} 3000 & 250 & 400 \end{bmatrix}^T & J_0 &= 65225 \\
 \hat{p} &= \begin{bmatrix} 2515.97 & 92.13 & 382.97 \end{bmatrix}^T & \hat{J} &= 39.432 \\
 t_{exc} &= 23.0s & k(\text{steps}) &= 36
 \end{aligned}$$

The system responses with the optimized gains are given in Figures 6.14-6.17. As it might have been expected, the system has a slower response (except for force errors) (Figures 6.14-6.16). Consequently, smaller valve openings are commanded during the transient (see Figures 6.7, 6.17).

6.6.5 Case 5: Effect of step length

To investigate the effect of the step length, $x_0 - x_d$, on the optimal gains, optimization was performed with a step length of 1cm as opposed to 3cm in the previous cases.

$$\begin{aligned}
 p_0 &= \begin{bmatrix} 3000 & 250 & 400 \end{bmatrix}^T & J_0 &= 26219 \\
 \hat{p} &= \begin{bmatrix} 4760.05 & 123.18 & 268.09 \end{bmatrix}^T & \hat{J} &= 14.35 \\
 t_{exc} &= 15.8s & k(\text{steps}) &= 35
 \end{aligned}$$

Interestingly, the optimal gains are almost the same as those obtained with a 3cm step. This suggests that the linear terms in the objective function, i.e. J_x , J_{t_f} and J_n dominate the nonlinear term J_u . This in fact turned out to be the case. For example, if one repeats the optimization in Case 1 without J_u included in the objective function, one would end up with the following optimal gains

$$\hat{p} = \begin{bmatrix} 4725.0 & 122.62 & 277.11 \end{bmatrix}^T \quad (6.44)$$

which are almost the same as those obtained when J_u was included. Several numerical experiments with different scenarios revealed that J_n can also play the role of J_u in many cases and prevent large control command so J_u could be removed from the objective function without significant change in the outcome. However, it turned out that J_u cannot replace J_n in the objective function.

6.7 Conclusions

In this chapter, the suboptimal control of hydraulic servo-systems was addressed. Instead of deriving the control law based on the optimality conditions, which is very difficult, a numerical approach was proposed. First, a simplified version of the nonlinear controller in Chapter 5 was derived by ignoring the valve dynamics and the parametric uncertainty. The resulting controller stabilizes the system and produces zero steady-state tracking errors. Then, the controller was parameterized in terms of the position, velocity and force feedback gains. A performance index

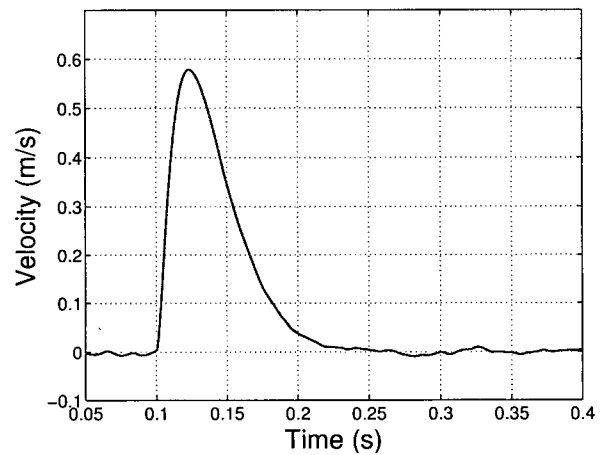
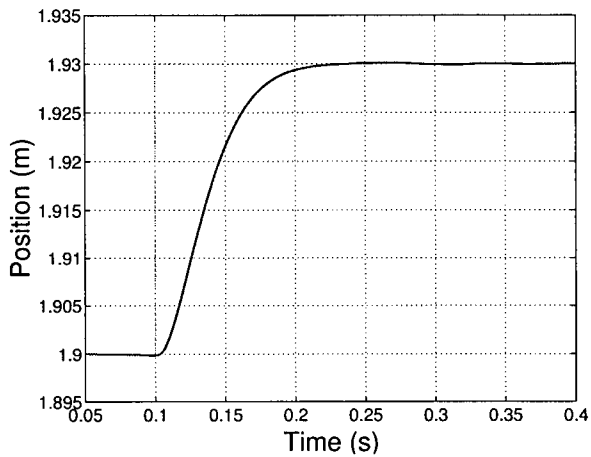


Figure 6.14: Position of the actuator (case 4).

Figure 6.15: Velocity of the actuator (case 4).

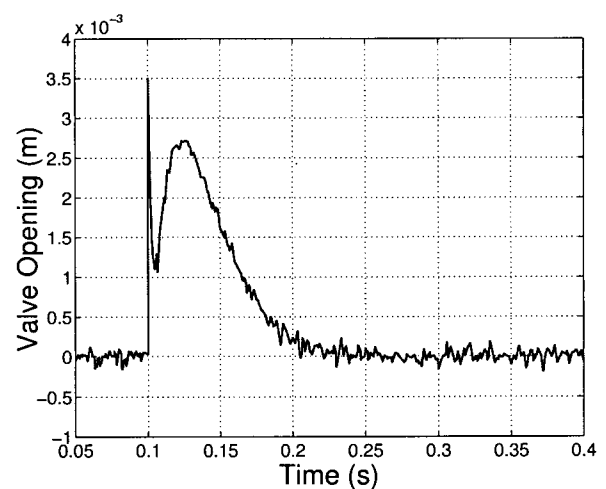
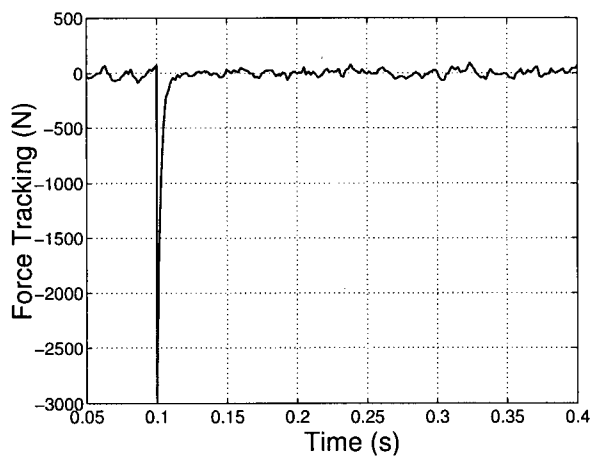


Figure 6.16: Force tracking of the actuator (case 4).

Figure 6.17: Control command (case 4).

was defined based on the transient response of the system to a position step input and also the steady state response to Gaussian measurement noise. The controller was successfully optimized with respect to the feedback gains using unconstrained optimization algorithms. Simulation studies demonstrated excellent responses for the controller with the optimized feedback gains. Interestingly, the optimized gains are comparable with their corresponding gains in Chapter 5 obtained through trial and error.

Chapter 7

Adaptive Nonlinear Control of Hydraulic Robots

7.1 Overview

The high performance control of single cylinder hydraulic actuators was addressed in Chapters 5 and 6 of this thesis. This chapter is concerned with the position control of robot manipulators driven by hydraulic actuators. In this chapter, the *backstepping* design methodology [60], [93] is adopted to develop a novel nonlinear controller for hydraulic manipulators. The method has become increasingly popular in the control community. For some recent applications of this method see [103], [25]. Both rigid body and actuator dynamics are incorporated into the design. The controller is also extended to compensate for parametric uncertainties in the system dynamics, including hydraulic and rigid body dynamics. Two types of observers are developed to avoid the use of acceleration feedback in the proposed adaptive control laws. The first observer is an extension of the passivity-based observers proposed in [11], to the case in which the system parameters are unknown. The concept of sliding observers [23] is also adopted to develop a robust acceleration observer. The tracking errors are proven to converge to zero asymptotically using Lyapunov analysis. It is shown that these errors remain bounded in the presence of Coulomb friction in the actuators. The bounds on the tracking errors are adjustable by the controller gains. To the best knowledge of the author, this is the first time that provably stable controllers are reported and evaluated for hydraulic robots.

The main differences between this work and the adaptive controller introduced in [16] (simultaneous to this work) are the following: (i) the adaptive controller / adaptive observer proposed here uses the same set of estimated rigid body parameters in the observer and controller, as opposed to the use of two distinct sets of parameter estimates and adaptation laws in [16]; and (ii) the introduction of an adaptive control method with a robust observer that is simpler to implement because it has reduced computational complexity. The form of the control laws and the observers are different from those of [16]. Position, velocity and hydraulic pressure measurements are required for the implementation of the proposed controllers.

The chapter is organized as follows. System dynamics, including rigid body and hydraulic dynamics are presented first. A nonlinear controller is proposed assuming that the dynamics are known exactly. Next, the adaptive control of hydraulic robots is addressed for the case in which the robot dynamics are subject to parametric uncertainty. Numerical simulations are performed to evaluate the proposed controllers and also to find proper control gains for experimentation. The proposed control laws are implemented on the UBC motion simulator and the results are presented here. The chapter ends with some concluding remarks.

7.2 Manipulator/Actuators Dynamics

The dynamics of a n -link robot with rigid links are governed by a second-order nonlinear differential equation

$$D(q)\ddot{q} + C(q, \dot{q})\dot{q} + G(q) = \tau \quad (7.1)$$

where $q \in R^n$ is a vector of generalized joint positions and $\tau \in R^n$ is a vector of generalized joint torques. $D(q) \in R^{n \times n}$ is the manipulator mass matrix, $C(q, \dot{q}) \in R^{n \times n}$ contains Coriolis and centripetal terms and $G(q) \in R^n$ represents gravitational effects. Unlike electrically driven manipulators, hydraulic robots exhibit significant nonlinear actuator dynamics. Assuming a three-way valve configuration, these dynamics can be written in the following form,

$$\dot{\tau} = f(q, \dot{q}) + g(q, \tau, u) \quad (7.2)$$

where u is the control command vector and f , g are nonlinear functions of q , \dot{q} and τ . The detailed expressions for f and g are given in Appendix B.

The matrices describing the rigid body dynamics in (7.1) satisfy the following properties [11]:

$$\begin{aligned}
(i) \quad & x^T \left(\dot{D}(q) - 2C(q, \dot{q}) \right) x = 0 \quad \forall x \in R^n \\
(ii) \quad & C(q, x)y = C(q, y)x \quad \forall q, x, y \in R^n \\
(iii) \quad & \exists D_m, D_M \text{ s.t. } 0 < D_m \leq \|D(q)\| \leq D_M < \infty \quad \forall q \in R^n \\
(iv) \quad & \exists C_M \text{ s.t. } \|C(q, x)\| \leq C_M \|x\| \quad \forall q, x \in R^n \\
(v) \quad & \exists G_M \text{ s.t. } \|G(q)\| \leq G_M \quad \forall q \in R^n
\end{aligned} \tag{7.3}$$

which are exploited in deriving the proposed control laws. According to (7.1) and (7.2), the overall actuator/manipulator dynamics are governed by a set of third-order nonlinear differential equations.

7.3 Nonadaptive Controller

In this section, the *backstepping* design methodology [60] is adopted to derive a nonlinear position tracking controller for hydraulic manipulators in the case in which the system parameters are known.

Theorem 1: Consider the system described by (7.1), (7.2) with the control law given by the solution u of the following algebraic equation:

$$g(q, \tau, u) = -f(q, \dot{q}) - \Gamma^{-1}s + \dot{\tau}_d - K_\tau \tilde{\tau} \tag{7.4}$$

and

$$\tau_d = D(q)\ddot{q}_r + C(q, \dot{q})\dot{q}_r + G(q) - K_p e - K_d s \tag{7.5}$$

with

$$\begin{aligned} e &= q - q_d, & \dot{q}_r &= \dot{q}_d - \Lambda e, \\ s &= \dot{q} - \dot{q}_r = \dot{e} + \Lambda e, & \tilde{\tau} &= \tau - \tau_d \end{aligned} \quad (7.6)$$

where K_p , K_d , K_τ , Γ and Λ are positive definite diagonal matrices, and $q_d \in R^n$ and $\dot{q}_d \in R^n$ are the desired joint position and velocity trajectories, respectively.

Then 0 is an exponentially stable equilibrium point of the state $\tilde{x} = \begin{bmatrix} e^T & s^T & \tilde{\tau}^T \end{bmatrix}^T$ of (7.1), (7.2), (7.4), (7.5).

Remark: From the expression of g from Appendix B, it can be seen that (7.4) can be easily solved for u .

Proof: Substituting (7.5) into (7.1) yields the following error dynamics,

$$D(q)\dot{s} + C(q, \dot{q})s + K_d s + K_p e = \tilde{\tau} \quad (7.7)$$

Note that the effect of actuator dynamics emerges as a non-zero $\tilde{\tau}$, as the controller reduces to a passivity-based controller [112] in the absence of actuator dynamics. Let V_1 be defined as

$$V_1 = \frac{1}{2}s^T D(q)s + \frac{1}{2}e^T K_p e \quad (7.8)$$

By taking the derivative of V_1 ,

$$\begin{aligned} \dot{V}_1 &= s^T D(q)\dot{s} + \frac{1}{2}s^T \dot{D}(q)s + e^T K_p \dot{e} \\ &= s^T [\tilde{\tau} - D(q)\dot{s} - C(q, \dot{q})s - K_d s - K_p e] + \frac{1}{2}s^T \dot{D}(q)s + e^T K_p (s - \Lambda e) \end{aligned} \quad (7.9)$$

Therefore, the derivative of V_1 along trajectories of the closed-loop system becomes

$$\dot{V}_1 = -s^T K_d s - e^T \Lambda K_p e + s^T \tilde{\tau} \quad (7.10)$$

where (7.7), (7.6) and the properties given in (7.3) have been used. Following the *backstepping*

methodology, V_2 , which is a Lyapunov function for the closed-loop system, is defined as

$$V_2 = V_1 + \frac{1}{2} \tilde{\tau}^T \Gamma \tilde{\tau} \quad (7.11)$$

with $\Gamma > 0$ diagonal. Note that:

$$\alpha_m \|\tilde{x}\|^2 < V_2 < \alpha_M \|\tilde{x}\|^2, \quad \alpha_m, \alpha_M > 0 \quad (7.12)$$

with

$$\alpha_m = \frac{1}{2} \min\{D_m, \underline{\sigma}(K_p), \underline{\sigma}(\Gamma)\} \quad (7.13)$$

$$\alpha_M = \frac{1}{2} \max\{D_M, \bar{\sigma}(K_p), \bar{\sigma}(\Gamma)\} \quad (7.14)$$

and $\underline{\sigma}(\cdot)$ and $\bar{\sigma}(\cdot)$ denote the minimum and maximum singular values, respectively. By taking the derivative of (7.11)

$$\dot{V}_2 = \dot{V}_1 + \tilde{\tau}^T \Gamma (\dot{\tau} - \dot{\tau}_d) = -s^T K_d s - e^T \Lambda K_p e + \tilde{\tau}^T \Gamma [\Gamma^{-1} s + f(q, \dot{q}) + g(q, \tau, u) - \dot{\tau}_d] \quad (7.15)$$

Using the control law (7.4), one can write

$$\dot{V}_2 = -s^T K_d s - e^T \Lambda K_p e - \tilde{\tau}^T \Gamma K_\tau \tilde{\tau} < -\beta \|\tilde{x}\|^2 \quad (7.16)$$

with $\beta > 0$. Therefore, the system is exponentially stable in the Lyapunov sense. This means that the position tracking error converges to zero exponentially. Furthermore, since $s = \dot{e} + \Lambda e$, the velocity tracking error is also exponentially stable. Note that in the realization of (7.4) one needs to compute $\dot{\tau}_d$ which is equal to

$$\dot{\tau}_d = \dot{D}(q) \ddot{q}_r + D(q) \ddot{\ddot{q}}_r + C(q, \dot{q}) \ddot{q}_r + \dot{C}(q, \dot{q}, \ddot{q}) \dot{q}_r + \dot{G}(q) - K_p \dot{e} - K_d \dot{s} \quad (7.17)$$

Since $\ddot{\ddot{q}}_r = \ddot{\ddot{q}}_d - \Lambda \ddot{e}$, $\dot{s} = \ddot{e} + \Lambda \dot{e}$ and \dot{C} are functions of \ddot{q} , link accelerations appear in the proposed control law. However, if τ is measured through pressure sensors, the link accelerations \ddot{q} can be obtained from position, velocity and pressure measurements and using the robot rigid

body model, i.e.,

$$\ddot{q} = D(q)^{-1} [\tau - C(q, \dot{q})\dot{q} - G(q)] \quad (7.18)$$

Thus q , \dot{q} and τ are required to implement the proposed control law which leads to exponentially stable tracking errors.

Remark: Since the system dynamics are fully known and the states are assumed to be measured, feedback linearization could also be used to derive a stabilizing controller.

7.4 Adaptive Controllers

The control law derived in the previous section requires full knowledge of the system parameters. However, the manipulator rigid body dynamics are uncertain and subject to changes, e.g., due to an unknown variable payload. It is also difficult to measure some of the manipulator's parameters. Moreover, the hydraulic parameters are usually unknown and time varying. In this section, the nonlinear controller proposed in the previous section is extended to compensate for parametric uncertainty in the system dynamics. To deal with uncertainties in rigid body dynamics, the linear parameterization of manipulator dynamics is used [112]:

$$D(q)\ddot{q} + C(q, \dot{q})\dot{q} + G(q) = Y(q, \dot{q}, \ddot{q})\theta \quad (7.19)$$

where $Y(q, \dot{q}, \ddot{q})$ is a regressor matrix and $\theta \in R^m$ is the vector of unknown parameters (see Appendix B). Similarly, as shown in Appendix B, the hydraulic dynamics (7.2) can be written as

$$\dot{\tau} = f_0(q, \dot{q})\gamma_1 + g_0(q, \tau, u)\gamma_2 \quad (7.20)$$

where $\gamma_1 = \begin{bmatrix} \gamma_1^1 & \dots & \gamma_1^n \end{bmatrix}^T$, $\gamma_2 = \begin{bmatrix} \gamma_2^1 & \dots & \gamma_2^n \end{bmatrix}^T$ are two sets of hydraulic parameters and f_0 , g_0 are defined as

$$\begin{aligned} f_0(q, \dot{q}) &= \text{diag}\{f_0^i(q^i, \dot{q}^i)\} \\ g_0(q, \tau, u) &= \text{diag}\{g_0^i(q^i, \tau^i, u^i)\} \end{aligned} \quad (7.21)$$

In the non-adaptive controller, (7.18) was used to compute joint accelerations from joint positions and velocities and hydraulic pressure measurements. This can not be done if $D(q)$, $C(q, \dot{q})$ and $G(q)$ are not known. To deal with this problem novel adaptive and robust observers are introduced. The following *Lemma* [141] will be used in the stability proofs.

Lemma 1: Consider the scalar function $\alpha = (\theta - \hat{\theta})^T (\rho - \hat{\rho})$, with $\theta, \hat{\theta}, \rho \in R^n$ and $a^i \leq \theta^i \leq b^i$. If $\hat{\theta} = \kappa(a, b, \rho)\rho$, where $\kappa(a, b, \rho)$ is a diagonal matrix with entries

$$\kappa^i(a, b, \rho) = \begin{cases} 0 & \text{if } \hat{\theta}^i \leq a^i, \rho^i \leq 0 \\ 0 & \text{if } \hat{\theta}^i \geq b^i, \rho^i \geq 0 \\ 1 & \text{otherwise} \end{cases} \quad (7.22)$$

then $\alpha \leq 0$.

7.4.1 Adaptive Controller/ Adaptive Observer

The first solution is an adaptive controller using an adaptive passivity-based observer. Before stating the result, the following notation must be defined:

$$\begin{aligned} \dot{q}_r &= \dot{q}_d - \Lambda_1(\hat{q} - q_d) = \dot{q}_d - \Lambda_1(e - \tilde{q}) \\ \dot{q}_o &= \dot{\hat{q}} - \Lambda_2(q - \hat{q}) = \dot{\hat{q}} - \Lambda_2\tilde{q} \\ s_1 &= \dot{q} - \dot{q}_r = \dot{e} + \Lambda_1(e - \tilde{q}) \\ s_2 &= \dot{q} - \dot{q}_o = \ddot{\hat{q}} + \Lambda_2\tilde{q} \end{aligned} \quad (7.23)$$

where $\hat{q} \in R^n$ is the estimated value of q , $e = q - q_d$, and $\tilde{q} = q - \hat{q}$ are position tracking and observation errors, respectively. $\Lambda_1, \Lambda_2 > 0$ are diagonal. Note that in the definitions of \dot{q}_r and

\dot{q}_o, \dot{q} has been replaced by \dot{q}_d and $\dot{\hat{q}}$. This will be shown to eliminate the need for acceleration feedback.

Theorem 2:

Consider the system described by (7.1), (7.2), the observer dynamics

$$\begin{aligned}\dot{\hat{q}} &= z + \Lambda_2 \tilde{q} \\ \dot{z} &= \hat{D}(q)^{-1} \left[\tau - \hat{C}(q, \dot{q}) \dot{q}_o - \hat{G}(q) + L_p \tilde{q} + K_d s_1 + K'_d s_2 \right]\end{aligned}\quad (7.24)$$

and the controller obtained by solving the following algebraic equation

$$g_0(q, \tau, u) \hat{\gamma}_2 = \dot{\tau}_d - f_0(q, \dot{q}) \hat{\gamma}_1 - \Gamma_\tau^{-1} s_1 - K_\tau \tilde{\tau} \quad (7.25)$$

where

$$\begin{aligned}\tau_d &= \hat{D}(q) \ddot{q}_r + \hat{C}(q, \dot{q}_r) \dot{q}_r + \hat{G}(q) - K_d (s_1 - s_2) - K_p e \\ &= Y_1(q, \dot{q}_r, \ddot{q}_r) \hat{\theta} - K_d (s_1 - s_2) - K_p e\end{aligned}\quad (7.26)$$

with unknown rigid body parameter adaptation law

$$\dot{\hat{\theta}} = -\kappa_\theta \Gamma^{-1} \left[Y_1^T(q, \dot{q}_r, \ddot{q}_r) s_1 + Y_2^T(q, \dot{q}, \dot{q}_o, \ddot{q}_o) s_2 \right] \quad (7.27)$$

where

$$\begin{aligned}Y_1(q, \dot{q}_r, \ddot{q}_r) \hat{\theta} &= \hat{D}(q) \ddot{q}_r + \hat{C}(q, \dot{q}_r) \dot{q}_r + \hat{G}(q) \\ Y_2(q, \dot{q}, \dot{q}_o, \ddot{q}_o) \hat{\theta} &= \hat{D}(q) \ddot{q}_o + \hat{C}(q, \dot{q}) \dot{q}_o + \hat{G}(q)\end{aligned}\quad (7.28)$$

and with hydraulic parameter adaptation law

$$\begin{aligned}\dot{\hat{\gamma}}_1 &= \kappa_{\gamma_1} \Gamma_{\gamma_1}^{-1} \Gamma_\tau f_0(q, \dot{q}) \tilde{\tau} \\ \dot{\hat{\gamma}}_2 &= \kappa_{\gamma_2} \Gamma_{\gamma_2}^{-1} \Gamma_\tau \Pi\left(\frac{\tilde{\tau}}{\hat{\gamma}_2}\right) (\dot{\tau}_d - f_0(q, \dot{q}) \hat{\gamma}_1 - \Gamma_\tau^{-1} s_1 - K_\tau \tilde{\tau})\end{aligned}\quad (7.29)$$

where $\Pi\left(\frac{\tilde{\tau}}{\hat{\gamma}_2}\right) = \text{diag}\left\{\frac{\tilde{\tau}^i}{\hat{\gamma}_2^i}\right\}$. Then, if the conditions given below in (7.30) are satisfied, $\underline{0}$ is an

asymptotically stable equilibrium point of the state $\tilde{x} = \begin{bmatrix} e^T & \tilde{q}^T & s_1^T & s_2^T & \tilde{\tau}^T \end{bmatrix}^T$.

$$\begin{aligned}
(a) \quad & \underline{\sigma}(K_p)\underline{\sigma}(L_p)\underline{\sigma}(\Lambda_1)\underline{\sigma}(\Lambda_2) > \frac{1}{4}\bar{\sigma}^2(K_p)\bar{\sigma}^2(\Lambda_1) \\
(b) \quad & \underline{\sigma}(K_d) > C_M\dot{q}_{dm} \\
(c) \quad & \frac{\alpha_m}{3} \left(\frac{\underline{\sigma}(K_d) - C_M\dot{q}_{dm}}{C_M\bar{\sigma}(\Lambda_1)} \right)^2 > V_{pM} - V_{pm} \\
(d) \quad & \|\tilde{x}(0)\| \leq \sqrt{\frac{\alpha_m}{3\alpha_M} \left(\frac{\underline{\sigma}(K_d) - C_M\dot{q}_{dm}}{C_M\bar{\sigma}(\Lambda_1)} \right)^2 - \frac{V_{pM} - V_{pm}}{\alpha_M}}
\end{aligned} \tag{7.30}$$

where

$$\begin{aligned}
\alpha_m &= \frac{1}{2} \min\{D_m, \underline{\sigma}(K_p), \underline{\sigma}(L_p), \underline{\sigma}(\Gamma_\tau)\} \\
\alpha_M &= \frac{1}{2} \max\{D_M, \bar{\sigma}(K_p), \bar{\sigma}(L_p), \bar{\sigma}(\Gamma_\tau)\} \\
V_{pm} &\leq \frac{1}{2} \left(\tilde{\theta}^T \Gamma \tilde{\theta} + \tilde{\gamma}_1^T \Gamma_{\gamma_1} \tilde{\gamma}_1 + \tilde{\gamma}_2^T \Gamma_{\gamma_2} \tilde{\gamma}_2 \right) \leq V_{pM}
\end{aligned} \tag{7.31}$$

Here, $\bar{\sigma}(\cdot)$ and $\underline{\sigma}(\cdot)$ denote the maximum and minimum singular values of their matrix argument, respectively, and \dot{q}_{dm} is an upper bound on the norm of the desired velocity. The projection gains κ_θ , κ_{γ_1} and κ_{γ_2} are defined as in (7.22). All of the gains used in the controller and observer, i.e., K_p , K_d , K'_d , L_p , Γ , Γ_{γ_1} , Γ_{γ_2} , Γ_τ , and K_τ are constant positive definite diagonal matrices.

Remark 1: In the above formulation, \hat{D} , \hat{C} and \hat{G} are the estimated dynamical matrices corresponding to $\hat{\theta}$. Note that the controller and observer use the same set of estimated parameters which compares favorably to the approach proposed in [16] in which different parameter estimates are employed in the controller and observer.

Remark 2: The use of projection gains κ in the adaptation laws guarantees that the estimate of each parameter remains in a predefined interval $[a, b]$. In particular, if $\hat{\gamma}_2^i$ becomes zero the control law u in (7.25) is undefined. This can be avoided by using $a^i > 0$ for the estimation of γ_2^i . Furthermore, the parameter estimates can not drift because of the upper and lower bounds on their values. Therefore, parameter adaptation is robust against unmodeled disturbances [141].

Proof : By substituting (7.26) into (7.1) the following error dynamics are obtained

$$D(q)\dot{s}_1 + C(q, \dot{q})s_1 + K_d s_1 + K_p e = K_d s_2 - C(q, s_1)(\dot{q} - s_1) - Y_1(q, \dot{q}_r, \ddot{q}_r)\tilde{\theta} + \tilde{\tau} \quad (7.32)$$

The observer closed-loop dynamics could also be written as

$$D(q)\dot{s}_2 + C(q, \dot{q})s_2 + K'_d s_2 + L_p \tilde{q} = -K_d s_1 - Y_2(q, \dot{q}, \dot{q}_o, \ddot{q}_o)\tilde{\theta} \quad (7.33)$$

where (7.1) and (7.24) have been used in deriving (7.33).

Now, let the Lyapunov-like function V_1 be defined as:

$$V_1 = \frac{1}{2}s_1^T D(q)s_1 + \frac{1}{2}e^T K_p e + \frac{1}{2}s_2^T D(q)s_2 + \frac{1}{2}\tilde{q}^T L_p \tilde{q} + \frac{1}{2}\tilde{\theta}^T \Gamma \tilde{\theta} \quad (7.34)$$

The derivative of V_1 along the trajectory of the closed loop system is then given by

$$\begin{aligned} \dot{V}_1 &= s_1^T \left[-C(q, \dot{q})s_1 - K_d s_1 - K_p e + K_d s_2 - C(q, s_1)(\dot{q} - s_1) - Y_1(q, \dot{q}_r, \ddot{q}_r)\tilde{\theta} + \tilde{\tau} \right] \\ &\quad + \frac{1}{2}s_1^T \dot{D}(q)s_1 + e^T K_p (s_1 - \Lambda_1 e + \Lambda_1 \tilde{q}) + s_2^T [-C(q, \dot{q})s_2 - K'_d s_2 - K_d s_1 - L_p \tilde{q} \\ &\quad - Y_2(q, \dot{q}, \dot{q}_o, \ddot{q}_o)\tilde{\theta}] + \tilde{q}^T L_p (s_2 - \Lambda_2 \tilde{q}) + \frac{1}{2}s_2^T \dot{D}(q)s_2 + \tilde{\theta}^T \Gamma \dot{\tilde{\theta}} \\ &= -s_1^T K_d s_1 - s_2^T K'_d s_2 - e^T K_p \Lambda_1 e - \tilde{q}^T L_p \Lambda_2 \tilde{q} + e^T K_p \Lambda_1 \tilde{q} + s_1^T \tilde{\tau} + \tilde{\theta}^T [-\Gamma \dot{\tilde{\theta}} - Y_1^T(q, \dot{q}_r, \ddot{q}_r)s_1 \\ &\quad - Y_2^T(q, \dot{q}, \dot{q}_o, \ddot{q}_o)s_2] - s_1^T C(q, s_1)(\dot{q} - s_1) \end{aligned} \quad (7.35)$$

With the adaptation law given in (7.27) and using *Lemma 1*, we have that

$$\begin{aligned} \dot{V}_1 &\leq -s_1^T K_d s_1 - s_2^T K'_d s_2 - e^T K_p \Lambda_1 e - \tilde{q}^T L_p \Lambda_2 \tilde{q} + e^T K_p \Lambda_1 \tilde{q} + s_1^T \tilde{\tau} - s_1^T C(q, s_1)(\dot{q}_d - \Lambda_1 e + \Lambda_1 \tilde{q}) \\ &\leq -(\underline{\sigma}(K_d) - C_M(\dot{q}_{dm} + \bar{\sigma}(\Lambda_1)\|e\| + \bar{\sigma}(\Lambda_1)\|\tilde{q}\|))\|s_1\|^2 - \underline{\sigma}(K'_d)\|s_2\|^2 - \underline{\sigma}(K_p)\underline{\sigma}(\Lambda_1)\|e\|^2 \\ &\quad - \underline{\sigma}(L_p)\underline{\sigma}(\Lambda_2)\|\tilde{q}\|^2 + \bar{\sigma}(K_p)\bar{\sigma}(\Lambda_1)\|e\|\|\tilde{q}\| + s_1^T \tilde{\tau} \\ &= H(\|e\|, \|\tilde{q}\|, \|s_1\|, \|s_2\|) + s_1^T \tilde{\tau} \end{aligned} \quad (7.36)$$

Note that since

$$\begin{aligned}
& -\underline{\sigma}(K_p)\underline{\sigma}(\Lambda_1)\|e\|^2 - \underline{\sigma}(L_p)\underline{\sigma}(\Lambda_2)\|\tilde{q}\|^2 + \bar{\sigma}(K_p)\bar{\sigma}(\Lambda_1)\|e\|\|\tilde{q}\| \\
& = - \begin{bmatrix} \|e\| & \|\tilde{q}\| \end{bmatrix} \begin{bmatrix} \underline{\sigma}(K_p)\underline{\sigma}(\Lambda_1) & -\frac{1}{2}\bar{\sigma}(K_p)\bar{\sigma}(\Lambda_1) \\ -\frac{1}{2}\bar{\sigma}(K_p)\bar{\sigma}(\Lambda_1) & \underline{\sigma}(L_p)\underline{\sigma}(\Lambda_2) \end{bmatrix} \begin{bmatrix} \|e\| \\ \|\tilde{q}\| \end{bmatrix} \quad (7.37)
\end{aligned}$$

the condition given in (7.30.a) and the inequality

$$\|e\| + \|\tilde{q}\| < \frac{\underline{\sigma}(K_d) - C_M \dot{q}_{dm}}{C_M \bar{\sigma}(\Lambda_1)} \quad (7.38)$$

guarantee that

$$H(\|e\|, \|\tilde{q}\|, \|s_1\|, \|s_2\|) \leq -\alpha(\|e\|^2 + \|\tilde{q}\|^2 + \|s_1\|^2 + \|s_2\|^2) \quad (7.39)$$

with $\alpha > 0$. (7.38) enforces (7.30.b), i.e.

$$\underline{\sigma}(K_d) > C_M \dot{q}_{dm} \quad (7.40)$$

Note that

$$\|e\| + \|q\| \leq \sqrt{3}\|\tilde{x}\| \quad (7.41)$$

Also from

$$\alpha_m \|\tilde{x}\|^2 + V_{p_m} \leq V_2 \leq \alpha_M \|\tilde{x}\|^2 + V_{p_M} \quad (7.42)$$

where V_2 will be defined shortly, and assuming $\dot{V}_2 < 0$, we have that

$$\|\tilde{x}\| \leq \sqrt{\frac{\alpha_M}{\alpha_m} \|x(0)\|^2 + \frac{V_{p_M} - V_{p_m}}{\alpha_m}} \quad (7.43)$$

This along with (7.38) and (7.41) lead to the conditions given in (7.30.c) and (7.30.d).

Following the backstepping approach, V_2 , which is a Lyapunov function for the system

dynamics, is defined as

$$V_2 = V_1 + \frac{1}{2}\tilde{\tau}^T\Gamma_\tau\tilde{\tau} + \frac{1}{2}\tilde{\gamma}_1^T\Gamma_{\gamma_1}\tilde{\gamma}_1 + \frac{1}{2}\tilde{\gamma}_2^T\Gamma_{\gamma_2}\tilde{\gamma}_2 \quad (7.44)$$

where $\tilde{\gamma}_1 = \begin{bmatrix} \tilde{\gamma}_1^1 & \dots & \tilde{\gamma}_1^n \end{bmatrix}^T$ and $\tilde{\gamma}_2 = \begin{bmatrix} \tilde{\gamma}_2^1 & \dots & \tilde{\gamma}_2^n \end{bmatrix}^T$ are the vectors of hydraulic parameter errors. By taking the derivative of (7.44)

$$\begin{aligned} \dot{V}_2 &= \dot{V}_1 + \tilde{\tau}^T\Gamma_\tau [f_0(q, \dot{q})\gamma_1 + g_0(q, \tau, u)\gamma_2 - \dot{\tau}_d] + \tilde{\gamma}_1^T\Gamma_{\gamma_1}\dot{\tilde{\gamma}}_1 + \tilde{\gamma}_2^T\Gamma_{\gamma_2}\dot{\tilde{\gamma}}_2 \\ &\leq H(\|e\|, \|\tilde{q}\|, \|s_1\|, \|s_2\|) + \tilde{\tau}^T\Gamma_\tau[\Gamma_\tau^{-1}s_1 + f_0(q, \dot{q})\gamma_1 + g_0(q, \tau, u)\gamma_2 - \dot{\tau}_d] \\ &\quad - \tilde{\gamma}_1^T\Gamma_{\gamma_1}\dot{\hat{\gamma}}_1 - \tilde{\gamma}_2^T\Gamma_{\gamma_2}\dot{\hat{\gamma}}_2 \end{aligned} \quad (7.45)$$

By employing the control law given in (7.25), one can show after some manipulation that

$$\begin{aligned} \dot{V}_2 &\leq H(\|e\|, \|\tilde{q}\|, \|s_1\|, \|s_2\|) - \tilde{\tau}^T\Gamma_\tau K_\tau \tilde{\tau} + \tilde{\gamma}_1^T \left[f_0(q, \dot{q})\Gamma_\tau \tilde{\tau} - \Gamma_{\gamma_1} \dot{\hat{\gamma}}_1 \right] \\ &\quad + \tilde{\gamma}_2^T \left[\Gamma_\tau \Pi\left(\frac{\tilde{\tau}}{\tilde{\gamma}_2}\right)(\dot{\tau}_d - f_0(q, \dot{q})\hat{\gamma}_1 - \Gamma_\tau^{-1}s_1 - K_\tau \tilde{\tau}) - \Gamma_{\gamma_2} \dot{\hat{\gamma}}_2 \right] \end{aligned} \quad (7.46)$$

Using the adaptation laws given in (7.29) and *Lemma 1*, the derivative of V_2 becomes

$$\dot{V}_2 \leq H(\|e\|, \|\tilde{q}\|, \|s_1\|, \|s_2\|) - \tilde{\tau}^T\Gamma_\tau K_\tau \tilde{\tau} \leq -\gamma(\|e\|^2 + \|\tilde{q}\|^2 + \|s_1\|^2 + \|s_2\|^2 + \|\tilde{\tau}\|^2) \quad (7.47)$$

Thus the position and velocity tracking errors converge to zero asymptotically.

Remark 1: for the parameter convergence the condition of persistency of excitation must be satisfied [112].

Remark 2: Inspection of (7.26) reveals that τ_d does not contain \dot{q} . This means that the acceleration term \ddot{q} does not appear in $\dot{\tau}_d$ and hence in the control law. This is achieved by the particular definition of \dot{q}_r in (7.23) and also by using $s_1 - s_2 = \dot{q}_o - \dot{q}_r$ instead of s_1 in (7.26). In summary, the proposed controller requires q , \dot{q} and τ to be measured.

Remark 3: In order to implement the observer proposed in (7.24), $\hat{D}^{-1}(q)$ must exist. This can be guaranteed by choosing proper bounds on the estimates of the rigid body parameters.

Remark 4: To guarantee the stability of the closed-loop system, the gains must satisfy the requirements given in (7.30.a)-(7.30.c). Furthermore, the initial tracking error must be within the

attraction region specified by (7.30).d and therefore the system is semiglobally asymptotically stable. The attraction region and can be enlarged by proper selection of the controller and the observer gains. While the controller is guaranteed to be stable, in practice the parameters should be tuned to achieve a desired performance.

Remark 5: The observer proposed here is an adaptive model based observer. It uses the model of rigid body dynamics and the input to this subsystem, τ , to estimate its states. However, since the model parameters are unknown, the adaptation laws have been proposed to cope with the uncertainty in the model.

7.4.2 Adaptive Controller/ Robust Observer

In this subsection, an adaptive/nonlinear controller utilizing a sliding type observer [23] is proposed that yields globally asymptotically stable tracking errors.

Before stating the result the following variables are defined:

$$\dot{q}_r = \dot{q}_d - \Lambda e, \quad s = \dot{q} - \dot{q}_r = \dot{e} + \Lambda e \quad (7.48)$$

where $\Lambda > 0$ is diagonal.

Theorem 3: Consider the system described by (7.1),(7.2) and the following observer:

$$\dot{z} = \Gamma_o \dot{\tilde{q}} + \Lambda_o \text{sgn}(\dot{\tilde{q}}) - W^T(q, \dot{q}_r, \hat{\theta})s + \ddot{\tilde{q}} \quad (7.49)$$

with

$$W(q, \dot{q}_r, \hat{\theta}) = -\hat{D}(q)\Lambda + \hat{C}(q, \dot{q}_r) - K_d \quad (7.50)$$

$$\ddot{\tilde{q}} = \bar{D}^{-1} [\tau - \bar{C}\dot{\tilde{q}} - \bar{G}] \quad (7.51)$$

where $z = \hat{q}$ is the observed velocity. \bar{D} , \bar{C} and \bar{G} are constant matrices (rough estimates of dynamical matrices). Let the control law be given by the solution u of the following algebraic

equation

$$g_0(q, \tau, u)\hat{\gamma}_2 = \dot{\tau}_d - f_0(q, \dot{q})\hat{\gamma}_1 - \Gamma_\tau^{-1}s - K_\tau\tilde{\tau} \quad (7.52)$$

where

$$\begin{aligned} \tau_d &= \hat{D}(q)(\ddot{q}_r + \Lambda\dot{\tilde{q}}) + \hat{C}(q, \dot{q})\dot{q}_r + \hat{G}(q) - K_d(s - \dot{\tilde{q}}) - K_p e \\ &= \hat{D}(q)\ddot{q}_r + \hat{C}(q, \dot{q})\dot{q}_r + \hat{G}(q) - K_d s - K_p e + \hat{D}(q)\Lambda\dot{\tilde{q}} - \hat{C}(q, \dot{q}_r)\dot{\tilde{q}} + K_d\dot{\tilde{q}} \end{aligned} \quad (7.53)$$

and let the adaptation laws be given by

$$\dot{\hat{\theta}} = -\kappa_\theta \Gamma_\theta^{-1} Y^T(q, \dot{q}, \dot{q}_r, \ddot{q}_r) s \quad (7.54)$$

and

$$\begin{aligned} \dot{\hat{\gamma}}_1 &= \kappa_{\gamma_1} \Gamma_1^{-1} \Gamma_\tau f_0(q, \dot{q}) \tilde{\tau} \\ \dot{\hat{\gamma}}_2 &= \kappa_{\gamma_2} \Gamma_2^{-1} \Gamma_\tau \Pi \left(\frac{\tilde{\tau}}{\hat{\gamma}_2} \right) (\dot{\tau}_d - f_0(q, \dot{q})\hat{\gamma}_1 - \Gamma_\tau^{-1}s - K_\tau\tilde{\tau}) \end{aligned} \quad (7.55)$$

for the rigid body and hydraulic parameters, respectively. Then, $\underline{0}$ is an asymptotically stable equilibrium point of the state $\tilde{x} = \begin{bmatrix} e^T & s^T & \dot{\tilde{q}}^T & \tilde{\tau}^T \end{bmatrix}^T$. In the above equations, K_p , K_d , Λ_o , Γ_θ , Γ_1 , Γ_2 , Γ_τ , and K_τ are positive definite diagonal matrices.

Remark : τ_d does not contain any velocity terms. This can be seen from:

$$\begin{aligned} \ddot{q}_r + \Lambda\dot{\tilde{q}} &= \ddot{q}_d - \Lambda(\dot{q} - \dot{q}_d) + \Lambda(\dot{q} - \dot{\tilde{q}}) = \ddot{q}_d - \Lambda(\dot{\tilde{q}} - \dot{q}_d) \\ s - \dot{\tilde{q}} &= \dot{q} - \dot{q}_r - \dot{q} + \dot{\tilde{q}} = \dot{\tilde{q}} - \dot{q}_r \end{aligned} \quad (7.56)$$

Proof: By substituting (7.53) into (7.1) the following closed loop dynamics are obtained

$$D(q)\dot{s} + C(q, \dot{q})s + K_d s + K_p e = -Y(q, \dot{q}, \dot{q}_r, \ddot{q}_r)\tilde{\theta} - W(q, \dot{q}_r, \hat{\theta})\dot{\tilde{q}} + \tilde{\tau} \quad (7.57)$$

Define the Lyapunov-like function V_1 to be

$$V_1 = \frac{1}{2}e^T K_p e + \frac{1}{2}s^T D(q)s + \frac{1}{2}\dot{\tilde{q}}^T \tilde{q} + \frac{1}{2}\tilde{\theta}^T \Gamma_\theta \tilde{\theta} \quad (7.58)$$

The derivative of V_1 becomes

$$\begin{aligned} \dot{V}_1 = s^T & \left[-Y(q, \dot{q}, \dot{q}_r, \ddot{q}_r)\tilde{\theta} - W(q, \dot{q}_r, \hat{\theta})\dot{\tilde{q}} - C(q, \dot{q})s - K_d s - K_p e + \tilde{\tau} \right] \\ & + \frac{1}{2}s^T \dot{D}(q)s + e^T K_p (s - \Lambda e) + \dot{\tilde{q}}^T \left[\ddot{\tilde{q}} - \Gamma_o \dot{\tilde{q}} - \Lambda_o \text{sgn}(\dot{\tilde{q}}) + W^T(q, \dot{q}_r, \hat{\theta})s - \ddot{\tilde{q}} \right] + \tilde{\theta}^T \Gamma_\theta \dot{\tilde{\theta}} \end{aligned} \quad (7.59)$$

which can be written in the following form:

$$\dot{V}_1 = -s^T K_d s - e^T K_p \Lambda e - \dot{\tilde{q}}^T \Gamma_o \dot{\tilde{q}} - \dot{\tilde{q}}^T \left[\ddot{\tilde{q}} - \ddot{\tilde{q}} + \Lambda_o \text{sgn}(\dot{\tilde{q}}) \right] + \tilde{\theta}^T \left[\Gamma_\theta \dot{\tilde{\theta}} - Y^T(q, \dot{q}, \dot{q}_r, \ddot{q}_r)s \right] + s^T \tilde{\tau} \quad (7.60)$$

With the adaptation law given in (7.54), \dot{V}_1 becomes

$$\dot{V}_1 = -s^T K_d s - e^T K_p \Lambda e - \dot{\tilde{q}}^T \Gamma_o \dot{\tilde{q}} + \Sigma + s^T \tilde{\tau} \quad (7.61)$$

where $\Sigma = -\dot{\tilde{q}}^T \left[\ddot{\tilde{q}} - \ddot{\tilde{q}} + \Lambda_o \text{sgn}(\dot{\tilde{q}}) \right]$. Note that

$$\ddot{\tilde{q}} - \ddot{\tilde{q}} = [\bar{D}^{-1} - D^{-1}(q)] \tau - \bar{D}^{-1} [\bar{C} - C(q, \dot{q})] \dot{q} - \bar{D}^{-1} [\bar{G} - G(q)] \quad (7.62)$$

Therefore, $\|\ddot{\tilde{q}} - \ddot{\tilde{q}}\|$ is bounded above by

$$\|\ddot{\tilde{q}} - \ddot{\tilde{q}}\| \leq \sigma_0 + \sigma_1 \|\dot{q}\|^2 + \sigma_2 \|\tau\| + \sigma_3 \|\dot{q}\|. \quad (7.63)$$

with $\sigma_i > 0$. The properties given in (7.3) have been exploited in deriving (7.63). The following choice of Λ_o makes $\Sigma < 0$

$$\Lambda_o = \text{diag}\{\Lambda_o^i\} \quad (7.64)$$

$$\Lambda_o^i = \lambda_0^i + \lambda_1^i \|\dot{q}\|^2 + \lambda_2^i \|\tau\| + \lambda_3^i \|\dot{q}\| \quad (7.65)$$

and $\lambda_k^i > \sigma_k$ for $i = 1, \dots, n$, $k = 0, \dots, 3$. The rest of the proof is the same as before and will not be presented here.

Note that there are no limitations on the norms of the initial state tracking errors in this approach. However, chattering phenomena which are inherent in sliding mode systems can affect the stability. For example, if high frequency dynamics (e.g. valve dynamics) are excited, instability could result. The problem could be solved by using a piecewise linear approximation to $\text{sgn}(\cdot)$.

Remark: The observer proposed in (7.49), (7.50) and (7.51) is a robust model based observer. It employs a rough model of the rigid body dynamics and the input to these dynamics, τ , to calculate a rough estimate of acceleration used in (7.49). The switching term in (7.49) compensates for the error due to the uncertainty in the rigid body dynamics.

7.4.3 Effect of Friction

In the controllers proposed in this chapter, friction in the hydraulic actuators has been neglected. It is easy to handle viscous friction because it behaves as additional damping in the system. In the presence of Coulomb friction one may write (for the second controller/observer):

$$\dot{V}_2 \leq -\alpha \|\tilde{x}\|^2 + \|\tilde{x}\| \tau_{fm} \quad (7.66)$$

where τ_{fm} is an upper bound for the Coulomb friction. Note that

$$\|\tilde{x}\| > \frac{\tau_{fm}}{\alpha} = R_0 \Rightarrow \dot{V}_2 < 0 \quad (7.67)$$

Using (7.67) and considering the fact that

$$\beta_m \|\tilde{x}\|^2 + V_m \leq V_2 \leq \beta_M \|\tilde{x}\|^2 + V_M \quad (7.68)$$

one can show that the tracking errors are bounded by

$$\|\tilde{x}\| \leq \sqrt{\frac{\beta_M R_0^2 + V_M - V_m}{\beta_m}} = R \quad (7.69)$$

Table 7.1: The parameters used in the simulations

Hydraulic Parameters				
Parameter	A (m ²)	a (m ²)	L (m)	P_s (psi)
Value	1.14×10^{-3}	6.33×10^{-4}	1.37 m	1500
Parameter	d (m)	c	β (Mpa)	–
Value	55.4×10^{-6}	1.5×10^{-4}	700	–
Rigid Body Parameters				
Parameter	M_p (kg)	I_x (kg.m ²)	I_y (kg.m ²)	I_z (kg.m ²)
Value	250	45	45	43

Clearly, the error bound can be adjusted by the controller gains. The first controller/observer can be treated similarly and this will not be discussed here.

7.5 Simulation Results

Simulations have been performed to investigate the effectiveness of the proposed controllers and obtain guidelines for experimentation. For this purpose, a realistic model of the experimental setup, a hydraulic Stewart-type platform, has been used (see Appendix B). The system parameters were selected based upon their actual values and are given in Table 7.1.

In the simulations and experiments conducted in this thesis, a task-space control strategy has been followed. The advantage of this approach is that the dynamical matrices have simpler forms in these coordinates for parallel manipulators such as the Stewart platform. However, the forward kinematics problem must be solved on-line to convert the measured link positions to robot positions in task-space coordinates. Newton's method was utilized for this purpose (see Appendix B). The control algorithms and the robot dynamics were all implemented using the *MatlabTM Simulink Toolbox*. The implementation block diagram of the controllers are shown in Figures 7.5, 7.6.

The system parameters were initially set to values different from those used in the model to investigate the ability of the controllers to cope with parametric uncertainties. The reference trajectory was chosen to be $x_d = 0.02 \sin(2\pi t) + 0.01 \sin(4\pi t) + 0.01 \sin(6\pi t)$, $y_d = 0$, $z_d = 0.02 \sin(2\pi t) + 0.01 \sin(4\pi t)$, $\psi_d = 0.0873 \sin(2\pi t) + 0.0349 \sin(4\pi t)$, $\theta_d = 0.0524 \sin(2\pi t) +$

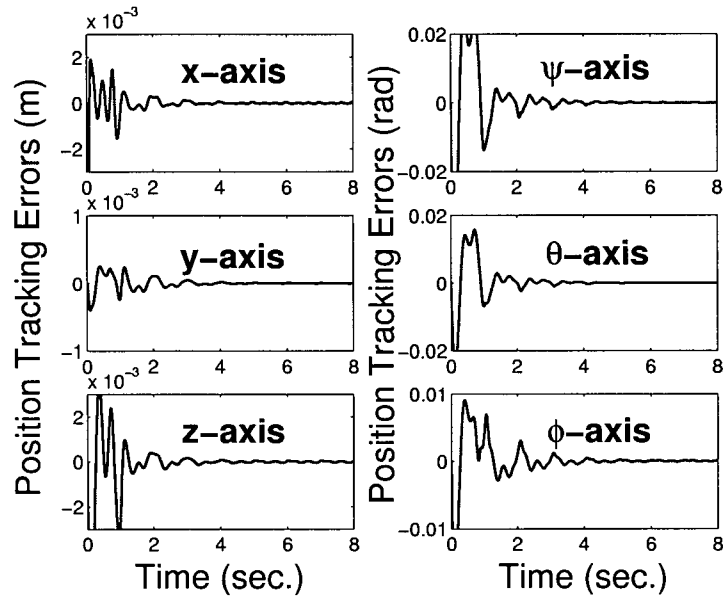


Figure 7.1: Position tracking errors for the controller with robust observer (simulation).

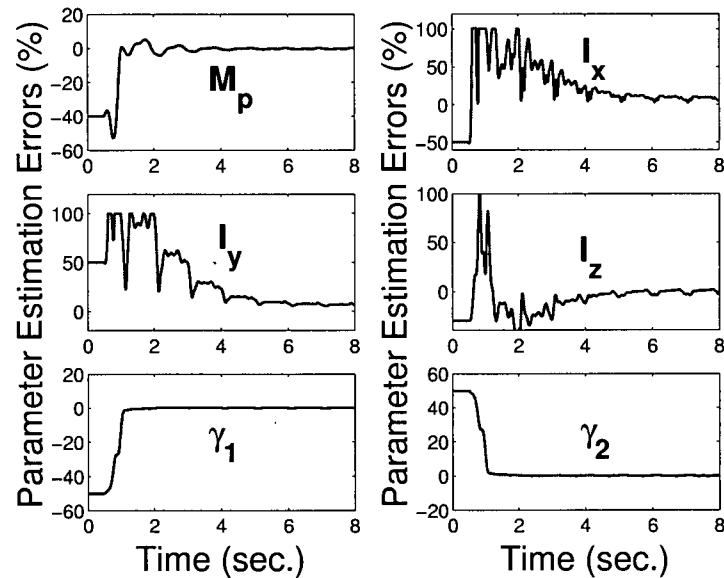


Figure 7.2: Parameter estimation errors for the controller with robust observer (simulation).

$0.0175 \sin(4\pi t)$, $\phi_d = 0.0524 \sin(2\pi t) + 0.0175 \sin(4\pi t)$. Positions and angles are expressed in meters and radians, respectively. The tracking errors clearly converge to zero in all coordinates for both controllers as shown in Figures 7.1 and 7.3, respectively. The profiles of the parameter estimates are given in Figures 7.2 and 7.4. The parameter adaptation laws were activated after

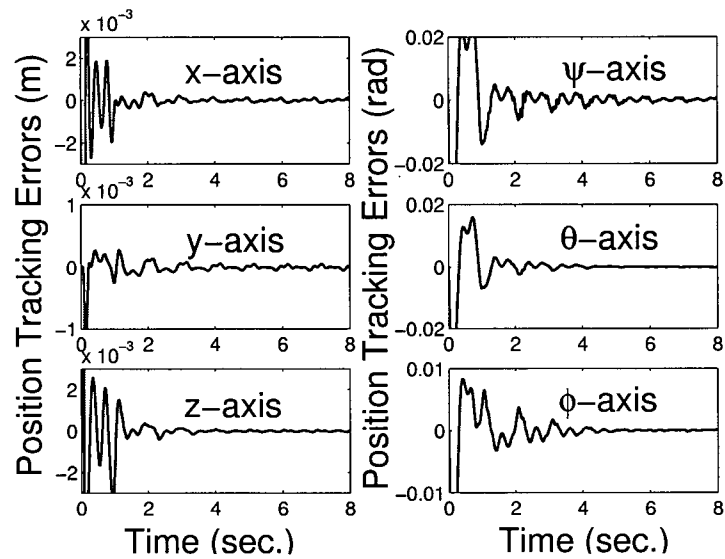


Figure 7.3: Position tracking errors for the controller with adaptive observer (simulation).

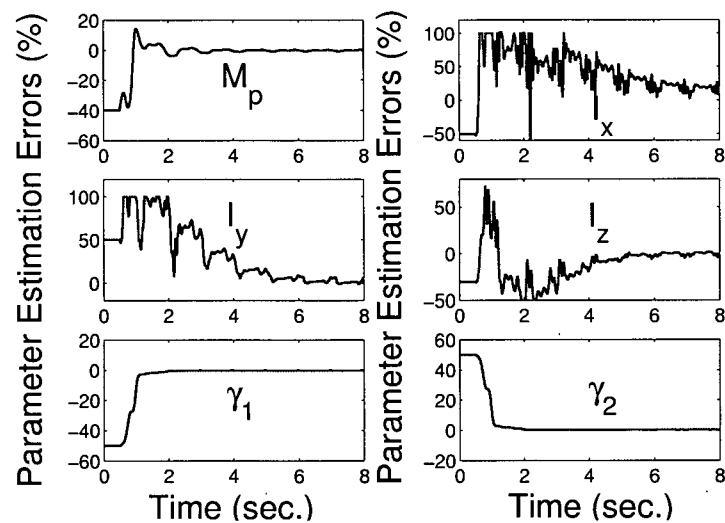


Figure 7.4: Parameter estimation errors for the controller with adaptive observer (simulation).

$t = 0.5$ s. Both rigid body and hydraulic parameters converge to their actual values even though the parameter convergence is not guaranteed in theory. The estimates of I_x, I_y reach their boundaries during some periods of the simulation as seen in Figures 7.2, 7.4.

In summary, the controller with the robust observer compares favorably to the one with adaptive observer since it requires fewer computations and performs similarly.

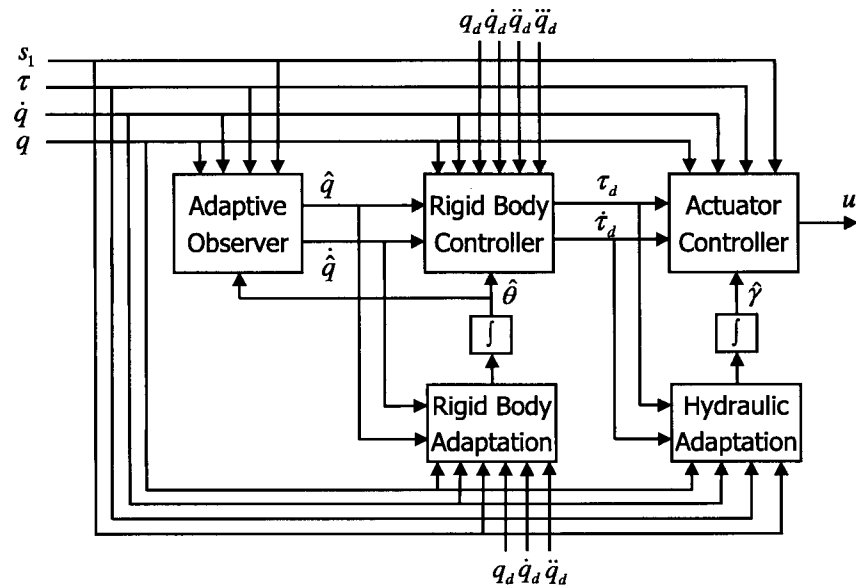


Figure 7.5: Controller with adaptive observer.

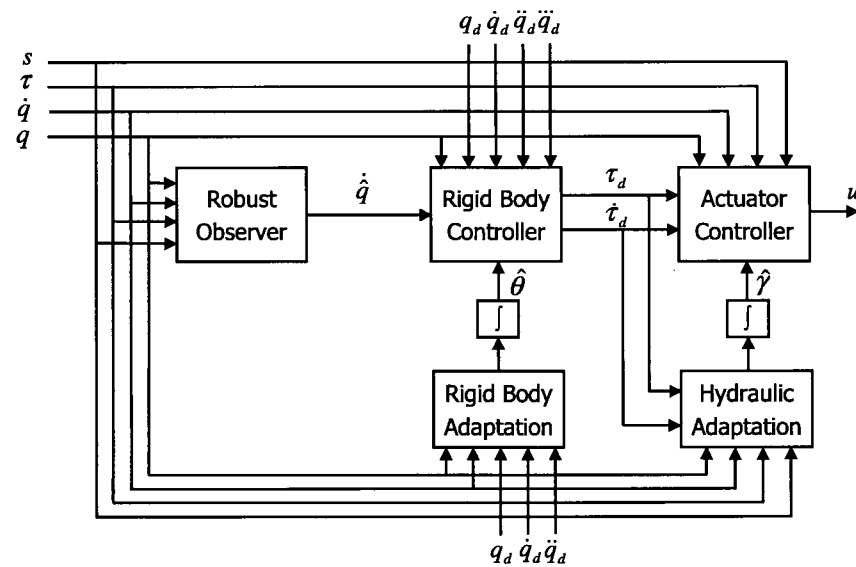


Figure 7.6: Controller with robust observer.

7.6 Experimental Results

The proposed control methods were experimentally evaluated using the University of British Columbia motion simulator [99] (see Figure 7.7). This simulator is driven by six hydraulic cylinders. Each cylinder is capable of exerting forces in excess of 4000 N at 1 m/s, and over 8000 N at zero rod speed. The hydraulic actuation system is equipped with *Rexroth 4WRDE*

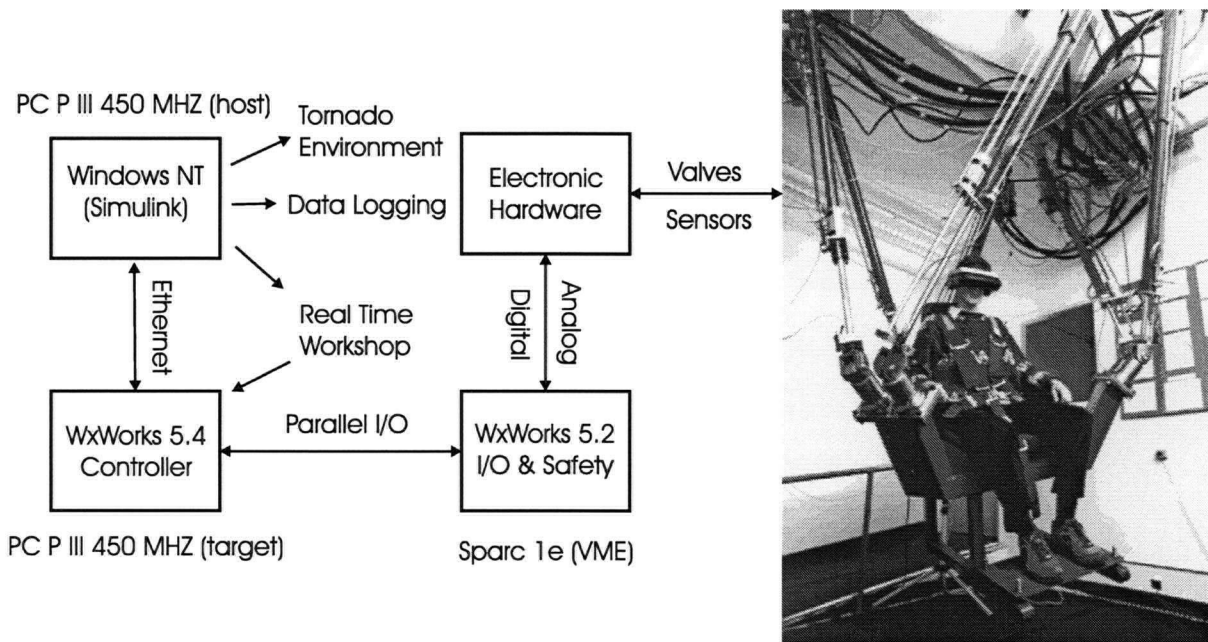


Figure 7.7: The experimental setup.

three-stage proportional valves connected in a three-way configuration. Low friction Teflon seals are used in the hydraulic cylinders. The installed sensors measure the actuator lengths, the valve spool positions, and the pressures both in the control and supply sides of the cylinders. High bandwidth valves with a bandwidth around 50 – 80Hz have been used in the setup so the dynamics of the valves may be ignored. The actuator velocities which are required in the control laws are estimated from the measured actuator lengths using fixed gain Kalman filters. Off-line experiments were performed to identify the initial values of the parameter estimates.

The computational setup was a PC running *VxWorksTM 5.4* and a Sparc 1e board running *VxWorksTM 5.2* (see Figure 7.7). The Sparc 1e performs the I/O and safety functions and the controller runs on the PC. The controller was implemented using the *Matlab Real Time WorkshopTM* toolbox targeting *TornadoTM 2.0*. Data between the PC and the VME board are communicated through a custom parallel I/O communication protocol. Using this setup a control frequency of 512 Hz was successfully achieved. The same controller block used in the simulation studies was utilized to control the platform.

Only the results of the experiments with adaptive controller/robust observer are presented here while similar performance was observed for the other controller. Figure 7.8 shows the

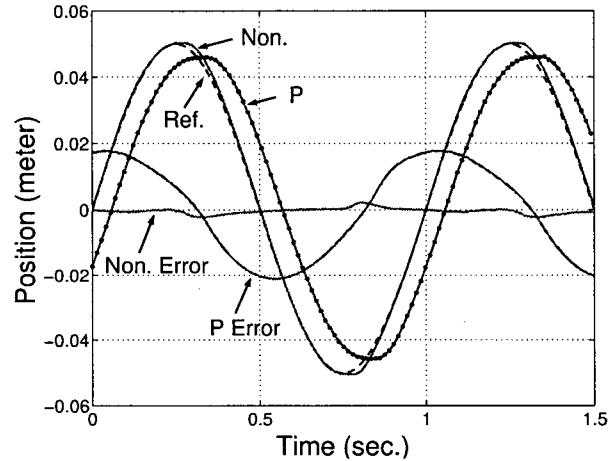


Figure 7.8: Position tracking (1Hz) along z coordinate (experiment).

tracking behavior of the nonlinear controller compared with that of a well-tuned P controller in tracking the reference trajectory $z_d = -2.34 + 0.05 \sin(2\pi t)$ m (the bias is not shown). The maximum tracking errors are 4% and 43% for the nonlinear and P controller, respectively. The response of the system to a 2Hz reference trajectory was also examined and is presented in Figure 7.9. In this case $z_d = -2.34 + 0.02 \sin(4\pi t)$ m whereas the maximum tracking errors are 14% and 69%. Similar results were obtained in the other coordinates. For example, Figure 7.10 shows the tracking results along the ψ axis where $\psi_d = 0.09 \sin(2\pi t)$ rad with 4% and 41% maximum tracking error for the nonlinear and P controller, respectively. Figure 7.11 demonstrates the tracking result when $\theta_d = 0.09 \sin(2\pi t)$. In all of these cases the proposed adaptive nonlinear controller clearly outperforms the well-tuned P controller and exhibits excellent tracking performance. Note that due to the friction in the actuators, tracking errors do not converge to zero but remain bounded as claimed earlier.

During the experiments, the estimated parameters did not converge to fixed values, contrary to what was observed in the simulations. Friction is an important factor which could introduce tracking errors and prevent the parameters from converging. The proposed controllers may be interpreted as cascade combinations of passivity-based position controllers and actuator force controllers. The very stiff dynamics of hydraulic actuators make the force (pressure) control loop sensitive to velocity estimation errors (or velocity measurement noise) and pressure measurement noise. This limits the level of the pressure feedback gains and may deteriorate force tracking and subsequently parameter estimation, especially for the hydraulic parameters. Other

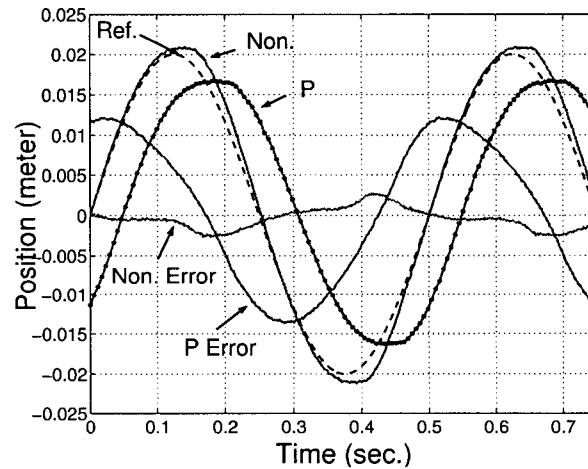


Figure 7.9: Position tracking (2Hz) along z coordinate (experiment).

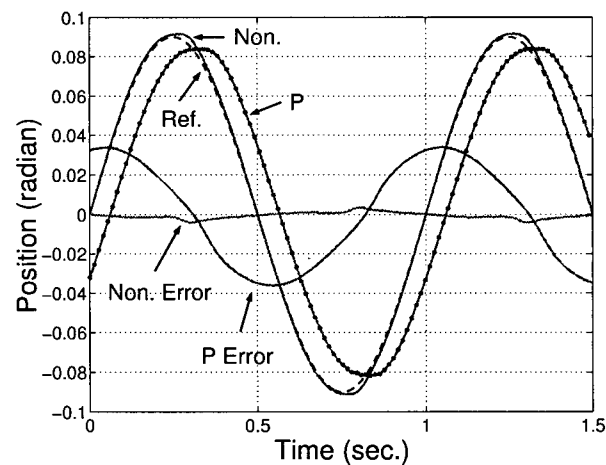


Figure 7.10: Position tracking (1Hz) along ψ coordinate (experiment).

factors such as unmodeled dynamics, e.g. valve and leg dynamics, and insufficient excitation could also prevent parameter convergence. Moreover, it should be stressed that the parameter convergence is not even guaranteed in theory, so the experimental results do not contradict the theoretical arguments. The adaptation was found to be helpful in improving the tracking performance. The projection gains used in the adaptation laws proved effective in preventing the large parameter swings that can occur especially during start-up transients. The step response of the controller along the z axis is also compared with that of the P controller in Figure 7.12. As it can be seen, the nonlinear controller exhibits a much faster response with some overshoot.

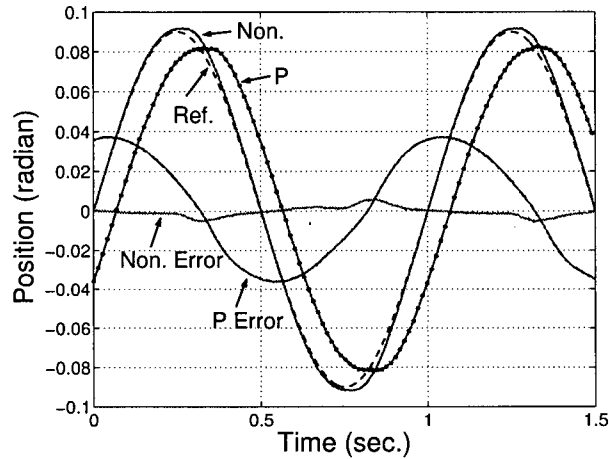


Figure 7.11: Position tracking (1Hz) along θ coordinate (experiment).

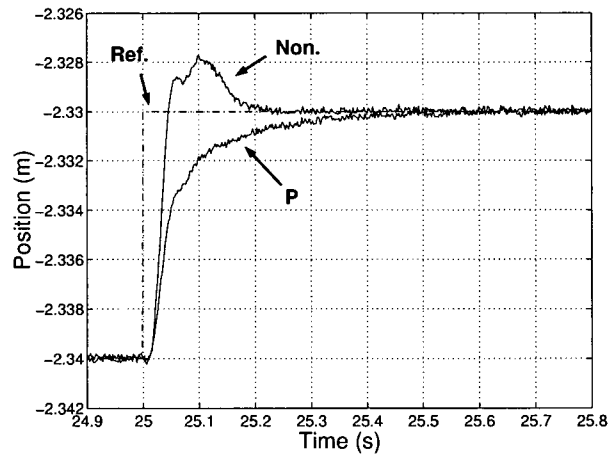


Figure 7.12: Step response along z coordinate (experiment).

7.7 Conclusions

This chapter addressed the control problem of hydraulically driven manipulators. The nonlinear dominant actuator dynamics prevent the use of standard robot control methods. In fact, inclusion of actuator dynamics in the design is of critical importance in hydraulic robots. While most of the reported work in the literature considers the control of single-rod hydraulic actuators, this research proposed novel nonlinear controllers for hydraulic manipulators using *backstepping*. A realistic model of the system was utilized in developing these Lyapunov-based controllers. To deal with parameter uncertainties, the controllers were augmented with adaptation laws. The need for acceleration feedback was eliminated by proposing adaptive and sliding-type observers.

Parameter drift was avoided using projection gains. Simulations and experiments were carried out with a hydraulic Stewart platform to investigate the effectiveness of these approaches. The results demonstrated excellent position tracking behavior and satisfactory transient responses for these new controllers. The controllers proposed here can be applied to a broad class of hydraulic robots, i.e. serial, parallel, and hybrid manipulators.

Chapter 8

Conclusions

In this chapter, the results of the thesis and its contributions are summarized. Some recommendations for future work are also made.

8.1 Thesis Contributions

This thesis is concerned with the modeling, analysis, design and evaluation of controllers for teleoperation/manual control systems with movable bases using a hydraulic motion simulator. The contributions of the thesis can be classified as follows.

1. **Modeling and Analysis of Teleoperation/Manual Control Systems with Movable Bases:** A framework for modeling and analysis of teleoperation/manual control systems with movable bases was proposed. A modified four-channel teleoperation control architecture was introduced that considers the base motion. This model was refined using results from conventional manual control systems. The resulting model places the analysis and design of teleoperation systems and that of manual control systems into a unified framework. The stability of typical two-channel and four-channel teleoperation architectures in the presence of biodynamic feedthrough was investigated using this framework.
2. **Design of Controllers for Teleoperation/Manual Control Systems with Movable Bases:** The performance and the stability of teleoperation/manual control systems with movable bases can be degraded by biodynamic interferences. This thesis addressed

the design of controllers for such systems. A novel approach was proposed that robustly suppresses feedthrough induced oscillations. The methodology was illustrated by means of a prototype manual control task. It was shown analytically that a control design that ignores the base motion can result in instability. Controllers based on μ -synthesis were then proposed to robustly stabilize the system with respect to uncertainties in the arm/joystick and biodynamic feedthrough dynamics. The controllers also provide a high level of performance based on position tracking between the base and joystick, as well as admittance shaping of the joystick. Experimental studies in position and rate modes demonstrated excellent system responses under the new robust controllers compared to those of the fixed base controllers. While the μ -synthesis based controllers exhibit very well-damped behavior, the controllers designed by ignoring the base motion tend to destabilize the system and produce highly oscillatory responses. The design approach proposed in the thesis is general, and with some minor modifications is applicable to any teleoperation/manual control system with a movable base.

- 3. Adaptive Nonlinear Control of Hydraulic Robots:** High performance control of hydraulic robots is more difficult than that of their electrical counterparts because of the dominant nonlinear actuator dynamics. The problem becomes challenging if uncertainties in the dynamics are also considered. This thesis studied the position control of robot manipulators driven by hydraulic actuators. A realistic model of the system that includes the actuator dynamics and the rigid body dynamics was used in the control synthesis. For the first time, a position controller was proposed that guarantees the stability of the closed-loop system and the convergence of the tracking errors to zero. Adaptive variations of the control law were also proposed to deal with the uncertainties. Two types of observers were developed to avoid acceleration measurement, namely an adaptive passivity-based observer and a robust sliding type μ observer. The proposed methods prevent the parameter estimates from drifting. The stability of the controller/observers closed-loop dynamics was proven using the Lyapunov analysis. Position, velocity and pressure measurements are needed to implement the control laws. The performance of the controllers was evaluated by numerical and experimental studies carried out using the UBC hydraulic Stewart platform. The proposed approaches reduced the peak sinusoidal position tracking errors

by a factor of between five and ten compared to well-tuned proportional controllers in the experiments.

4. **Adaptive Nonlinear Control of Single-Actuator Hydraulic Servo-systems:** High performance position control of electrohydraulic actuators was addressed by this thesis. This is a difficult problem particularly due to the nonlinear nature of the system dynamics. The backstepping design approach was employed to develop a novel Lyapunov-based position tracking controller for hydraulic servo-systems. Load, hydraulic and first-order valve dynamics were incorporated in the design of the controller. An adaptive version of the controller was also proposed to cope with uncertainties in the hydraulic parameters. The stability of the system under the proposed control laws was proven via Lyapunov analysis. Position, velocity, hydraulic pressure and spool position measurements are required in the control laws. The proposed controllers were evaluated in simulation and experiments. They demonstrated excellent position tracking behavior compared to well-tuned PD controllers, and improved the tracking errors by a factor of between three and six in the experiments.
5. **Modeling and Identification of Biodynamic Feedthrough:** Two models were introduced and identified for biodynamic feedthrough. The acceleration based model proved effective in describing the feedthrough effects for the particular design example studied in this research. However, this model may not be accurate enough in applications where is large base acceleration. In this thesis, the stochastic embedding technique was employed to identify a feedthrough response based on experimental data. This approach also provides error bounds for the identified response. The estimated model and the frequency domain uncertainty bounds can be incorporated in the design of robust controllers for the suppression of biodynamic feedthrough using the framework presented in this thesis.
6. **Optimization of a Nonlinear Controller for Hydraulic Servo-systems:** A numerical approach to the optimization of the proposed nonlinear position tracking controllers for single-actuator hydraulic servo-systems was introduced. A simplified model of the system that ignores the valve dynamics and the dynamic uncertainties was used in the control synthesis. This reduces the controller to a feedback linearization control law, pa-

parameterized by the feedback gains, that guarantees convergence of the tracking errors to zero. A performance index that captures some features of the system step response of the system and its response to measurement noise was defined. The controller was successfully optimized with respect to the feedback gains using unconstrained optimization algorithms. Simulation studies demonstrated excellent responses for the controller with the optimized feedback gains.

8.2 Future Work

The work of this thesis may be continued in one or more of the following directions:

1. The feedthrough cancellation design problem discussed in this thesis was a single-degree-of-freedom task. The proposed approach can be employed to suppress feedthrough induced oscillations in multi-degree-of-freedom applications, e.g. the control of excavators. The high performance nonlinear controller can also be used to simulate the base motion for applications that involve high frequency base motions.
2. The proposed identification based approach to feedthrough modeling may be used in robust feedthrough cancellation especially in applications with large base accelerations. The current model has been obtained from experiments performed with one subject. In order to further validate the model, the experiments must be carried out using several subjects. The results can be combined to obtain a nominal feedthrough response and its associated uncertainties.
3. The feedthrough cancellation framework can be modified to allow for uncertainties in the plant dynamics and variations in communication time delay.
4. The combined teleoperation/manual control framework proposed here can be used to design controllers that improve performance in fixed base teleoperation applications. For example, using the model presented in Chapter 2, one may design teleoperation controllers that facilitate the crossover behavior of the operator.
5. The suboptimal nonlinear controller proposed for hydraulic servo-systems needs to be evaluated experimentally, although the optimized gains are not very different from the ones

found through manual tuning. The inclusion of the valve dynamics in the optimization of the controller can also be studied. Extension of the approach to the control of hydraulic robots could also be pursued.

6. The valve dynamics were ignored in the proposed adaptive nonlinear controllers for hydraulic robots. These dynamics may be considered in the design of provably stable controllers for such manipulators.

Bibliography

- [1] C. Abdallah, D. Dawson, P. Dorato, and M. Jamshidi. Survey of robust control for rigid robots. *IEEE Control Systems*, pages 24–30, 1991.
- [2] A. Alleyne. Nonlinear force control of an electro-hydraulic actuator. In *Proc. 1996 Japan/USA Symp. Flexible Automat.*, pages 193–200, 1996.
- [3] A. Alleyne and K. Hedrick. Nonlinear adaptive control of active suspensions. *IEEE Tran. Contr. Sys. Tech.*, 3(2):94–101, 1995.
- [4] R.J. Anderson and M.W. Spong. Bilateral control of teleoperators with time delay. *IEEE Tran. Automat. Cont.*, 34(5):494–501, May 1989.
- [5] R.J. Anderson and M.W. Spong. Asymptotic stability for force reflecting teleoperators with time delay. *Int. Journ. Robotics Research*, 11(2):135–142, April 1992.
- [6] F. Arai, J. Tateishi, and T. Fukuda. Dynamical analysis and suppression of human hunting in the excavator operation. In *Proc. of the 2000 Int. Workshop on Robot and Human Interactive Communication*, pages 394–399, 2000.
- [7] A. Bagchi. *Optimal control of stochastic systems*. Prentice Hall International, New Jersey, 1993.
- [8] D. Banerjee and M.L. Jordan. Modeling the effects of inertial reactions on occupants of moving power wheelchairs.
- [9] H. Bang, J.L. Junkins, and P.J. Fleming. Lyapunov optimal control laws for flexible structure maneuver and vibration control. *The Journal of the Astronautical Sciences*, 41(1):91–118, 1993.
- [10] Y. Bar-Shalom and T. Fortmann. *Tracking and Data Association*. Academic Press INC., 1988.
- [11] H. Berhuis and H. Nijmeijer. A passivity approach to controller-observer design for robots. *IEEE Tran. Robot. Automat.*, 9(6):740–754, 1993.
- [12] H. Berhuis, R. Ortega, and H. Nijmeijer. A robust adaptive robot controller. *IEEE Tran. Robot. Automat.*, 9(6):825–830, 1993.
- [13] W. Bernzen, T. Wey, and B. Riege. Nonlinear control of hydraulic differential cylinders actuating a flexible robot. In *Proc. 36th Conf. Decision and Contr.*, pages 1333–1334, 1997.

- [14] J.E. Bobrow and K. Lum. Adaptive, high bandwidth control of a hydraulic actuator. In *Proc. 1995 American Control Conf.*, pages 71–75, June 1995.
- [15] S.P. Boyd and G.H. Barratt. *Linear controller design: Limits of performance*. Prentice-Hall Inc., New Jersey, 1991.
- [16] F. Bu and B. Yao. Observer based coordinated adaptive robust control of robot manipulators driven by single-rod hydraulic actuators. In *IEEE Int. Conf. Robot. Automat.*, pages 3034–3039, April 2000.
- [17] T. Burg, D. Dawson, J. Hu, and M. de Queiroz. An adaptive partial state-feedback controller for RLED robot manipulators. *IEEE Tran. Automat. Contr.*, 41(7):1024–1030, July 1996.
- [18] Y. Cao. Nonadaptive and adaptive sliding mode control for robotic systems with a general sliding surface. In *Proc. IEEE Int. Conf. Sys. Man Cyber.*, pages 716–724, 1993.
- [19] J.D. Chapel. Performance limitations of bilateral force reflection imposed by operator dynamic characteristics. In *NASA Conf. Space Telerobotics*, pages 91–100, 1989.
- [20] C.-T. Chen. *Linear system theory and design*. HRW Series in Electrical and Computer Eng., New York, 1970.
- [21] J. Chiriboga, M.L. Thein, and E.A. Misawa. Input-output feedback linearization control of a load-sensing hydraulic servo system. In *Proc. IEEE Conf. Contr. Appl.*, pages 910–915, 1995.
- [22] J.E. Colgate. Robust impedance shaping telemanipulation. *IEEE Tran. Robot. Automat.*, 9(4):374–384, August 1993.
- [23] C.C. de Wit and J.-J.E. Slotine. Sliding observers for robot manipulators. *Automatica*, 27(5):859–864, 1991.
- [24] P. Dieudonne. *An actuator extension transformation for a motion simulator and inverse transformation applying Newton Raphson's method*. Technical Report D-7067, NASA, 1972.
- [25] W.E. Dixon, E. Zergeroglu, D.M. Dawson, and M.W. Hannan. Global adaptive partial state feedback tracking control of rigid-link flexible-joint robots. *Robotica*, 18:325–336, May-June 2000.
- [26] J.M. Dolan, M.B. Friedman, and M.L. Nagurka. Dynamic and loaded impedance components in the maintenance of human arm posture. *IEEE Tran. Sys. Man Cyber.*, 23(3):607–623, May/June 1993.
- [27] P. Drexel. *A Six Degree-of-Freedom, Hydraulic, One Person Motion Simulator*. Master's Thesis, The University of British Columbia, 1992.
- [28] K.A. Edge and F. Gomes de Almeida. Decentralized adaptive control of a directly driven hydraulic manipulator Part I: theory. In *Instn. Mech. Engr.*, volume 209, pages 191–196, 1995.

- [29] K.A. Edge and F. Gomes de Almeida. Decentralized adaptive control of a directly driven hydraulic manipulator Part II: experiments. In *Instn. Mech. Engr.*, volume 209, pages 197–202, 1995.
- [30] G.J. Balas et. al. *mu-Analysis and Synthesis Toolbox*. The MathWorks Inc., 2001.
- [31] R.B. Gillespie et. al. Cancellation of feedthrough dynamics using a force-reflecting joystick. In *Proc. ASME Dyn. Sys. Cont. Division*, pages 319–326, 1999.
- [32] S.S. Ge, T.H. Lee, and G. Zhu. Genetic algorithm tuning of Lyapunov-based controllers: an application to single-link flexible robot system. *IEEE Tran. Industrial Electronics*, 43(5):567–574, October 1996.
- [33] S.S. Ge and I. Postlethwaite. Nonlinear adaptive control of robots including motor dynamics. In *Proc. Amer. Cont. Conf.*, pages 1423–1427, 1993.
- [34] B. Golubev and I.M. Horowitz. Plant rational transfer function approximation from input-output data. *Int. Journal of Control*, 36(4):711–732, 1982.
- [35] G.C. Goodwin, M. Gevers, and B. Ninness. Quantifying the error in estimated transfer functions with application to model order selection. *IEEE Trans. Auto. Cont.*, 37(7):913–927, July 1992.
- [36] D.E. Greene. A mathematical theory for sequential input adaptive systems with applications to man-machine tracking systems. *IEEE Tran. Sys. Man Syber.*, 8(6):498–507, June 1978.
- [37] D.E. Greene. Stochastic sequential input adaptive system theory. *IEEE Tran. Sys. Man Syber.*, 10(4):197–202, April 1980.
- [38] G. Gu and P.P. Khargonekar. Linear and nonlinear algorithms for identification in Hinf with error bounds. *IEEE Tran. Auto. Contr.*, 37(7):953–963, July 1992.
- [39] R. Guenther and L. Hsu. Variable structure adaptive cascade control of rigid-link electrically-driven robot manipulators. In *Proc. 32th Conf. Dec. Cont.*, pages 2137–2142, 1993.
- [40] H. Hahn, A. Piepenbrink, and K.D. Leimbach. Input/output linearization control of an electro-servo-hydraulic actuator. In *Proc. IEEE Int. Conf. Cont. Appl.*, pages 995–1000, 1994.
- [41] B. Hannaford. A design framework for teleoperators with kinesthetic feedback. *IEEE Tran. Robt. Automat.*, 5(4):426–434, August 1989.
- [42] B. Hannaford. Stability and performance tradeoffs in bi-lateral telemanipulation. In *Proc. IEEE Int. Conf. Robot. Auto.*, pages 1764–1767, 1989.
- [43] K. Hashtrudi-Zaad. *Design, Implementation and Evaluation of Stable Bilateral Teleoperation Control Architectures for Enhanced Telepresence*. Ph.D. Thesis, University of British Columbia, 2000.

- [44] R.A. Hess. A model for the human's use of motion cues in vehicular control. *Journal of Guidance, Control, and Dynamics*, 13(3):476–482, 1990.
- [45] R.A. Hess. Analyzing manipulator and feel system effects in aircraft flight control. *IEEE Trans. Sys., Man, and Cyber.*, 20(4):923–931, 1990.
- [46] R.A. Hess. Unified theory for aircraft handling qualities and adverse aircraft-pilot coupling. *Journal of Guidance, Control, and Dynamics*, 20(6):1141–1148, November–December 1997.
- [47] R.A. Hess. Theory for roll-ratchet phenomenon in high-performance aircraft. *Journal of Guidance, Control, and Dynamics*, 14(1):651–655, 1998.
- [48] R.A. Hess and A. Modjtahedzadeh. A control theoretic model of driver steering behavior. *IEEE Control Systems Magazine*, 10(5):3–8, 1990.
- [49] N. Hogan. Controlling impedance at the man/machine interface. In *Proc. IEEE Int. Conf. Robot. Auto.*, pages 1626–1631, 1989.
- [50] Z. Hu, S.E. Salcudean, and P.D. Loewen. Robust controller design for teleoperation systems. In *Proc. 1995 IEEE Int. Conf. Sys. Man Cyber.*, pages 2127–2132, 1995.
- [51] M. Idan and S.J. Merhav. Effects of biodynamic coupling on the human operator model. *Journal of Guidance*, 13(4):630–637, 1989.
- [52] G.A. Ingram, M.A. Francheck, and G.T.-C Chiu. Reducing operator-induced machine vibration using a complex pole/zero prefilter. *Journal Sound and Vibration*, 250(2):197–213, 2002.
- [53] M.S. Jankovic. Exact n 'th derivatives of eigenvalues and eigenvectors. *Journal of Guidance*, 17(1):136–144, 1994.
- [54] A. Jaritz and M.W. Spong. An experimental comparison of robust control algorithms on a direct drive manipulator. *IEEE Trans. Control Syst. Tech.*, 4(6):627–640, Nov. 1996.
- [55] H.R. Jex and R.E. Magdanelo. Biomechanical models for vibration feedthrough to hands and head for a semisupine pilot. *Aviation, Space, and Environment Medicine*, 49:304–316, 1978.
- [56] R. Johansson. Quadratic optimization of motion coordination and control. *IEEE Tran. Automatic Control*, 35(11):1197–1208, November 1990.
- [57] H. Kazerooni, T. Tsay, and K. Hollerbach. A controller design framework for telerobotic systems. *IEEE Tran. Cont. Sys. Tech.*, 1(1):50–62, March 1993.
- [58] H.K. Khalil. *Nonlinear Systems*. Prentice-Hall Inc., New York, 1992.
- [59] D.L. Kleinman, S. Baron, and W.H. Levison. A control theoretic approach to manned-vehicle systems analysis. *IEEE Tran. Auto. Cont.*, 16(6):824–832, December 1971.

- [60] M. Krstic, I. Kanellakopoulos, and P. Kokotovic. *Nonlinear and Adaptive Control Design*. Wiley and Sons, New York, 1995.
- [61] L. Laval, N.K. M'Siridi, and J.C. Cadiou. Hinf force control of hydraulic servo-actuator with environmental uncertainties. In *Proc. IEEE Int. Conf. Robot. Auto.*, pages 1566–1571, April 1996.
- [62] D.A. Lawrence. Stability and transparency in bilateral teleoperation. *IEEE Tran. Robot. Automat.*, 9(5):624–637, October 1993.
- [63] R.L. Leal and C.C. DeWit. Passivity based adaptive control for mechanical manipulators using LS-type estimation. *IEEE Trans. Auto. Control*, 35(12):1363–1365, Dec. 1990.
- [64] S. Lee and H.S. Lee. Teleoperator control system design with human in control loop and telemonitoring force feedback. In *Proc. 31st Conf. Decision Cont.*, pages 2674–2679, 1992.
- [65] S. Lee and H.S. Lee. Modeling, design, and evaluation of advanced teleoperator control systems with short time delay. *IEEE Tran. Robot. Auto.*, 9(5):607–623, 1993.
- [66] S. Lee and H.S. Lee. Design of optimal time delayed teleoperator control system. In *Proc. IEEE Int. Conf. on Robot. Auto.*, pages 3252–3258, 1994.
- [67] G.M.H. Leung, B.A. Francis, and J. Apkarian. Bilateral controller for teleoperators with time delay via mu-synthesis. *IEEE Tran. Robot. Auto.*, 11(1):105–116, 1995.
- [68] W.H. Levison. Model for human controller performance in vibration environments. *Journal of Aviation, Space, and Environment Medicine*, 49(1):321–327, Jan. 1978.
- [69] C. H. Lewis and M. J. Griffin. A review of the effects of vibration on visual acuity and continuous manual control, part ii: continuous manual control. *Journal of Sound and Vibration*, 56(3):415–457, 1978.
- [70] F.L. Lewis and V.L. Syrmos. *Optimal control*. Wiley, New York, 1995.
- [71] D. Li. *Modeling, Simulation, and Control of a Stewart Platform*. Master's Thesis, The University of British Columbia, 1996.
- [72] D. Li and S.E. Salcudean. Modeling, simulation and control of a hydraulic Stewart platform. In *IEEE Int. Conf. Robot. Automat.*, pages 3360–3366, April 1997.
- [73] K.B. Lim and J.L. Junkins. Re-examination of eigenvector derivatives. *Journal of Guidance*, 10(6):581–587, 1987.
- [74] S.Y. Lim, J. Hu, and D. M. Dawson. An output feedback controller for trajectory tracking of RLED robots using an observed backstepping approach. In *Proc. IEEE Int. Conf. Cont. Appl.*, pages 71–76, 1994.
- [75] R. Liu and A. Alleyne. Nonlinear force control of an electro-hydraulic actuator. In *Proc. 1996 Japan/USA Symp. Flexible Automat.*, pages 193–200, 1996.

- [76] L. Ljung. *System Identification - Theory for the User*. Prentice Hall Inc., Englewood Cliffs NJ, 1987.
- [77] H. Lu and W. Lin. Robust controller with disturbance rejection for hydraulic servo systems. *IEEE Trans. Indus. Elec.*, 39(1):157–162, February 1993.
- [78] J.Y.S. Luh, M.W. Walker, and R.P.C. Paul. Resolved acceleration control of mechanical manipulators. *IEEE Tran. Automat. Cont.*, 25:468–474, 1980.
- [79] R.W. McLeod and M.J. Griffin. A review of the effects of translational whole-body vibration on continuous manual control performance. *Journal of Sound and Vibration*, 133(1):55–115, 1989.
- [80] D.T. McRuer, D. Graham, and E.S. Krendel. Manual control of single-loop systems: Parts I and II. *Journal of the Franklin Institute*, 283(5), Jan.-Feb. 1967.
- [81] D.T. McRuer and H.R. Jex. A review of quasi-linear pilot models. *IEEE Tran. Human Factors in Electronics*, 8(3):231–249, September 1967.
- [82] C. Melchiorri and A. Eusebi. Telemanipulation: system aspects and control issues. In *Proc. Model. Cont. Mechan. Robot.*, pages 149–183, 1996.
- [83] H.E. Merritt. *Hydraulic Control Systems*. Wiley and Sons, New York, 1967.
- [84] S. Nicosia and P. Tomei. Robot control by using only joint position measurements. *IEEE Trans. Auto. Cont.*, 35(9):1058–1061, Sept. 1990.
- [85] G. Niemeyer and J.-J.E. Slotine. Teleoperation controller design using Hinfinity - optimization with application to motion-scaling. *IEEE J. Ocean. Eng.*, 16(1):152–162, Jan. 1991.
- [86] G. Niemeyer and J.-J.E. Slotine. Towards force-reflecting teleoperation over Internet. In *IEEE Int. Conf. Robot. Auto.*, pages 1909–1915, 1998.
- [87] N. Niksefat and N. Sepehri. Robust force controller design for an electro-hydraulic actuator based on nonlinear model. In *Proc. IEEE Int. Conf. Robot. Auto.*, pages 200–206, 1999.
- [88] J. Nocedal and S.J. Wright. *Numerical Optimization*. Springer, New York, 1999.
- [89] B. Novel, M.A. Garnero, and A. Abichou. Nonlinear control of a hydraulic robot using singular perturbations. In *Int. Conf. Syst. Man and Cyber.*, pages 1932–1937, 1994.
- [90] R. Ortega and M.W. Spong. Adaptive motion control of rigid robots: A tutorial. *Automatica*, 25:877–888, 1989.
- [91] R. Paassen. A model of the arm's neuromuscular system for manual control. In *Proc. of 6th IFAC/IFIP/IFORS/IEA Symposium on Analysis, Design and Evaluation of Man-Machine Systems*, pages 599–604, 1995.

- [92] B. Paden and R. Panja. Globally asymptotically stable 'PD+' controller for robot manipulators. *Int. J. Control*, 47:1697–1712, 1988.
- [93] Z. Pan and T. Basar. Adaptive controller design for tracking and disturbance attenuation in parametric strict-feedback nonlinear systems. *IEEE Tran. Automat. Control*, 43(8):1066–1083, August 1998.
- [94] L.F. Pcnin, A. Caballero, R. Aracil, and A. Barrientos. Human behavior modeling in master-slave teleoperation with kinesthetic feedback. In *IEEE Int. Conf. Robot. Auto.*, pages 2244–2249, 1998.
- [95] G.J. Raju, G.C. Verghese, and T.B. Sheridan. Design issues in 2-port network models of bilateral remote teleoperation. In *Proc. IEEE Int. Conf. Robot. Automat.*, pages 1317–1321, 1989.
- [96] N. Sadegh and R. Horowitz. Stability analysis of an adaptive controller for robotic manipulators. In *Proc. IEEE Int. Conf. Robot. Auto.*, pages 1223–1229, 1987.
- [97] N. Sadegh and R. Horowitz. Stability and robustness analysis of a class of adaptive controllers for robotic manipulators. *Int. J. Robot. Research*, 9(3):74–92, June 1990.
- [98] S.E. Salcudean. *Control for Teleoperation and Haptic Interfaces*. Control Problems in Robotics and Automation; B. Siciliano and K.P. Valavanis (Eds.), Springer, 1997.
- [99] S.E. Salcudean, P.A. Drexel, D. Ben-Dov, A.J. Taylor, and P.D. Lawrence. A six degree-of-freedom, hydraulic, one person motion simulator. In *Int. Conf. Robot. Automat.*, pages 859–864, May 1994.
- [100] S.E. Salcudean, N.M. Wong, and R.L. Hollis. A force-reflecting teleoperation system with magnetically levitated master and wrist. In *Proc. IEEE Int. Conf. Robot. Auto.*, pages 1420–1426, 1992.
- [101] T.B. Sheridan. Telerobotics. *Automatica*, 25(4):487–507, 1989.
- [102] T.S. Sherman and M.G. Lance. A design study of a positioning system with electrohydraulic actuation. In *Proc. Amer. Contr. Conf.*, pages 1853–1858, 1987.
- [103] H.-J. Shieh and K.-K. Shyu. Nonlinear sliding-mode torque control with adaptive backstepping approach for induction motor drive. *IEEE Tran. Indus. Elect.*, 46(2):380–389, April 1999.
- [104] M.R. Sirouspour, S.P. Dimaio, S.E. Salcudean, P. Abolmaesumi, and C. Jones. Haptic interface control-design issues and experiments with a planar device. In *Proc. IEEE Int. Conf. Robot. Automat.*, pages 789–794, April 2000.
- [105] M.R. Sirouspour and S.E. Salcudean. Suppressing operator-induced oscillations in manual control systems with movable bases. *to appear in IEEE Tran. Cont. Sys. Tech.*
- [106] M.R. Sirouspour and S.E. Salcudean. On the nonlinear control of hydraulic servo-systems. In *Int. Conf. Robot. Automat.*, pages 1276–1282, April 2000.

- [107] M.R. Sirouspour and S.E. Salcudean. A new approach to the control of a hydraulic Stewart platform. *Experimental Robotics VII. D. Rus and S. Singh (Eds.). Springer*, pages 447–460, 2001.
- [108] M.R. Sirouspour and S.E. Salcudean. Nonlinear control of a hydraulic parallel manipulator. In *Proc. IEEE Int. Conf. Robot. Auto.*, pages 3760–3765, 2001.
- [109] M.R. Sirouspour and S.E. Salcudean. Nonlinear control of hydraulic robots. *IEEE Tran. Robot. Automat.*, 17(2):173–182, 2001.
- [110] M.R. Sirouspour and S.E. Salcudean. Robust cancellation of biodynamic feedthrough in manual control systems. In *to appear in the Video Proc. IEEE Int. Conf. Robot. Auto.*, 2003.
- [111] M.R. Sirouspour and S.E. Salcudean. Robust Controller Design for Canceling Biodynamic Feedthrough. *B. Siciliano and P. Dario (Eds.): Experimental Robotics VIII., Springer-Verlag*, pages 123–133, 2003.
- [112] J.-E. Slotine and W. Li. *Applied Nonlinear Control*. Prentice-Hall Inc., New Jersey, 1991.
- [113] J.-J. Slotine and W. Li. Composite adaptive control of robot manipulators. *Automatica*, 25(4):509–519, July 1989.
- [114] J.J.-E Slotine and W. Li. On the adaptive control of robot manipulators. *Int. J. Robot. Research*, 6(3):49–59, 1987.
- [115] J.W. Smith and T. Montgomery. *Biomechanically induced and controller coupled oscillations experienced on the F-16XL aircraft during rolling maneuvers*. NASA Technical Memorandum 4752, 1996.
- [116] G.A. Sohl and J.E. Bobrow. Experiments and simulations on the nonlinear control of a hydraulic servosystem. *IEEE Trans. Cont, Sys. Tech.*, 3(2):238–247, March 1999.
- [117] M.W. Spong. On the robust control of robot manipulators. *IEEE Tran. Automat. Cont.*, 37:1782–1786, 1992.
- [118] Y. Strassberg, A.A. Goldenberg, and J.K. Mills. A new control scheme for bilateral teleoperating systems: Lyapunov stability analysis. In *Proc. IEEE Int. Conf. Robot. Auto.*, pages 837–842, 1992.
- [119] C.-Y. Su, T.-P. Leung, and Y. Stepanenko. Real-time implementation of regressor-based sliding mode control algorithm for robotic manipulators. *IEEE Trans. Ind. Electron.*, 40(1):71–79, Feb. 1993.
- [120] S. Tafazoli, C.W. de Silva, and P.D. Lawrence. Tracking control of an electrohydraulic manipulator in the presence of friction. *IEEE Tran. Cont. Syst. Tech.*, 6(3):401–411, May 1998.
- [121] Y. Tang and M.A. Arteaga. Adaptive control of robot manipulators based on passivity. *IEEE Trans. Auto. Cont.*, 39(4):1871–1875, Sept. 1994.

- [122] T.-J. Tarn, A.K. Bejczy, X. Yun, and Z. Li. Effect of motor dynamics on nonlinear feedback robot arm control. *IEEE Tran. Robot. Automat.*, 7(1):114–122, February 1991.
- [123] S. Toffner-Clausen. *System Identification and Robust Control*. Springer-Verlag, London, 1996.
- [124] M. Velger. Adaptive filtering of biodynamic stick feedthrough in manipulation tasks on board moving platforms. *Journal of Guidance, Control, and Dynamics*, 11(2):153–158, 1988.
- [125] M. Velger, A. Grunwald, and S. Merhav. Suppression of biodynamic disturbance and pilot-induced oscillations by adaptive filtering. *Journal of Guidance, Control, and Dynamics*, 7(4):401–409, 1984.
- [126] G. Vossoughi and M. Donath. Dynamic feedback linearization for electrohydraulically actuated control systems. *J. Dyn. Sys., Meas. and Contr.*, 117:468–477, Dec. 1995.
- [127] B. Wahlberg. System identification using Laguerre models. *IEEE Trans. Auto. Cont.*, 36(5):551–562, May 1991.
- [128] B. Wahlberg. System identification using Kautz models. *IEEE Auto. Cont.*, 39(6):1276–1282, June 1994.
- [129] B. Wahlberg and L. Ljung. Hard frequency-domain model error bounds from least-squares like identification techniques. *IEEE Trans. Auto. Cont.*, 37(7):900–912, July 1992.
- [130] L. Whitcomb, A. Rizzi, and D.E. Koditschek. Comparative experiments with a new adaptive controller for robot arms. *IEEE Trans. Robot. Autom.*, 9(1):59–70, Feb. 1993.
- [131] J. Yan and S.E. Salcudean. Teleoperation controller design using Hinfinity -optimization with application to motion-scaling. *IEEE Tran. Cont. Syst. Tech.*, 45(11):244–258, May 1996.
- [132] H. Yanada and M. Shimahara. Sliding mode control of an electrohydraulic servo motor using a gain scheduling type observer and controller. *Proc. Inst. Mech. Engrs.*, 211:407–416, 1997.
- [133] C. Yi and Y. Stepanenko. Hybrid adaptive/robust control of rigid-link electrically-driven robot manipulators. *IEEE Trans. Robot. Auto.*, 11(3):426–432, June 1995.
- [134] C. Yi and Y. Stepanenko. Redesign of hybrid adaptive/robust motion control of rigid-link electrically-driven robot manipulators. *IEEE Trans. Robot. Autom.*, 14(4):651–655, Aug. 1998.
- [135] Y. Yokokohji and T. Yoshikawa. Bilateral control of master-slave manipulators for ideal kinesthetic coupling-formulation and experiment. *IEEE Tran. Robot. Automat.*, 10(5):605–620, October 1994.
- [136] J. Yuan. Adaptive control of robotic manipulators including motor dynamics. *IEEE Tran. Robot. Automat.*, 11(4):612–617, 1995.

-
- [137] J.S. Yun and H.S. Cho. Adaptive model following of electrohydraulic velocity control systems subjected to known disturbances. *IEE Proc.*, 135(2):149–156, March 1988.
- [138] J.S. Yun and H.S. Cho. An optimal variable structure control with integral compensation for electrohydraulic position servo control systems. *IEEE Trans. Indust. Elec.*, 39(5):460–463, October 1992.
- [139] K. Zhou and J.C. Doyle. *Essentials of Robust Control*. Prentice-Hall Inc., New Jersey, 1998.
- [140] W.-H. Zhu and S.E. Salcudean. Stability guaranteed teleoperation: an adaptive motion/force control approach. *IEEE Tran. Auto. Cont.*, 45(11):1951–1969, November 2000.
- [141] W.-H. Zhu and J. De Schutter. Adaptive control of mixed rigid/flexible joint robot manipulators based on virtual decomposition. *IEEE Tran. Robot. Automat.*, 15(2):310–317, April 1999.

Appendix A

Evaluation of the Objective Function and its Gradient

In Chapter 6, a suboptimal nonlinear controller was proposed for hydraulic servo-systems. The optimization is performed by numerically minimizing a performance index over all allowable control gains. This appendix addresses the computation of the performance and its gradient which are required by the optimization routines.

A.1 Objective Function

There are terms in the objective function defined by (6.37), i.e. J_x , J_{t_f} and J_n , that can be computed analytically. Consider the following dynamics

$$\dot{X}(t) = A(p)X(t) + BN \quad X(0) = X_0 \quad (\text{A-1})$$

Assume that matrix A is diagonalizable (i.e., it does not have any degenerate eigenvalues), that is

$$U_t A V = \Lambda; \quad \Lambda = \text{diag}\{\lambda_i\} \quad i = 1, \dots, n \quad (\text{A-2})$$

where λ_i is the i 'th eigenvalue of matrix A and

$$V = \begin{bmatrix} v_1 & v_2 & \dots & v_n \end{bmatrix} \quad Av_k = \lambda_k v_k \quad (\text{A-3})$$

$$U_t = V^{-1} = \begin{bmatrix} u_1^t \\ u_2^t \\ \vdots \\ u_n^t \end{bmatrix} \quad u_k^t A = \lambda_k u_k^t \quad (\text{A-4})$$

contain the right and left eigenvectors of A , respectively. The solution $X(t)$ of (A-1) is given by [20] (if $N = 0$)

$$X(t) = e^{At} X_0 \quad (\text{A-5})$$

or

$$X(t) = V e^{\Lambda t} U_t X_0 \quad (\text{A-6})$$

J_x can be calculated using the solution $X(t)$

$$\begin{aligned} J_x &= \int_0^{t_f} X(t)^T Q X(t) dt = X_0^T U_t^* \left(\int_0^{t_f} e^{\Lambda^* t} V^* Q V e^{\Lambda t} dt \right) U^* X_0 \\ &= X_0^T U_t^* \left(\int_0^{t_f} (V^* Q V) \cdot \left[e^{(\lambda_i^* + \lambda_j)t} \right] dt \right) U_t X_0 \\ &= X_0^T U_t^* (V^* Q V) \cdot \left[\frac{1}{\lambda_i^* + \lambda_j} \left(e^{(\lambda_i^* + \lambda_j)t_f} - 1 \right) \right] U_t X_0 \end{aligned} \quad (\text{A-7})$$

In (A-7), "*" is conjugate transpose and "(.)[]" denotes component-wise product of two matrices.

Similarly, J_{t_f} is given by

$$\begin{aligned} J_{t_f} &= X(t_f)^T H X(t_f) = X_0^T e^{A^T t_f} H e^{A t_f} X_0 \\ &= X_0^T U_t^* e^{\Lambda^* t_f} V^* H V e^{\Lambda t_f} U_t X_0 \end{aligned} \quad (\text{A-8})$$

In order to compute J_n , one needs to find the covariance matrix P of the state tracking errors

$$\begin{aligned}
 P &= \int_0^{\infty} e^{At} B B^T e^{A^T t} dt = \int_0^{\infty} V e^{\Lambda t} U_t B B^T U_t^* e^{\Lambda^* t} V^* dt \\
 &= V(U_t B B^T U_t^*) \cdot \left[\int_0^{\infty} e^{(\lambda_i + \lambda_j^*) t} dt \right] V^* \\
 &= V(U_t B B^T U_t^*) \cdot \left[-\frac{1}{\lambda_i + \lambda_j^*} \right] V^*
 \end{aligned} \tag{A-9}$$

and

$$J_n = r_x P(1,1) + r_v P(2,2) + r_r P(3,3) \tag{A-10}$$

To compute J_u , one has to use a numerical integration routine. Once $X(t)$ is calculated, $u(t)$ can be derived from (6.6) and then used in an integration routine. In this thesis, function *quad* from *Matlab*[®] is employed for this purpose.

Remark 1: For the evaluation of J_x , J_{t_f} and J_u all matrices have a (3×3) reduced form. However, to compute J_p full (6×6) matrices must be used. Once U_t and V are found for \bar{A} in (6.26), the upper diagonal blocks of these matrices correspond to A_0 in (6.11) and can be used in the computation of J_x , J_{t_f} and J_u .

Remark 2: Only first three diagonal terms of P are required in J_n . This has been exploited to reduce the computation.

A.2 Gradient of Objective Function

The optimization routines that are used in this research require the gradient of the objective function at each point. This section briefly describes how these gradients are calculated. To this end, the derivatives of eigenvalues and eigenvectors with respect to each parameter must be computed first. Only the results are presented here and the detailed derivations can be found in [53, 73]. Assuming v_k 's and u_k^t 's are the right and left eigenvectors of matrix A with the

following properties

$$Av_k = \lambda_k v_k \quad k = 1, \dots, n \quad (\text{A-11})$$

$$u_k^t A = \lambda_k u_k^t \quad k = 1, \dots, n \quad (\text{A-12})$$

$$v_k^* v_k = 1 \quad u_k^t v_j = \delta_{kj} \quad (\text{A-13})$$

then the derivative of each eigenvalue with respect to parameter p_m is given by

$$\frac{\partial \lambda_k}{\partial p_m} = u_k^t \frac{\partial A}{\partial p_m} v_k \quad (\text{A-14})$$

The derivatives of the right eigenvectors using $\{v_1, \dots, v_n\}$ as basis vectors can be expressed as follows

$$\frac{\partial v_i}{\partial p_m} = \sum_{j=1}^n \alpha_{ij} v_j \quad (\text{A-15})$$

where

$$a_{ik} = \begin{cases} \frac{1}{\lambda_i - \lambda_k} u_k^t \frac{\partial A}{\partial p_m} v_i & \text{if } k \neq i \\ -\sum_{j \neq i}^n \alpha_{ij} v_j^* v_j & \text{if } k = i \end{cases} \quad (\text{A-16})$$

Similarly, for the left eigenvectors

$$\frac{\partial u_i^t}{\partial p_m} = \sum_{j=1}^n \gamma_{ij} u_j^t \quad (\text{A-17})$$

and $[\gamma_{ij}] = -[\alpha_{ij}]^T$.

Remark: In general the eigenvalues and eigenvectors are complex-valued. Since $v_k^* v_k = 1$, one may write

$$\frac{\partial}{\partial p_m} (v_k^* v_k) = \frac{\partial v_k^*}{\partial p_m} v_k + v_k^* \frac{\partial v_k}{\partial p_m} = 0 \quad (\text{A-18})$$

From here reference [73] concludes that $\frac{\partial v_k^*}{\partial p_m} v_k = 0$ which, clearly, is true only if $\frac{\partial v_k^*}{\partial p_m} v_k$ is real.

Reference [53] makes the same assumption and points out this problem but it does not give the solution for the case in which this assumption does not hold. Despite the fact that the computed derivatives of the eigenvectors may not be always correct, the derivatives of the performance measure obtained using the above formulas were found to be correct. This was validated by comparing the results with those calculated through numerical differentiation. Since we are only concerned with the derivative of performance measure, the above results are employed in the implementation.

At this stage everything is ready for the evaluation of the gradient of the performance measure. The partial derivative of the state tracking errors with respect to parameter p_m is given by

$$\begin{aligned} \frac{\partial X(t)}{\partial p_m} &= \frac{\partial}{\partial p_m} (e^{At} X_0) = \frac{\partial V}{\partial p_m} e^{At} U_t X_0 + V e^{At} \frac{\partial U_t}{\partial p_m} X_0 \\ &\quad + V \frac{\partial e^{At}}{\partial p_m} U_t X_0 + V e^{At} U_t \frac{\partial X_0}{\partial p_m} \end{aligned} \quad (\text{A-19})$$

where

$$\frac{\partial e^{At}}{\partial p_m} = t e^{At} \frac{\partial \Lambda}{\partial p_m} \quad \text{and} \quad \frac{\partial \Lambda}{\partial p_m} = \text{diag} \left\{ \frac{\partial \lambda_i}{\partial p_m} \right\} \quad (\text{A-20})$$

and

$$\frac{\partial X_0}{\partial p_1} = \begin{bmatrix} 0 & 0 & me(0) \end{bmatrix}^T \quad \frac{\partial X_0}{\partial p_2} = 0 \quad \frac{\partial X_0}{\partial p_3} = 0 \quad (\text{A-21})$$

Using (A-7), $\frac{\partial J_x}{\partial p_m}$ is computed as follows

$$\begin{aligned} \frac{\partial J_x}{\partial p_m} &= 2\text{Re} \left\{ X_0^T U_t^* (V^* Q V) \cdot \left[\frac{1}{\lambda_i^* + \lambda_j} \left(e^{(\lambda_i^* + \lambda_j)t_f} - 1 \right) \right] \left(\frac{\partial U_t}{\partial p_m} X_0 + U_t \frac{\partial X_0}{\partial p_m} \right) \right\} \\ &\quad + X_0^T U_t^* \frac{\partial}{\partial p_m} (V^* Q V) \cdot \left[\frac{1}{\lambda_i^* + \lambda_j} \left(e^{(\lambda_i^* + \lambda_j)t_f} - 1 \right) \right] U_t X_0 \\ &\quad + X_0^T U_t^* (V^* Q V) \cdot \frac{\partial}{\partial p_m} \left(\left[\frac{1}{\lambda_i^* + \lambda_j} \left(e^{(\lambda_i^* + \lambda_j)t_f} - 1 \right) \right] \right) U_t X_0 \end{aligned} \quad (\text{A-22})$$

with

$$\frac{\partial}{\partial p_m} \left[\frac{1}{\lambda_i^* + \lambda_j} \dots \right] = \left[\frac{-1}{(\lambda_i^* + \lambda_j)^2} \left(e^{(\lambda_i^* + \lambda_j)t_f} - 1 \right) + \frac{t_f}{\lambda_i^* + \lambda_j} e^{(\lambda_i^* + \lambda_j)t} \right] \cdot \left[\frac{\partial \lambda_i^*}{\partial p_m} + \frac{\partial \lambda_j}{\partial p_m} \right] \quad (\text{A-23})$$

and

$$\frac{\partial}{\partial p_m} (V^* Q V) = \frac{\partial V^*}{\partial p_m} Q V + V^* Q \frac{\partial V}{\partial p_m} = \frac{\partial V^*}{\partial p_m} Q V + \left(\frac{\partial V^*}{\partial p_m} Q V \right)^* \quad (\text{A-24})$$

$\frac{\partial J_{t_f}}{\partial p_m}$ can be obtained by taking the partial derivative of (A-8) with respect to p_m .

$$\begin{aligned} \frac{\partial J_{t_f}}{\partial p_m} = & 2\text{Re} \left\{ X_0^T U_t^* e^{\Lambda^* t_f} V^* H V e^{\Lambda t_f} \left(\frac{\partial U_t}{\partial p_m} X_0 + U_t \frac{\partial X_0}{\partial p_m} \right) \right\} \\ & + X_0^T U_t^* \frac{\partial}{\partial p_m} \left(e^{\Lambda^* t_f} V^* H V e^{\Lambda t_f} \right) U_t X_0 \end{aligned} \quad (\text{A-25})$$

with

$$\begin{aligned} \frac{\partial}{\partial p_m} \left(e^{\Lambda^* t_f} V^* H V e^{\Lambda t_f} \right) = & \frac{\partial}{\partial p_m} (V^* H V) \cdot \left[e^{(\lambda_i^* + \lambda_j)t_f} \right] \\ & + (V^* H V) \cdot \left[t_f e^{(\lambda_i^* + \lambda_j)t_f} \left(\frac{\partial \lambda_i^*}{\partial p_m} + \frac{\partial \lambda_j}{\partial p_m} \right) \right] \end{aligned} \quad (\text{A-26})$$

The partial derivative of covariance matrix P is required in the calculation of $\frac{\partial J_n}{\partial p_m}$ and is given by

$$\begin{aligned} \frac{\partial P}{\partial p_m} = & V (U_t B B^T U_t^*) \cdot \left[\frac{-1}{\lambda_i + \lambda_j^*} \right] \frac{\partial V^*}{\partial p_m} + \frac{\partial V}{\partial p_m} (U_t B B^T U_t^*) \cdot \left[\frac{-1}{\lambda_i + \lambda_j^*} \right] V^* \\ & + V \frac{\partial}{\partial p_m} \left((U_t B B^T U_t^*) \cdot \left[\frac{-1}{\lambda_i + \lambda_j^*} \right] \right) V^* \end{aligned} \quad (\text{A-27})$$

and

$$\begin{aligned} \frac{\partial}{\partial p_m} \left((U_t B B^T U_t^*) \cdot \left[\frac{-1}{\lambda_i + \lambda_j^*} \right] \right) = & \frac{\partial}{\partial p_m} (U_t B B^T U_t^*) \cdot \left[\frac{-1}{\lambda_i + \lambda_j^*} \right] \\ & + (U_t B B^T U_t^*) \cdot \left[\frac{1}{(\lambda_i + \lambda_j^*)^2} \left(\frac{\partial \lambda_i}{\partial p_m} + \frac{\partial \lambda_j^*}{\partial p_m} \right) \right] \end{aligned} \quad (\text{A-28})$$

Once $\frac{\partial P}{\partial p_m}$ is found, $\frac{\partial J_n}{\partial p_m}$ is computed using

$$\frac{\partial J_n}{\partial p_m} = r_x \frac{\partial P(1,1)}{\partial p_m} + r_v \frac{\partial P(2,2)}{\partial p_m} + r_\tau \frac{\partial P(3,3)}{\partial p_m} \quad (\text{A-29})$$

Remark: In general the dimension of the system is six in the presence of noise. However, as it was mentioned earlier, for the calculation of $\frac{\partial J_x}{\partial p_m}$, $\frac{\partial J_f}{\partial p_m}$ and $\frac{\partial J_u}{\partial p_m}$ only the upper diagonal blocks of matrices of V , U_t , $\frac{\partial V}{\partial p_m}$ and $\frac{\partial U_t}{\partial p_m}$ are used. Furthermore, for the special problem under study, many of the matrices are sparse and calculation can be performed more efficiently if special care is taken. These facts have been partially considered in the implementation.

To derive $\frac{\partial J_u}{\partial p_m}$, one may write

$$\frac{\partial J_u}{\partial p_m} = \frac{\partial}{\partial p_m} \left(\int_0^{t_f} r u(t)^2 dt \right) = 2r \int_0^{t_f} u \frac{\partial u}{\partial p_m} dt \quad (\text{A-30})$$

Therefore, the problem comes down to the calculation of $\frac{\partial u}{\partial p_m}$. Using (6.4),

$$\frac{\partial \tau_d}{\partial p_1} = -me - k_p \frac{\partial e}{\partial p_1} - k_d \frac{\partial \dot{e}}{\partial p_1} \quad (\text{A-31})$$

$$\frac{\partial \tau_d}{\partial p_2} = -k_p \frac{\partial e}{\partial p_2} - m\dot{e} - k_d \frac{\partial \dot{e}}{\partial p_2} \quad (\text{A-32})$$

$$\frac{\partial \tau_d}{\partial p_3} = -k_p \frac{\partial e}{\partial p_3} - k_d \frac{\partial \dot{e}}{\partial p_3} \quad (\text{A-33})$$

Similarly, by taking the partial derivatives of (6.9) with respect to p_i 's

$$\frac{\partial \dot{\tau}_d}{\partial p_1} = k_d e + \frac{k_d(k+k_p)}{m} \frac{\partial e}{\partial p_1} - m\dot{e} - \left(k_p - \frac{k_d(b+k_d)}{m} \right) \frac{\partial \dot{e}}{\partial p_1} - \frac{k_d}{m} \frac{\partial \tilde{\tau}}{\partial p_1} \quad (\text{A-34})$$

$$\frac{\partial \dot{\tau}_d}{\partial p_2} = \frac{k_d(k+k_p)}{m} \frac{\partial e}{\partial p_2} + (k+k_p)e + \left(\frac{k_d(b+k_d)}{m} - k_p \right) \frac{\partial \dot{e}}{\partial p_2} + (2k_d+b)\dot{e} - \tilde{\tau} - \frac{k_d}{m} \frac{\partial \tilde{\tau}}{\partial p_2} \quad (\text{A-35})$$

$$\frac{\partial \dot{\tau}_d}{\partial p_3} = \frac{k_d(k+k_p)}{m} \frac{\partial e}{\partial p_3} + \left(\frac{k_d(b+k_d)}{m} - k_p \right) \frac{\partial \dot{e}}{\partial p_3} - \frac{k_d}{m} \frac{\partial \tilde{\tau}}{\partial p_3} \quad (\text{A-36})$$

The partial derivatives of f and \bar{g} used in the feedback law given in (6.6) are also required.

$$\frac{\partial f}{\partial p_m} = \frac{\partial f}{\partial e} \frac{\partial e}{\partial p_m} + \frac{\partial f}{\partial \dot{e}} \frac{\partial \dot{e}}{\partial p_m} \quad (\text{A-37})$$

where

$$\frac{\partial f}{\partial e} = \frac{A\beta\dot{x}}{(x-L)^2} \quad (\text{A-38})$$

$$\frac{\partial f}{\partial \dot{e}} = -\frac{A\beta}{x-L} \quad (\text{A-39})$$

Similarly,

$$\frac{\partial \bar{g}}{\partial p_m} = \frac{\partial \bar{g}}{\partial e} \frac{\partial e}{\partial p_m} + \frac{\partial \bar{g}}{\partial \tilde{\tau}} \frac{\partial \tilde{\tau}}{\partial p_m} + \frac{\partial \bar{g}}{\partial \tau_d} \frac{\partial \tau_d}{\partial p_m} \quad (\text{A-40})$$

with

$$\frac{\partial \bar{g}}{\partial e} = \begin{cases} -\frac{\beta c}{(x-L)^2} \sqrt{(\tau + p_s a)/A} & \text{if } u_d \leq 0 \\ -\frac{\beta c}{(x-L)^2} \sqrt{p_s - (\tau + p_s a)/A} & \text{if } u_d > 0 \end{cases} \quad (\text{A-41})$$

and

$$\frac{\partial \bar{g}}{\partial \tilde{\tau}} = \frac{\partial \bar{g}}{\partial \tau_d} = \begin{cases} \frac{\beta c}{2A(x-L)\sqrt{(\tau + p_s a)/A}} & \text{if } u_d \leq 0 \\ \frac{-\beta c}{2A(x-L)\sqrt{p_s - (\tau + p_s a)/A}} & \text{if } u_d > 0 \end{cases} \quad (\text{A-42})$$

Finally, the derivatives of u with respect to p_i 's are computed as follows

$$\frac{\partial \bar{g}}{\partial p_1} u + \bar{g} \frac{\partial u}{\partial p_1} = \frac{\partial \dot{\tau}_d}{\partial p_1} - \frac{\partial f}{\partial p_1} - k_\tau \frac{\partial \tilde{\tau}}{\partial p_1} \quad (\text{A-43})$$

$$\frac{\partial \bar{g}}{\partial p_2} u + \bar{g} \frac{\partial u}{\partial p_2} = \frac{\partial \dot{\tau}_d}{\partial p_2} - \frac{\partial f}{\partial p_2} - k_\tau \frac{\partial \tilde{\tau}}{\partial p_2} \quad (\text{A-44})$$

$$\frac{\partial \bar{g}}{\partial p_3} u + \bar{g} \frac{\partial u}{\partial p_3} = \frac{\partial \dot{\tau}_d}{\partial p_3} - \frac{\partial f}{\partial p_3} - k_\tau \frac{\partial \tilde{\tau}}{\partial p_3} - \tilde{\tau} \quad (\text{A-45})$$

This completes the computation of the gradient of the objective function.

Appendix B

Stewart Platform Kinematics and Dynamics

In this appendix, the kinematic and dynamic equations of the UBC hydraulic Stewart platform are derived. These are required in the implementation of the control laws proposed in Chapter 7. First, the kinematics of the robot are presented. This contains the inverse kinematics, the Jacobian matrix and the forward kinematics. The rigid body dynamics in workspace coordinates are also introduced. A linear-in-parameters formulation of the rigid body dynamics, needed in the proposed adaptive controllers, is developed. This appendix concludes by presenting the hydraulic actuator dynamics.

B.1 Platform Kinematics

The Stewart platform is a parallel manipulator widely used in conventional motion simulators. The schematic of the UBC motion simulator, an inverted ceiling mounted Stewart platform is shown in Figure B.1. The kinematics of the UBC Stewart platform have been derived in [71] and [27].

B.1.1 Inverse Kinematics

Two coordinate frames, namely $\{P\}$ and $\{B\}$ are assigned to the mobile platform and the stationary base as shown in Figure B.1. The platform configuration is specified by the position

and orientation of frame $\{P\}$ with respect to frame $\{B\}$. Let $q = [x \ y \ z \ \psi \ \theta \ \phi]^T$ be the generalized position of the platform in the workspace. Here, x , y and z are the Cartesian coordinates of $\{P\}$ with respect to $\{B\}$ and ψ , θ and ϕ are the platform roll, pitch and yaw angles, respectively. The platform orientation with respect to the base frame $\{B\}$ is determined by the following rotation matrix

$$\begin{aligned} {}^b R_p(\psi, \theta, \phi) &= \begin{bmatrix} \cos \phi & -\sin \phi & 0 \\ \sin \phi & \cos \phi & 0 \\ 0 & 0 & 1 \end{bmatrix} \begin{bmatrix} \cos \theta & 0 & \sin \theta \\ 0 & 1 & 0 \\ -\sin \theta & 0 & \cos \theta \end{bmatrix} \begin{bmatrix} 1 & 0 & 0 \\ 0 & \cos \psi & -\sin \psi \\ 0 & \sin \psi & \cos \psi \end{bmatrix} \\ &= \begin{bmatrix} \cos \theta \cos \phi & \sin \phi \sin \theta \cos \phi - \cos \psi \sin \phi & \cos \psi \sin \theta \cos \phi + \sin \psi \sin \phi \\ \cos \theta \sin \phi & \sin \psi \sin \theta \sin \phi + \cos \psi \cos \phi & \cos \psi \sin \theta \sin \phi - \sin \psi \cos \phi \\ -\sin \theta & \sin \psi \cos \theta & \cos \psi \cos \theta \end{bmatrix} \end{aligned} \quad (\text{B-1})$$

The i 'th actuator vector ${}^b a_i$, which is the vector from the center of the i 'th base attached joint B_i to the center of the i 'th platform attached joint P_i can be written as

$${}^b a_i = {}^b R_p {}^p p_i + {}^b d_p - {}^b b_i \quad (\text{B-2})$$

with ${}^b d_p = [x \ y \ z]^T$ and ${}^p p_i$, ${}^b b_i$ are defined in Figure B.1. In the UBC Stewart platform,

$${}^p p_i = \begin{bmatrix} r_p \cos \gamma_{pi} & r_p \sin \gamma_{pi} & \frac{h_p}{2} \end{bmatrix}^T \quad (\text{B-3})$$

and

$${}^b b_i = \begin{bmatrix} r_b \cos \gamma_{bi} & r_b \sin \gamma_{bi} & 0 \end{bmatrix}^T \quad (\text{B-4})$$

The values of the angles are given in Table B-1.

The link lengths can be computed as functions of the platform generalized position vector

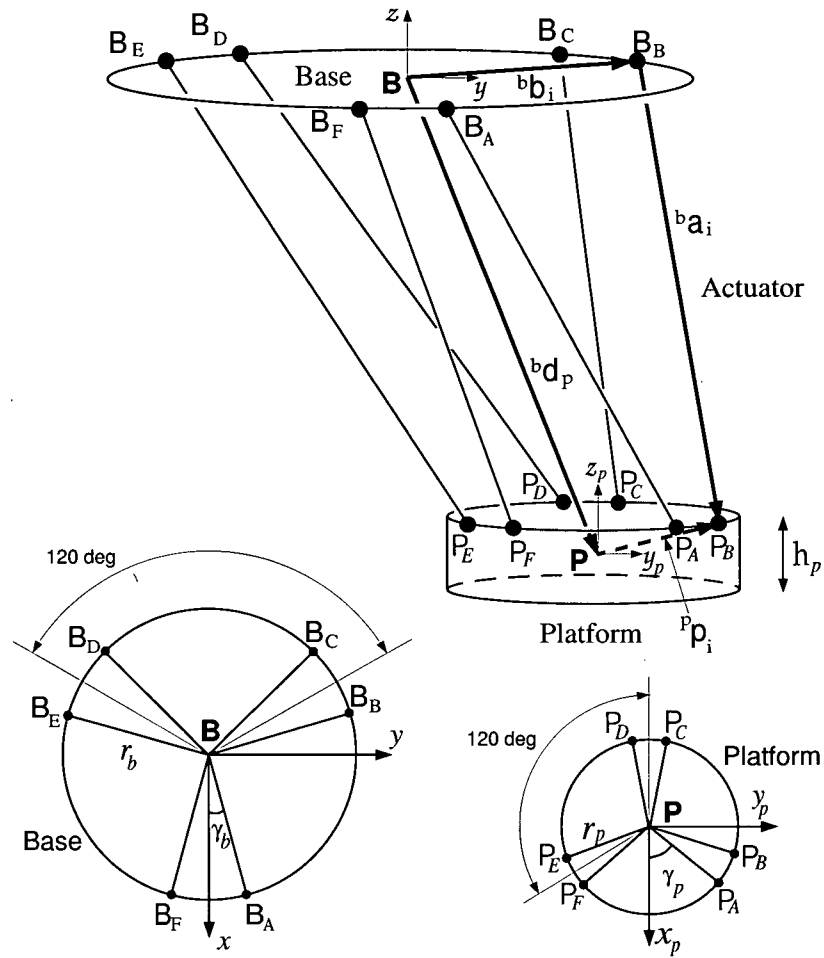


Figure B.1: The schematic of the UBC Stewart platform.

q using

$$l_i = \sqrt{{}^b a_i^T {}^b a_i} \tag{B-5}$$

B.1.2 Platform Jacobian

The link and workspace velocities can be related through the Jacobian matrix of the robot, i.e.,

$$\dot{l} = J(q) \begin{bmatrix} {}^b \dot{d}_p \\ {}^b \omega_p \end{bmatrix} \tag{B-6}$$

Table B-1: Platform and base actuator endpoint angles.

i	γ_{pi}	γ_{bi}
A	$\gamma_p = 53.4^\circ$	$\gamma_b = 7.75^\circ$
B	$120^\circ - \gamma_p$	$120^\circ - \gamma_b$
C	$120^\circ + \gamma_p$	$120^\circ + \gamma_b$
D	$-120^\circ - \gamma_p$	$-120^\circ - \gamma_b$
E	$120^\circ + \gamma_p$	$120^\circ + \gamma_b$
F	$-\gamma_p$	$-\gamma_b$

where ${}^b\omega_p$ is the platform angular velocity vector expressed in frame $\{B\}$. This vector can be written in terms of the derivatives of the platform's rotation angles as

$${}^b\omega_p = T \begin{bmatrix} \dot{\psi} \\ \dot{\theta} \\ \dot{\phi} \end{bmatrix} \quad (\text{B-7})$$

with

$$T = \begin{bmatrix} \cos \theta \cos \phi & -\sin \phi & 0 \\ \cos \theta \sin \phi & \cos \phi & 0 \\ -\sin \theta & 0 & 1 \end{bmatrix} \quad (\text{B-8})$$

It can be shown that [71]

$$\dot{i} = \begin{bmatrix} \dot{i}_A \\ \dot{i}_B \\ \dot{i}_C \\ \dot{i}_D \\ \dot{i}_E \\ \dot{i}_F \end{bmatrix} = \begin{bmatrix} ({}^bR_p{}^p p_A + {}^b d_p - {}^b b_A)^T & [({}^bR_p{}^p p_A) \times ({}^b d_p - {}^b b_A)]^T \\ ({}^bR_p{}^p p_B + {}^b d_p - {}^b b_B)^T & [({}^bR_p{}^p p_B) \times ({}^b d_p - {}^b b_B)]^T \\ \vdots & \vdots \\ ({}^bR_p{}^p p_F + {}^b d_p - {}^b b_F)^T & [({}^bR_p{}^p p_F) \times ({}^b d_p - {}^b b_F)]^T \end{bmatrix} \begin{bmatrix} {}^b \dot{d}_p \\ {}^b \omega_p \end{bmatrix} \quad (\text{B-9})$$

This completes the derivation of the Jacobian matrix.

B.1.3 Forward Kinematics

In general, there is no known closed-form solution to the forward kinematics of the Stewart platform. Dieudonne et al. in [24] use Newton's method to solve the forward kinematics problem numerically. This approach is adopted in this thesis.

Let $q = \begin{bmatrix} x & y & z & \psi & \theta & \phi \end{bmatrix}^T$ be the generalized workspace position of the platform. Consider the following nonlinear function

$$N(q) = \begin{bmatrix} |{}^b R_p{}^p p_A + {}^b d_p - {}^b b_A| - l_A \\ \vdots \\ |{}^b R_p{}^p p_F + {}^b d_p - {}^b b_F| - l_F \end{bmatrix} \quad (\text{B-10})$$

Clearly, the solution to $N(q) = 0$ is the solution to the forward kinematics problem. This is a nonlinear algebraic equation and can be solved by the Newton's iterative method. i.e.,

$$q_{k+1} = q_k - \left(\frac{\partial N(q_k)}{\partial q_k} \right)^{-1} N(q_k) \quad (\text{B-11})$$

Note that

$$\frac{\partial N(q)}{\partial q} = J(q)L \quad (\text{B-12})$$

with

$$L = \begin{bmatrix} I_{3 \times 3} & 0 \\ 0 & T \end{bmatrix} \quad (\text{B-13})$$

and T was defined in (B-8). It is worth noticing that the iteration in (B-11) involves inversion of a variable Jacobian matrix at each of its steps. However, it turned out that if the initial estimate is sufficiently close to the actual value of q , a constant J can be used. Hence, one inversion is required in each step of the forward kinematics calculation. This significantly speeds up the computation time which is important from implementation point of view. In this thesis, the realtime control of the platform is performed in the workspace. Therefore, the forward kinematics must be run at each control sample time ($f_s = 512\text{Hz}$). Considering this

sample rate, the platform position from the previous sample time is a very good candidate for the initial guess of the position at the current sample time. The forward kinematics was successfully computed in realtime with the above control update rate.

B.2 UBC Motion Simulator Dynamics

The dynamics of the UBC motion simulator can be separated into the rigid body and the hydraulic actuator dynamics. These dynamics are presented below.

B.2.1 Platform Rigid Body Dynamics

The full rigid body dynamics of the UBC Stewart platform have been derived in [71]. A simplified dynamics that ignore the leg dynamics has also been given in this reference. A slightly modified version of the simplified dynamics is used in this thesis. In the workspace coordinates, the dynamics of the platform are governed by:

$$D(q)\ddot{q} + C(q, \dot{q})\dot{q} + G = (JL)^T \tau \quad (\text{B-14})$$

where J and L have been defined in (B-9) and (B-13). The mass matrix $D(q)$ has the following form

$$D(q) = \begin{bmatrix} M_p I_{3 \times 3} & 0 \\ 0 & T^{T^b} I_p T \end{bmatrix} \quad (\text{B-15})$$

with M_p being the platform mass. Matrix C represents the Coriolis and centrifugal effects and can be written as

$$C(q, \dot{q}) = \begin{bmatrix} 0 & 0 \\ 0 & c_{22} \end{bmatrix} \quad (\text{B-16})$$

with

$$c_{22} = T^T S({}^b \omega_p)^b I_p T + T^{T^b} I_p \dot{T} \quad (\text{B-17})$$

and ${}^b I_p$ is the platform inertia matrix with respect to the base frame which is given by

$${}^b I_p = {}^b R_p {}^p I_p {}^b R_p^T \quad (\text{B-18})$$

where

$${}^p I_p = \begin{bmatrix} I_x & 0 & 0 \\ 0 & I_y & 0 \\ 0 & 0 & I_z \end{bmatrix} \quad (\text{B-19})$$

is the platform inertia in the platform attached frame $\{P\}$. The derivative of T is given below

$$\dot{T} = \begin{bmatrix} -\sin \theta \cos \phi \dot{\theta} - \cos \theta \sin \phi \dot{\phi} & \cos \phi \dot{\phi} & 0 \\ -\sin \theta \sin \phi \dot{\theta} + \cos \theta \cos \phi \dot{\phi} & -\sin \phi \dot{\phi} & 0 \\ -\cos \theta \dot{\theta} & 0 & 0 \end{bmatrix} \quad (\text{B-20})$$

Also, ${}^b \omega_p = \begin{bmatrix} \omega_x & \omega_y & \omega_z \end{bmatrix}^T$ is the angular velocity vector of the platform defined earlier and

$$S({}^b \omega_p) = \begin{bmatrix} 0 & -\omega_z & \omega_y \\ \omega_z & 0 & -\omega_x \\ -\omega_y & \omega_x & 0 \end{bmatrix} \quad (\text{B-21})$$

Finally, the gravity induced term is given by

$$G = \begin{bmatrix} 0 & 0 & M_p g & 0 & 0 & 0 \end{bmatrix}^T \quad (\text{B-22})$$

Note that (B-14) is not exactly as (7.1). Nevertheless, since J is a function of the platform position and is known, the controllers can be easily modified to be used in this case. The rigid body dynamics may be written in the *linear-in-parameters* form.

$$D(q)\ddot{q} + C(q, \dot{q})\dot{q} + G = Y_{6 \times 4}(q, \dot{q}, \ddot{q})\theta \quad (\text{B-23})$$

where $\theta = \begin{bmatrix} M_p & I_x & I_y & I_z \end{bmatrix}^T$ is the vector of unknown parameters. The derivation of Y is fairly straightforward and only the final results are presented here.

$$Y_{6 \times 4}(q, \dot{q}_1, \dot{q}_2, \ddot{q}) = \begin{bmatrix} \ddot{x} & 0 & 0 & 0 \\ \ddot{y} & 0 & 0 & 0 \\ \ddot{z} + g & 0 & 0 & 0 \\ 0 & Y_\theta(1, 1) & Y_\theta(1, 2) & Y_\theta(1, 3) \\ 0 & Y_\theta(2, 1) & Y_\theta(2, 2) & Y_\theta(2, 3) \\ 0 & Y_\theta(3, 1) & Y_\theta(3, 2) & Y_\theta(3, 3) \end{bmatrix} \quad (\text{B-24})$$

where

$$Y_\theta = T^T (Y_D + Y_C) \quad (\text{B-25})$$

with

$$Y_C(1, 1) = r_{21}r_{31}(v_y\omega_y - v_z\omega_z) + \omega_y r_{31}(v_x r_{11} + v_z r_{31}) - \omega_z r_{21}(v_y r_{21} + v_x r_{11}) \quad (\text{B-26})$$

$$Y_C(1, 2) = v_z r_{32}(\omega_y r_{32} - \omega_z r_{22}) + v_x r_{12}(\omega_y r_{32} - \omega_z r_{22}) + v_y r_{22}(\omega_y r_{32} - \omega_z r_{22}) \quad (\text{B-27})$$

$$Y_C(1, 3) = v_x r_{13}(\omega_y r_{33} - \omega_z r_{23}) + v_y r_{23}(\omega_y r_{33} - \omega_z r_{23}) + v_z r_{33}(\omega_y r_{33} - \omega_z r_{23}) \quad (\text{B-28})$$

$$Y_C(2, 1) = v_y r_{21}(\omega_z r_{11} - \omega_x r_{31}) + v_z r_{31}(\omega_z r_{11} - \omega_x r_{31}) + v_x r_{11}(\omega_z r_{11} - \omega_x r_{31}) \quad (\text{B-29})$$

$$Y_C(2, 2) = r_{12}r_{32}(v_z\omega_z - v_x\omega_x) - \omega_x r_{32}(v_z r_{32} + v_y r_{22}) + \omega_z r_{12}(v_x r_{12} + v_y r_{22}) \quad (\text{B-30})$$

$$Y_C(2, 3) = v_x r_{13}(\omega_z r_{13} - \omega_x r_{33}) + v_y r_{23}(\omega_z r_{13} - \omega_x r_{33}) + v_z r_{33}(\omega_z r_{13} - \omega_x r_{33}) \quad (\text{B-31})$$

$$Y_C(3, 1) = -\omega_y r_{11}(v_z r_{31} + v_y r_{21}) + \omega_x r_{21}(v_y r_{21} + v_z r_{31}) + v_x r_{11}(\omega_x r_{21} - \omega_y r_{11}) \quad (\text{B-32})$$

$$Y_C(3, 2) = v_z r_{32}(\omega_x r_{22} - \omega_y r_{12}) + v_x r_{12}(\omega_x r_{22} - \omega_y r_{12}) + v_y r_{22}(\omega_x r_{22} - \omega_y r_{12}) \quad (\text{B-33})$$

$$Y_C(3, 3) = r_{13}r_{23}(v_x\omega_x - v_y\omega_y) + \omega_x r_{23}(v_z r_{33} + v_y r_{23}) - \omega_y r_{13}(v_z r_{33} + v_x r_{13}) \quad (\text{B-34})$$

$$Y_D(1, 1) = \alpha_x r_{11}^2 + \alpha_y r_{11} r_{21} + \alpha_z r_{11} r_{31} \quad (\text{B-35})$$

$$Y_D(1, 2) = \alpha_x r_{12}^2 + \alpha_y r_{12} r_{22} + \alpha_z r_{12} r_{32} \quad (\text{B-36})$$

$$Y_D(1, 3) = \alpha_x r_{13}^2 + \alpha_y r_{13} r_{23} + \alpha_z r_{13} r_{33} \quad (\text{B-37})$$

$$Y_D(2, 1) = \alpha_x r_{11} r_{21} + \alpha_y r_{21}^2 + \alpha_z r_{21} r_{31} \quad (\text{B-38})$$

$$Y_D(2, 2) = \alpha_x r_{12} r_{22} + \alpha_y r_{22}^2 + \alpha_z r_{22} r_{32} \quad (\text{B-39})$$

$$Y_D(2, 3) = \alpha_x r_{13} r_{23} + \alpha_y r_{23}^2 + \alpha_z r_{23} r_{33} \quad (\text{B-40})$$

$$Y_D(3, 1) = \alpha_x r_{11} r_{31} + \alpha_y r_{21} r_{31} + \alpha_z r_{31}^2 \quad (\text{B-41})$$

$$Y_D(3, 2) = \alpha_x r_{12} r_{32} + \alpha_y r_{22} r_{32} + \alpha_z r_{32}^2 \quad (\text{B-42})$$

$$Y_D(3, 3) = \alpha_x r_{13} r_{33} + \alpha_y r_{23} r_{33} + \alpha_z r_{33}^2 \quad (\text{B-43})$$

In the above formulas,

$$\begin{bmatrix} \omega_x \\ \omega_y \\ \omega_z \end{bmatrix} = T \begin{bmatrix} \dot{\psi}_1 \\ \dot{\theta}_1 \\ \dot{\phi}_1 \end{bmatrix} \quad (\text{B-44})$$

and

$$\begin{bmatrix} v_x \\ v_y \\ v_z \end{bmatrix} = T \begin{bmatrix} \dot{\psi}_2 \\ \dot{\theta}_2 \\ \dot{\phi}_2 \end{bmatrix} \quad (\text{B-45})$$

Furthermore,

$$\begin{bmatrix} \alpha_x \\ \alpha_y \\ \alpha_z \end{bmatrix} = T \begin{bmatrix} \ddot{\psi} \\ \ddot{\theta} \\ \ddot{\phi} \end{bmatrix} + \dot{T} \begin{bmatrix} \dot{\psi} \\ \dot{\theta} \\ \dot{\phi} \end{bmatrix} \quad (\text{B-46})$$

It is also assumed that

$${}^b R_p(\psi, \theta, \phi) = [r_{ij}] \quad (\text{B-47})$$

The linear-in-parameters form of the rigid body dynamics obtained here are used in the adaptive control of the UBC motion simulator in Chapter 7.

B.2.2 Actuator Dynamics

The dynamics of the Stewart platform hydraulic actuators are presented in this Appendix. A three-way valve configuration is assumed to be used in the actuators, as shown in Figure B.2. For such configuration, the control pressure dynamics are governed by [83]

$$\frac{V_t}{\beta} \dot{p}_c = q_l + c_l(p_s - p_c) - \dot{V}_t \quad (\text{B-48})$$

where V_t is the trapped fluid volume in the control side, β is the effective bulk modulus, p_c is the control pressure acting on the control side, p_s is the supply pressure acting on the rod side, q_l is the load flow, and c_l is the coefficient of total leakage. The load flow, q_l , is a nonlinear function of the control pressure and the valve spool position and is given by

$$q_l = \begin{cases} c(u - d)\sqrt{p_c} & u < -d \\ c(u + d)\sqrt{p_s - p_c} + c(u - d)\sqrt{p_c} & -d \leq u \leq d \\ c(u + d)\sqrt{p_s - p_c} & u > d \end{cases} \quad (\text{B-49})$$

and $c = c_d w \sqrt{\frac{2}{\rho}}$, where c_d is the effective discharge coefficient, w is the port width of the valve, ρ is the density of the fluid, d is the valve underlap length and u is the valve spool position which is the control command. Note that the actuator output force is $\tau = p_c A - p_s a$. Therefore, using (B-48) and (B-49), the dynamics of the i 'th hydraulic actuator can be written in the following form (assuming $c_l \approx 0$)

$$\dot{\tau}^i = -\frac{A\beta^i \dot{q}^i}{q^i - l^i} + \frac{\beta^i}{q^i - l^i} q_l^i(\tau^i, u^i) = f^i(q^i, \dot{q}^i) + g^i(q^i, \tau^i, u^i) \quad (\text{B-50})$$

where l is the actuator stroke length. For a Stewart platform, there are six actuators driving

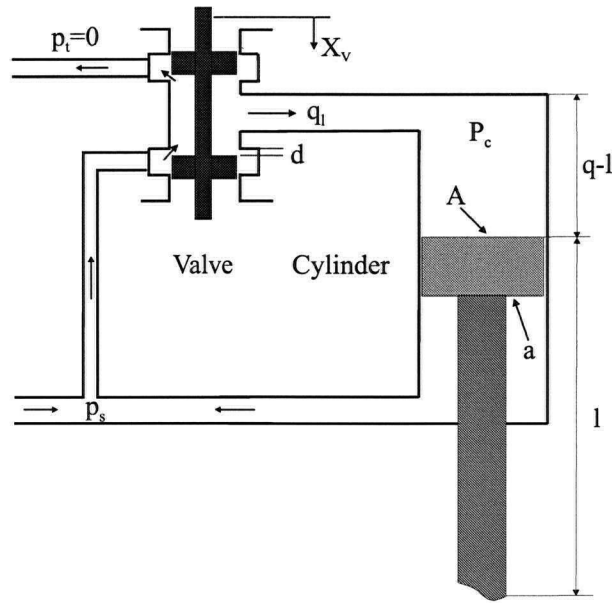


Figure B.2: A typical three-way valve configuration.

the system. The actuator subsystem dynamics can be represented in matrix form as follows

$$\dot{\tau} = f(q, \dot{q}) + g(q, \tau, u) \quad (\text{B-51})$$

where u is the control command vector and f , g are nonlinear functions of q , \dot{q} and τ . These vectors are obtained by stacking τ^i , f^i and g^i from above. Note that (B-50) can be rewritten in the following form which is suitable for adaptive control:

$$\dot{\tau}^i = \gamma_1^i f_0^i(q^i, \dot{q}^i) + \gamma_2^i g_0^i(q^i, \tau^i, u^i) \quad (\text{B-52})$$

where $\gamma^i = \begin{bmatrix} \beta^i & \beta^i c^i \end{bmatrix}^T$, $f_0^i = -\frac{A^i \dot{q}^i}{q^i - l^i}$, and $g_0^i = \frac{q_l^i}{c_i(q^i - l^i)}$ (does not depend on c_i^s , see (B-49)). These equations can also be expressed in matrix form as

$$\dot{\tau} = f_0(q, \dot{q})\gamma_1 + g_0(q, \tau, u)\gamma_2 \quad (\text{B-53})$$

Appendix C

Joystick Kinematics and Control

In this appendix, the kinematic equations of the twin-pantograph interface used in this thesis are derived. A linear-in-parameters model for the effect of gravity is also obtained. The parameters of this model are identified experimentally. The model along with the identified parameters are used to compensate for the effect of gravity on the joystick. The control of the joystick in the workspace coordinates is also addressed. To exploit the redundancy in the actuation, a minimum-torque solution for the problem is developed.

C.1 Joystick Kinematics

A schematic of the twin-pantograph force-feedback joystick is shown in Figure C.1. As can be seen from this figure, the device is formed by connecting two ideal pantographs through a handle bar. Each of the pantographs has two degrees of freedom. The resultant manipulator has only three degrees of freedom due to the kinematic constraint in its closed chain structure. Therefore, there is one degree of redundancy in the actuation of the interface.

Point C in Figure C.1 is where the operator grasps the joystick. The device position in the workspace coordinates is determined by the following vector:

$$X_C = \begin{bmatrix} x_c & y_c & \phi \end{bmatrix}^T \quad (\text{C-1})$$

The end points of the two pantographs and the joystick workspace position can be related as

follows

$$P_5 = x_5 \hat{i} + y_5 \hat{j} = (x_c - \lambda l_b \cos \phi) \hat{i} + (y_c - \lambda l_b \sin \phi) \hat{j} \quad (C-2)$$

$$P_6 = x_6 \hat{i} + y_6 \hat{j} = [x_c + (1 - \lambda)l_b \cos \phi] \hat{i} + [y_c + (1 - \lambda)l_b \sin \phi] \hat{j} \quad (C-3)$$

with λ and l_b defined in Figure C.1. Equivalently, the workspace positions can be expressed in terms of the endpoint positions.

$$\phi = \tan^{-1} \left(\frac{y_6 - y_5}{x_6 - x_5} \right) \quad (C-4)$$

$$x_c = x_5 + \lambda l_b \cos \phi \quad (C-5)$$

$$y_c = y_5 + \lambda l_b \sin \phi \quad (C-6)$$

By taking the derivatives of (C-2) and (C-3),

$$\dot{X}_e = J_c \dot{X}_C \quad (C-7)$$

where $\dot{X}_e = \begin{bmatrix} \dot{x}_5 & \dot{y}_5 & \dot{x}_6 & \dot{y}_6 \end{bmatrix}^T$ and J_c is a Jacobian matrix relating the workspace velocities to the endpoint velocities.

$$J_{c(4 \times 3)} = \begin{bmatrix} 1 & 0 & \lambda l_b \sin \phi \\ 0 & 1 & -\lambda l_b \cos \phi \\ 1 & 0 & -(1 - \lambda)l_b \sin \phi \\ 0 & 1 & (1 - \lambda)l_b \cos \phi \end{bmatrix} \quad (C-8)$$

Now, the Jacobian matrix relating the endpoint velocities to the joint velocities of a single pantograph must be found. Note from Figure C.1 that

$$P_1 = (l_1 \cos \theta_1 + d) \hat{i} + (l_1 \sin \theta_1) \hat{j} \quad (C-9)$$

$$P_2 = (l_1 \cos \theta_2) \hat{i} + (l_1 \sin \theta_2) \hat{j} \quad (C-10)$$

$$(C-11)$$

with

$$\rho_1 = \frac{|h_1|}{|P_{12}|} \quad (\text{C-15})$$

Note that

$$|h_1|^2 = l_2^2 - \frac{|P_{12}|^2}{4} \quad (\text{C-16})$$

therefore, one can write

$$\rho_1 = \sqrt{\frac{l_2^2}{|P_{12}|^2} - \frac{1}{4}} \quad (\text{C-17})$$

The position of Point #5 in terms of joint variables θ_1 and θ_2 is given by

$$P_5 = x_5 \hat{i} + y_5 \hat{j} = P_2 + \frac{1}{2}(P_1 - P_2) + h_1 = \frac{1}{2}(P_1 + P_2) + h_1 \quad (\text{C-18})$$

Similarly, Point #6 can be expressed in terms of joint variables θ_3 and θ_4 .

$$P_6 = x_6 \hat{i} + y_6 \hat{j} = P_4 + \frac{1}{2}(P_3 - P_4) + h_2 = \frac{1}{2}(P_3 + P_4) + h_2 \quad (\text{C-19})$$

The Jacobian matrix J_{e1} relating the joint velocities to the endpoint velocities can be written as

$$J_{e1} = \begin{bmatrix} \frac{\partial x_5}{\partial \theta_1} & \frac{\partial x_5}{\partial \theta_2} \\ \frac{\partial y_5}{\partial \theta_1} & \frac{\partial y_5}{\partial \theta_2} \end{bmatrix} \quad (\text{C-20})$$

with

$$\frac{\partial x_5}{\partial \theta_1} = \frac{1}{2} \frac{\partial x_1}{\partial \theta_1} + \frac{1}{2} \frac{\partial x_2}{\partial \theta_1} + \frac{\partial \rho_1}{\partial \theta_1} (y_2 - y_1) + \rho_1 \left(\frac{\partial y_2}{\partial \theta_1} - \frac{\partial y_1}{\partial \theta_1} \right) \quad (\text{C-21})$$

$$\frac{\partial x_5}{\partial \theta_2} = \frac{1}{2} \frac{\partial x_1}{\partial \theta_2} + \frac{1}{2} \frac{\partial x_2}{\partial \theta_2} + \frac{\partial \rho_1}{\partial \theta_2} (y_2 - y_1) + \rho_1 \left(\frac{\partial y_2}{\partial \theta_2} - \frac{\partial y_1}{\partial \theta_2} \right) \quad (\text{C-22})$$

$$\frac{\partial y_5}{\partial \theta_1} = \frac{1}{2} \frac{\partial y_1}{\partial \theta_1} + \frac{1}{2} \frac{\partial y_2}{\partial \theta_1} + \frac{\partial \rho_1}{\partial \theta_1} (x_1 - x_2) + \rho_1 \left(\frac{\partial x_1}{\partial \theta_1} - \frac{\partial x_2}{\partial \theta_1} \right) \quad (\text{C-23})$$

$$\frac{\partial y_5}{\partial \theta_2} = \frac{1}{2} \frac{\partial y_1}{\partial \theta_2} + \frac{1}{2} \frac{\partial y_2}{\partial \theta_2} + \frac{\partial \rho_1}{\partial \theta_2} (x_1 - x_2) + \rho_1 \left(\frac{\partial x_1}{\partial \theta_2} - \frac{\partial x_2}{\partial \theta_2} \right) \quad (\text{C-24})$$

Furthermore,

$$\frac{\partial x_1}{\partial \theta_1} = -l_1 \sin \theta_1 \quad \frac{\partial x_1}{\partial \theta_2} = 0 \quad (\text{C-25})$$

$$\frac{\partial y_1}{\partial \theta_1} = l_1 \cos \theta_1 \quad \frac{\partial y_1}{\partial \theta_2} = 0 \quad (\text{C-26})$$

$$\frac{\partial x_2}{\partial \theta_1} = 0 \quad \frac{\partial x_2}{\partial \theta_2} = -l_1 \sin \theta_2 \quad (\text{C-27})$$

$$\frac{\partial y_2}{\partial \theta_1} = 0 \quad \frac{\partial y_2}{\partial \theta_2} = l_2 \cos \theta_2 \quad (\text{C-28})$$

and

$$\frac{\partial \rho_1}{\partial \theta_1} = -\frac{l_2^2}{2|P_{12}|^4 \rho_1} \frac{\partial |P_{12}|^2}{\partial \theta_1} \quad (\text{C-29})$$

$$\frac{\partial \rho_1}{\partial \theta_2} = -\frac{l_2^2}{2|P_{12}|^4 \rho_1} \frac{\partial |P_{12}|^2}{\partial \theta_2} \quad (\text{C-30})$$

The followings are also needed in the calculation of the above partial derivatives

$$\frac{\partial |P_{12}|^2}{\partial \theta_1} = -2l_1 d \sin \theta_1 + 2l_1^2 \sin(\theta_1 - \theta_2) \quad (\text{C-31})$$

$$\frac{\partial |P_{12}|^2}{\partial \theta_2} = 2l_1 d \sin \theta_2 - 2l_1^2 \sin(\theta_1 - \theta_2) \quad (\text{C-32})$$

This completes the derivation of J_{e1} . Similar steps can be taken to compute J_{e2} . The endpoint

velocities can be related to the joint velocities as follows

$$\begin{bmatrix} \dot{x}_5 \\ \dot{y}_5 \\ \dot{x}_6 \\ \dot{y}_6 \end{bmatrix} = \begin{bmatrix} J_{e1} & 0 \\ 0 & J_{e2} \end{bmatrix} \begin{bmatrix} \dot{\theta}_1 \\ \dot{\theta}_2 \\ \dot{\theta}_3 \\ \dot{\theta}_4 \end{bmatrix} \quad (\text{C-33})$$

Using (C-7) and (C-33),

$$\dot{\theta} = J_e^{-1} J_c \dot{X}_C = J_{(4 \times 3)} \dot{C} \quad (\text{C-34})$$

where $\theta = \begin{bmatrix} \theta_1 & \theta_2 & \theta_3 & \theta_4 \end{bmatrix}^T$ and J is a Jacobian matrix relating the workspace velocities to the joint space velocities.

C.2 Gravity Compensation

In order to remove the effect of gravity on the joystick, a gravity compensation term is proposed here. It is assumed that base of the joystick is horizontal in this derivation. This is in fact the case in the feedthrough cancelation experiments carried out in this research. The resultant gravity compensation would not be accurate if the platform rolls, pitches or yaws.

As it is shown in Figure C.1, the joint masses are replaced with point masses m_1 - m_6 . The handle bar is represented by an equivalent point mass m_7 at a distance αl_b from Point #5. The masses of the links are negligible compared to those of the joints. Note that since m_5 , m_6 and m_7 always lie on a line, they may be replaced by a single point mass m_7 along that line. Hence, m_5 and m_6 are ignored in the gravity compensation.

To begin, the gravity force in the joint space due to masses m_1 and m_2 are calculated.

$$\tau_{g1} = m_1 g \begin{bmatrix} \frac{\partial y_1}{\partial \theta_1} & \frac{\partial y_1}{\partial \theta_2} & \frac{\partial y_1}{\partial \theta_3} & \frac{\partial y_1}{\partial \theta_4} \end{bmatrix}^T = \begin{bmatrix} m_1 g l_1 \cos \theta_1 & 0 & 0 & 0 \end{bmatrix}^T \quad (\text{C-35})$$

$$\tau_{g2} = m_2 g \begin{bmatrix} \frac{\partial y_2}{\partial \theta_1} & \frac{\partial y_2}{\partial \theta_2} & \frac{\partial y_2}{\partial \theta_3} & \frac{\partial y_2}{\partial \theta_4} \end{bmatrix}^T = \begin{bmatrix} 0 & m_2 g l_1 \cos \theta_2 & 0 & 0 \end{bmatrix}^T \quad (\text{C-36})$$

Similarly, for Points #3 and #4

$$\tau_{g3} = m_3g \begin{bmatrix} \frac{\partial y_3}{\partial \theta_1} & \frac{\partial y_3}{\partial \theta_2} & \frac{\partial y_3}{\partial \theta_3} & \frac{\partial y_3}{\partial \theta_4} \end{bmatrix}^T = \begin{bmatrix} 0 & 0 & m_3gl_1 \cos \theta_3 & 0 \end{bmatrix}^T \quad (\text{C-37})$$

$$\tau_{g4} = m_4g \begin{bmatrix} \frac{\partial y_4}{\partial \theta_1} & \frac{\partial y_4}{\partial \theta_2} & \frac{\partial y_4}{\partial \theta_3} & \frac{\partial y_4}{\partial \theta_4} \end{bmatrix}^T = \begin{bmatrix} 0 & 0 & 0 & m_4gl_1 \cos \theta_4 \end{bmatrix}^T \quad (\text{C-38})$$

The effect of the handle bar is introduced by the following generalized workspace force vector

$$f_{g7} = \begin{bmatrix} 0 & m_7g & -\beta m_7gl_b \cos \phi \end{bmatrix}^T \quad (\text{C-39})$$

with $\beta = \lambda - \alpha$. The total generalized workspace force required to balance the joystick can be computed as

$$f_g = f_{g7} + J^T (\tau_{g1} + \tau_{g2} + \tau_{g3} + \tau_{g4}) \quad (\text{C-40})$$

where J is the device Jacobian in (C-34). Interestingly, this work-space force does not correspond to a unique motor torque vector (i.e. due to redundancy in actuation). A minimum-norm solution for the equivalent joint space torque can be computed as follows

$$\tau_g = J (J^T J)^{-1} f_g \quad (\text{C-41})$$

C.2.1 Identification of the Parameters

The values of parameters m_1, m_2, m_3, m_4, m_7 and β are required for the gravity compensation. A *Least Squares* based identification approach is used to estimate these unknown parameters. A workspace PD controller was implemented on the device. The joystick was positioned in different locations in the workspace using this controller. The required work-space force to hold the joystick against gravity and the joint angles were measured at each point.

The workspace gravity force at the k 'th point may be written as

$$f_g(k) = Y(k)\zeta \quad (\text{C-42})$$

$$\text{with } \theta(k) = \begin{bmatrix} \theta_1(k), \theta_2(k), \theta_3(k), \theta_4(k) \end{bmatrix}^T \text{ and } \zeta = \begin{bmatrix} m_1g & m_2g & m_3g & m_4g & m_7g & \beta m_7g \end{bmatrix}^T.$$

Also,

$$Y(k) = J^T \begin{bmatrix} l_1 \cos \theta_1(k) & 0 & 0 & 0 & 0 & 0 \\ 0 & l_1 \cos \theta_2(k) & 0 & 0 & 0 & 0 \\ 0 & 0 & l_1 \cos \theta_3(k) & 0 & 0 & 0 \\ 0 & 0 & 0 & l_1 \cos \theta_4(k) & 0 & 0 \end{bmatrix} \quad (C-43)$$

$$+ \begin{bmatrix} 0 & 0 & 0 & 0 & 0 & 0 \\ 0 & 0 & 0 & 0 & 1 & 0 \\ 0 & 0 & 0 & 0 & 0 & -l_b \cos \phi(k) \end{bmatrix}$$

The measurements from $N = 300$ different points were stacked and the parameter estimates were found using the *Least Squares* technique, i.e.,

$$f_g^N = \begin{bmatrix} f_g(1) \\ \vdots \\ f_g(N) \end{bmatrix} = \begin{bmatrix} Y(1) \\ \vdots \\ Y(N) \end{bmatrix} \zeta = Y_N \zeta \quad (C-44)$$

$$\hat{\zeta} = (Y_N^T Y_N)^{-1} Y_N^T f_g^N \quad (C-45)$$

The followings were obtained from the experiment ($\lambda = 2$):

$$\begin{aligned} m_{1g} &= 0.2054\text{N} & m_{2g} &= 0.5319\text{N} & m_{3g} &= 0.2414\text{N} \\ m_{4g} &= 0.320172\text{N} & m_{7g} &= 5.7695\text{N} & \beta &= 0.8165 \end{aligned}$$

The discrepancies in the estimated mass of similar joints are likely to be due to friction in the joints and the gearheads. The estimated parameters were successfully used to compensate for the effect of gravity.

To control the joystick in the workspace coordinates, the following minimum-norm torque solution is employed

$$\tau_c = J (J^T J)^{-1} [\hat{f}_g + f_c] \quad (C-46)$$

where f_c is the desired generalized control force in the workspace coordinates.